On-board geolocation by satellite constellations: advanced algorithms ready for programmable hardware

Original Citation:
On-board geolocation by satellite constellations: advanced algorithms ready for programmable hardware / Asciolla, Marcello. - ELETTRONICO. - (2026). [10.60576/poliba/iris/asciolla-marcello_phd2026]

Availability:
This version is available at http://hdl.handle.net/11589/295300 since: 2026-01-08

Published version
DOI:10.60576/poliba/iris/asciolla-marcello_phd2026

Publisher: Politecnico di Bari

Finanziato dall'Unione europea
NextGenerationEU
Ministero dell'Università e della Ricerca
Italiadomani
PIANO NAZIONALE DI RIPRESA E RESILIENZA
Politecnico di Bari

POLITECNICO DI BARI

DEPARTMENT OF ELECTRICAL AND INFORMATION ENGINEERING
Scientific-disciplinary sector: IINF-01/A – Electronics

Philosophiae Doctor Dissertation

ON-BOARD GEOLOCATION BY SATELLITE CONSTELLATIONS: ADVANCED ALGORITHMS READY FOR PROGRAMMABLE HARDWARE

Author
Marcello Asciolla

Supervisor
Prof. Eng. Francesco Dell'Olio

Co-supervisors
Prof. Eng. Vittorio M. N. Passaro
Eng. Riccarco Albi
Eng. Filippo Speziali

Coordinator
Prof. Eng. Mario Carpentieri

Funded by the European Union, Next Generation EU, Mission 4 Comp. 2, CUP D93D22001320001

Cycle XXXVIII, 01 Nov. 2022 - 31 Oct. 2025

Finanziato dall'Unione europea
NextGenerationEU
Ministero dell'Università e della Ricerca
Italiadomani
PIANO NAZIONALE DI RIPRESA E RESILIENZA
Politecnico di Bari

POLITECNICO DI BARI

DEPARTMENT OF ELECTRICAL AND INFORMATION ENGINEERING
Scientific-disciplinary sector: IINF-01/A – Electronics

Philosophiae Doctor Dissertation

On-Board Geolocation by Satellite Constellations: Advanced Algorithms Ready for Programmable Hardware

Author
Marcello Asciolla Marcello Asciolla

Supervisor
Prof. Eng. Francesco Dell'Olio Francesco Dell'Olio

Co-supervisors
Prof. Eng. Vittorio M. N. Passaro
Eng. Riccarco Albi Riccardo Albi
Eng. Filippo Speziali

Coordinator
Prof. Eng. Mario Carpentieri Mario Carpentieri

Referees
Prof. Eng. Rodrigo Blázquez-García
Eng. Philipp Markiton (né Wojaczek)

Funded by the European Union, Next Generation EU, Mission 4 Comp. 2, CUP D93D22001320001

Cycle XXXVIII, 01 Nov. 2022 - 31 Oct. 2025

Abstract

The objective of the thesis is the study of the geolocation systems of sources of electromagnetic waves based on satellite platforms in Low Earth Orbit (LEO). Among the main technologies, Angle of Arrival (AOA) based on arrays of antennas gained recent interest thanks to miniaturization of electronic components and has been considered as reference payload for the satellite platforms. The context of the research is at multiple levels: it started with a conceptual design of a possible abstract architecture to be implemented at hardware level in a Field Programmable Gate Array (FPGA), then it moved toward its possibility to be simulated in a dedicated environment for performance prediction. The characterization of antenna array performance has also been conducted and new frontiers on relativistic and atmospheric effects on time delay, longitude shift, changes in frequency, bending of electromagnetic waves, and beam wander have been explored. Firstly, the toy-model considered a geolocation scenario involving a single emitter of signal on the surface of the Earth and a single satellite platform, then multi-satellite systems, and also multi-constellations have been studied. Among the research objectives are: the development of algorithms of error detection and correction to be performed onboard, in particular with respect to the phenomenon of the divergence of the dispersion of the measurement due to the influence of the Attitude Determination and Control System (ADCS); the optimization of clusters of satellites; the investigation of possibility to integrate the payload in hybrid measurements with Time Difference of Arrival (TDOA) technology or the possibility to exploit opportunities of measurement from multiple constellations. The importance of the study which constitutes also the main motivation is on the set of operations of search and rescue and spectrum monitoring of jamming signals. Each research objective has been defined in order to address industrial needs or unexplored fields in the existing literature. To support the need for the development of new models, the research methodology is mainly formal and analytical, with simulation support when needed.

Preface

This work of thesis is the result of three years of research. In particular:

- 24 months at the Department of Electrical and Information Engineering of the Polytechnic University of Bari (Bari, Italy);
- 6 months at the facilities of MetaSensing S.r.l. (Milan, Italy) as visiting researcher;
- 6 months at the Department of Signals, Systems and Radiocommunications (SSR) of Universidad Politécnica de Madrid (Madrid, Spain) as visiting researcher.

The author acknowledges the financial support of the Ph.D. programme provided by the Italin Ministry of University and Research (MUR), the Polytechnic University of Bari (Italy), and MetaSensing S.r.l.. This doctoral research has been co-funded under the Italian National Recovery and Resilience Plan (PNRR), Mission 4, DM 352/2022.

The author acknowledges also the interactions and exchange of ideas with the European Commission, Joint Research Center, Space Sector (Italy), which commissioned two works on a *pro bono* basis without financial compensation.

The content of this document represents a summary of the published work of the author and does not represent the official point of view or the set of products and services of the financial sponsor MetaSensing S.r.l. or the activities of European Commission, Joint Research Center, Space Sector.

The activities began on the 1st of November 2022 and ended on the 31st of October 2025.

Contents

Acronyms

ADCS Attitude Determination and Control System

AOA Angle of Arrival

AWGN Additive White Gaussian Noise

BRF Body Reference Frame

BVP Boundary Value Problem

CRLB Cramér-Rao Lower Bound

DOA Direction of Arrival

DOP Dilution of Precision

DRFM Digital Radio Frequency Memory

DS Direct Search

DSSS Direct Sequence Spread Spectrum

ECCM Electronic Counter-Countermeasure

ECEF Earth-Centered Earth-Fixed

ECI Earth-Centered Inertial

ECM Electronic Countermeasure

ESPRIT Estimation of Signal Parameters via Rotational Invariance Techniques

EW Electromagnetic Wave

FHSS Frequency-Hopping Spread Spectrum

FPGA Field Programmable Gate Array

FSM Finite State Machine

GEO	Geosynchronous Earth Orbit
GNC	Guidance, Navigation, and Control
GNSS	Global Navigation Satellite System
GS	General Search
HEO	High Earth Orbit
IVP	Initial Value Problem
LEO	Low Earth Orbit
LLH	Latitude, Longitude, and Height
LOB	Line of Bearing
LOS	Line of Sight
MEMS	Micro-Electro-Mechanical Systems
MEO	Medium Earth Orbit
MLE	Maximum Likelihood Estimation
MUSIC	Multiple Signal Classification
ORF	Orbiting Reference Frame
PDOP	Position Dilution of Precision
PQW	Perifocal Coordinate System
RF	Radio Frequency
RMS	Root Mean Square
ROC	Receiver Operating Characteristic
RSS	Received Signal Strength
SEU	Single Event Upset
SHF	Super High Frequency
SNR	Signal-to-Noise Ratio
TDOA	Time Difference of Arrival

TOA Time of Arrival

UHF Ultra High Frequency

ULA Uniform Linear Array

URA Uniform Rectangular Array

VHF Very High Frequency

Chapter 1

Reference System and Performances

This section is intended to introduce the reader to the reference mission and presents the architecture conceived for the satellite system used for the geolocation problem. Then, there is the description of the payload, which is based on antenna array and its measurement principle. In the end, methods are presented to predict the performance of the payload.

1.1 Reference Mission and Use Cases

The reference mission considers an emitter of electromagnetic waves, in the following denoted by E, and a satellite platform, in the following denoted by S, with a receiver of electromagnetic waves based on AOA technology. It is supposed that the emitter of signal is non-cooperative with respect to the satellite. A source of signal is denoted as non-cooperative when it is not supposed to be known in terms of presence, location, and transmitted message.

The point of view of the study is the satellite system, and the objective of its mission is the geolocation of the source of the signal.

The model considers two actors, the emitter of signal E (actor 1) and the satellite system S (actor 2), and there are four use cases: 'signal emission', 'signal reception', 'geolocation of the signal', and 'tracking of the signal'.

The use case 'signal emission' is the only one involved in the the process of emission of the signal and is performed by actor 1 (emitter): in the context of this study it is supposed to happen in any case, because the interest of the thesis is on the satellite system. The emitted signal can be instantaneous or persistent in a certain interval of time.

The set of use cases 'signal reception', 'geolocation of the signal', and 'tracking of the signal' represents the process of geolocation performed by actor 2 (satellite). In particular, the process is articulated as follows:

- The use case 'signal reception' is performed by actor 2 and this is conditioned

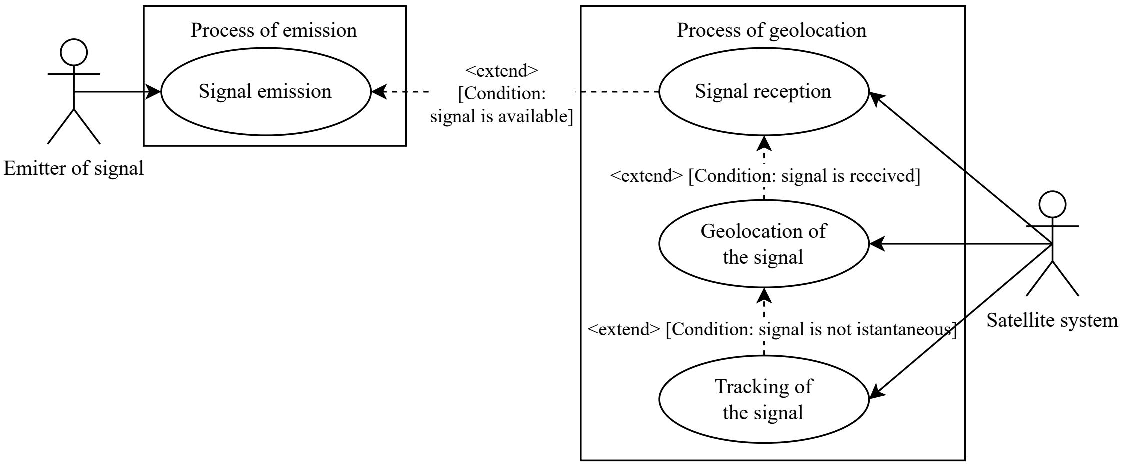

Figure 1.1: Use cases diagram used as reference.

to the availability of the signal by the reception system and conditioned to the verification of use case 'signal emission';

- The use case 'geolocation of the signal' is performed by actor 2 and this event is conditioned to the verification of use case 'signal reception'.
- The use case 'tracking of the signal' is performed by actor 2, it is conditioned to the availability of the signal in a certain interval of time (i.e., the emitted signal is not instantaneous), and it is conditioned to verification of multiple times of the use case 'geolocation of the signal'.

To summarise the interaction of the actors with the processes, the use case diagram is reported in Fig. 1.1.

1.2 Finite State Machines

Each system can be designed according to the requirements. The main ones considered in the study are the following:

Requirement 1: the platform is a satellite system in LEO;

Requirement 2: the payload is an antenna array receiver with electronic scanning capabilities;

Requirement 3: the system must be able to scan an area for a Radio Frequency (RF) signal (idle / listening state);

Requirement 4: the system must be able to recognise a RF signal (detection);

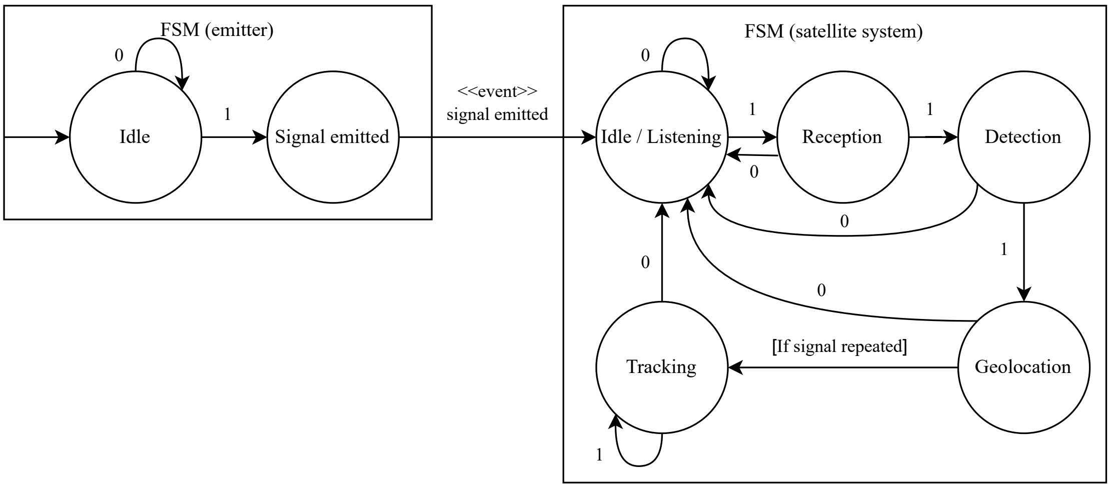

Figure 1.2: FSM diagram of the system built from the requirements.

Requirement 5: the system must be able to estimate the position of a RF signal (geolocation);

Requirement 6: the system must be able to track a geolocated RF signal when its detection and geolocation are repeated over time (tracking).

From the requirements and the use case diagram in Fig. 1.1, a first broad description of the behaviour of the system in the form of two Finite State Machine (FSM) with an interface between them has been conceived, as shown in Fig. 1.2.

Each FSM is modelled without an ‘end’ state. The FSM (emitter) has not an ‘end’ state for simplicity of representation, because for this work of thesis the situation when a signal is not generated is not of interest. The FSM (satellite system) has not an ‘end’ state because it is supposed to be cyclic (i.e., the system is always in listening mode for a signal), it is conceived as a reactive system (i.e., the system waits indefinitely for a signal), and because it is an embedded system (i.e., it is supposed to be always turned on).

The diagram can be extended with ‘end’ states: this can be done to represent the situation of the deactivation of the emitter of signal, or the end of the satellite mission, or as a first attempt to contemplate possible failures of the systems[1].

The first FSM (emitter) is supposed to be able to emit an instantaneous signal or a signal within a finite time window. For simplicity, this distinction is not reported and only a single state ‘signal emitted’ is provided.

When the signal is emitted, then the event denoted as ‘«event» signal emitted’ is triggered, which activates the behaviour of the second FSM (satellite system).

---

[1] The failure management is beyond the purposes of the activities, however it is interesting topic and it can be also modelled with a dedicated FSM.

It is supposed that when the satellite starts the mission or when, in general, it has not received a RF signal yet, the payload performs its electronic scanning activities and the satellite is orientated in a manner to always have the payload in the Nadir direction. This state is indicated with ‘idle / listening’.

After the trigger ‘«event» signal emitted’ and if the signal can be received from the satellite system because the satellite is supposed to be within the line of sight of the propagation of the signal, then the satellite system can reach the ‘reception’ state.

When a signal is received, this does not mean exactly that the source of signal can be detected: it is possible that the signal is too low in terms of power or disturbed because of interferences[2].

When the detection is possible, then the satellite system reach the ‘detection’ state and algorithms of detection can be employed to estimate the parameters of the signal.

In the ‘detection’ state, if the estimation of the signal succeeds, then the operation of geolocation can be performed reaching the ‘geolocation’ state. If the ‘detection’ fails, because of ambiguities or incompleteness of the data, then the system returns back in ‘listening’ state.

In the ‘geolocation’ state the satellite systems tries to estimate the position of the emitter of signal. This operation is a geometrical problem and it can fail if the problem is not solvable.

If the emitted signal is not instantaneous, then the operations of ‘reception’, ‘detection’, and ‘geolocation’ can be repeated over time on the same signal: in this case it is possible to reach the ‘tracking’ state, which is conditioned to the transition denoted as ‘[if signal repeated]’.

1.3 A General Architecture

From the FSM of the satellite system elaborated in Fig. 1.2, an overall conceptual architecture with correspondences of the components of the satellites can be conceived as represented in Fig. 1.3.

In particular, the starting point is the Electromagnetic Wave (EW) (i.e., a RF signal), which can be sensed by the antenna array payload. If this happens, then the ‘reception’ state of the FSM is reached.

Then, it is supposed that the signal is represented and saved in memory in a discrete form within the satellite system.

---

[2] The system is supposed to be a Electronic Countermeasure (ECM) system to be employed in spectrum monitoring of the interferences, so it is legit to ask what does mean an interference over a jamming signal of interference. More broadly, this situation can be framed within the case of an emitter system with Electronic Counter-Countermeasure (ECCM) capabilities.

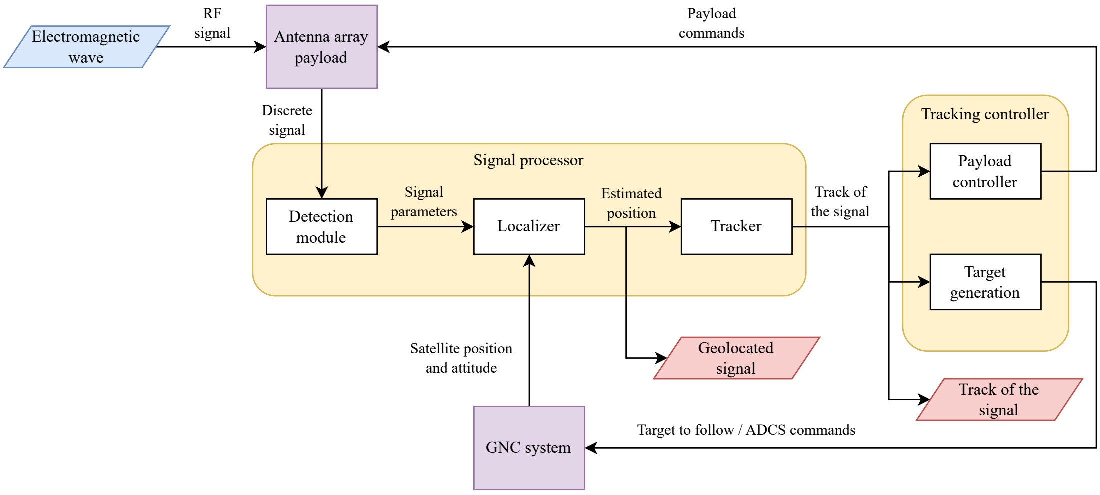

Figure 1.3: General architecture of the system; in particular, in yellow are the activities of signal processing and tracking of the signals, and in purple are the payload, and the Guidance, Navigation, and Control (GNC) subsystem.

In order to elaborate and process the signal, a processor is needed: since the target application is the set of real-time operations this processor can be implemented on a dedicated FPGA.

The three activities of ‘detection’, ‘geolocation’, and ‘tracking’ can be associated to three processing modules named ‘detector’, ‘localizer’, and ‘tracker’.

In particular, to perform the geolocation both the position and the attitude of the satellite are needed.

The system produces two main outputs: the ‘geolocated signal’ and the ‘track of the signal’.

When tracking is possible, the ‘track of the signal’ can be used for two operations: to command the antenna array and to orient the satellite toward the emitter of signal. To achieve these two results, a ‘tracking controller’ can be built to generate a target to follow and to obtain both the ‘payload commands’ and the ‘ADCS commands’.

1.4 Simulation

To predict the performance of a system, it is useful to perform a simulation before its realisation. A general modular simulative system, in terms of class diagram, is conceived and proposed here.

As stated in Sec. 1.1, the main actors of the study are the emitter of the signal and the satellite system. Everything external to them is considered part of the ‘environment’ and, in particular, it is the place in which the propagation of the signal is supposed to happen. Depending on the problem, the environment can be modelled in a detailed manner; in general, at least the presence of the Earth, an atmosphere profile and a noise profile are considered because they affect the propagation of the electromagnetic waves.

For each of these three physical items, a dedicated class can be associated: `Emitter`, `Satellite`, and `Environment`. A first-level simulation can be kinematic, so possible attributes to associate with the emitter and receiver platforms, such as their position and velocity, are included in attributes of ‘state’.

Operations of the ‘signal processor’ and ‘tracking controller’ classes can be associated into a single abstract functional module, here denoted as `SignalProcessor` class.

Other classes to be introduced are a `SimulationManager` and a `PostProcessor`.

The `SimulationManager` is the facade manager and has the goal to start, end and orchestrate the whole simulation.

The `PostProcessor` has the goal to elaborate the data and determine the performances of the system considering reference metrics and with the aid of filters and ground truths; for the user this class is supposed to provide operations of elaboration, visualization and to export data (i.e., save in a dedicated files) for further analysis.

To improve the structure of the code, the main design pattern considered for the simulations are a facade pattern and a strategy pattern.

A facade pattern has been chosen to separate the functions of coordination and implementation using a main class with a manager role (the `SimulationManager`).

A strategy pattern has been chosen to model the behaviour of the signal processor (and consequently, the possibilities of post processing) with interchangeable algorithms.

In the following are reported the details of the classes in terms of attributes and methods.

Class `SimulationManager`:
  Attributes: ‘emitter’, ‘satellite’, ‘environment’, ‘signalProcessor’, ‘postProcessor’;
  Methods: ‘run()’.

Class `Emitter`:
  Attributes: ‘emitterState’, ‘signalProfile’;
  Methods: ‘loadDataEmitter()’, ‘simulateKinematicsEmitter(time)’, ‘generateSignal(time)’.

Class `Satellite`:
  Attributes: ‘satelliteState’, ‘payloadModel’;
  Methods: ‘loadDataSatellite()’, ‘simulateKinematicsSatellite(time)’, ‘receiveSignal(time, signal)’;

Class `Environment`:
  Attributes: ‘atmosphereModel’, ‘earthModel’, ‘noiseProfile’;

Methods: ‘loadDataEnvironment()’, ‘propagateSignal(emitterState, satelliteState, signalProfile)’;

Class `SignalProcessor`:

Attributes: ‘parameters’, ‘trackingEnabled’;

Methods: ‘detectSignal(time, signal)’, ‘localizeSignal(time, signal)’, ‘trackSignal(time, signal)’.

Class `PostProcessor`:

Attributes: ‘metrics’, ‘filters’, ‘groundTruth’;

Methods: ‘evaluatePerformances(signal)’, ‘visualizeData(signal)’, ‘exportData(signal)’.

Class diagram has been reported in Fig. 1.4; in particular, the relationship of aggregation of kind 1-to-1 between the `SimulationManager` and other classes are reported. It is possible to extend the diagram considering a multiplicity of emitters or a multiplicity of satellites: in the first case the signal processor must be able to simultaneously detect, geolocate, and track multiple signals; in the second case, multiple platforms must be coordinated at centralized level or at distributed level.

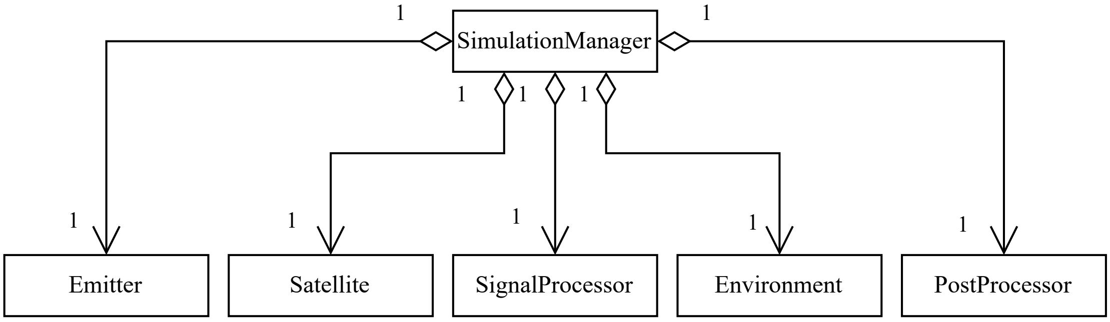

Figure 1.4: Class diagram of the simulated system.

A pseudocode on the use of simulation manager is reported in Listing 1.1.

```
%   Instantiate objects.
emitter = Emitter();
satellite = Satellite();
environment = Environment();
signalProcessor = SignalProcessor();
postProcessor = PostProcessor();

% Instantiate simulation manager.
simulationManager = SimulationManager(emitter, satellite,
    environment, signalProcessor, postProcessor);

% Execute the simulation.
simulationManager.run();
```

Listing 1.1: Use of simulation manager.

A pseudocode on the actual implementation inside the ‘run()’ method of the simulation manager is reported in Listing 1.2

```
%   Flux of SimulationManager.run().
trackingEnabled = true;  %   It can be false.

%   Load data.
emitter.loadEmitterData();
satellite.loadSatelliteData();
environment.loadEnvironmentData();

%   Main loop of the program.
for time = 0:dt:T
    %   Simulate kinematics.
    emitter.simulateEmitterKinematics(time);
    satellite.simulateSatelliteKinematics(time);

    %   Generate and propagate the signal.
    generatedSignal = emitter.generateSignal(time, emitter.signalProfile);
    propagatedSignal = environment.propagateSignal(generatedSignal, emitter.emitterState, satellite.satelliteState, environment.atmosphereModel, environment.earthModel, environment.noiseProfile);
    receivedSignal = satellite.receiveSignal(propagatedSignal, satellite.payloadModel);

    %   Processing of the signal.
    detectedSignal = signalProcessor.detectSignal(time, receivedSignal, signalProcessor.parameters);
    localizedSignal = signalProcessor.localizeSignal(time, detectedSignal, signalProcessor.parameters);
    if trackingEnabled
        trackedSignal = signalProcessor.trackSignal(time, localizedSignal, signalProcessor.parameters);
    end
end

%   Postprocessing of the signal.
if trackingEnabled
    postProcessor.evaluatePerformance(trackedSignal);
    postProcessor.exportData(trackedSignal);
    postProcessor.visualizeData(trackedSignal);
else
    postProcessor.evaluatePerformance(localizedSignal);
    postProcessor.exportData(localizedSignal);
    postProcessor.visualizeData(localizedSignal);
end
```

Listing 1.2: Implementation of run() method of the simulation manager.

It is possible to improve the code with the aid of a template method pattern. This has been chosen because the simulative system is supposed to have a fixed flux of information with variable modules, and this is useful to model different instances of the same macroscopic physical situation. To achieve this result, the `SimulationManager` changes with the introduction of three new methods ('initialize()', 'step(time)', and 'collectResults()') to be employed inside 'run()' method.

Class `SimulationManager`:

Attributes: 'emitter', 'satellite', 'environment', 'signalProcessor', 'postProcessor';

Methods: 'run()', 'initialize()', 'step(time)', 'collectResults()'.

A pseudocode on the use of template method pattern for the simulation manager is reported in Listing 1.3.

```
%   Implementation of simulationManager.run() with a template
    method pattern.

function run(simulationObject)
    simulationObject.trackingEnabled = true;  %   It can be false.

    %   Preparation of modules.
    simulationObject.initialize();

    %   Iterations.
    for time = 0:dt:T
        simulationObject.step(time);
    end

    %   Collect and post-processing of results.
    simulationObject.collectResults();
end
```

Listing 1.3: Application of template method pattern to the simulation manager.

A pseudocode for the initialisation of the code is reported in Listing 1.4.

```
%   Initialisation of the code.

function initialize(simulationObject)
    simulationObject.emitter.loadEmitterData();
    simulationObject.satellite.loadSatelliteData();
    simulationObject.environment.loadEnvironmentData();
end
```

Listing 1.4: Initialisation of the code.

A pseudocode for the single iteration of the code is reported in Listing 1.5.

```
%   Single iteration of the code.

function step(simulationObject, time)
    %   Simulate kinematics.
```

```
    simulationObject.emitter.simulateEmitterKinematics(time);
    simulationObject.satellite.simulateSatelliteKinematics(time);

    %   Generate and propagate the signal.
    generatedSignal = simulationObject.emitter.generateSignal(time,
    simulationObject.emitter.signalProfile);
    propagatedSignal = simulationObject.environment.propagateSignal
   (generatedSignal, simulationObject.emitter.emitterState,
   simulationObject.satellite.satelliteState, simulationObject.
   environment.atmosphereModel, simulationObject.environment.
   earthModel, simulationObject.environment.noiseProfile);
    receivedSignal = simulationObject.satellite.receiveSignal(
   propagatedSignal, simulationObject.satellite.payloadModel);

    %   Processing of the signal.
    detectedSignal = simulationObject.signalProcessor.detectSignal(
   time, receivedSignal, simulationObject.signalProcessor.
   parameters);
    localizedSignal = simulationObject.signalProcessor.
   localizeSignal(time, detectedSignal, simulationObject.
   signalProcessor.parameters);
    if trackingEnabled
        trackedSignal = simulationObject.signalProcessor.
   trackSignal(time, localizedSignal, simulationObject.
   signalProcessor.parameters);
    end
end
```

Listing 1.5: Single iteration of the code.

A pseudocode for data collection and post-processing is reported in Listing 1.6.

```
%   Data collection and post-processing of the signal.

function collectResults(simulationObject)
    if simulationObject.trackingEnabled
        simulationObject.postProcessor.evaluatePerformance(
   trackedSignal);
        simulationObject.postProcessor.exportData(trackedSignal);
        simulationObject.postProcessor.visualizeData(trackedSignal)
   ;
    else
        simulationObject.postProcessor.evaluatePerformance(
   localizedSignal);
        simulationObject.postProcessor.exportData(localizedSignal);
        simulationObject.postProcessor.visualizeData(
   localizedSignal);
    end
end
```

Listing 1.6: Data collection and post-processing of the code.

The reader can notice that the signal goes through different representations, named ‘generatedSignal’, ‘propagatedSignal’, ‘receivedSignal’, ‘detectedSignal’, ‘localizedSignal’, and ‘trackedSignal’. It is possible to adapt the code considering a unique merged representation and, in general, there are two approaches: the first one considers an evolution of the signal (progressive enrichment approach), while the second one considers an aggregation of the different representations (signal envelope approach).

Other expansions can be in the form of composite pattern, which has the role to define and hierarchically group different results in a flexible packet.

This simulative framework constitutes the common starting reference considered for the thesis; the particular implementation of each published work is more detailed and differs depending on the published work of the author.

In each activity of the thesis, the data types are synthetic with particular attention to aspects of variable control, when possible, and reproducibility of the results.

To perform the numerical simulations, the software MATLAB® [1] with an academic licence has been used.

1.5 Coordinate Systems

It is considered that the satellite is surrounded by the void: the operative consequence of the absence of a medium is that the dynamics of the satellite does not consider the presence of the drag force. This assumption can be considered true if the satellite is far from the surface of the Earth (i.e., the height of the orbit is more than 400 km) or for predictions within small intervals of time.

Two levels of approximation for the satellite are assumed: to be a material point with no extension or, when attitude kinematics is relevant, a rigid body with orientation. Local changes in terms of shape or dimensions, e.g. due to thermal expansion or mechanical displacements, are considered absent or not influencing the performances of the payload.

The second assumption is to consider that the only gravitational force acting on the satellite is the Earth’s gravitational field. The operative consequence is to consider a two-body problem for the dynamics and a Keplerian kinematics.

It is also assumed that the electromagnetic field of the Earth does not interfere with the measurement process.

Furthermore, it is assumed that cosmic radiation is absent or does not cause irreversible Single Event Upset (SEU) in the representation of the signal in the components of the onboard electronics.

To represent the data, coordinate systems are needed. In particular, for this work of thesis the following ones are of interest: Latitude, Longitude, and Height

(LLH), Earth-Centered Earth-Fixed (ECEF), Earth-Centered Inertial (ECI), Perifocal Coordinate System (PQW), Body Reference Frame (BRF), and Orbiting Reference Frame (ORF).

Generally, the orbit of a satellite is classified by its shape and its size. From the assumption of two-body model, the solution in the shape of closed curves of the Keplerian kinematics around a gravitational body (e.g., around the Earth) can only be ellipses and circumferences as their particular case. Here it is supposed that the satellite system orbits the Earth on an elliptic orbit or, as a particular case, on a circular orbit.

Classification by size follows the dimension of the orbit or its height[3]. The current common classification considers LEO from 200 km to 2000 km, Medium Earth Orbit (MEO) from 2000 km to 35786 km, and High Earth Orbit (HEO) if it is beyond 35786 km. The value of 35786 km is generally referred to Geosynchronous Earth Orbit (GEO).

The position of the satellite is denoted with $\mathbf{x}_\mathrm{S}$. For elliptic orbits the position of the satellite is generally expressed in terms of orbital parameters [2]: the semi-major axis a, the eccentricity of the orbit e, the inclination of the orbit i, the right ascension of the ascending node Ω, the argument of the perigee ω, and the true anomaly $\nu\left(t\right)$, which is the only parameter that depends on time t. A first representation of the satellite position is in PQW, which has its centre in one of the foci of the orbit, where the Earth is located, as shown in (1.1).

$$\mathbf{x}_\mathrm{S}\big|_\mathrm{PQW} = \frac{a\left(1-e^2\right)}{1+e\cos\left(\nu\right)}\begin{pmatrix}\cos\left(\nu\right)\\ \sin\left(\nu\right)\\ 0\end{pmatrix} \tag{1.1}$$

To convert satellite data from the PQW coordinate system into the ECI coordinate system three rotations are needed, as shown in (1.2), where $\mathbf{R}$ represents the matrix of rotation of the angle in the first argument about the axis of the second argument.

$$\mathbf{x}_\mathrm{S}\big|_\mathrm{ECI} = \mathbf{R}_{(\Omega,3)}\mathbf{R}_{(i,1)}\mathbf{R}_{(\omega,3)}\ \mathbf{x}_\mathrm{S}\big|_\mathrm{PQW} \tag{1.2}$$

In particular [3], the three matrices of rotations $\mathbf{R}_{(\Omega,3)}$, $\mathbf{R}_{(i,1)}$, and $\mathbf{R}_{(\omega,3)}$ are reported in (1.3).

---

[3] In general, height denotes the vertical distance with respect to the ground, while altitude denotes the vertical distance with respect to the mean sea level. Their use is relevant when a particular coordinate point on the surface of the Earth is considered. Here in this work of thesis, the objective is a general evaluation of the performances of the satellite system, so altitude and heights are used interchangeably and considered with respect to the mean sea level.

$$\begin{aligned}\mathbf{R}_{(\omega,3)} &= \begin{bmatrix}\cos(\omega) & -\sin(\omega) & 0\\ \sin(\omega) & \cos(\omega) & 0\\ 0 & 0 & 1\end{bmatrix}\\ \mathbf{R}_{(i,1)} &= \begin{bmatrix}1 & 0 & 0\\ 0 & \cos(i) & -\sin(i)\\ 0 & \sin(i) & \cos(i)\end{bmatrix}\\ \mathbf{R}_{(\Omega,3)} &= \begin{bmatrix}\cos(\Omega) & -\sin(\Omega) & 0\\ \sin(\Omega) & \cos(\Omega) & 0\\ 0 & 0 & 1\end{bmatrix}\end{aligned} \tag{1.3}$$

Other quantities used in this thesis to describe the elliptical orbit are the perigee $r_{\mathrm{S,p}}$, the apogee $r_{\mathrm{S,a}}$, and the local height of the satellite at perigee $h_{\mathrm{S,p}}$. A possible relationship between the perigee $r_{\mathrm{S,p}}$ and the local height of the satellite at perigee $h_{\mathrm{S,p}}$ is as in (1.4), where $R_{\oplus}$ is the local value of the Earth radius. In case of the ellipsoidal model of Earth, this value can be calculated considering the latitude Λ_{S} resulting from the Nadir projection of the satellite on the surface of Earth.

$$r_{\mathrm{S,p}} = h_{\mathrm{S,p}} + R_{\oplus}(\Lambda_{\mathrm{S}}) \tag{1.4}$$

The relationship among perigee $r_{\mathrm{S,p}}$, apogee $r_{\mathrm{S,a}}$, semi-major axis a and eccentricity e are the ones reported in (1.5).

$$\begin{aligned} r_{\mathrm{S,a}} &= a(1+e)\\ r_{\mathrm{S,p}} &= a(1-e)\\ a &= \frac{r_{\mathrm{S,a}} + r_{\mathrm{S,p}}}{2}\end{aligned} \tag{1.5}$$

In general, the perigee $r_{\mathrm{S,p}}$ (or, alternatively, the local height of the satellite at perigee $h_{\mathrm{S,p}}$) and the eccentricity e are given, then the semi-major axis is calculated as function of the two $a = a(r_{\mathrm{S,p}}, e)$ considering (1.4) and (1.5).

The velocity of a satellite in an elliptical orbit [2] represented in the PQW coordinate system is given by (1.6), where $\mu_{\oplus}$ is the standard gravitational parameter of the Earth equal to $3.986005 \cdot 10^{14}\ \mathrm{m}^3/\mathrm{s}^{-2}$.

$$\mathbf{v}_{\mathrm{S}}|_{\mathrm{PQW}} = \sqrt{\frac{\mu_{\oplus}}{a(1-e^2)}}\begin{pmatrix}-\sin(\nu(t))\\ e+\cos(\nu(t))\\ 0\end{pmatrix} \tag{1.6}$$

Also the conversion of the satellite velocity $\mathbf{v}_{\mathrm{S}}$ from the coordinate system PQW to ECI is performed considering same matrices of rotations employed for the position, i.e., the ones in (1.3); the conversion is reported in (1.7).

$$\mathbf{v}_{\mathrm{S}}|_{\mathrm{ECI}} = \mathbf{R}_{(\Omega,3)}\mathbf{R}_{(i,1)}\mathbf{R}_{(\omega,3)}\mathbf{v}_{\mathrm{S}}|_{\mathrm{PQW}} \tag{1.7}$$

Also the emitter of the signal is modelled as a geometrical point and it is denoted by $\mathbf{x}_{\mathrm{E}}$.

Commonly, for a terrestrial system the representation is expected to be in LLH coordinate system in which it can be represented through the quantities of geodetic latitude Λ, longitude λ, and height h, as shown in (1.8).

$$\mathbf{x}_{\mathrm{E}}|_{\mathrm{LLH}} = \begin{pmatrix} \Lambda \\ \lambda \\ h \end{pmatrix} \tag{1.8}$$

Data conversion from LLH to ECEF is nonlinear [4] and, for an ellipsoidal model of the Earth, it is given by (1.9), where $N(\Lambda)$ is defined as in (1.10); $e_{\oplus}$ is the eccentricity of the ellipsoid and $a_{\oplus}$ is the ellipsoidal equatorial radius of the Earth.

For a WGS84 model [5] it is $e_{\oplus}^2 = 0.00669437999$ and $a_{\oplus} = 6378.137$ km.

$$\mathbf{x}_{\mathrm{E}}|_{\mathrm{ECEF}} = \begin{pmatrix} (N(\Lambda) + h)\cos(\Lambda)\cos(\lambda) \\ (N(\Lambda) + h)\cos(\Lambda)\sin(\lambda) \\ \left(N(\Lambda)\left(1 - e_{\oplus}^2\right) + h\right)\sin(\Lambda) \end{pmatrix} \tag{1.9}$$

$$N(\Lambda) = \frac{a_{\oplus}}{\sqrt{1 - e_{\oplus}^2 \sin^2(\Lambda)}} \tag{1.10}$$

The conversion from ECEF to ECI is in (1.11); in particular, $\alpha_{\mathrm{GR}}(t)$ is the position of the Greenwich meridian and it is a function of time t. The matrix of rotation is reported in (1.12).

$$\mathbf{x}_{\mathrm{E}}|_{\mathrm{ECI}} = \mathbf{R}_{(\alpha_{\mathrm{GR}}(t),3)}\mathbf{x}_{\mathrm{E}}|_{\mathrm{ECEF}} \tag{1.11}$$

$$\mathbf{R}_{(\alpha_{\mathrm{GR}}(t),3)} = \begin{bmatrix} \cos(\alpha_{\mathrm{GR}}(t)) & -\sin(\alpha_{\mathrm{GR}}(t)) & 0 \\ \sin(\alpha_{\mathrm{GR}}(t)) & \cos(\alpha_{\mathrm{GR}}(t)) & 0 \\ 0 & 0 & 1 \end{bmatrix} \tag{1.12}$$

Under the assumption that the emitter is fixed on the surface of the Earth, the velocity of the emitter $\mathbf{v}_{\mathrm{E}}$ depends only on the angular velocity of the rotation of the Earth $\boldsymbol{\Omega}_{\oplus}$, which in ECI has only a component along the z axis: $\Omega_{z\oplus}$. The velocity of the emitter $\mathbf{v}_{\mathrm{E}}$ can be evaluated through the cross product between the angular velocity of the Earth and the position of the emitter, as shown in (1.13).

$$\begin{aligned} \mathbf{v}_{\mathrm{E}}|_{\mathrm{ECI}} &= \boldsymbol{\Omega}_{\oplus}|_{\mathrm{ECI}} \times \overrightarrow{OE}|_{\mathrm{ECI}} = \boldsymbol{\Omega}_{\oplus}|_{\mathrm{ECI}} \times \mathbf{x}_{\mathrm{E}}|_{\mathrm{ECI}} \\ &= \begin{pmatrix} 0 \\ 0 \\ \Omega_{z\oplus} \end{pmatrix} \times \begin{pmatrix} x_{\mathrm{E}}|_{\mathrm{ECI}} \\ y_{\mathrm{E}}|_{\mathrm{ECI}} \\ z_{\mathrm{E}}|_{\mathrm{ECI}} \end{pmatrix} = \begin{pmatrix} -\Omega_{z\oplus} y_{\mathrm{E}}|_{\mathrm{ECI}} \\ \Omega_{z\oplus} x_{\mathrm{E}}|_{\mathrm{ECI}} \\ 0 \end{pmatrix} \end{aligned} \tag{1.13}$$

To model the orientation of the payload into the space, it is important to consider both the orientation of the satellite platform and the mounting parameters, i.e., how the translation and rotation of the payload with respect to the centre of mass of the satellite system.

The attitude of the satellite is generally modelled with respect to the ORF coordinate system and considering three angles of rotation, denoted as roll θ_1, pitch θ_2, and yaw θ_3.

The conversion from ECI to ORF is shown in (1.14).

$$\left.\begin{pmatrix} x_\mathrm{S} \\ y_\mathrm{S} \\ z_\mathrm{S} \end{pmatrix}\right|_\mathrm{ORF} = \begin{bmatrix} \frac{[(-\mathbf{x}_\mathrm{S}\times\mathbf{v}_\mathrm{S})\times(-\mathbf{x}_\mathrm{S})]_\mathrm{x}}{\|(-\mathbf{x}_\mathrm{S}\times\mathbf{v}_\mathrm{S})\times(-\mathbf{x}_\mathrm{S})\|} & \frac{[(-\mathbf{x}_\mathrm{S}\times\mathbf{v}_\mathrm{S})\times(-\mathbf{x}_\mathrm{S})]_\mathrm{y}}{\|(-\mathbf{x}_\mathrm{S}\times\mathbf{v}_\mathrm{S})\times(-\mathbf{x}_\mathrm{S})\|} & \frac{[(-\mathbf{x}_\mathrm{S}\times\mathbf{v}_\mathrm{S})\times(-\mathbf{x}_\mathrm{S})]_\mathrm{z}}{\|(-\mathbf{x}_\mathrm{S}\times\mathbf{v}_\mathrm{S})\times(-\mathbf{x}_\mathrm{S})\|} \\ \frac{[-\mathbf{x}_\mathrm{S}\times\mathbf{v}_\mathrm{S}]_\mathrm{x}}{\|\mathbf{x}_\mathrm{S}\times\mathbf{v}_\mathrm{S}\|} & \frac{[-\mathbf{x}_\mathrm{S}\times\mathbf{v}_\mathrm{S}]_\mathrm{y}}{\|\mathbf{x}_\mathrm{S}\times\mathbf{v}_\mathrm{S}\|} & \frac{[-\mathbf{x}_\mathrm{S}\times\mathbf{v}_\mathrm{S}]_\mathrm{z}}{\|\mathbf{x}_\mathrm{S}\times\mathbf{v}_\mathrm{S}\|} \\ \frac{-[\mathbf{x}_\mathrm{S}]_\mathrm{x}}{\|\mathbf{x}_\mathrm{S}\|} & \frac{-[\mathbf{x}_\mathrm{S}]_\mathrm{y}}{\|\mathbf{x}_\mathrm{S}\|} & \frac{-[\mathbf{x}_\mathrm{S}]_\mathrm{z}}{\|\mathbf{x}_\mathrm{S}\|} \end{bmatrix} \left.\begin{pmatrix} x_\mathrm{S} \\ y_\mathrm{S} \\ z_\mathrm{S} \end{pmatrix}\right|_\mathrm{ECI} \tag{1.14}$$

In particular, the operators $[\cdot]_\mathrm{x}$, $[\cdot]_\mathrm{y}$, and $[\cdot]_\mathrm{z}$ denote, respectively, the components of the vector expression between the square brackets along the directions x, y, and z.

The conversion from ORF to BRF occurs through (1.15) with the aid of the matrices of rotation on the attitude angles of roll θ_1, pitch θ_2, and yaw θ_3, reported in (1.16).

$$\mathbf{x}_\mathrm{S}|_\mathrm{BRF} = \mathbf{R}_{(\theta_3,3)}\mathbf{R}_{(\theta_2,2)}\mathbf{R}_{(\theta_1,1)}\ \mathbf{x}_\mathrm{S}|_\mathrm{ORF} \tag{1.15}$$

$$\begin{aligned} \mathbf{R}_{(\theta_1,1)} &= \begin{bmatrix} 1 & 0 & 0 \\ 0 & \cos(\theta_1) & -\sin(\theta_1) \\ 0 & \sin(\theta_1) & \cos(\theta_1) \end{bmatrix} \\ \mathbf{R}_{(\theta_2,2)} &= \begin{bmatrix} \cos(\theta_2) & 0 & \sin(\theta_2) \\ 0 & 1 & 0 \\ -\sin(\theta_2) & 0 & \cos(\theta_2) \end{bmatrix} \\ \mathbf{R}_{(\theta_3,3)} &= \begin{bmatrix} \cos(\theta_3) & -\sin(\theta_3) & 0 \\ \sin(\theta_3) & \cos(\theta_3) & 0 \\ 0 & 0 & 1 \end{bmatrix} \end{aligned} \tag{1.16}$$

Attitude representation is generally in the form of Euler angles or quaternions. Both are equivalent parametrization of the same set of variables of state, however Euler angles are affected by the problem of Gimbal lock so, when possible, quaternions are always preferred, despite they are less intuitive to recognize. Due to their simplicity, in this thesis a parametrization in the form of Euler angles is assumed; it is also assumed that that the attitude state is not in a situation of Gimbal lock.

In general, the mounting parameters are made up of a rotation and a translation. Two kinds of mounting parameters are of interest for these problems: the translation and rotation of the coordinate system of the payload, here denoted by subscript Ar from antenna array, with respect to the BRF, and the mounting parameters of the ADCS with respect to the BRF, as shown in (1.17).

$$\begin{aligned} \mathbf{x}|_{\text{BRF}} &= \Delta\mathbf{x}|_{\text{Ar}\to\text{BRF}} + \mathbf{R}|_{\text{Ar}\to\text{BRF}}\, \mathbf{x}|_{\text{Ar}} \\ \mathbf{x}|_{\text{BRF}} &= \Delta\mathbf{x}|_{\text{ADCS}\to\text{BRF}} + \mathbf{R}|_{\text{ADCS}\to\text{BRF}}\, \mathbf{x}|_{\text{ADCS}} \end{aligned} \tag{1.17}$$

For simplicity, in this thesis, the mounting parameters are supposed to be known and their influence is neglected. Without loss of generality it is then assumed that the payload coordinate system and the one associated to the ADCS are coincident to the BRF. In mathematical terms, this means that $\Delta\mathbf{x}|_{\text{Ar}\to\text{BRF}} = \Delta\mathbf{x}|_{\text{ADCS}\to\text{BRF}} = \mathbf{0}$ and $\mathbf{R}|_{\text{Ar}\to\text{BRF}} = \mathbf{R}|_{\text{ADCS}\to\text{BRF}} = \mathbf{I}_3$, where $\mathbf{I}_3$ denotes the identity matrix of dimensions 3×3.

1.6 Geolocation Problem

Part of this section is extracted from the published work of the author [6].

It is supposed that the payload is able to perform AOA measurements, which are measurements of direction, generally called Line of Bearing (LOB).

A single AOA measurement does not directly give the position of the emitter. In order to obtain it, two or more AOA measurements are needed from different platform positions. This can be done considering multiple platforms of measurements (multi-satellite systems) or multiple measurements over time with a single satellite.

Alternatively, a geometrical constraint can be exploited, and this is the case for a fixed emitter on the surface of the Earth: the geolocation can be performed considering the intersection between the LOB and the surface of the Earth.

1.6.1 Best Estimation with Single Measurement

The first level of estimation is when only a single receiver and a single measurement is available: in this case the best estimation that can be performed is to check if there is an intersection between the measured direction, the LOB, and the surface of the Earth.

There could be three possibilities: there are two distinct points of intersection, there are two coincident points, there is not an intersection.

Assumed that the detected signal is real and not a false positive, the first case is the most common case in which an emitter of signal is on the surface of the Earth or above it, and the relative position of the satellite from the emitter perspective is such that it is not close to the horizon.

The second case is the limit case in which the LOB is tangent to the surface of the Earth and this means that from the emitter perspective the satellite is at the horizon.

The third case is representative of an emitter of signal is not on the surface of the Earth and the satellite is far from the Zenith direction.

Formally, for the first case given $\mathbf{x}_\mathrm{S}$ the position of the satellite and $\mathbf{v}_\mathrm{LOB}$ the measured direction, given a parametric representation of the surface of the Earth as $\Sigma\left(u,v\right)$ with parameters $u \in [u_1, u_2]$ and $v \in [v_1, v_2]$, and given a representation of the LOB as $l\left(t\right) : \mathbf{x}\left(t\right) = \mathbf{x}_\mathrm{S} + \mathbf{v}_\mathrm{LOB} t$ with $t \in [t_1, t_2]$, then the solutions $\{\mathbf{x}_1, \mathbf{x}_2\}$ of the problem can be retrieved as in (1.18).

$$\{\mathbf{x}_1\left(u_1, v_1, l_1\right), \mathbf{x}_2\left(u_2, v_2, l_2\right)\} = \begin{cases} \Sigma\left(u,v\right) & u \in \left[u_1, u_2\right], v \in \left[v_1, v_2\right] \\ \quad\quad l\left(t\right) & t \in \left[t_1, t_2\right] \end{cases} \tag{1.18}$$

For the LOB the most correct representation is in form of ray with $t \in [0, +\infty[$, however in this work of thesis the representation in form of line with $t \in]-\infty, +\infty[$ has been considered.

Between the two solutions $\mathbf{x}_1$ and $\mathbf{x}_2$, the one with the minimum distance has to be considered as best estimation of the emitter position $\hat{\mathbf{x}}_\mathrm{E}$, as shown in (1.19).

$$\hat{\mathbf{x}}_\mathrm{E} = \underset{\mathbf{x}\in\{\mathbf{x}_1, \mathbf{x}_2\}}{\arg\min}\left(\|\mathbf{x} - \mathbf{x}_\mathrm{S}\|\right) \tag{1.19}$$

The second case, in which the LOB is supposed to be tangent to the surface of the Earth, can be modelled as (1.18). In that case there will be two coincident solutions $\hat{\mathbf{x}}_\mathrm{E} = \mathbf{x}_1 = \mathbf{x}_2$.

If there is not an intersection, then best estimation is to consider the projection on the surface of the Earth of the point that realizes the minimum distance between the LOB and the surface of the Earth.

The geolocation problem can be formulated and solved in any reference system, but, in general, the orbit of the satellite is commonly expressed in PQW, while the result of geolocation (i.e., the position of the emitter) is expected to be expressed in LLH; ECI and ECEF are two convenient reference systems to transform coordinates from PQW to LLH and vice versa.

Starting from a coordinate system centered in the centre of the Earth with origin in O, the geolocation is performed considering the vectorial sum of two quantities: the position of the satellite S with respect to the reference system, denoted with $\overrightarrow{OS}$ and the position of the emitter E with respect to the satellite S, denoted with $\overrightarrow{SE}$.

The position of the emitter can then be calculated with the simple expression $\overrightarrow{OE} = \overrightarrow{OS} + \overrightarrow{SE}$. The picture in Fig. 1.5 shows an example of a representation of the geolocation problem in the ECI coordinate system.

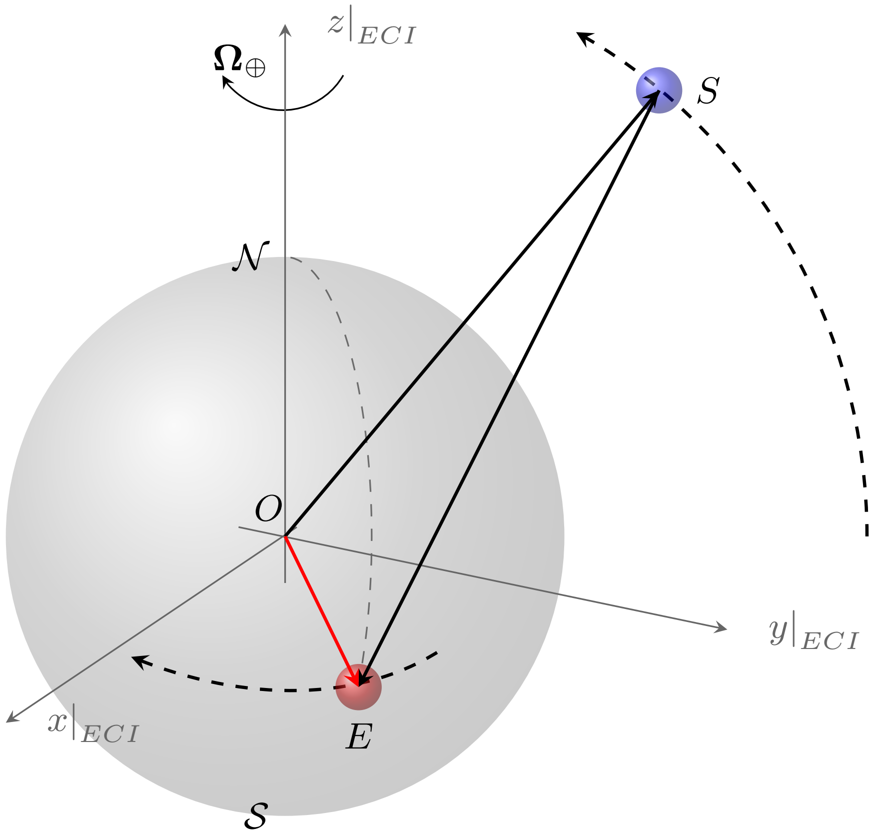

Figure 1.5: The idea behind a geolocation problem: given a reference system on Earth (e.g., here ECI, Earth Centered Inertial, is represented), the geolocation $\overrightarrow{OE}$ can be performed considering the vectors $\overrightarrow{OS}$ and $\overrightarrow{SE}$, where O is the origin of ECI reference system, S is the position the satellite, and E is the position of the emitter.

Looking at this sum, the reader can identify two classes of errors: errors in the estimation of the position of the satellite S and errors in the estimation of the position of the emitter E (with respect to the satellite position S). The first class of errors is beyond the purposes of this study and the focus is on the second ones.

Given an AOA measurement[4] in the form $\hat{\mathbf{v}}_{\mathrm{LOB}} = \left(\hat{\mathbf{x}}_{\mathrm{E}} - \mathbf{x}_{\mathrm{S}}\right) / \|\hat{\mathbf{x}}_{\mathrm{E}} - \mathbf{x}_{\mathrm{S}}\|$, a first estimation of emitter position $\hat{\mathbf{x}}_{\mathrm{E}}$ can be obtained solving the geometric problem in (1.20), where the first equation is the vectorial parametric representation of the line of the measurement and the second equation is the surface of the Earth modelled as a spheroid. The set of unknown of the system are $\hat{x}_{\mathrm{E}}, \hat{y}_{\mathrm{E}}, \hat{z}_{\mathrm{E}}$, and t is the parameter of the LOB.

$$\begin{cases} \hat{\mathbf{x}}_{\mathrm{E}} = \left\{\mathbf{x}_{\mathrm{S}} + t\hat{\mathbf{v}}_{\mathrm{LOB}}, t \in \mathbb{R}\right\} \\ \dfrac{\hat{x}_{\mathrm{E}}^2}{a_{\oplus}^2} + \dfrac{\hat{y}_{\mathrm{E}}^2}{b_{\oplus}^2} + \dfrac{\hat{z}_{\mathrm{E}}^2}{c_{\oplus}^2} = 1 \end{cases} \tag{1.20}$$

Depending on the published studies, two models have been considered during the activities: a spherical Earth and WGS84 ellipsoidal model.

The spherical Earth considers a value of the radius of the Earth equal to $R_{\oplus} = a_{\oplus} = b_{\oplus} = c_{\oplus} = 6378$ km.

The WGS84 ellipsoidal model of the Earth [5] considers values of $a_{\oplus} = b_{\oplus} = 6378.137$ km for the semi-major axis and a value of $c_{\oplus} = 6356.752$ km for the semi-minor axis.

1.6.2 General Case with Multiple Measurements

When multiple LOBs are involved, then the problem is to find the point $\hat{\mathbf{x}}_{\mathrm{E}}$ that minimizes the sum of the distances between each line with the unknown point.

Let's represent the lines as

$$\begin{aligned} l_1\left(t_1\right) &: \mathbf{x}_1 = \mathbf{x}_{0,1} + \mathbf{v}_1 t_1 \quad t_1 \in \mathbb{R} \\ l_2\left(t_2\right) &: \mathbf{x}_2 = \mathbf{x}_{0,2} + \mathbf{v}_2 t_2 \quad t_2 \in \mathbb{R} \\ &\vdots \\ l_{\mathrm{k}}\left(t_{\mathrm{k}}\right) &: \mathbf{x}_{\mathrm{k}} = \mathbf{x}_{0,\mathrm{k}} + \mathbf{v}_{\mathrm{k}} t_{\mathrm{k}} \quad t_{\mathrm{k}} \in \mathbb{R} \\ &\vdots \\ l_{\mathrm{n}}\left(t_{\mathrm{n}}\right) &: \mathbf{x}_n = \mathbf{x}_{0,\mathrm{n}} + \mathbf{v}_{\mathrm{n}} t_{\mathrm{n}} \quad t_{\mathrm{n}} \in \mathbb{R} \end{aligned} \tag{1.21}$$

each distance d_{k} between the unknown point $\hat{\mathbf{x}}_{\mathrm{E}}$ and the k-th line can be calculated as in (1.22).

---

[4] Depending on the published work of the author, over time this quantity has been denoted with $\mathbf{u}_{\mathrm{LOB}}$ or $\mathbf{v}_{\mathrm{LOB}}$.

$$\begin{aligned}
d_1\left(\hat{\mathbf{x}}_{\mathrm{E}}\right) &= \min_{t_1\in\mathbb{R}} \left\|\hat{\mathbf{x}}_{\mathrm{E}} - \mathbf{x}_1\right\| = \min_{t_1\in\mathbb{R}} \left\|\hat{\mathbf{x}}_{\mathrm{E}} - \left(\mathbf{x}_{0,1} + \mathbf{v}_1 t_1\right)\right\| \\
d_2\left(\hat{\mathbf{x}}_{\mathrm{E}}\right) &= \min_{t_2\in\mathbb{R}} \left\|\hat{\mathbf{x}}_{\mathrm{E}} - \mathbf{x}_2\right\| = \min_{t_2\in\mathbb{R}} \left\|\hat{\mathbf{x}}_{\mathrm{E}} - \left(\mathbf{x}_{0,2} + \mathbf{v}_2 t_2\right)\right\| \\
&\vdots \\
d_{\mathrm{k}}\left(\hat{\mathbf{x}}_{\mathrm{E}}\right) &= \min_{t_{\mathrm{k}}\in\mathbb{R}} \left\|\hat{\mathbf{x}}_{\mathrm{E}} - \mathbf{x}_{\mathrm{k}}\right\| = \min_{t_{\mathrm{k}}\in\mathbb{R}} \left\|\hat{\mathbf{x}}_{\mathrm{E}} - \left(\mathbf{x}_{0,\mathrm{k}} + \mathbf{v}_{\mathrm{k}} t_{\mathrm{k}}\right)\right\| \\
&\vdots \\
d_{\mathrm{n}}\left(\hat{\mathbf{x}}_{\mathrm{E}}\right) &= \min_{t_{\mathrm{n}}\in\mathbb{R}} \left\|\hat{\mathbf{x}}_{\mathrm{E}} - \mathbf{x}_{\mathrm{n}}\right\| = \min_{t_{\mathrm{n}}\in\mathbb{R}} \left\|\hat{\mathbf{x}}_{\mathrm{E}} - \left(\mathbf{x}_{0,\mathrm{n}} + \mathbf{v}_{\mathrm{n}} t_{\mathrm{n}}\right)\right\|
\end{aligned} \tag{1.22}$$

To obtain the best estimation $\hat{\mathbf{x}}_{\mathrm{E,best}}$ of the unknown point $\hat{\mathbf{x}}_{\mathrm{E}}$ a minimization problem can be written as in (1.23).

$$\begin{aligned}
\hat{\mathbf{x}}_{\mathrm{E,best}} &= \arg\min_{\hat{\mathbf{x}}_{\mathrm{E}}} \left(\sum_{k=1}^{n} d_{\mathrm{k}}^2\left(\hat{\mathbf{x}}_{\mathrm{E}}\right)\right) \\
&= \arg\min_{\hat{\mathbf{x}}_{\mathrm{E}}} \left(\sum_{k=1}^{n} \left(\min_{t_{\mathrm{k}}\in\mathbb{R}} \left\|\hat{\mathbf{x}}_{\mathrm{E}} - \left(\mathbf{x}_{0,\mathrm{k}} + \mathbf{v}_{\mathrm{k}} t_{\mathrm{k}}\right)\right\|\right)^2\right)
\end{aligned} \tag{1.23}$$

The reason behind the choice of the squared value of the distances d_{k} is because their sum is differentiable and quadratic; this means that the derivatives of the sum of the distances exists and it is possible to solve the (1.23) considering the point of the gradient that realizes the null value, as shown in (1.24).

$$\hat{\mathbf{x}}_{\mathrm{E,best}} = \arg\min_{\hat{\mathbf{x}}_{\mathrm{E}}} \left(\sum_{k=1}^{n} d_{\mathrm{k}}^2\left(\hat{\mathbf{x}}_{\mathrm{E}}\right)\right) \iff \nabla\left(\sum_{k=1}^{n} d_{\mathrm{k}}^2\left(\hat{\mathbf{x}}_{\mathrm{E,best}}\right)\right) = \mathbf{0} \tag{1.24}$$

A possible enrichment of the model (1.24) is to take into account the reliability of the measurement with a multiplicative weighing factor w_{k} for each k-th distance, as shown in (1.25).

$$\hat{\mathbf{x}}_{\mathrm{E,best}} = \arg\min_{\hat{\mathbf{x}}_{\mathrm{E}}} \left(\sum_{k=1}^{n} w_{\mathrm{k}} d_{\mathrm{k}}^2\left(\hat{\mathbf{x}}_{\mathrm{E}}\right)\right) \iff \nabla\left(\sum_{k=1}^{n} w_{\mathrm{k}} d_{\mathrm{k}}^2\left(\hat{\mathbf{x}}_{\mathrm{E,best}}\right)\right) = \mathbf{0} \tag{1.25}$$

The weighting factor must satisfy the set of conditions reported in (1.26).

$$\begin{cases} 0 \leq w_{\mathrm{1}} \leq 1 \\ 0 \leq w_{\mathrm{2}} \leq 1 \\ \quad\vdots \\ 0 \leq w_{\mathrm{k}} \leq 1 \\ \quad\vdots \\ 0 \leq w_{\mathrm{n}} \leq 1 \\ \sum_{k=1}^{n} (w_{\mathrm{k}}) = 1 \end{cases} \tag{1.26}$$

1.7 Signals of Interest and Detection

Part of this subsection is extracted from a published work of the author [6].

The receiver can have its own source of target illumination (e.g., microwaves or laser pulses), or it can exploit external sources. In the first case, the receiver is an active sensor (and can also operate as a transmitter), in the second case it is denoted as a passive sensor [7]. The study focuses the attention on the second class of receivers in which the received electromagnetic waves can either be directly generated by the target or can come from third party sources and then reflected by the target to the receiver. In the latter case, the reflected wave can potentially be exploited to determine the location of the target.

The basic sensing element of a receiving system of electromagnetic waves is an antenna. If it consists of only passive devices, it is also denoted as ‘reciprocal’, which means that its capabilities and performances of transmission and reception are the same. This is not true when it contains active components (e.g., an amplifier) [8].

It is common to distinguish between General Search (GS), when the parameters of the signal are totally unknown, and Direct Search (DS), when some of the parameters are known. In GS the first operation is the scanning on a certain range of frequencies — through a Fourier transform of an acquisition of all impinging signals over a certain interval of time — in order to record the energy levels, from which there is the identification of other parameters of interest. Typically, the results of a GS are: frequency, power level, modulation type, and geolocation [9].

Typically, among the possible electromagnetic signals of interest for EW purposes the frequencies are below 1 GHz for communication signals and above 1 GHz for surveillance radar emitters or weapons systems [7]. In particular [10]: signals in the Very High Frequency (VHF) band (30 MHz to 300 MHz) are used for C2 communication operations and television broadcast, signals in Ultra High Frequency (UHF) band (300 MHz to 3 GHz) are used for cellular communication and Global

Navigation Satellite System (GNSS) constellations, and signals in Super High Frequency (SHF) band (3 GHz to 30 GHz) are used for satellite communication signals.

Among the difficulties [11] in the detection and interception of a signal are: Direct Sequence Spread Spectrum (DSSS), when the signal is spread below the noise level, and Frequency-Hopping Spread Spectrum (FHSS), when the signal changes its carrier frequency of transmission over time.

When the emitter target is a radar, a parabolic reflector is usually used. In particular, there are two kinds of antennas of peculiar interest [7]: the Cassegrain reflector for tracking radars and the cosecant-squared reflector for 2D surveillance radars.

For a receiver composed of an antenna array, classic antenna elements of the array can be one of the following [7] [8]: dipoles, slots, spirals, wideband flared notch (Vivaldi) radiators.

Other promising recent antenna technologies [8] consider fractal structures or genetic algorithms for the generation of complex geometries of the antenna element.

The first documented technique for geolocation purposes is in [12]: it is an application of Maximum Likelihood Estimation (MLE) to a problem of triangulation.

Exploiting one or more properties related to the nature of electromagnetic waves, there are different technologies of localization. The most common ones are [13] [11] [7] [14] AOA, also called Direction of Arrival (DOA), TDOA, and Received Signal Strength (RSS). This study considers AOA technology, which is a measurement of direction, often known as the LOB from which the signal comes from. This kind of measurement can be achieved through array-beamforming technology with an array of antennas [8].

The representation of the signal and the process of detection are summarized in the following steps:

at the emission the signal has the form of electromagnetic wave in components of electric and magnetic fields;

the signal arrives to the receiving antenna element, where the readout circuit generates the signal in the form of current or voltage;

the current or voltage signal is processed in with operations of impedance matching, RF filtering, amplification, frequency down-conversion, baseband filtering, gain control, analog-to-digital conversion, and digital signal processing.

Among the algorithms of detection for antenna arrays there are the Capon method [15], Multiple Signal Classification (MUSIC) [16], and Estimation of Signal Parameters via Rotational Invariance Techniques (ESPRIT) [17].

Errors in an AOA measurement include systematic errors (bias) and random errors (noise). In magnitude, the main sources of errors in the position estimation with these receiving systems are represented by noise [14]. The topic is well covered in the literature [18] and its presence produces more concerns in the detection phase (i.e., if the signal of interest is clearly distinguished) than in the tracking phase (i.e., the signal is clearly received and the receiving system wants to follow it over time). Its characterization is statistical, and a classical modeling approach [13] considers a mean Additive White Gaussian Noise (AWGN). Noise is generally leveraged, when possible, by multiple measurements through multiple platforms or through multiple measurements over time with one single moving platform.

In general, a starting reference model for a real signal $s(t)$ has the representation in (1.27), where $S(f)$ is the spectrum of the signal, A is its amplitude, f is its frequency, f_c is its carrier frequency, B is its band, ϕ is its initial phase, $n_\mathrm{s}(t)$ is the noise associated to the signal, and $i_\mathrm{s}(t)$ is a set of intentional or non-intentional interferences.

$$s(t) = A\,\mathrm{Re}\left\{\int_{f_\mathrm{c}-\frac{B}{2}}^{f_\mathrm{c}+\frac{B}{2}} S(f)\, e^{2\pi f t+\phi} df\right\} + n_\mathrm{s}(t) + i_\mathrm{s}(t) \tag{1.27}$$

The model of $s(t)$ can be used to represent values of voltage or the current of the readout circuits of the receiving antenna.

A possible model of convenience to model the noise $n_\mathrm{s}(t)$ is the AWGN, reported in (1.28), which is additive with respect to the signal, it has a Gaussian distribution and has uniform power spectral density across the frequency band.

$$n_\mathrm{s}(t) \sim \mathcal{N}\left(0, \sigma_\mathrm{N}^2\right) \tag{1.28}$$

The value of $\sigma_\mathrm{N}^2 = N = kTB$ represents the variance of the noise N. When the complex representation of the signal is considered, it is conventionally assumed $\sigma_\mathrm{I,N}^2 = \sigma_\mathrm{Q,N}^2 = N/2$, where $\sigma_\mathrm{I,N}$ and $\sigma_\mathrm{Q,N}$ are, respectively, the in-phase and quadrature standard deviations of the components of the complex signal.

In general, in the on-board processing of the signal, the real representation is preferred at the front-end processing level, while the complex representation is employed in the demodulation of the signal.

After the demodulation there is the sampling of the signal, which can be done multiplying the signal with a train of unitary pulses with a sampling frequency f_s. The discrete representation $s_\mathrm{d}(t)$ is reported in (1.29) or equivalently in (1.30).

$$s_\mathrm{d}(t) = s(t) \sum_{n=-\infty}^{+\infty} \left(\delta\left(t - \frac{n}{f_\mathrm{s}}\right)\right) = \sum_{n=-\infty}^{+\infty} \left(s\left(\frac{n}{f_\mathrm{s}}\right) \delta\left(t - \frac{n}{f_\mathrm{s}}\right)\right) \tag{1.29}$$

$$s_\mathrm{d}[n] = s\left(\frac{n}{f_\mathrm{s}}\right) \tag{1.30}$$

The sampling frequency has to satisfy the condition $f_\mathrm{s} > 2B$ to avoid aliasing.

For geolocation problems involving detection, geolocation, and tracking of jamming signals $i_\mathrm{j}(t)$, which is a form of intentional interference, possible reference models to be considered as starting point are the following ones.

Jamming noise: reported in (1.31), which considers a noise-like model n_{j} with variance N_{j}. This model is generally employed to model a jamming signal that has the purposes to cover the useful signal.

$$i_{\mathrm{j}}\left(t\right) = n_{\mathrm{j}}\left(t\right) \sim \mathcal{N}\left(0, N_{\mathrm{j}}\right) \tag{1.31}$$

Tone jamming: reported in (1.32), which considers a co-sinusoidal (or sinusoidal) model with a certain amplitude A_{j}, frequency f_{j}, and initial phase ϕ_{j}. This model is generally employed to model attacks that have the purpose of saturating the receiver.

$$i_{\mathrm{j}}\left(t\right) = A_{\mathrm{j}} \cos\left(2\pi f_{\mathrm{j}} t + \phi_{\mathrm{j}}\right) \tag{1.32}$$

Multi-tone jamming: reported in (1.33). It has the same purpose of a tone-jamming, but extended over a selected number of frequencies.

$$i_{\mathrm{j}}\left(t\right) = \sum_{k} A_{\mathrm{j},k} \cos\left(2\pi f_{\mathrm{j},k} t + \phi_{\mathrm{j},k}\right) \tag{1.33}$$

Chirp jamming: it employs a modulated value in frequency f_{j}. It has the purposes to create disturbances over a broadband system. An example with a linear chirp with parameters $f_{0,\mathrm{j}}$ and k_{j} is reported in (1.34).

$$i_{\mathrm{j}}\left(t\right) = A_{\mathrm{j}} \cos\left(2\pi\left(f_{0,\mathrm{j}} t + \frac{k_{\mathrm{j}}}{2} t^2\right) + \phi_{\mathrm{j}}\right) \tag{1.34}$$

Digital Radio Frequency Memory (DRFM) jamming: reported in (1.35). It captures a certain original signal s_{o} and replicates it with a gain g_{j}, delay τ_{j}, and additional phase ϕ_{j}.

$$i_{\mathrm{j}}\left(t\right) = g_{\mathrm{j}} s_{\mathrm{o}}\left(t - \tau_{\mathrm{j}}\right) e^{j\phi_{\mathrm{j}}} \tag{1.35}$$

1.8 Antenna Array Payload

The idea behind AOA technology is that as the plane wave propagates across the array, it will arrive at each element at a different instants of time. What happens is time delays can be observed as phase delays in the received signals.

Technical activities involved also the characterisation of the payload of the satellite, which is supposed to be made up of arrays of antennas. Performance evaluation was in terms of 3D response pattern and directivity.

The Phased Array System Toolbox in MATLAB [19] has been used to predict the performance of the linear antenna arrays. It provides algorithms for designing and simulating sensor array and beamforming systems in wireless communication, radar, sonar, and acoustic applications. Furthermore, it can generate C code from the functions in the toolbox.

In particular, the transmitter (and the receiver) can be an antenna or an array of antennas.

Common antenna objects are:

`phased.IsotropicAntennaElement`
`phased.CosineAntennaElement`
`phased.CustomAntennaElement`

The linear array object is defined through `phased.ULA` with inputs:

the number of the elements of the array `numberOfElementsArray`
the element spacing `elementSpacing`
the antenna element `antennaElement`
the axis of the array `arrayAxis` (if not specified the default axis is y)

It is possible to generate Uniform Rectangular Array (URA), `phased.URA` or the geometry can be also completely defined by the user.

Depending on the published activity, 2D cross-array of Uniform Linear Array (ULA), planar URA, and 3D tri-axial ULA have been considered as reference.

An example of object generated with 7 elements spaced at 1/4 of the wavelength is reported in Fig. 1.6.

3D response pattern and directivity pattern in E1/L1 band, employed for GNSS signals are shown in Fig. 1.6 and Fig. 1.7.

Polar plots in Azimuth and Elevation are reported in Fig. 1.9 and Fig. 1.10.

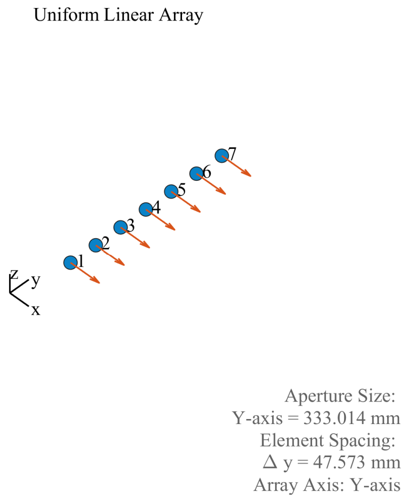

Figure 1.6: ULA generated with `phased.ULA` and `phased.IsotropicAntennaElement` objects for CubeSats with length $L = 0.334$ m, number of elements $M = 7$, and frequency $f = 1575.42$ MHz.

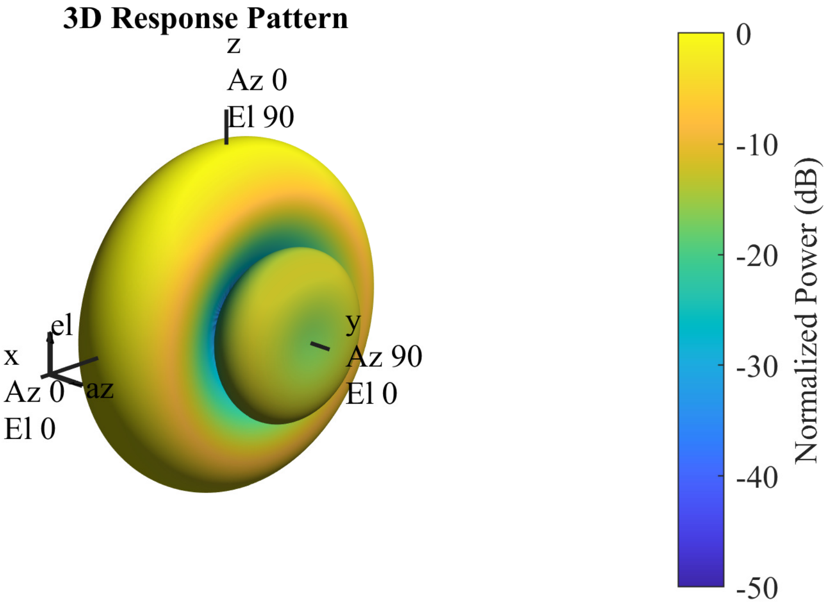

Figure 1.7: 3D Response pattern for an ULA generated with `phased.ULA` and `phased.IsotropicAntennaElement` objects for CubeSats with length $L = 0.334$ m, number of elements $M = 7$, and frequency $f = 1575.42$ MHz.

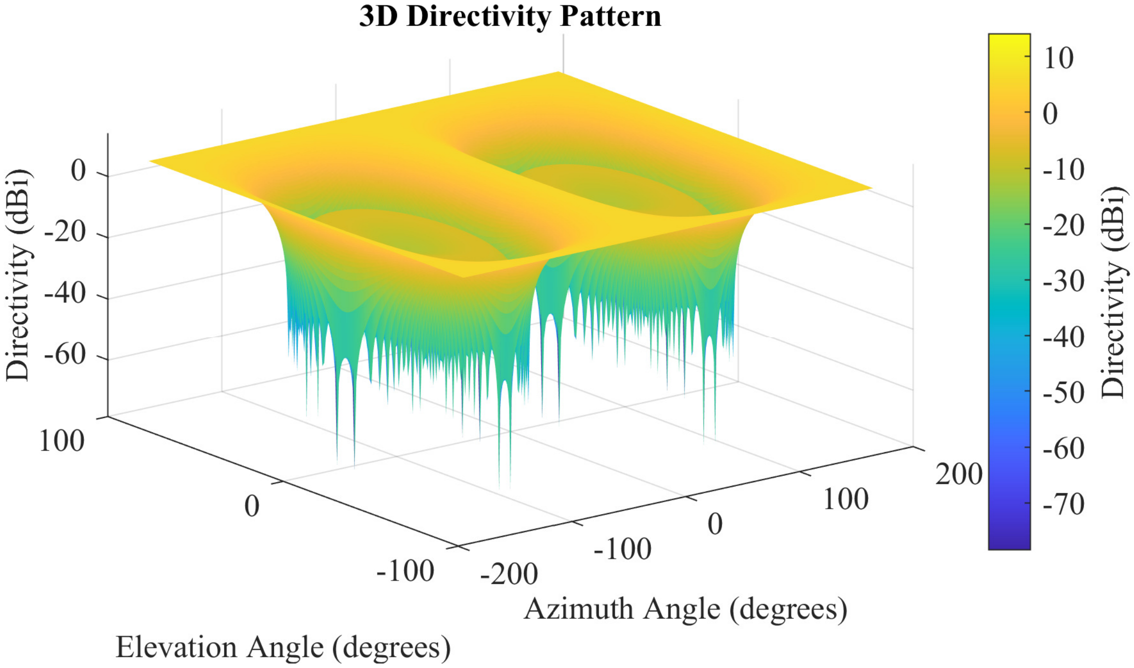

Figure 1.8: Directivity pattern for an ULA generated with `phased.ULA` and `phased.IsotropicAntennaElement` objects for CubeSats with length $L = 0.334$ m, number of elements $M = 7$, and frequency $f = 1575.42$ MHz.

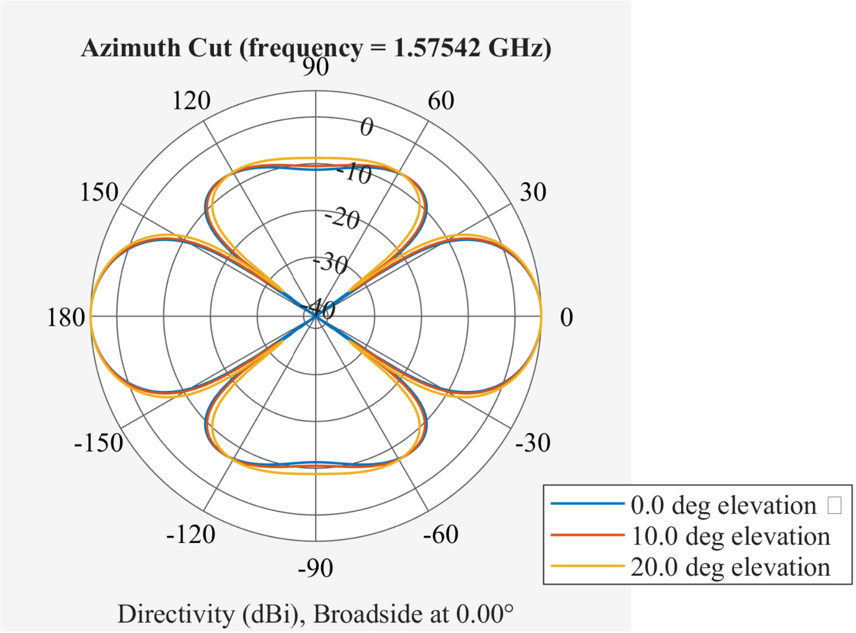

Figure 1.9: Example of azimuth polar pattern for an ULA generated with `phased.ULA` and `phased.IsotropicAntennaElement` objects for CubeSats with length $L = 0.334$ m, number of elements $M = 7$, and frequency $f = 1575.42$ MHz..

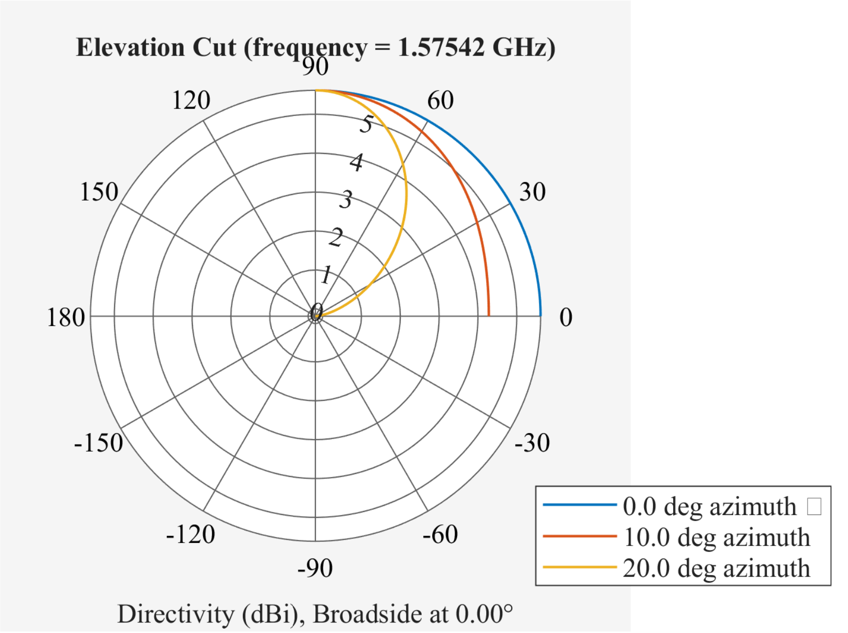

Figure 1.10: Example of elevation polar pattern for an ULA generated with `phased.ULA` and `phased.IsotropicAntennaElement` objects for CubeSats with length $L = 0.334$ m, number of elements $M = 7$, and frequency $f = 1575.42$ MHz..

1.9 External Contributions to the Thermal Noise

This section is intended to give a reference model for temperature modelling in noise for satellite receivers. The main contributions are on: cosmic sources (e.g., stars), Earth's atmosphere, Earth's ground, Sun, and Moon. The main consulted reference is [20].

Noise has thermal origin and, under the assumption of White Gaussian Noise Model, the noise power spectral density N_0 is as shown in (1.36), where k is the constant of Boltzmann equal to $1.38 \cdot 10^{-23} Ws/K$ and T is a reference temperature (in general, for performance evaluations a value of 290 K is assumed).

$$N_0 = kT \tag{1.36}$$

The value of N_0 is in $[Ws] = [W/Hz]$. The total (received) noise power integrated for all frequencies in a certain band of reference B_n is N, as shown in (1.37).

$$N = N_0 B_\mathrm{n} = kTB_\mathrm{n} \tag{1.37}$$

Deviations between the model N and measured value $\tilde{N}$ of the noise are generally expressed in term of a factor F_n, as shown in (1.38).

$$F_\mathrm{n} = \frac{\tilde{N}}{N} = \frac{\tilde{N}}{kTB_\mathrm{n}} \tag{1.38}$$

In general, F_n is denoted as noise factor and it is expressed in linear units. It is denoted as 'noise figure' NF when it is expressed in decibels, as shown in (1.39).

$$NF = 10 \log \left(F_\mathrm{n} \right) \tag{1.39}$$

In decibel units the measured noise is expressed as in (1.40).

$$\tilde{N}_\mathrm{dB} = 10 \log \left(kTB_\mathrm{n} \right) + NF \tag{1.40}$$

In order to predict the value of the noise, the internal and external contributions on the system temperature have to be analyzed. A possible approach is to consider additive models for external contributions.

The general model of a modified system temperature T_eff is as shown in (1.41), where T_c is the cosmic noise contribution, T_a the temperature contribution due to the presence of the atmosphere, T_g is the temperature contribution due to the ground, T_s is the temperature contribution due to the Sun, and T_m is the temperature contribution due to the Moon.

$$T_\mathrm{eff} = T + T_\mathrm{c} + T_\mathrm{a} + T_\mathrm{g} + T_\mathrm{s} + T_\mathrm{m} \tag{1.41}$$

The model for cosmic noise T_c is reported in (1.42), where α_c is the fraction of total integrated antenna pattern pointed above horizon, L_a is the average atmospheric loss (across different portions of the sky), T_{100} is a reference temperature between 500 K and 18650 K (a common assumption is the geometric mean, so $T_{100} = 3050$ K), f_MHz is the frequency of the signal in MHz, and 2.7 is the value of the galactic background noise.

$$T_\mathrm{c} = \frac{\alpha_\mathrm{c}}{L_\mathrm{a}} \left(T_{100} \left(\frac{100}{f_\mathrm{MHz}} \right)^{2.5} + 2.7 \right) \tag{1.42}$$

In general, for frequencies above 2 GHz the dependence on the frequency is negligible, so an approximate model is given in (1.43).

$$T_\mathrm{c}|_{f>2\mathrm{GHz}} \simeq \frac{\alpha_\mathrm{c}}{L_\mathrm{a}} 2.7 \tag{1.43}$$

For the dependence on the layers L_a there are models in literature, e.g. [21].

The model for the contribution due to the presence of the Sun noise T_s is reported in (1.44), where G_s is the portion of antenna gain directed toward the Sun and $\tilde{T}_\mathrm{s}$ is the Sun temperature (it depends on the frequency).

$$T_\mathrm{s} = 4.75 \cdot 10^{-6} \frac{G_\mathrm{s} \tilde{T}_\mathrm{s}}{L_\mathrm{a}} \tag{1.44}$$

A similar model can be written for the presence of the Moon, as shown in (1.45), in which G_m is the portion of antenna gain directed toward the Moon and $\tilde{T}_\mathrm{m}$ is the Moon temperature, which can be set to 200 K. The model is valid from 1 GHz to 100 GHz.

$$T_\mathrm{m} = 4.75 \cdot 10^{-6} \frac{G_\mathrm{m} \tilde{T}_\mathrm{m}}{L_\mathrm{a}} \tag{1.45}$$

The contribution of the atmosphere T_a can be evaluated with (1.46), where T_t is an averaged temperature of the atmosphere over the propagation path, α_a is the fraction of antenna's receiver energy over the path defined. When the atmospheric noise is coming from all angles $\alpha_\mathrm{a} = 1$ can be considered.

$$T_\mathrm{a} = \alpha_\mathrm{a} T_\mathrm{t} \left(1 - \frac{1}{L_\mathrm{a}} \right) \tag{1.46}$$

The contribution on the noise due to the Earth is T_g is reported in (1.47), where G_g is the average antenna gain toward the Earth surface, Ω_g is the percentage of antenna FoV (Field of View) occupied by the Earth (in steradiants), and $\mathcal{E}$ is the surface emissivity of the Earth.

$$T_\mathrm{g} = \frac{\Omega_g G_\mathrm{g} \mathcal{E} T_\mathrm{t}}{4\pi} \tag{1.47}$$

1.10 CRLB Curves for Linear Arrays

This section is intended to give a first introduction on the detectability and the performance metrics for angular error and distance error for a receiver embarked on a satellite and an emitter placed on the surface of the Earth.

The detectability is generally evaluated through the Signal-to-Noise Ratio (SNR) SNR, which is the ratio between the received power of the signal P_{r} and the noise N, as shown in (1.48). Generally, the higher the SNR the higher is the possibility to clearly distinguish the signal of interest.

$$SNR = \frac{P_{\mathrm{r}}}{N} \tag{1.48}$$

The received power P_{r} can be evaluated through the classic Friis transmission equation [18], as shown in (1.49), where G_{E} is the gain of the emitter of signal, G_{S} is the gain of the receiver on the satellite platform, and P_{E} is the emitted power; w_{f} is the wavelength of the signal and $R = \|\mathbf{x}_{\mathrm{S}} - \mathbf{x}_{\mathrm{E}}\|$ is the distance between the position of the emitter of signal $\mathbf{x}_{\mathrm{E}}$ and the satellite $\mathbf{x}_{\mathrm{S}}$.

$$P_{\mathrm{S}} = P_{\mathrm{E}} G_{\mathrm{E}} G_{\mathrm{S}} \left(\frac{w_{\mathrm{f}}}{4\pi R}\right)^2 \tag{1.49}$$

At first stages of a project, when there is the lack of detailed information on the noise N and gains, G_{E} and G_{S}, a good practice is to consider the SNR as a parameter ranging from 1 to 30 dB.

The angular error [22] is evaluated through the Cramér-Rao Lower Bound (CRLB), as shown in (1.50). In particular, ζ is supposed to be the bearing angle of the signal and $\hat{\zeta}$ its estimation. L is the total length of the antenna array, M is the number of elements.

$$\sigma^2_{\hat{\zeta}} = \frac{12}{(2\pi)^2\, SNR \frac{(M+1)}{(M-1)} M \left(\frac{L}{w_{\mathrm{f}}}\right)^2 \sin^2(\zeta)} \tag{1.50}$$

In this study the number of elements are calculated considering (1.51): the elements of the antenna array are supposed to be evenly spaced with a fixed distance $d = w_{\mathrm{f}}/4$. This is a classic choice to avoid aliasing and it is considered as first attempt to have an idea of the performance of the system.

$$M = \left\lfloor \frac{L}{d} \right\rfloor = \left\lfloor \frac{4L}{w_{\mathrm{f}}} \right\rfloor \tag{1.51}$$

For a matter of completeness, it is recalled that the wavelength w_{f} and the frequency f of the signals are connected through (1.52), where c is the speed of the propagation of the signal. For this work of thesis the signal of interest is a L1/E1 signal used for GNSS in civil applications and the propagation is supposed to follow the speed of light in vacuum c, equal to 299792458 m/s.

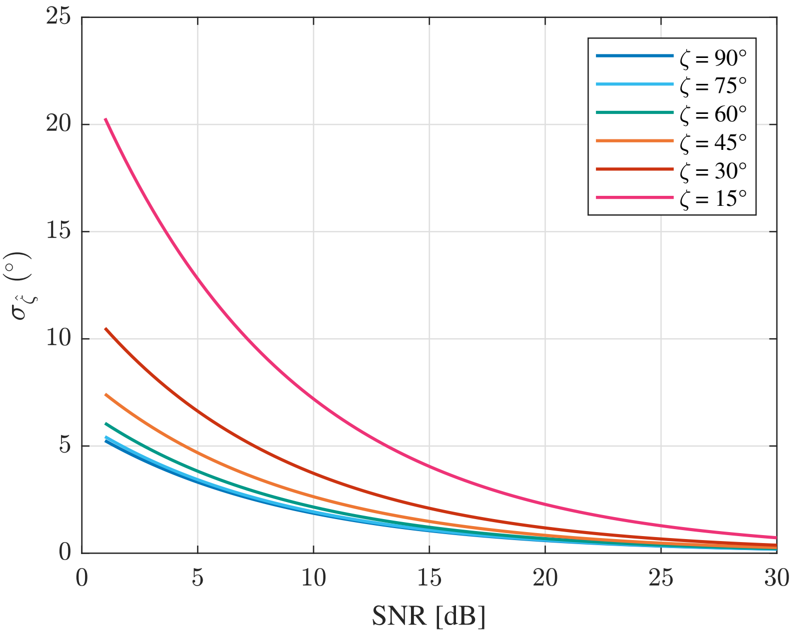

Figure 1.11: CRLB curves for a linear antenna array with length $L = 0.334$ m, number of elements $M = 7$, and frequency $f = 1575.42$ MHz.

$$w_{\mathrm{f}} = \frac{c}{f} \tag{1.52}$$

Simulated values are in Fig. 1.11 with values of $M = 7$ elements and an array length of $L = 0.334$ m, representative of a possible payload for CubeSat platforms.

1.11 Receiver Operating Characteristic

The approach and results obtained in this section are extracted from a published work of the author in [23].

As shown in (1.50), the predicted variance depends on the value of the SNR. From a mission perspective, the receiver must be designed in order to have a minimum value of the SNR, which is enough to guarantee a certain probability of detection.

It is possible to calculate the minimum value considering the Friis model of propagation and the relative geometry between the emitter of signal $\mathbf{x}_{\mathrm{E}}$ and the satellite platform $\mathbf{x}_{\mathrm{S}}$.

A free space propagation and without losses can be assumed for first-level evaluations. In particular, from (1.49) the (1.53) can be obtained.

$$SNR = \frac{P_{\mathrm{S}}}{N} = \frac{P_{\mathrm{E}} G_{\mathrm{E}} G_{\mathrm{S}}}{N} \left(\frac{c}{4\pi f R} \right)^2 = \frac{P_{\mathrm{E}} G_{\mathrm{E}} G_{\mathrm{S_k}}}{N} \left(\frac{c}{4\pi f \| \mathbf{x}_{\mathrm{S}} - \mathbf{x}_{\mathrm{E}} \|} \right)^2 \tag{1.53}$$

Defining SNR_0 as in (1.54), it is possible to write a convenient expression in the form $SNR = SNR\,(R)$, as a function of the distance R, shown in (1.55), which is useful for a first-level evaluation of the performances of the cluster of satellites, because it isolates the device-dependent variables (i.e., P_{E}, G_{E}, G_{S}) and the geometrical-dependent ones (i.e., $\mathbf{x}_{\mathrm{S}}$ and $\mathbf{x}_{\mathrm{E}}$).

$$SNR_0 = \frac{P_{\mathrm{E}} G_{\mathrm{E}} G_{\mathrm{S}}}{N} \left(\frac{c}{4\pi f} \right)^2 \tag{1.54}$$

$$SNR\,(R) = SNR_0 \left(\frac{1}{R} \right)^2 = SNR_0 \left(\frac{1}{\| \mathbf{x}_{\mathrm{S}} - \mathbf{x}_{\mathrm{E}} \|} \right)^2 \tag{1.55}$$

Assigned a certain height h_{S} for the satellite, the maximum value of the distance $R_{\max}$ can be calculated from geometrical considerations as in (1.56), where $R_{\oplus}$ is the radius of the Earth.

$$\begin{aligned} R_{\max} = max\,(R) &= \sqrt{(R_{\oplus} + h_{\mathrm{S}})^2 - R_{\oplus}^2} = \sqrt{R_{\oplus}^2 + h_{\mathrm{S}}^2 + 2R_{\oplus} h_{\mathrm{S}} - R_{\oplus}^2} \\ &= \sqrt{h_{\mathrm{S}}^2 + 2R_{\oplus} h_{\mathrm{S}}} \end{aligned} \tag{1.56}$$

The reader can notice that the height h_{S} of the satellite is also the minimum value of the distance, since it corresponds to the limit case of Nadir alignment between the satellite S and the emitter of signal E, so $R_{\min} = \min\,(R) = h_{\mathrm{S}}$.

Substituting the minimum distance $R = h_{\mathrm{S}}$ and the maximum distance $R = R_{\max}$ in (1.55), the SNRs in (1.57) are obtained.

$$\begin{cases} SNR\,(R_{\max}) = SNR_0 \left(\dfrac{1}{\sqrt{h_{\mathrm{S}}^2 + 2R_{\oplus} h_{\mathrm{S}}}} \right)^2 \\ SNR\,(R_{\min}) = SNR_0 \left(\dfrac{1}{h_{\mathrm{S}}} \right)^2 \end{cases} \tag{1.57}$$

Combining the expressions in (1.57), the equation (1.58) is obtained.

$$SNR\,(R_{\max}) = SNR\,(R_{\min}) \left(\frac{h_S}{\sqrt{h_{\mathrm{S}}^2 + 2R_{\oplus} h_{\mathrm{S}}}} \right)^2 \tag{1.58}$$

At this point, if a certain orbit radius r is assigned (i.e., equivalently $h_{\mathrm{S}} = r - R_{\oplus}$ is assigned), the ratio ρ in (1.59) is uniquely determined.

$$\rho = \frac{h_S}{\sqrt{h_{\mathrm{S}}^2 + 2R_{\oplus} h_{\mathrm{S}}}} \tag{1.59}$$

Considering (1.59), equation (1.58) can be rewritten as in (1.60).

$$SNR\,(R_{\max}) = SNR\,(R_{\min})\,\rho^2 = SNR_0 \left(\frac{1}{h_{\mathrm{S}}}\right)^2 \rho^2 \tag{1.60}$$

Given a certain detector, the value of the required SNR is generally determined by the set of Receiver Operating Characteristic (ROC) curves, which are functions that relate the probability of false alarm p_{FA}, the probability of detection p_{D} and the SNR [24].

Assigning a certain of level of performances in terms of p_{FA} and probability of detection p_{D}, then the condition on the detection is $SNR\,(p_{\mathrm{FA}}, p_{\mathrm{D}}) \leq SNR\,(R_{\max})$, so (1.61) and (1.62) can be written.

$$SNR\,(p_{\mathrm{FA}}, p_{\mathrm{D}}) \leq SNR_0 \left(\frac{1}{h_{\mathrm{S}}}\right)^2 \rho^2 \tag{1.61}$$

$$SNR_0 \geq SNR\,(p_{\mathrm{FA}}, p_{\mathrm{D}}) \left(\frac{1}{\rho}\right)^2 h_{\mathrm{S}}^2 \tag{1.62}$$

Substituting the value of SNR_0 from (1.62) into (1.55), the condition in (1.63) is obtained.

$$SNR\,(R) \geq SNR\,(p_{\mathrm{FA}}, p_{\mathrm{D}}) \left(\frac{1}{\rho}\right)^2 h_{\mathrm{S}}^2 \left(\frac{1}{\|\mathbf{x}_{\mathrm{S}} - \mathbf{x}_{\mathrm{E}}\|}\right)^2 \tag{1.63}$$

In Table 1.1, values for ρ^{-1} are reported with respect to common values of heights h_{S} of the satellite S.

For modelling the detector operational characteristics, a linear detector, non-fluctuating signals with an unknown phase, and Gaussian noise are assumed. Therefore, the calculated ROC curves are the ones reported in Fig. 1.12, which relates the Signal-to-Noise ratio SNR to different values of probability of detection p_{D} and probability of false alarm p_{FA}.

Other assumptions concern signal transmission and propagation, which are supposed to be omnidirectional and isotropic, respectively. Phenomena of reflection, refraction, and multi-path are neglected. The speed of propagation of the signal is supposed to be constant.

A flowchart to calculate the required minimum value of SNR is reported in Fig. 1.13. For unmodelled effects it is possible to assume an additional safety margin.

In this work of thesis the following values are assumed: probabilities of false alarm $p_{\mathrm{FA}} = 10^{-6}$ and of detection $p_{\mathrm{D}} = 0.997$. The ROC curve in Fig. 1.12 gives

Table 1.1: Values of the factor ρ^{-1} with respect to the height h_{S} of the satellite S.

h_{S} [km]	ρ^{-1}
400	5.7319
600	4.7156
800	4.1143
1000	3.7070
1200	3.4086
1400	3.1783
1600	2.9940
1800	2.8423
2000	2.7150

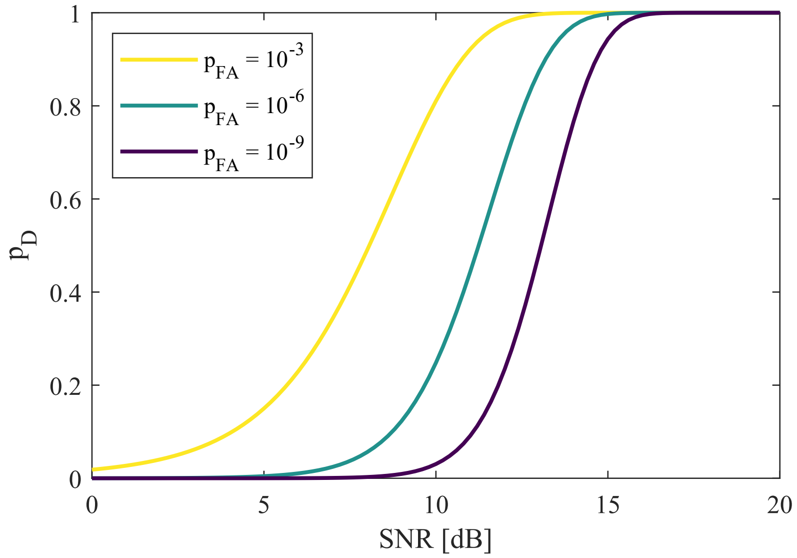

Figure 1.12: Probability of detection p_{D} vs. Signal-to-Noise ratio SNR for different values of probability of false alarm p_{FA} considering a linear detector, a non-fluctuating signal with unknown phase, and Gaussian noise.

a minimum value of $SNR\,(p_{\mathrm{FA}}, p_{\mathrm{D}}) \approx 15$ dB, which has been used as worst case of maximum distance. In Additionally, a value of $+3$ dB is assumed as safety margin for unmodelled effects (e.g., the presence of the atmosphere).

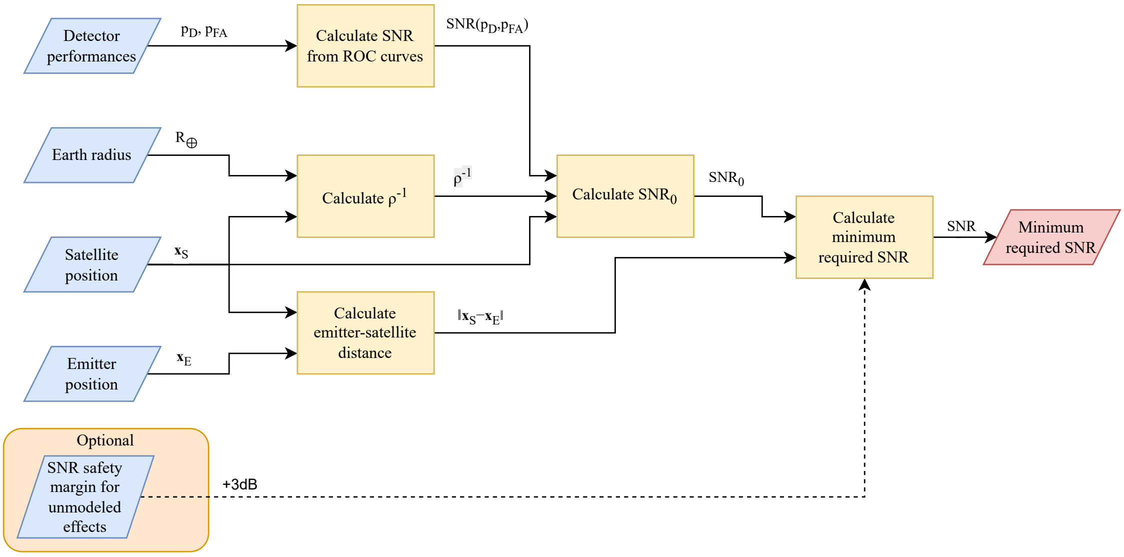

Figure 1.13: A flowchart to calculate the required minimum value of SNR between an emitter of signal E and a satellite S.

Chapter 2

Signal Propagation, Time Delay and Frequency Errors

This chapter is intended to explore aspects related to the propagation of the signal in terms of time delay, changes in the frequency of the signal, and reconstruction of the path of electromagnetic waves in the atmosphere. Advanced topics on relativistic effects and turbulence are also presented and discussed.

Sec. 2.1 presents a methodology to perform the estimation and compensation of the Doppler factor in case of the propagation of a signal from an emitter on the Earth and measurement performed with AOA technology from a satellite platform. Sec. 2.2 introduces the reader to the topic of time delay with a Newtonian approach; a scheme of estimation of this effect directly onboard the satellite is presented, and two possible alternative equivalent algorithms of simulation are shown to the reader. In Sec. 2.3 an enrichment of the model for time delay is presented from a relativistic perspective. Produced results are an analytical model, a formal development of a correction algorithm for relativistic time delay, an order of magnitude analysis, and a strategy for worst-case prediction. The most interesting result from the industrial perspective is that, given the starting information on the desynchronization, it has been demonstrated that the relativistic correction can be implemented considering only the available onboard information, so the relativistic correction can be implemented considering only a software update and without the use of external sensors. In Sec. 2.4 a further exploration on the topic of time delay is presented considering the presence of the atmosphere. In Sec. 2.5 the bending of electromagnetic waves due to changes in refraction index is exposed with possible strategy to evaluate it. In Sec. 2.6 the phenomenon of beam wander, mainly relevant for space-optic links, is described with some numerical parametric evaluations.

2.1 Doppler Effect

This section summarises models, methods, and results in the published article of the author [25].

The main goal of the section is to present a real-time estimation and compensation strategy for the Doppler factor considering only the current instantaneous kinematic information, without the information on the history of the signal over time.

Doppler effect is the apparent shift in the wavelength and in the frequency of an electromagnetic wave due to the relative movement of the source of the wave and the receiver [26].

Denoting the observed frequency of the signal with f_o and the effective frequency of the signal with f_e, the Doppler effect can be calculated using (2.1), where $D\left(\Delta v\right)$ is the Doppler factor, which depends on the component of the relative velocity along the line from the receiver to the emitter.

$$f_\mathrm{e} = D\left(\Delta v\right) f_\mathrm{o} \tag{2.1}$$

It can be demonstrated [26] that $D\left(\Delta v\right)$ is equal to the expression in (2.2), where $\gamma = \left(1-\beta^2\right)^{-1/2}$ is the Lorentz factor, $\beta = \Delta v / c$ is the ratio of velocities, and c is the speed of light.

$$D\left(\Delta v\right) = \gamma\left(1+\beta\right) \tag{2.2}$$

Expressing the Lorentz factor and the ratio of velocities, the equation in (2.3) can be obtained.

$$D\left(\Delta v\right) = \frac{\left(1+\beta\right)}{\sqrt{1-\beta^2}} = \frac{1+\frac{\Delta v}{c}}{\sqrt{1-\left(\frac{\Delta v}{c}\right)^2}} \tag{2.3}$$

Considering that, in general, the variations of D occur in very small figures, the data are conveniently represented in terms of the red shift z, which is defined as in (2.4).

$$z = D - 1 \tag{2.4}$$

The component of the difference of velocities in (2.3) can be calculated considering the projection of the difference of velocity vectors on the line of the propagation of the signal from the emitter of signal E to the position of the satellite receiver S.

Denoting with $\mathbf{v}_\mathrm{E}$ the velocity vector of the emitter, with $\mathbf{v}_\mathrm{S}$ the velocity vector of the satellite receiver, and with $\mathbf{u}_\mathrm{LOB}$ the LOB, then the projected component of the difference in the velocity vectors Δv can be calculated considering the dot product in (2.5).

$$\Delta v = (\mathbf{v}_{\mathrm{E}} - \mathbf{v}_{\mathrm{S}}) \cdot \mathbf{u}_{\mathrm{LOB}} = (\mathbf{v}_{\mathrm{E}} - \mathbf{v}_{\mathrm{S}}) \cdot \frac{(\mathbf{x}_{\mathrm{E}} - \mathbf{x}_{\mathrm{S}})}{\|\mathbf{x}_{\mathrm{E}} - \mathbf{x}_{\mathrm{S}}\|} \tag{2.5}$$

The functional dependency in (2.5) is as shown in (2.6).

$$\Delta v = f\left(\mathbf{x}_{\mathrm{S}}, \mathbf{x}_{\mathrm{E}}, \mathbf{v}_{\mathrm{S}}, \mathbf{v}_{\mathrm{E}}\right) \tag{2.6}$$

Assuming the representation of the data in ECI, as reported in Sec. 1.5, then the functional representations in (2.7) can be written.

$$\begin{aligned} \mathbf{x}_{\mathrm{S}} &= f\left(a, e, i, \Omega, \omega, \nu\left(t\right)\right) \\ \mathbf{x}_{\mathrm{E}} &= f\left(\Lambda, \lambda, h, \alpha_{\mathrm{GR}}\left(t\right)\right) \\ \mathbf{v}_{\mathrm{S}} &= f\left(a, e, i, \Omega, \omega, \nu\left(t\right)\right) \\ \mathbf{v}_{\mathrm{E}} &= f\left(\Lambda, \lambda, h, \alpha_{\mathrm{GR}}\left(t\right)\right) \end{aligned} \tag{2.7}$$

At this point it is possible to reconstruct the overall dependence of Δv, as shown in (2.8).

$$\Delta v = f\left(\Lambda, \lambda, h, \alpha_{\mathrm{GR}}\left(t\right), a, e, i, \Omega, \omega, \nu\left(t\right)\right) \tag{2.8}$$

For a satellite in LEO, considering the available data onboard, only a, e, i, Ω, ω, and $\nu\left(t\right)$ are directly available, as they are representative of the current state of the satellite at time t. The value of $\alpha_{\mathrm{GR}}\left(t\right)$, depending only on the time t, is also a known quantity onboard the satellite.

Conversely, the position of a noncooperative emitter is not directly known by the satellite. However, its position can be estimated in terms of geodetic latitude $\hat{\Lambda}$ and longitude $\hat{\lambda}$ by solving the geolocation problem with a single measurement; $\hat{h}$, can be obtained furthermore through multiple platforms or with multiple measurements over time with a single receiver. The velocity of the emitter can be estimated in the same way.

With this latter case then an approximate estimation is as shown in (2.9) or, equivalently, as in (2.10).

$$\Delta v \approx f\left(\hat{\Lambda}, \hat{\lambda}, \hat{h}, \alpha_{\mathrm{GR}}\left(t\right), a, e, i, \Omega, \omega, \nu\left(t\right)\right) \tag{2.9}$$

$$\Delta v \approx (\hat{\mathbf{v}}_{\mathrm{E}} - \mathbf{v}_{\mathrm{S}}) \cdot \hat{\mathbf{u}}_{\mathrm{LOB}} = (\hat{\mathbf{v}}_{\mathrm{E}} - \mathbf{v}_{\mathrm{S}}) \cdot \frac{(\hat{\mathbf{x}}_{\mathrm{E}} - \mathbf{x}_{\mathrm{S}})}{\|\hat{\mathbf{x}}_{\mathrm{E}} - \mathbf{x}_{\mathrm{S}}\|} \tag{2.10}$$

Generally, the geolocation procedure is iterative and can be performed autonomously onboard in the case of AOA measurements. Here the position of the emitter is supposed to be already calculated and known.

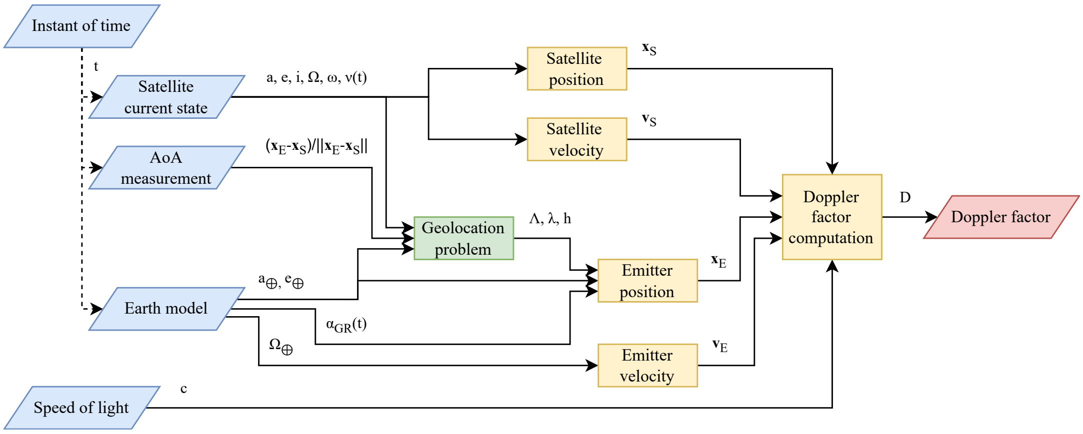

Figure 2.1: Example of computation of Doppler factor D in case of a satellite in LEO and an emitter of signal on the surface of the Earth. In this study the geolocation problem, represented in green, is assumed to be solved.

Considering all these premises, in principle, the expression for Δv in (2.5) and also the value of the Doppler factor $D(\Delta v)$ in (2.3) can be completely evaluated on-board and without external aids. An example of a possible scheme of computation is represented in Fig. 2.1.

For demonstrative purposes, simulations with an emitter of signal on the surface of the Earth, i.e. $h = 0$, is considered. Furthermore, and only for evaluative purposes in the simulation environment, a convenient instant of time t such that $\alpha_{\mathrm{GR}} = 0$ is considered. Since this variable is representative of the angular position of the Greenwich meridian, this assumption is equivalent to a shift in the value of the longitude for the emitter of the signal, which is not relevant for the purposes of the study.

The simulations considered the following set of input data:

— geodetic latitude of the emitter $\Lambda \in$ [-15, 15]°,
— longitude of the emitter $\lambda \in$ [-15, 15]°,
— semi-major axis of the orbit $a \in$ [6671, 8171] km,
— eccentricity of the orbit $e \in$ [0, 0.3],
— inclination of the orbit $i \in$ [75, 105]°,
— right ascension of the ascending node $\Omega \in$ [-15, 15]°,
— argument of perigee $\omega \in$ [-15, 15]°,
— true anomaly $\nu \in$ [-15, 15]°.

For every variable 9 evenly spaced values have been considered, for a total number of simulations of 43046721.

The histogram of the values of the Doppler factor is shown in Fig. 2.2.

The maximum value of the red shift z is $3.52474 \cdot 10^{-5}$ and the minimum value is $-3.52462 \cdot 10^{-5}$.

Data have been fitted in a first degree polynomial model D_1, as reported in

(2.11).

$$\begin{aligned} D\left(\Lambda, \lambda, a, e, i, \Omega, \omega, \nu\right) &\simeq D_1\left(\bar{\Lambda}, \bar{\lambda}, \bar{a}, \bar{e}, \bar{i}, \bar{\Omega}, \bar{\omega}, \bar{\nu}\right) \\ &= k_1\bar{\Lambda} + k_2\bar{\lambda} + k_3\bar{a} + k_4\bar{e} + k_5\bar{i} + k_6\bar{\Omega} + k_7\bar{\omega} \\ &\quad + k_8\bar{\nu} + k_9 \end{aligned} \tag{2.11}$$

In particular, the values of the coefficients $k_1, k_2, \ldots, k_9$ are related to the set of normalized variables as defined in (2.12), in which a 'minmax' normalization $\bar{w}$ of a variable w is reported. This operation guarantees both the dimensionlessness of the variables and their scaling, because the domain is transformed into a hypercube, where every variable is scaled from original values into the range from 0 to 1.

$$\bar{w}_{\mathrm{j}} = \frac{w_{\mathrm{j}} - \min\limits_{l}\left(w_l\right)}{\max\limits_{l}\left(w_l\right) - \min\limits_{l}\left(w_l\right)} \tag{2.12}$$

The values of the coefficients of the polynomial model D_1 are reported in Table 2.1.

In order to evaluate the goodness of the first degree polynomial model D_1, the percentage difference with respect to the analytical value D has been considered, as shown in (2.13), which compares the absolute difference to the mean value.

$$\delta_1 = 100\frac{|D - D_1|}{\left(\frac{D+D_1}{2}\right)} \tag{2.13}$$

The histogram of the values of the percentage difference δ_1 is reported in Fig. 2.3, the maximum value resulted in $8.14434 \cdot 10^{-3}$ % and the mean value resulted in $3.27606 \cdot 10^{-3}$ %.

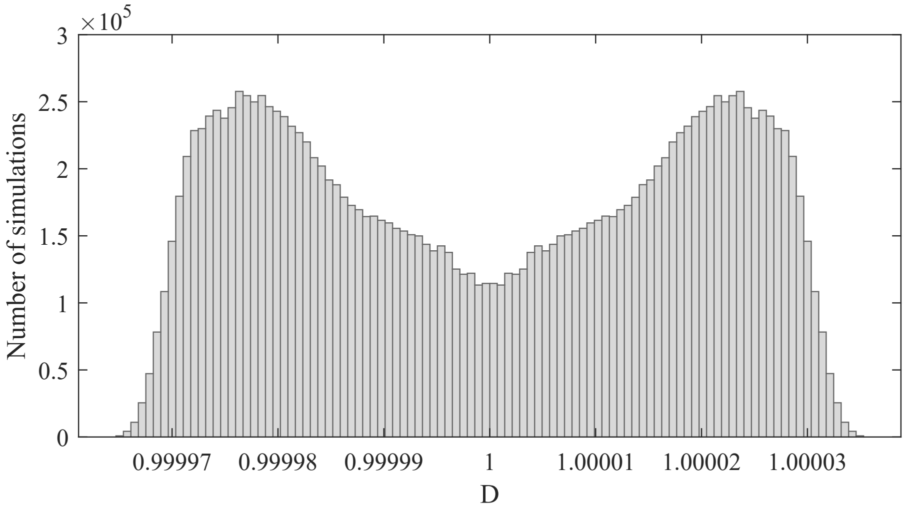

Figure 2.2: Histogram of the Doppler factor D in case of a satellite in LEO and an emitter of signal on the surface of the Earth.

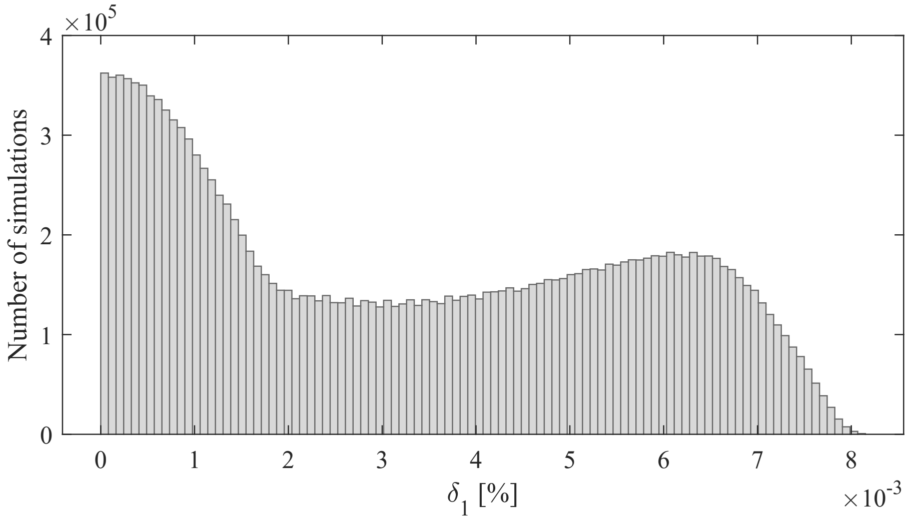

Figure 2.3: Histogram of the percentage difference of the Doppler factor δ_1 in case of a satellite in LEO and an emitter of signal on the surface of the Earth.

Table 2.1: Values of the coefficients for the polynomial model D_1.

Coefficient	**Value**
k_1	$3.04616 \cdot 10^{-6}$
k_2	$-1.80155 \cdot 10^{-6}$
k_3	$1.14970 \cdot 10^{-11}$
k_4	$3.08047 \cdot 10^{-5}$
k_5	$1.80156 \cdot 10^{-6}$
k_6	$1.32067 \cdot 10^{-10}$
k_7	$-4.63610 \cdot 10^{-11}$
k_8	$-3.11687 \cdot 10^{-5}$
k_9	$9.99998 \cdot 10^{-1}$

2.2 Newtonian Time Delay and Longitude Shift

This section summarises models, methods, and results in the published articles of the author [27] and [6].

The analysis considers one single emitter placed on the surface of the Earth and a receiver mounted on a satellite in LEO, which is able to perform AOA measurements. Through the study of relative geometry between the satellite and the emitter of signal the shift on the longitude component of the position error is predicted and a strategy of error compensation is derived.

Two alternative algorithms of simulation are presented and simulated.

Finally, the fitting of simulated data in the form of first degree and second degree polynomial models are presented.

The error measurement for the emitter $\mathbf{e}_{\mathrm{E}}$ can be defined as in (2.14).

$$\mathbf{e}_{\mathrm{E}} = |\mathbf{x}_{\mathrm{E}} - \hat{\mathbf{x}}_{\mathrm{E}}| \tag{2.14}$$

There are multiple sources of error, and an engineering method for error modelling involves expressing this measurement as the total of different contributions coming from the physical elements: position errors from the receiver $\mathbf{e}_{\mathrm{E,r}}$, the satellite platform $\mathbf{e}_{\mathrm{E,sat}}$, and signal propagation $\mathbf{e}_{\mathrm{E,s.p.}}$ constitute a first level of subdivision, as shown in (2.15).

$$\mathbf{e}_{\mathrm{E}} = \mathbf{e}_{\mathrm{E,r}} + \mathbf{e}_{\mathrm{E,sat}} + \mathbf{e}_{\mathrm{E,s.p.}} \tag{2.15}$$

The main topic of this work is the contribution of position error of the emitter due to signal propagation $\mathbf{e}_{\mathrm{E,s.p.}}$, which takes into account the finite speed of the propagation of the electromagnetic waves, the relativistic effects, and the presence of the atmosphere.

The signal is considered always detected and omnidirectional; phenomena of reflection and multipath are neglected.

The expression of the contribution of the position error $\mathbf{e}_{\mathrm{E,s.p.}}$ can be expressed in LLH as shown in (2.16); the pedix $\mathrm{E,s.p.}$ is omitted in the components of the vector and in all subsequent formulae to avoid excessive verbosity.

$$\mathbf{e}_{\mathrm{E,s.p.}} = \begin{pmatrix} e_{\Lambda_{\mathrm{E,s.p.}}} \\ e_{\lambda_{\mathrm{E,s.p.}}} \\ e_{\mathrm{h}_{\mathrm{E,s.p.}}} \end{pmatrix} = \begin{pmatrix} e_{\Lambda} \\ e_{\lambda} \\ e_{\mathrm{h}} \end{pmatrix} \tag{2.16}$$

Considering that by definition the error is defined by the absolute difference between the exact value and the estimated one, the set of equations in (2.17) can be written.

$$
\begin{aligned}
e_{\Lambda} &= \left|\Lambda - \hat{\Lambda}\right| \\
e_{\lambda} &= \left|\lambda - \hat{\lambda}\right| \\
e_{\mathrm{h}} &= \left|h - \hat{h}\right|
\end{aligned} \tag{2.17}
$$

Furthermore, considering as first level of approximation the propagation in vacuum and assuming Newtonian mechanics, the sole cause of error is due to the rotation of the Earth, as shown in Fig. 2.4.

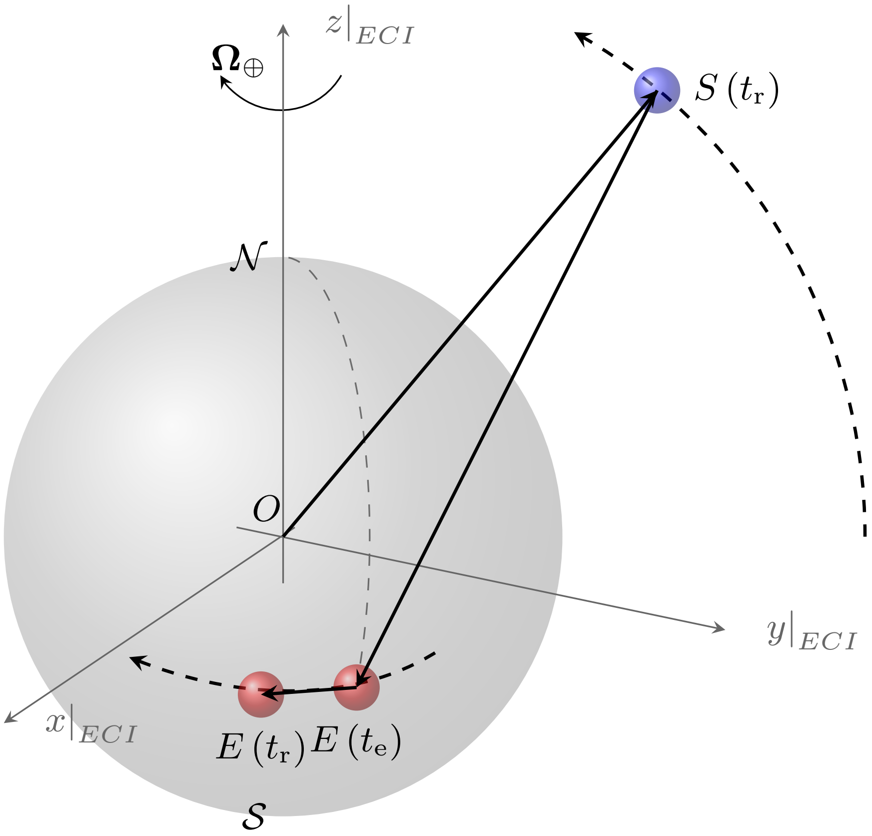

Figure 2.4: While the signal is going from the emitter position at instant of emission, $E\left(t_{\mathrm{e}}\right)$, to the satellite position at instant of reception, $S\left(t_{\mathrm{r}}\right)$, the emitter has moved from the position $E\left(t_{\mathrm{e}}\right)$ to the position $E\left(t_{\mathrm{r}}\right)$ due to the rotation of the Earth.

In particular, denoting with t_{e} the emission instant of time and with t_{r} the instant of time of reception, while the electromagnetic wave is travelling through the space, the emitter has moved from the position $\mathbf{x}_{\mathrm{E}}\left(t_{\mathrm{e}}\right)$ to the position $\mathbf{x}_{\mathrm{E}}\left(t_{\mathrm{r}}\right)$, so the set of equations (2.18) can be considered.

$$\begin{aligned} e_{\Lambda} &= \left|\Lambda\left(t_{\mathrm{r}}\right) - \Lambda\left(t_{\mathrm{e}}\right)\right| \\ e_{\lambda} &= \left|\lambda\left(t_{\mathrm{r}}\right) - \lambda\left(t_{\mathrm{e}}\right)\right| \\ e_{\mathrm{h}} &= \left|h\left(t_{\mathrm{r}}\right) - h\left(t_{\mathrm{e}}\right)\right| \end{aligned} \tag{2.18}$$

For an emitter on the surface of the Earth, $\Lambda\left(t_{\mathrm{e}}\right) = \Lambda\left(t_{\mathrm{r}}\right)$ and $h\left(t_{\mathrm{e}}\right) = h\left(t_{\mathrm{r}}\right)$, so (2.19) is valid.

$$\mathbf{e}_{\mathrm{E,s.p.}} = \begin{pmatrix} 0 \\ \left|\lambda\left(t_{\mathrm{r}}\right) - \lambda\left(t_{\mathrm{e}}\right)\right| \\ 0 \end{pmatrix} \tag{2.19}$$

Since Earth's rotation is the source of the longitude error, the position error contribution can be calculated by taking into account the Earth's angular speed $\Omega_{\oplus} = 0.0042°/\mathrm{s}$ and the delay caused by the signal propagation $\Delta t = t_{\mathrm{r}} - t_{\mathrm{e}}$, as shown in (2.20).

$$e_{\lambda} = \Omega_{\oplus}\Delta t = \Omega_{\oplus}\left(t_{\mathrm{r}} - t_{\mathrm{e}}\right) \tag{2.20}$$

With local values of the radius of the Earth $R_{\oplus}$ and the cosine of the geodetic latitude Λ, the linear displacement error l_{λ} can be derived from the angular error e_{λ}, as shown in (2.21).

$$l_{\lambda} = e_{\lambda} R_{\oplus}\left(\Lambda, \lambda\right)\cos\left(\Lambda\right) \tag{2.21}$$

Equation (2.21) can be rewritten as in (2.22) for an ellipsoidal model with two equal axes on the equatorial plane and a different axis along the North-South direction. In this case, the radius of Earth $R_{\oplus}$ depends only on the geodetic latitude of the emitter Λ.

$$l_{\lambda} = e_{\lambda} R_{\oplus}\left(\Lambda\right)\cos\left(\Lambda\right) \tag{2.22}$$

Under the set of assumptions considered in this subsection, the angular position e_{λ} and the linear position error l_{λ} are deterministic. In a real-case scenario they can be compensated evaluating the time delay Δt_{n} as in (2.23) and considering the finite speed of propagation of the signal in vacuum equal to $c_0 = 299792458$ m/s. The subscript n indicates that this delay has been calculated considering Newtonian mechanics.

$$\Delta t_{\mathrm{n}} = \frac{\left\|\mathbf{x}_{\mathrm{S}}\left(t_{\mathrm{r}}\right) - \hat{\mathbf{x}}_{\mathrm{E}}\left(t_{\mathrm{e}}\right)\right\|}{c_0} \tag{2.23}$$

Even if, from the satellite perspective, only the instant of time t_{r} is known, while the emission instant of time t_{e} is unknown, the position of the emitter $\hat{\mathbf{x}}_{\mathrm{E}}\left(t_{\mathrm{e}}\right)$ at emission instant of time can still be obtained from the problem formulated in (1.20),

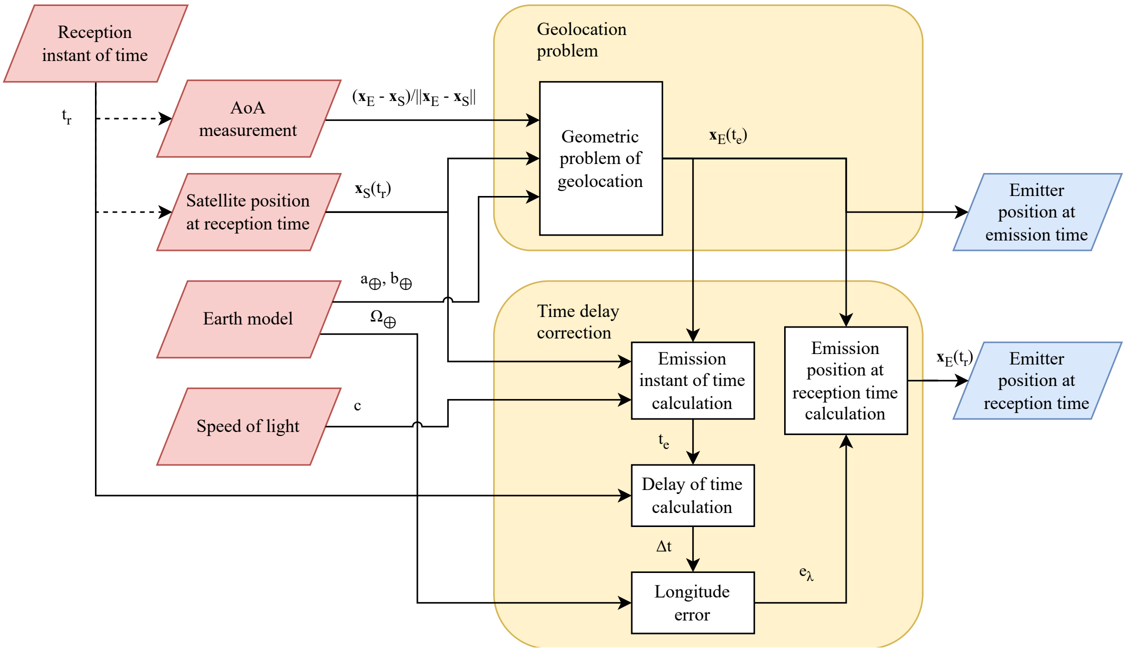

Figure 2.5: Block diagram for the geolocation problem with a single AOA measurement for an emitter on the surface of the Earth and error compensation on longitude position due to time delay.

in which the position error does not explicitly depend on the emission instant of time. Then, the emission instant of time can be obtained considering $t_\mathrm{e} = t_\mathrm{r} - \Delta t_\mathrm{n}$.

Under this set of assumptions, the longitude error modelled in (2.20) and (2.22) have deterministic nature.

The procedure of error compensation on longitude direction in geolocation is shown in the block diagram in Fig. 2.5.

The angular and linear errors on the longitude direction, e_λ and d_λ, depend only on the delay Δt, as shown in (2.20), but, as can be noticed in (2.23), this delay can be obtained from the satellite position at reception time t_r and the emitter position at emission time t_e, but not on their particular coordinate frame representation, so generally (2.24) can be written.

$$\begin{aligned} e_\lambda &= f\left(\mathbf{x}_\mathrm{E}\left(t_\mathrm{e}\right), \mathbf{x}_\mathrm{S}\left(t_\mathrm{r}\right)\right) \\ l_\lambda &= g\left(\mathbf{x}_\mathrm{E}\left(t_\mathrm{e}\right), \mathbf{x}_\mathrm{S}\left(t_\mathrm{r}\right)\right) \end{aligned} \tag{2.24}$$

Considering the conversion among the coordinate systems in 1.5, for (2.24) the functional dependencies in (2.25) can be written. It is recalled for the reader that for an orbit only the true anomaly ν is a function of time t, while the other orbital parameters are supposed to be constants: their variation over time are due to external disturbances or intentional maneuvers.

$$\begin{aligned} e_\lambda &= f\left(\Lambda_{\mathrm{E}}, \lambda_{\mathrm{E}}\left(t_{\mathrm{e}}\right), a, e, i, \omega, \Omega, \nu\left(t_{\mathrm{r}}\right)\right) \\ l_\lambda &= g\left(\Lambda_{\mathrm{E}}, \lambda_{\mathrm{E}}\left(t_{\mathrm{e}}\right), a, e, i, \omega, \Omega, \nu\left(t_{\mathrm{r}}\right)\right) \end{aligned} \tag{2.25}$$

For a circular orbit the expressions (2.25) can be simplified in (2.26). This is because the eccentricity e is 0, and the semi-major axis a becomes equal to the radius of the orbit r which is given by the sum of the altitude of the orbit h_{S} and the mean radius of the Earth, which is equal to 6371.009 km. Furthermore, since it is no more possible to define the orientation of the ellipse (i.e., the line of apsides), the argument of perigee becomes a meaningless quantity, and by definition it is posed $\omega = 0$.

$$\begin{aligned} e_\lambda &= f\left(\Lambda_{\mathrm{E}}, \lambda_{\mathrm{E}}\left(t_{\mathrm{e}}\right), r, i, \Omega, \nu\left(t_{\mathrm{r}}\right)\right) \\ l_\lambda &= g\left(\Lambda_{\mathrm{E}}, \lambda_{\mathrm{E}}\left(t_{\mathrm{e}}\right), r, i, \Omega, \nu\left(t_{\mathrm{r}}\right)\right) \end{aligned} \tag{2.26}$$

In simulation environment to simulate a single AOA measurement, the two instants of time t_{e} and t_{r} are not available together, because it is possible to have only one of the two information, so their simulated positions of the satellite and emitter, i.e., the couple of vectors $\left(\mathbf{x}_{\mathrm{E}}\left(t_{\mathrm{e}}\right), \mathbf{x}_{\mathrm{S}}\left(t_{\mathrm{e}}\right)\right)$ or $\left(\mathbf{x}_{\mathrm{E}}\left(t_{\mathrm{r}}\right), \mathbf{x}_{\mathrm{S}}\left(t_{\mathrm{r}}\right)\right)$. However, it is possible to evaluate the delay Δt through an iterative procedure. Depending on the instant of time chosen in the simulation, there are two ways to simulate the scenario:

- in the first case t_{r} is supposed to be known, $\mathbf{x}_{\mathrm{S}}\left(t_{\mathrm{r}}\right)$ is also known, but the emitter position is iteratively updated from $\mathbf{x}_{\mathrm{E}}\left(t_{\mathrm{r}}\right)$ to $\mathbf{x}_{\mathrm{E}}\left(t_{\mathrm{e}}\right)$, as shown in the algorithm in subsection 2.2.1;

- in the second option t_{e} is supposed to be known, $\mathbf{x}_{\mathrm{E}}\left(t_{\mathrm{e}}\right)$ is also known, but the satellite position is iteratively updated from $\mathbf{x}_{\mathrm{S}}\left(t_{\mathrm{e}}\right)$ to $\mathbf{x}_{\mathrm{S}}\left(t_{\mathrm{r}}\right)$, as shown in the algorithm in subsection 2.2.2.

However, both of them can be depicted in a logical scheme of Fig. 2.6.

About the numerical simulation of the scenario, the algorithm depicted in Sec. 2.2.2 has been used to calculate the time delay in Sec. 2.2.3 and Sec. 2.2.4. In particular, the algorithm moves on a grid of the sampled arc of the ellipse and interpolates the current position among these points with a local spline. Approximating the arc of the ellipse with 800 points, there is a corresponding precision on the satellite position between 10^{-6} m and 10^{-9} m depending on the orbit size. The observed precision on the simulated time delay is up to the 48th decimal figure (values in seconds). However, results have been truncated to the 6th figure because of the precision of other physical quantities (i.e., mainly the model of Earth).

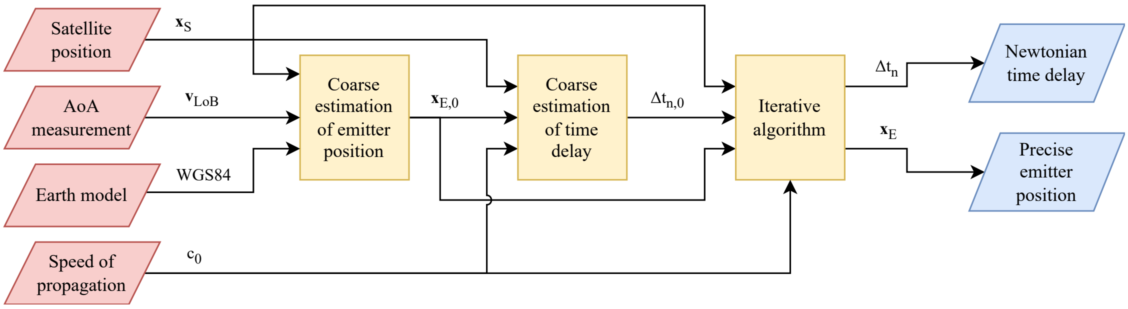

Figure 2.6: Block diagram for the calculation of Newtonian time delay Δt_n from satellite position $\mathbf{x}_\mathrm{S}$, AOA measurement $\mathbf{v}_\mathrm{LoB}$, and a model of Earth's surface (in the example WGS84). The algorithm firstly calculates a coarse estimation of the emitter position considering $\mathbf{x}_{\mathrm{E},0}$. Secondly, it calculates a coarse estimate of Newtonian time delay $\Delta t_{\mathrm{n},0}$ from the satellite position and the coarse emitter position considering the speed of propagation of the signal c_0. In the end, an iterative predictor-corrector procedure can be exploited to obtain a precise estimation of emitter position $\mathbf{x}_\mathrm{E}$.

2.2.1 Algorithm of Simulation I

In this version of the algorithm the instant of time t_{r} is known, so the positions of the satellite S and the emitter E in this instant of time. The goal of this algorithm is to obtain the position of the emitter at instant of time t_{e} due to time delay Δt through a correction on the longitude $\Delta\lambda_{\mathrm{E}}$. Conceptually, as shown in (2.27) and (2.28), it is a two-step algorithm:

- Firstly, a prediction of the longitude correction $(\Delta\lambda)_k$ is obtained considering an approximate interval of time $(\Delta t)_k$, which can be calculated from the distance $(d)_k$ between the satellite at instant of time t_{r} and the emitter at instant of time $(t)_{k-1}$, with $(t)_0 = t_{\mathrm{r}}$;
- in the second step, the longitude of the emitter $(\lambda_{\mathrm{E}})_k$ is corrected with the value of $(\Delta\lambda_{\mathrm{E}})_k$ and it is used for the estimation of a new position of the emitter $(\mathbf{x}_E)_k$, which is used in the step one.

$$(\Delta\lambda_{\mathrm{E}})_k = \Omega_{\oplus} (\Delta t)_k = \Omega_{\oplus} \frac{(d)_k}{c} = \Omega_{\oplus} \frac{\left\| \mathbf{x}_{\mathrm{S}} (t_{\mathrm{r}}) - \mathbf{x}_{\mathrm{E}} \left((t)_{k-1} \right) \right\|}{c} \tag{2.27}$$

$$(\lambda_{\mathrm{E}})_k = \lambda_{\mathrm{E}} (t_{\mathrm{r}}) + (\Delta\lambda_{\mathrm{E}})_k \tag{2.28}$$

As illustrated in Fig. 2.7, the algorithm produces a sequences of distances $(d)_1, (d)_2, ..., (d)_k, ..., (d)_\infty$, time delays $(\Delta t)_1, (\Delta t)_2, ..., (\Delta t)_k, ..., (\Delta t)_\infty$ and longitude intervals $(\Delta\lambda_{\mathrm{E}})_1, (\Delta\lambda_{\mathrm{E}})_2, ..., (\Delta\lambda_{\mathrm{E}})_k, ..., (\Delta\lambda_{\mathrm{E}})_\infty$. In the end, the error on the longitude e_λ is equal to the limit to infinity of the sequence of the compensations on longitude component, as shown in (2.29).

$$e_\lambda = \left| \lim_{k \to \infty} (\Delta\lambda_{\mathrm{E}})_k \right| \tag{2.29}$$

A possible implementation of algorithm is depicted in Fig. 2.8, where the difference in the position of (2.27) is performed in ECI reference frame and the update of the longitude is performed in LLH reference frame. The cycle ends when a condition on the position of the emitter is met through a threshold θ_{E}.

2.2.2 Algorithm of Simulation II

In this second version of the algorithm the instant of time t_{e} is known, so the positions of the satellite S and the emitter E in this instant of time. The goal of this algorithm is to obtain the position of the satellite at instant of time t_{r} due to time delay Δt through a correction on the true anomaly ν.

During the delay Δt the signal has moved from the emitter $\mathbf{x}_{\mathrm{E}} (t_{\mathrm{e}})$ to the satellite $\mathbf{x}_{\mathrm{S}} (t_{\mathrm{e}} + \Delta t)$ propagating with speed c. In the same amount of time the satellite has moved from $\mathbf{x}_{\mathrm{S}} (t_{\mathrm{e}})$ to $\mathbf{x}_{\mathrm{S}} (t_{\mathrm{e}} + \Delta t)$ with velocity $\|\mathbf{v}_{\mathrm{S}}\|$, that for a circular orbit

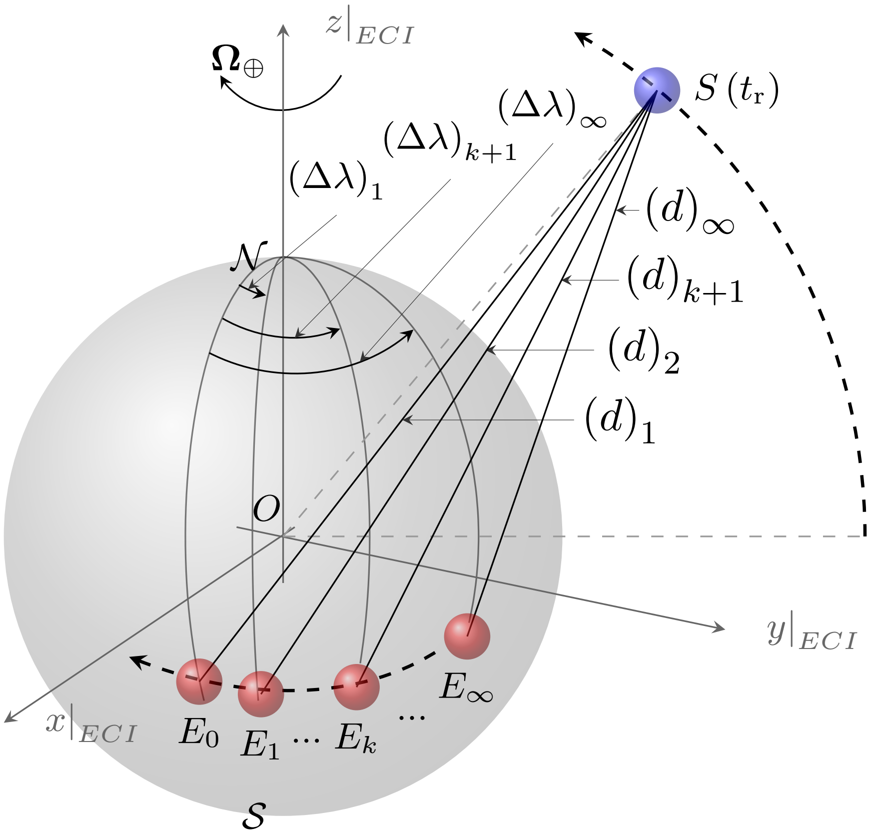

Figure 2.7: Illustration of positions in algorithm I: $\{E_0, E_1, ..., E_k, ..., E_{\infty}\}$ is the sequence of emitter positions calculated by the algorithm with $E_0 = E\left(t_{\mathrm{r}}\right)$ and $E_{\infty} = E\left(t_{\mathrm{e}}\right)$, while $S\left(t_{\mathrm{r}}\right)$ is the satellite position at reception time t_{r}.

is equal to $\|\mathbf{v}_{\mathrm{S}}\| = \sqrt{\mu_{\oplus}/r}$ with $\mu_{\oplus} = 3.986005 \cdot 10^{14}\ \mathrm{m}^3/\mathrm{s}^{-2}$, the standard gravitational parameter for Earth. Considering this fact, a two-step algorithm can be built, as shown in (2.30) and (2.31). In particular:

- A prediction of the true anomaly correction $(\Delta\nu)_k$ is obtained considering an approximate interval of time $(\Delta t)_k$, which can be calculated from the radius of the orbit r, the speed of the satellite $\|\mathbf{v}_{\mathrm{S}}\|$, and distance $(d)_k$ between the emitter at instant of time t_{e} and the satellite at instant of time $(t)_{k-1}$, with $(t)_0 = t_{\mathrm{e}}$;

- in the second step, the true anomaly of the satellite $(\nu)_k$ is corrected with the value of $(\Delta\nu)_k$ and it is used for the estimation of a new position of the satellite $(\mathbf{x}_S)_k$, which is used in the step one.

```
set $t_\mathrm{r}$                                                        ▷ Reception instant of time
set $\theta_\mathrm{E}$                                                   ▷ Cycle threshold
load $\Omega_\oplus$                                                      ▷ Earth angular speed
load $r,\ i,\ \Omega,\ \nu\left(t_\mathrm{r}\right)$                      ▷ Satellite position
load $\Lambda_\mathrm{E}\left(t_\mathrm{r}\right), \lambda_\mathrm{E}\left(t_\mathrm{r}\right)$   ▷ Emitter position
initialize $\left(\Delta_\mathrm{E}\right)_0 = +\infty$
while $\left(\Delta_\mathrm{E}\right)_k \geq \theta_\mathrm{E}$ do
    $(d)_k \leftarrow \left\|\mathbf{x}_\mathrm{S}\left(t_\mathrm{r}\right) - \mathbf{x}_\mathrm{E}\left(\left(\lambda_\mathrm{E}\right)_{k-1}\right)\right\|$   ▷ Distance
    $(\Delta t)_k \leftarrow (d)_k / c$                                   ▷ Time delay
    $(t)_k \leftarrow t_\mathrm{r} - (\Delta t)_k$                        ▷ Update emission instant of time
    $\left(\Delta\lambda_\mathrm{E}\right)_k \leftarrow \Omega_\oplus (\Delta t)_k$   ▷ Longitude correction
    $\left(\lambda_\mathrm{E}\right)_k \leftarrow \lambda_E\left(t_\mathrm{r}\right) + \left(\Delta\lambda_\mathrm{E}\right)_k$   ▷ Longitude update
    $\left(\Delta_\mathrm{E}\right)_k \leftarrow \left\|\mathbf{x}_\mathrm{E}\left((\lambda)_k\right) - \mathbf{x}_\mathrm{E}\left((\lambda)_{k-1}\right)\right\|$   ▷ Condition
end while
$e_\lambda \leftarrow \left|\Delta\lambda_\mathrm{E}\right|$             ▷ Longitude error (angle)
$d_\lambda \leftarrow e_\lambda R_\oplus\left(\Lambda_\mathrm{E}\right)\cos\left(\Lambda_\mathrm{E}\right)$   ▷ Longitude error (distance)
return $e_\lambda, d_\lambda, t_\mathrm{e}$
```

Figure 2.8: First algorithm of simulation for the Newtonian time delay.

$$
\begin{aligned}
(\Delta\nu)_k &= \frac{\left\|\mathbf{v}_\mathrm{S}\right\|}{r}(\Delta t)_k = \frac{1}{r}\sqrt{\frac{\mu_\oplus}{r}}(\Delta t)_k = \frac{1}{r}\sqrt{\frac{\mu_\oplus}{r}}\frac{(d)_k}{c} \\
&= \frac{1}{r}\sqrt{\frac{\mu_\oplus}{r}}\frac{\left\|\mathbf{x}_\mathrm{S}\left((t)_{k-1}\right) - \mathbf{x}_\mathrm{E}\left(t_\mathrm{e}\right)\right\|}{c}
\end{aligned}
\tag{2.30}
$$

$$
(\nu)_k = \nu\left(t_\mathrm{e}\right) + (\Delta\nu)_k \tag{2.31}
$$

As illustrated in Fig. 2.10, the algorithm produces a sequence of time delays $(\Delta t)_1, (\Delta t)_2, ..., (\Delta t)_k, ..., (\Delta t)_\infty$.

Consequently, a sequence of true anomalies $(\Delta\nu)_1, (\Delta\nu)_2, ..., (\Delta\nu)_k, ..., (\Delta\nu)_\infty$ is also produced.

Similarly to the previous algorithm, the error on the longitude e_λ can be calculated from the time delay Δt.

An implementation of algorithm is depicted in Fig. 2.9, where, again, the difference in the position of (2.28) is performed in ECI reference frame and the update of the longitude is performed in LLH reference frame. The cycle ends when a condition on the position of the satellite is met through a threshold θ_S.

2.2.3 First Campaign of Simulations

Here are reported the results obtained in a first campaign of simulations, as published in a work of the author [27]. In this first set of results the analysis is limited to circular orbits.

```
set $t_\mathrm{e}$                                                     ▷ Emission instant of time
set $\theta_\mathrm{S}$                                                ▷ Cycle threshold
load $\mu_\oplus$                                                      ▷ Earth standard gravitational parameter
load $r$, $i$, $\Omega$, $\nu(t_\mathrm{e})$                           ▷ Satellite position
load $\Lambda_\mathrm{E}(t_\mathrm{e}), \lambda_\mathrm{E}(t_\mathrm{e})$   ▷ Emitter position
initialize $(\Delta_\mathrm{S})_0 = +\infty$
while $(\Delta_\mathrm{S})_k \geq \theta_\mathrm{S}$ do
    $(d)_k \leftarrow \left\|\mathbf{x}_\mathrm{S}\left((\nu)_{k-1}\right) - \mathbf{x}_\mathrm{E}(t_\mathrm{e})\right\|$   ▷ Distance
    $(\Delta t)_k \leftarrow (d)_k / c$                                ▷ Time delay
    $(t)_k \leftarrow t_\mathrm{e} + (\Delta t)_k$                     ▷ Update reception instant of time
    $(\Delta\nu)_k \leftarrow \left(\sqrt{\mu_\oplus/r}\,(\Delta t)_k\right)/r$   ▷ True anomaly correction
    $(\nu)_k \leftarrow \nu(t_\mathrm{e}) + (\Delta\nu)_k$             ▷ Update true anomaly
    $(\Delta_\mathrm{S})_k \leftarrow \left\|\mathbf{x}_\mathrm{S}((\nu)_k) - \mathbf{x}_\mathrm{S}\left((\nu)_{k-1}\right)\right\|$   ▷ Condition
end while
$e_\lambda \leftarrow \Omega_\oplus \Delta t$                          ▷ Longitude error (angle)
$d_\lambda \leftarrow e_\lambda R_\oplus(\Lambda_\mathrm{E})\cos(\Lambda_\mathrm{E})$   ▷ Longitude error (distance)
return $e_\lambda, d_\lambda, t_\mathrm{r}$
```

Figure 2.9: Second algorithm of simulation for the Newtonian time delay.

The simulations of the model (2.26) have been conducted in MATLAB environment considering the following input ranges:

— Geodetic latitude of the emitter $\Lambda_\mathrm{E} \in [-15°, 15°]$;
— Longitude of the emitter $\lambda_\mathrm{E} \in [-15°, 15°]$;
— Altitude of the orbit $h_\mathrm{S} \in [300\text{ km}, 1800\text{ km}]$;
— Inclination of the orbit $i \in [75°, 105°]$;
— Right ascension of the ascending node $\Omega \in [-15°, 15°]$;
— True anomaly $\nu \in [-15°, 15°]$.

The values of input data are evenly spaced with a step of 3° for angles and 150 km for the radius of the orbit. The total number of of simulations resulted in 1771561 cases.

The range of Λ_E is centered in 0°, because it represents the worst case scenario for the contribution of the error d_λ. The choice of the ranges for Λ_E, λ_E, Ω, and ν is limited by the geometry: depending on the radius of the orbit r, there is a corresponding set of angles to keep the line of sight, otherwise the satellite (or the emitter) goes beyond the horizon. The radii of the orbit r are chosen within LEO range of missions and the inclination of the orbit i is centered in 90°, because it is representative of the operative scenario of the whole Earth scanning. Time delays Δt resulted in a minimum value of 0.977 ms, a maximum value of 19.262 ms, and a mean value of 7.895 ms. Values of the longitude error displacement d_λ have been reported in the histogram in Fig. 2.11 with a minimum value of 0.444 m, a maximum value of 8.697 m, and a mean value of 3.637 m. The minimum value of

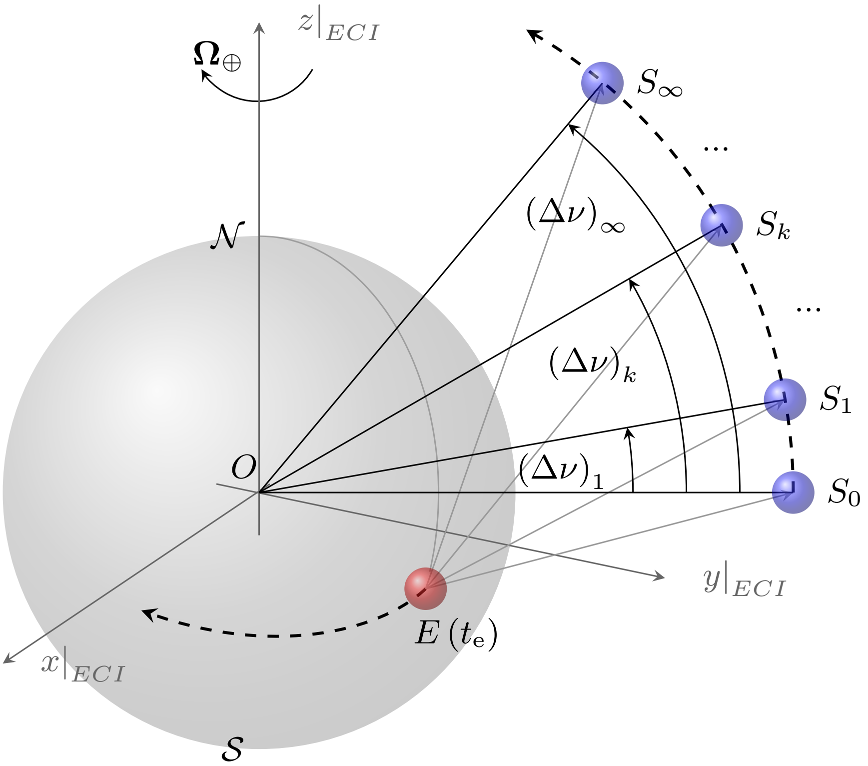

Figure 2.10: Illustration of positions in algorithm II: $\{S_0, S_1, ..., S_k, ..., S_\infty\}$ is the sequence of satellite position with with $S_0 = S(t_\mathrm{e})$ and $S_\infty = S(t_\mathrm{r})$, while $E(t_\mathrm{e})$ is the emitter position at emission time t_e.

error is observed in multiple points. In particular, when the height of the orbit is minimum $h_\mathrm{S} = 300$ km, the inclination is $i = 90°$, the latitude is far from Equator, $\Lambda_\mathrm{E} = \pm 15°$, $\lambda_\mathrm{E} = -\Omega$, and ν realizes Nadiral pointing. For a value of $\theta_\mathrm{S} = 10^{-9}$ m the simulation algorithm II, Fig. 2.9, required no more than 3 iterations. For comparison, on the same cases, a bisection method applied on (2.23) required more than 30 iterations for a precision of 10^{-9} s on the delay Δt.

Starting from the data gathered in simulations performed in subsection, approximations of the function (2.26) based on Taylor's expansion and regression of data in the form of first degree polynomial $d_{\lambda,1}$ and second degree polynomial $d_{\lambda,2}$ are reported in (2.32) and (2.33).

$$d_\lambda \simeq d_{\lambda,1}(\Lambda_\mathrm{E}, \lambda_\mathrm{E}, r, i, \Omega, \nu) = k_1\Lambda_\mathrm{E} + k_2\lambda_\mathrm{E} + k_3 r + k_4 i + k_5\Omega + k_6\nu + k_7 \quad (2.32)$$

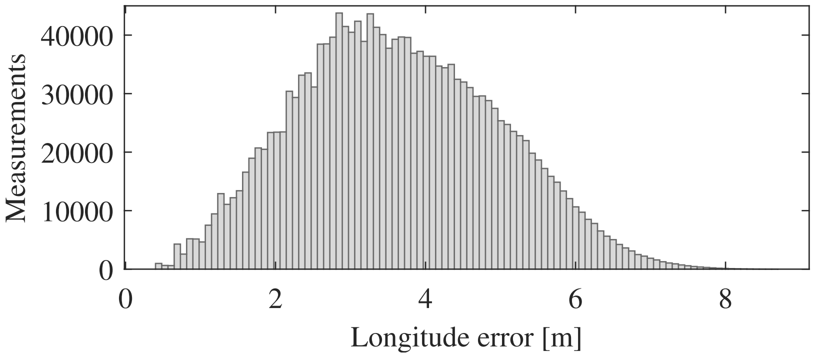

Figure 2.11: Errors on the longitude estimation d_λ due to signal propagation delay in case of an emitter on the surface of the Earth and a receiver mounted on a satellite in a circular orbit.

$$
\begin{aligned}
d_\lambda \simeq d_{\lambda,2}\left(\Lambda_{\mathrm{E}}, \lambda_{\mathrm{E}}, r, i, \Omega, \nu\right) &= k_1\Lambda_{\mathrm{E}}^2 + k_2\Lambda_{\mathrm{E}}\lambda_{\mathrm{E}} + k_3\Lambda_{\mathrm{E}}r + k_4\Lambda_{\mathrm{E}}i + k_5\Lambda_{\mathrm{E}}\Omega \\
&+ k_6\Lambda_{\mathrm{E}}\nu + k_7\Lambda_{\mathrm{E}} + k_8\lambda_{\mathrm{E}}^2 + k_9\lambda_{\mathrm{E}}r + k_{10}\lambda_{\mathrm{E}}i + k_{11}\lambda_{\mathrm{E}}\Omega + k_{12}\lambda_{\mathrm{E}}\nu + k_{13}\lambda_{\mathrm{E}} \\
&+ k_{14}r^2 + k_{15}ri + k_{16}r\Omega + k_{17}r\nu + k_{18}r + k_{19}i^2 + k_{20}i\Omega + k_{21}i\nu + k_{22}i \\
&+ k_{23}\Omega^2 + k_{24}\Omega\nu + k_{25}\Omega + k_{26}\nu^2 + k_{27}\nu + k_{28}
\end{aligned}
\tag{2.33}
$$

The values of coefficients are:

- For first degree polynomial $k_1 = 8.618 \times 10^{-1}$ m/rad, $k_2 = 3.189 \times 10^{-2}$ m/rad, $k_3 = 3.285 \times 10^{-10}$, $k_4 = 2.703$ m/rad, $k_5 = -3.189 \times 10^{-2}$ m/rad, $k_6 = -8.608 \times 10^{-1}$ m/rad, $k_7 = -5.769 \times 10^{-1}$ m;

- For second degree polynomial $k_1 = 1.259 \times 10$ m/rad^2, $k_2 = -5.329 \times 10^{-3}$ m/rad^2, $k_3 = -1.002 \times 10^{-8}$ 1/rad, $k_4 = -2.167 \times 10^{-1}$ m/rad^2, $k_5 = 5.329 \times 10^{-3}$ m/rad^2, $k_6 = -2.709 \times 10^{1}$ m/rad^2, $k_7 = 1.749$ m/rad, $k_8 = 1.264 \times 10^{1}$ m/rad^2, $k_9 = -2.684 \times 10^{-7}$ 1/rad, $k_{10} = 1.038 \times 10^{-2}$ m/rad^2, $k_{11} = -2.729 \times 10^{1}$ m/rad^2, $k_{12} = 4.153 \times 10^{-3}$ m/rad^2, $k_{13} = 2.007$ m/rad, $k_{14} = -4.000 \times 10^{-15}$ 1/m, $k_{15} = -1.365 \times 10^{-10}$ 1/rad, $k_{16} = 2.684 \times 10^{-7}$ 1/rad, $k_{17} = -1.3336 \times 10^{-9}$ 1/rad, $k_{18} = 5.782 \times 10^{-8}$, $k_{19} = 1.692$ m/rad^2, $k_{20} = -1.038 \times 10^{-2}$ m/rad^2, $k_{21} = 2.184 \times 10^{-1}$ m/rad^2, $k_{22} = -2.615$ m/rad, $k_{23} = 1.264 \times 10^{1}$ m/rad^2, $k_{24} = -4.153 \times 10^{-3}$ m/rad^2, $k_{25} = -2.007$ m/rad, $k_{26} = 1.053 \times 10$ m/rad^2, $k_{27} = -1.562$ m/rad, $k_{28} = 2.017$ m.

The goodness of these models is evaluated considering the evaluations of the error of longitude in the exact case d_λ and the approximated ones $d_{\lambda,1}$ and $d_{\lambda,2}$, as shown in (2.34).

$$
\begin{aligned}
\delta_{\lambda,1} &= \left|d_\lambda - d_{\lambda,1}\right| \\
\delta_{\lambda,2} &= \left|d_\lambda - d_{\lambda,2}\right|
\end{aligned}
\tag{2.34}
$$

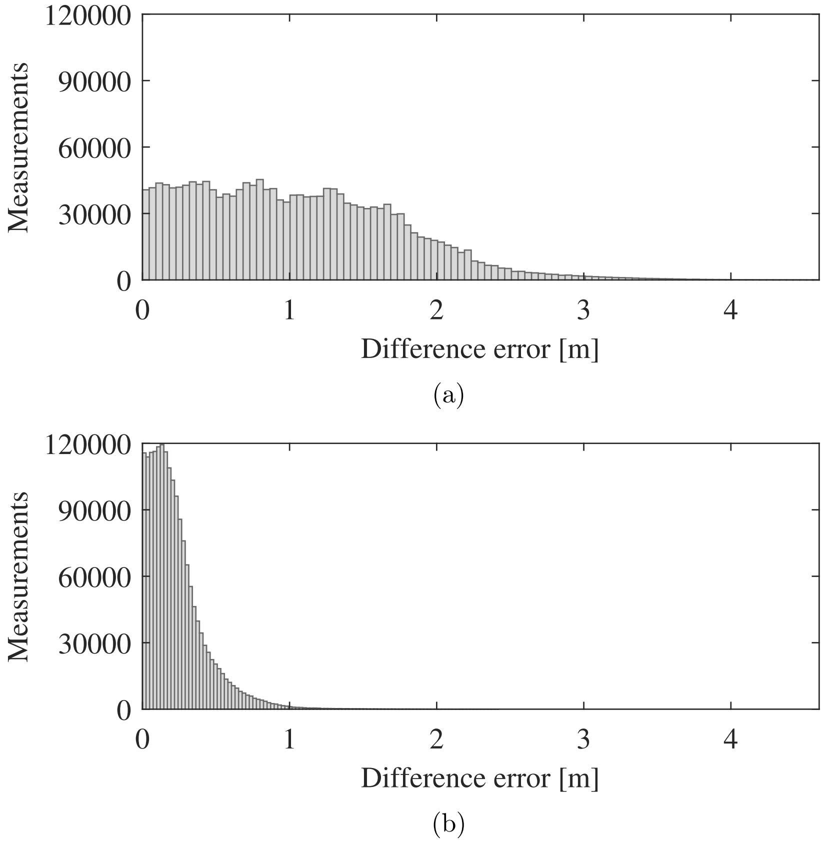

Figure 2.12: Difference on the longitude error between analytical formula and a first degree polynomial approximation, $\delta_{\lambda,1}$ (a), and second degree polynomial approximation, $\delta_{\lambda,2}$ (b).

Table 2.2: Statistics on the longitude error difference $\delta_{\lambda,1}$ and $\delta_{\lambda,2}$

	$\delta_{\lambda,1}$	$\delta_{\lambda,2}$
Max (m)	4.553	2.416
Mean (m)	1.045	0.229

Results are reported in Fig. 2.12 with statistics in table 2.2. In terms of percentage, the difference on the estimation of the error resulted in a mean of 36.8107 % in the case of first degree polynomial and a mean of 8.6027 % in the second degree polynomial.

2.2.4 Second Campaign of Simulations

Here are reported the results obtained in a second campaign of simulations, as published in the work of the author [6]. In this case the satellite orbit is elliptical.

— Geodetic latitude of the emitter $\Lambda_E \in [-15°, 15°]$;

- Longitude of the emitter $\lambda_{\mathrm{E}} \in [-15°, 15°]$;
- Height at perigee $h_{\mathrm{S,p}} \in [300 \text{ km}, 11250 \text{ km}]$; corresponding values of semi-major axis of the orbit $a_{\mathrm{S}}(h_{\mathrm{S,p}}, e_{\mathrm{S}}) \in [6671 \text{ km}, 44052.5 \text{ km}]$ resulted from models in (1.4) and (1.5);
- Eccentricity of the orbit $e_{\mathrm{S}} \in [0.0, 0.6]$;
- Inclination of the orbit $i_{\mathrm{S}} \in [75°, 105°]$;
- Argument of perigee $\omega_{\mathrm{S}} \in [-15°, 15°]$;
- Right ascension of the ascending node $\Omega_{\mathrm{S}} \in [-15°, 15°]$;
- For true anomaly ν_{S} it is important to remember that it is the only variable that depends on the time t. For this work the total duration of signal acquisition is supposed to be in an interval of time of measurements of 452 s which corresponds to about 30° of true anomaly range ν_{S} in the case of smallest orbit (i.e., 6671 km) and a range of about 3.424° for the biggest one (i.e., 45000 km) [1].

The ranges of the variables have been chosen considering the possible missions of interest for geolocation purposes: the semi-major axis a_{S} ranges from LEO to GEO; e_{S} from circular orbit $e_{\mathrm{S}} = 0$ to very elongated ones; the inclination i_{S} is around $\pi/2$, because this orientation into space guarantees the whole Earth scanning (i.e., the ground track of the satellite is in North-South direction, but at the same time the Earth rotates around its axis); the latitude Λ_{E} is around the Equator because it is the worst case scenario in position errors, as shown in the cosine of (2.22); the remaining angles λ_{E}, Ω_{S}, ω_{S}, and ν_{S} have to be chosen in a manner that the line-of-sight between the emitter and the satellite is guaranteed.

For every set of ranges, 7 evenly spaced samples have been considered for a total of 5764801 simulations.

The maximum value of the Newtonian time delay Δt_{n} is $4.74248 \cdot 10^{-2}$ s, the minimum value is $9.76886 \cdot 10^{-4}$ s, and the mean value is $2.24960 \cdot 10^{-2}$ s.

In Fig. 2.13 there is the shape of Δt_{n} as a function of the position of the emitter on the surface of the Earth (represented by its geodetic latitude Λ_{E} and longitude λ_{E}).

In Fig. 2.14 there is the shape of Δt_{n} as a function of the size and shape of the orbit: a_{S} and e_{S}.

In Fig. 2.15 there is the shape of Δt_{n} as a function of the satellite position on its orbit: ν_{S}.

From data gathered in simulation environment, an approximate model based on a Taylor's expansion polynomial can be built.

This study considers an expanded version in the form of a second-order model

---

[1] Considering the true anomaly ν_{S} ranging from 0 to 2π and the time t from 0 to the period T_{S} to travel the entire orbit, the relationship between the true anomaly and time is $\nu_{\mathrm{S}}/t = 2\pi/T$: for a certain interval of time t, the bigger the period T is, the smaller the true anomaly ν_{S} will be.

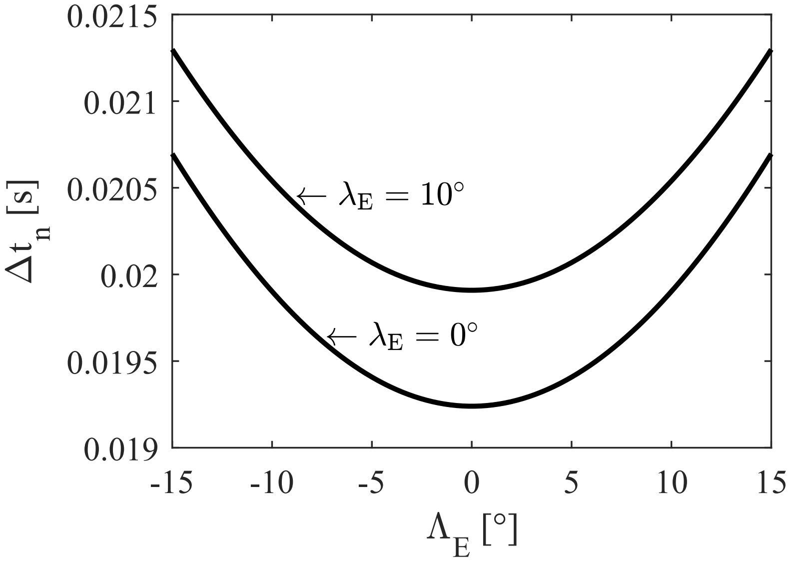

Figure 2.13: Shape of Newtonian time delay Δt_n as function of emitter position on the surface of the Earth, geodetic latitude Λ_E and longitude λ_E, in the point ($a_\mathrm{S} = 1735.143$ km, $e_\mathrm{S} = 0.3$, $i_\mathrm{S} = 90°$, $\Omega_\mathrm{S} = 0°$, $\omega_\mathrm{S} = 0°$, $\nu_\mathrm{S} = 0°$).

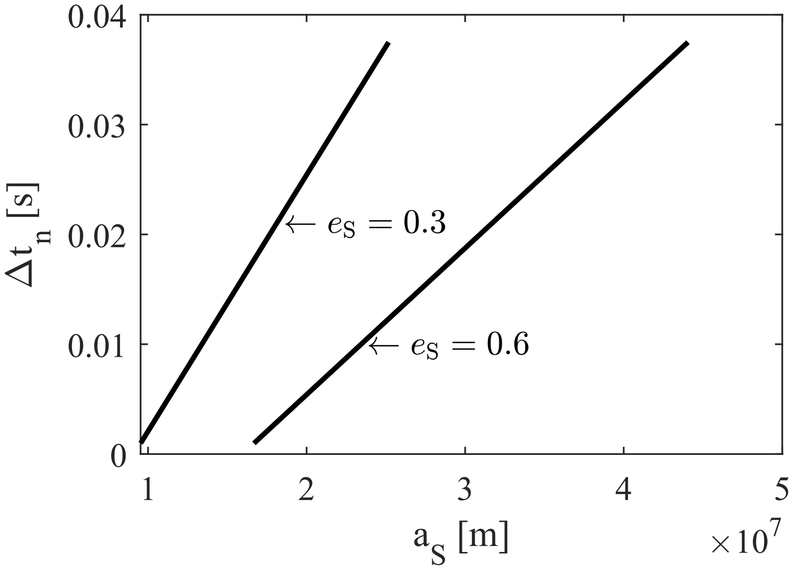

Figure 2.14: Shape of Newtonian time delay Δt_n as function of size and shape of the orbit in the point ($\Lambda_\mathrm{E} = 0°$, $\lambda_\mathrm{E} = 0°$, $i_\mathrm{S} = 90°$, $\Omega_\mathrm{S} = 0°$, $\omega_\mathrm{S} = 0°$, $\nu_\mathrm{S} = 0°$).

with variables $(x_1, x_2, x_3, x_4, x_5, x_6, x_7, x_8) = (\Lambda_\mathrm{E}, \lambda_\mathrm{E}, a_\mathrm{S}, e_\mathrm{S}, i_\mathrm{S}, \omega_\mathrm{S}, \Omega_\mathrm{S}, \nu_\mathrm{S})$, as shown in (2.35), also taking into account the elliptic shapes of the orbit. The subscript n indicates that this contribution of error is of Newtonian origin.

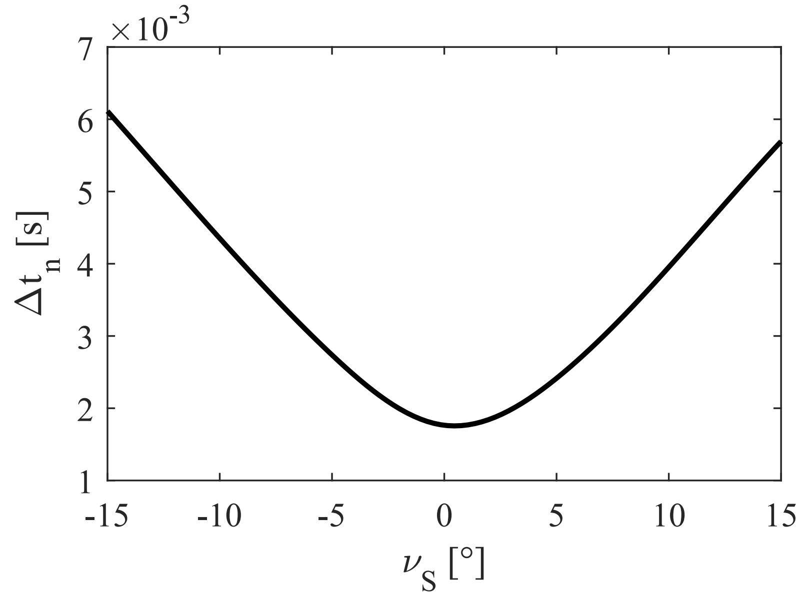

Figure 2.15: Shape of Newtonian time delay Δt_n as function of satellite position on its orbit in the point ($\Lambda_\mathrm{E} = 0°$, , $\lambda_\mathrm{E} = 0°$, $a_\mathrm{S} = 1735.143$ km, $e_\mathrm{S} = 0.3$, $i_\mathrm{S} = 90°$, $\Omega_\mathrm{S} = 0°$, $\omega_\mathrm{S} = 0°$).

$$\begin{aligned}\Delta t_\mathrm{n} \simeq &= t_{\mathrm{n},0} + (\mathbf{x}-\mathbf{x}_0)^\mathsf{T} D t_\mathrm{n} + \frac{1}{2}(\mathbf{x}-\mathbf{x}_0)^\mathsf{T} D^2 t_\mathrm{n} (\mathbf{x}-\mathbf{x}_0) \\ &= t_{\mathrm{n},0} + \sum_{k_1=1}^{8} \frac{\partial t_\mathrm{n}}{\partial x_{k_1}} (x_{k_1} - x_{k_1,0}) \\ &+\frac{1}{2}\sum_{k_1=1}^{8}\sum_{k_2=1}^{8} \frac{\partial^2 t_\mathrm{n}}{\partial x_{k_1}\partial x_{k_2}} (x_{k_1} - x_{k_1,0})(x_{k_2} - x_{k_2,0})\end{aligned} \tag{2.35}$$

The expressions of the constant term $t_{\mathrm{n},0}$, the gradient Dt_n, and the Hessian matrix $D^2 t_\mathrm{n}$ are reported in (2.36), (2.37), and (2.38).

$$t_{\mathrm{n},0} = k_\mathrm{n} \tag{2.36}$$

$$Dt_\mathrm{n} = (k_{\mathrm{n},1}, k_{\mathrm{n},2}, \ldots, k_{\mathrm{n},8})^\mathsf{T} \tag{2.37}$$

$$D^2 t_\mathrm{n} = \begin{bmatrix} k_{\mathrm{n},11} & k_{\mathrm{n},12} & \ldots & k_{\mathrm{n},18} \\ k_{\mathrm{n},21} & k_{\mathrm{n},22} & \ldots & k_{\mathrm{n},28} \\ \vdots & \vdots & \ddots & \vdots \\ k_{\mathrm{n},81} & k_{\mathrm{n},82} & \ldots & k_{\mathrm{n},88} \end{bmatrix} \tag{2.38}$$

The values of the coefficients of the polynomial model are reported in Table 2.3.

Table 2.3: Coefficients of the Newtonian time delay Δt_{n}.

Coef.	**Value**	**Meas. unit**	**Coef.**	**Value**	**Meas. unit**
k_{n}	$1.98206 \cdot 10^{-2}$	s	$k_{\mathrm{n},1}$	$-5.82243 \cdot 10^{-3}$	$\mathrm{s} \cdot \mathrm{rad}^{-1}$
$k_{\mathrm{n},2}$	$5.01246 \cdot 10^{-4}$	$\mathrm{s} \cdot \mathrm{rad}^{-1}$	$k_{\mathrm{n},3}$	$2.06328 \cdot 10^{-12}$	$\mathrm{s} \cdot \mathrm{m}^{-1}$
$k_{\mathrm{n},4}$	$-8.41362 \cdot 10^{-3}$	s	$k_{\mathrm{n},5}$	$-5.01246 \cdot 10^{-4}$	$\mathrm{s} \cdot \mathrm{rad}^{-1}$
$k_{\mathrm{n},6}$	$3.59904 \cdot 10^{-4}$	$\mathrm{s} \cdot \mathrm{rad}^{-1}$	$k_{\mathrm{n},7}$	$6.40943 \cdot 10^{-2}$	$\mathrm{s} \cdot \mathrm{rad}^{-1}$
$k_{\mathrm{n},8}$	$1.15329 \cdot 10^{-5}$	$\mathrm{s} \cdot \mathrm{rad}^{-1}$	$k_{\mathrm{n},11}$	$9.09002 \cdot 10^{-3}$	$\mathrm{s} \cdot \mathrm{rad}^{-1}$
$k_{\mathrm{n},12}, k_{\mathrm{n},21}$	$6.69003 \cdot 10^{-16}$	$\mathrm{s} \cdot \mathrm{rad}^{-2}$	$k_{\mathrm{n},13}, k_{\mathrm{n},31}$	$-9.75711 \cdot 10^{-13}$	$\mathrm{s} \cdot \mathrm{rad}^{-1} \cdot \mathrm{m}^{-1}$
$k_{\mathrm{n},14}, k_{\mathrm{n},41}$	$1.94689 \cdot 10^{-2}$	$\mathrm{s} \cdot \mathrm{rad}^{-1}$	$k_{\mathrm{n},15}, k_{\mathrm{n},51}$	$3.32073 \cdot 10^{-15}$	$\mathrm{s} \cdot \mathrm{rad}^{-2}$
$k_{\mathrm{n},16}, k_{\mathrm{n},61}$	$3.92884 \cdot 10^{-7}$	$\mathrm{s} \cdot \mathrm{rad}^{-2}$	$k_{\mathrm{n},17}, k_{\mathrm{n},71}$	$-9.41489 \cdot 10^{-7}$	$\mathrm{s} \cdot \mathrm{rad}^{-2}$
$k_{\mathrm{n},18}, k_{\mathrm{n},81}$	$-2.62873 \cdot 10^{-5}$	$\mathrm{s} \cdot \mathrm{rad}^{-2}$	$k_{\mathrm{n},22}$	$1.89458 \cdot 10^{-2}$	$\mathrm{s} \cdot \mathrm{rad}^{-2}$
$k_{\mathrm{n},23}, k_{\mathrm{n},32}$	$-4.86695 \cdot 10^{-11}$	$\mathrm{s} \cdot \mathrm{rad}^{-1} \cdot \mathrm{m}^{-1}$	$k_{\mathrm{n},24}, k_{\mathrm{n},42}$	$1.41334 \cdot 10^{-3}$	$\mathrm{s} \cdot \mathrm{rad}^{-1}$
$k_{\mathrm{n},25}, k_{\mathrm{n},52}$	$-3.94284 \cdot 10^{-2}$	$\mathrm{s} \cdot \mathrm{rad}^{-2}$	$k_{\mathrm{n},26}, k_{\mathrm{n},62}$	$9.25645 \cdot 10^{-15}$	$\mathrm{s} \cdot \mathrm{rad}^{-2}$
$k_{\mathrm{n},27}, k_{\mathrm{n},72}$	$4.63674 \cdot 10^{-17}$	$\mathrm{s} \cdot \mathrm{rad}^{-2}$	$k_{\mathrm{n},28}, k_{\mathrm{n},82}$	$4.56204 \cdot 10^{-18}$	$\mathrm{s} \cdot \mathrm{rad}^{-2}$
$k_{\mathrm{n},33}$	$-2.75890 \cdot 10^{-20}$	$\mathrm{s} \cdot \mathrm{m}^{-2}$	$k_{\mathrm{n},34}, k_{\mathrm{n},43}$	$1.69210 \cdot 10^{-12}$	$\mathrm{s} \cdot \mathrm{m}^{-1}$
$k_{\mathrm{n},35}, k_{\mathrm{n},53}$	$4.86695 \cdot 10^{-11}$	$\mathrm{s} \cdot \mathrm{rad}^{-1} \cdot \mathrm{m}^{-1}$	$k_{\mathrm{n},36}, k_{\mathrm{n},63}$	$-9.67855 \cdot 10^{-13}$	$\mathrm{s} \cdot \mathrm{rad}^{-1} \cdot \mathrm{m}^{-1}$
$k_{\mathrm{n},37}, k_{\mathrm{n},73}$	$-1.68884 \cdot 10^{-11}$	$\mathrm{s} \cdot \mathrm{rad}^{-1} \cdot \mathrm{m}^{-1}$	$k_{\mathrm{n},38}, k_{\mathrm{n},83}$	$1.64793 \cdot 10^{-15}$	$\mathrm{s} \cdot \mathrm{rad}^{-1} \cdot \mathrm{m}^{-1}$
$k_{\mathrm{n},44}$	$1.39006 \cdot 10^{-2}$	s	$k_{\mathrm{n},45}, k_{\mathrm{n},54}$	$-1.41334 \cdot 10^{-3}$	$\mathrm{s} \cdot \mathrm{rad}^{-1}$
$k_{\mathrm{n},46}, k_{\mathrm{n},64}$	$2.82814 \cdot 10^{-5}$	$\mathrm{s} \cdot \mathrm{rad}^{-1}$	$k_{\mathrm{n},47}, k_{\mathrm{n},74}$	$4.90076 \cdot 10^{-4}$	$\mathrm{s} \cdot \mathrm{rad}^{-1}$
$k_{\mathrm{n},48}, k_{\mathrm{n},84}$	$-3.85479 \cdot 10^{-5}$	$\mathrm{s} \cdot \mathrm{rad}^{-1}$	$k_{\mathrm{n},55}$	$1.89458 \cdot 10^{-2}$	$\mathrm{s} \cdot \mathrm{rad}^{-2}$
$k_{\mathrm{n},56}, k_{\mathrm{n},65}$	$2.80701 \cdot 10^{-15}$	$\mathrm{s} \cdot \mathrm{rad}^{-2}$	$k_{\mathrm{n},57}, k_{\mathrm{n},75}$	$5.36540 \cdot 10^{-15}$	$\mathrm{s} \cdot \mathrm{rad}^{-2}$
$k_{\mathrm{n},58}, k_{\mathrm{n},85}$	$-2.36351 \cdot 10^{-10}$	$\mathrm{s} \cdot \mathrm{rad}^{-2}$	$k_{\mathrm{n},66}$	$-9.52127 \cdot 10^{-6}$	$\mathrm{s} \cdot \mathrm{rad}^{-2}$
$k_{\mathrm{n},67}, k_{\mathrm{n},76}$	$-1.37600 \cdot 10^{-3}$	$\mathrm{s} \cdot \mathrm{rad}^{-2}$	$k_{\mathrm{n},68}, k_{\mathrm{n},86}$	$4.78427 \cdot 10^{-10}$	$\mathrm{s} \cdot \mathrm{rad}^{-2}$
$k_{\mathrm{n},77}$	$2.77254 \cdot 10^{-2}$	$\mathrm{s} \cdot \mathrm{rad}^{-2}$	$k_{\mathrm{n},78}, k_{\mathrm{n},87}$	$4.55585 \cdot 10^{-18}$	$\mathrm{s} \cdot \mathrm{rad}^{-2}$
$k_{\mathrm{n},88}$	$2.46339 \cdot 10^{-8}$	$\mathrm{s} \cdot \mathrm{rad}^{-2}$			

Due to the symmetry of the second derivatives as a result of the Clairaut-Schwarz theorem, the values in the Hessian matrix in (2.38) are such that $k_{\mathrm{n},ij} = k_{\mathrm{n},ji}\ \forall i \neq j$. Furthermore, in order to reconstruct the polynomial in (2.35), both the values of $k_{\mathrm{n},ij}$ and $k_{\mathrm{n},ji}$ with a multiplicative factor 1/2 have to be considered in the sum such that $\left(k_{\mathrm{n},ij} + k_{\mathrm{n},ji}\right)/2 = k_{\mathrm{n},ij} = k_{\mathrm{n},ji}$. The same applies for the value of the coefficient of the same index $k_{\mathrm{n},ii}$, so the value in table 2.3 have to be considered twice in the sum: $\left(k_{\mathrm{n},ii} + k_{\mathrm{n},ii}\right)/2 = 2k_{\mathrm{n},ii}/2 = k_{\mathrm{n},ii}$.

2.3 Relativistic Effects

This section summarises models, methods, and results in the published articles of the author [28] and [6]. The main results have also been presented at the virtual conference [29].

When relativistic effects are considered, position and time data have to consider their representation with respect to a clock.

In space applications a clock on the emitter and a clock on the satellite are at different gravitational potentials, so they do not run at the same rate.

The concept of time is a fundamental parameter in relativistic satellite applications. This is introduced through coordinate time t and proper time τ, as well as terrestrial time. The problem of clock synchronization is also a key aspect in this context.

The exact solution for the squared line element ds, obtained by Schwarzchild [30] for general relativity in a centrally symmetric gravitational field, is shown in (2.39), where (ϕ, θ, r) is the set of spherical coordinates, G is the gravitational constant equal to $6.67430 \cdot 10^{-11}\ \mathrm{m^3 kg^{-1} s^{-2}}$ and M is the mass of the central body.

$$ds^2 = -\left(1 - \frac{2GM}{c^2 r}\right)^{-1} dr^2 - r^2 d\theta^2 - r^2 \sin^2(\theta) d\phi^2 + c^2\left(1 - \frac{2GM}{c^2 r}\right) dt^2 \tag{2.39}$$

Considering first-order terms in $1/c^2$ and small velocities such that $\frac{v^2}{c^2} \gg \frac{2GM}{c^4 r}\frac{dr}{dt}^2$, it can be demonstrated [31] that a simpler approximate equation, expressed by (2.40), can be obtained, where dt is the coordinate time and $\Phi(r) = -\mu/r$ is the Newtonian potential, which can be expressed in terms of μ, the standard gravitational parameter.

$$ds \approx c\,dt\left(1 - \frac{2\Phi(r)}{c^2} - \frac{v^2}{c^2}\right)^{\frac{1}{2}} \tag{2.40}$$

In terms of proper time $ds = c\,d\tau$, then (2.40) becomes (2.41).

$$d\tau \approx \left(1 - \frac{2\Phi(r)}{c^2} - \frac{v^2}{c^2}\right)^{\frac{1}{2}} dt \tag{2.41}$$

For two observers (A) and (B) with different velocities and at different potentials, $dt_{\mathrm{A}} = dt_{\mathrm{B}}$, but $d\tau_{\mathrm{A}} \neq d\tau_{\mathrm{B}}$. When $v \to 0$ and $\Phi(r) \to 0$, then $d\tau = dt$.

Considering an emitter (E) on the surface of the Earth and a receiver (S) on the satellite, the ratio $d\tau_{\mathrm{S}}$ on $d\tau_{\mathrm{E}}$, approximated to order $1/c^2$, is shown in (2.42).

$$\frac{d\tau_{\mathrm{S}}}{d\tau_{\mathrm{E}}} \approx 1 + \frac{1}{c^2}\left(\Phi(r_{\mathrm{S}}) - \frac{v_{\mathrm{S}}^2}{2}\right) - \frac{1}{c^2}\left(\Phi(r_{\mathrm{E}}) - \frac{v_{\mathrm{E}}^2}{2}\right) \tag{2.42}$$

The brackets in (2.42) represent a specific form of the differences between the potential energy $V = m\Phi(r)$ and the non-relativistic kinetic energy $K = mv^2/2$, where m is the mass of the object. Considering the Earth as central body and the satellite as receiver, the masses are $M = M_{\oplus}$ and $m = m_{\mathrm{S}}$. From orbital mechanics fundamentals [2], the total energy for a satellite is $E_{\mathrm{m}} = -\mu_{\oplus} m_{\mathrm{S}}/(2a)$, where the standard gravitational parameter $G(M_{\oplus} + m_{\mathrm{S}}) \approx GM_{\oplus} = \mu_{\oplus}$ is equal to $3.986005 \cdot 10^{14}$ $\mathrm{m}^3/\mathrm{s}^{-2}$. Considering also $V - K = V - (E_{\mathrm{m}} - V) = 2V - E_{\mathrm{m}}$, the expression in the first brackets of (2.42) can be rewritten as shown in (2.43).

$$\frac{d\tau_{\mathrm{S}}}{d\tau_{\mathrm{E}}} \approx 1 + \frac{2\mu_{\oplus}}{c^2}\left(\frac{1}{r_{\mathrm{S}}} - \frac{1}{4a_{\mathrm{S}}}\right) - \frac{1}{c^2}\left(\frac{\mu_{\oplus}}{r_{\mathrm{E}}} - \frac{v_{\mathrm{E}}^2}{2}\right) \tag{2.43}$$

By definition, $r_{\mathrm{S}} = a_{\mathrm{S}}(1 - e_{\mathrm{S}}\cos(E_{\mathrm{S}}(\tau_{\mathrm{E}})))$, then (2.43) can be rewritten as (2.44), where $E_{\mathrm{S}}(\tau_{\mathrm{E}})$ is the eccentric anomaly of the receiver considered with proper time of the emitter τ_{E}, because the reference is usually chosen on the ground.

$$\begin{aligned}\frac{d\tau_{\mathrm{S}}}{d\tau_{\mathrm{E}}} \approx 1 &+ \frac{2\mu_{\oplus}e_{\mathrm{S}}}{a_{\mathrm{S}}c^2}\left(\frac{\cos(E_{\mathrm{S}}(\tau_{\mathrm{E}}))}{1 - e_{\mathrm{S}}\cos(E_{\mathrm{S}}(\tau_{\mathrm{E}}))}\right) \\ &- \frac{1}{c^2}\left(\frac{\mu_{\oplus}}{r_{\mathrm{E}}} - \frac{3\mu_{\oplus}}{2a_{\mathrm{S}}} + \frac{v_{\mathrm{E}}^2}{2}\right)\end{aligned} \tag{2.44}$$

The integration of (2.44) gives the relativistic correction, in which there is also periodic term, as shown in (2.45), where κ is the constant of integration.

$$\tau_{\mathrm{S}} \approx \tau_{\mathrm{E}} + \frac{2e_{\mathrm{S}}\sqrt{\mu_{\oplus}a_{\mathrm{S}}}}{c^2}\sin(E_{\mathrm{S}}(\tau_{\mathrm{E}})) - \frac{1}{c^2}\left(\frac{\mu_{\oplus}}{r_{\mathrm{E}}} - \frac{3\mu_{\oplus}}{2a_{\mathrm{S}}} + \frac{v_{\mathrm{E}}^2}{2}\right)\tau_{\mathrm{E}} + \kappa \tag{2.45}$$

In general, [31], κ is evaluated considering the instant of synchronization when $\tau_{\mathrm{S}} = \tau_{\mathrm{E}} = \tau_0$, obtaining the expression in (2.46).

$$\kappa = \frac{1}{c^2}\left(\frac{\mu_{\oplus}}{r_{\mathrm{E}}} - \frac{3\mu_{\oplus}}{2a_{\mathrm{S}}} + \frac{v_{\mathrm{E}}^2}{2}\right)\tau_0 - \frac{2e_{\mathrm{S}}\sqrt{\mu_{\oplus}a_{\mathrm{S}}}}{c^2}\sin(E_{\mathrm{S}}(\tau_0)) \tag{2.46}$$

Considering (2.45) and (2.46), the (2.47) is obtained.

$$\begin{aligned}\tau_{\mathrm{S}} \approx \tau_{\mathrm{E}} &+ \frac{2e_{\mathrm{S}}\sqrt{\mu_{\oplus}a_{\mathrm{S}}}}{c^2}\sin\left(E_{\mathrm{S}}\left(\tau_{\mathrm{E}}\right)\right) - \frac{1}{c^2}\left(\frac{\mu_{\oplus}}{r_{\mathrm{E}}} - \frac{3\mu_{\oplus}}{2a_{\mathrm{S}}} + \frac{v_{\mathrm{E}}^2}{2}\right)\tau_{\mathrm{E}} \\ &+\frac{1}{c^2}\left(\frac{\mu_{\oplus}}{r_{\mathrm{E}}} - \frac{3\mu_{\oplus}}{2a_{\mathrm{S}}} + \frac{v_{\mathrm{E}}^2}{2}\right)\tau_0 - \frac{2e_{\mathrm{S}}\sqrt{\mu_{\oplus}a_{\mathrm{S}}}}{c^2}\sin\left(E_{\mathrm{S}}\left(\tau_0\right)\right)\end{aligned} \tag{2.47}$$

When relativistic effects are taken into account, the time delay Δt has to be updated with a new contribution coming from (2.45) and they depend not only on the satellite position and the emitter position, but also on their velocities $\|\mathbf{v}_{\mathrm{E}}\|$ and $\|\mathbf{v}_{\mathrm{S}}\|$. Then the contribution to the relativistic angular position error $e_{\lambda,\mathrm{rel}}$ and the contribution to the relativistic linear position error $d_{\lambda,\mathrm{rel}}$ can be written as in (2.48) and (2.49), respectively.

$$e_{\lambda,\mathrm{rel}} = f'\left(\mathbf{x}_{\mathrm{S}}\left(\tau_S\right), \|\mathbf{v}_{\mathrm{S}}\left(\tau_S\right)\|, \mathbf{x}_{\mathrm{E}}\left(\tau_E\right), \|\mathbf{v}_{\mathrm{E}}\left(\tau_E\right)\|\right) \tag{2.48}$$

$$d_{\lambda,\mathrm{rel}} = g'\left(\mathbf{x}_{\mathrm{S}}\left(\tau_S\right), \|\mathbf{v}_{\mathrm{S}}\left(\tau_S\right)\|, \mathbf{x}_{\mathrm{E}}\left(\tau_E\right), \|\mathbf{v}_{\mathrm{E}}\left(\tau_E\right)\|\right) \tag{2.49}$$

However, since for a fixed emitter on the surface of the Earth the velocity $\|\mathbf{v}_{\mathrm{E}}\|$ is expressed as $\|\mathbf{v}_{\mathrm{E}}\| = \Omega_{\oplus}R_{\oplus}\left(\Lambda_{\mathrm{E}}\right)\cos\left(\Lambda_{\mathrm{E}}\right)$ and considering that $\Omega_{\oplus}$ is a known constant, there is no real dependence on new variables.

Also considering a decomposition of satellite velocity in radial and normal components, $\mathbf{v}_{\mathrm{S}} = \left(v_{\mathrm{S,r}}, v_{\mathrm{S,n}}, 0\right)^T$, where $v_{\mathrm{S,r}}$ and $v_{\mathrm{S,n}}$ are reported in (2.50), again, there is not a dependence on new variables.

$$\begin{aligned} v_{\mathrm{S,r}} &= \sqrt{\frac{\mu_{\oplus}}{a\left(1-e^2\right)}}e\sin\left(\nu\right) \\ v_{\mathrm{S,n}} &= \sqrt{\frac{\mu_{\oplus}}{a\left(1-e^2\right)}}\left(1+e\cos\left(\nu\right)\right)\end{aligned} \tag{2.50}$$

Considering these two facts, also for relativistic contributions of errors $e_{\lambda,\mathrm{rel}}$ and $d_{\lambda,\mathrm{rel}}$ there is the same set of variables of $e_{\lambda,\mathrm{n}}$, and $d_{\lambda,\mathrm{n}}$ as shown in (2.51) and (2.52).

$$\begin{aligned} e_{\lambda,\mathrm{rel}} &= f'\left(\Lambda_{\mathrm{E}}\left(\tau_E\right), \lambda_{\mathrm{E}}\left(\tau_E\right), a, e, i, \omega, \Omega, \nu\left(\tau_S\right)\right) \\ &= f'\left(\Lambda_{\mathrm{E}}\left(\tau_E\right), \lambda_{\mathrm{E}}\left(\tau_E\right), a, e, i, \omega, \Omega, \nu\left(\tau_E, \tau_0\right)\right)\end{aligned} \tag{2.51}$$

$$\begin{aligned} d_{\lambda,\mathrm{rel}} &= g'\left(\Lambda_{\mathrm{E}}\left(\tau_E\right), \lambda_{\mathrm{E}}\left(\tau_E\right), a, e, i, \omega, \Omega, \nu\left(\tau_S\right)\right) \\ &= g'\left(\Lambda_{\mathrm{E}}\left(\tau_E\right), \lambda_{\mathrm{E}}\left(\tau_E\right), a, e, i, \omega, \Omega, \nu\left(\tau_E, \tau_0\right)\right)\end{aligned} \tag{2.52}$$

This dependence analysis has an important consequence on system design, software development, and data processing, because for an upgrade from a Newtonian result to a relativistic result there is no need to supply new input data, except for the instant of time of synchronization between clocks τ_0. This means that there is no need of system modification, but there is only need for a change at level of processing algorithm. A possible high-level implementation is shown in Fig. 2.16. Details of the simulation algorithm is presented and Sec. 2.3.1.

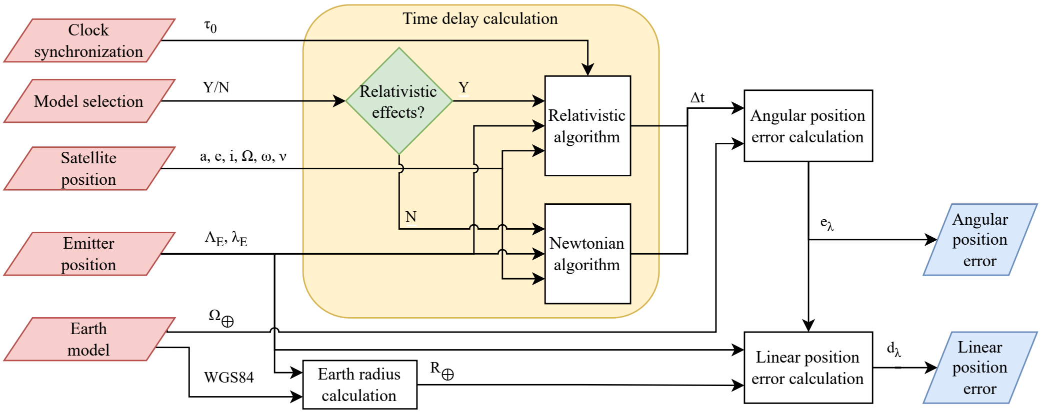

Figure 2.16: Block diagram for the calculation of angular position error e_λ and linear position error d_λ due to time delay Δt; in this diagram there is the possibility to chose between the Newtonian and relativistic algorithm.

2.3.1 Relativistic Version of Simulation Algorithm

With Newtonian mechanics, there is no distinction between proper time τ and coordinate time t, so the time delay is the same $\Delta t = \Delta\tau$.

During the time delay Δt the signal has moved from the emitter $\mathbf{x}_\mathrm{E}\left(t_\mathrm{e}\right)$ to the satellite $\mathbf{x}_\mathrm{S}\left(t_\mathrm{e}+\Delta t\right)$ propagating at speed c. In the same amount of time the satellite has moved from $\mathbf{x}_\mathrm{S}\left(t_\mathrm{e}\right)$ to $\mathbf{x}_\mathrm{S}\left(t_\mathrm{e}+\Delta t\right)$. Considering this fact, the time delay can be written as in (2.53), where $\left\|\bar{\mathbf{v}}_\mathrm{S}\left(\Delta t\right)\right\|$ is the mean magnitude of the velocity vector of the satellite over Δt.

$$\Delta t = \frac{\left\|\mathbf{x}_\mathrm{S}\left(t_\mathrm{e}+\Delta t\right)-\mathbf{x}_\mathrm{E}\left(t_\mathrm{e}\right)\right\|}{c} = \frac{\left\|\mathbf{x}_\mathrm{S}\left(t_\mathrm{e}+\Delta t\right)-\mathbf{x}_\mathrm{S}\left(t_\mathrm{e}\right)\right\|}{\left\|\bar{\mathbf{v}}_\mathrm{S}\left(\Delta t\right)\right\|} \tag{2.53}$$

Rigorously, $\left\|\bar{\mathbf{v}}_\mathrm{S}\left(\Delta t\right)\right\|$ has to be intended as integral mean as shown in (2.54).

$$\left\|\bar{\mathbf{v}}_\mathrm{S}\left(\Delta t\right)\right\| = \frac{1}{\Delta t}\int_{t_\mathrm{e}}^{t_\mathrm{e}+\Delta t}\left\|\mathbf{v}_\mathrm{S}\left(t'\right)\right\| dt' \tag{2.54}$$

Equation (2.53) can be solved with root-finding methods, e.g. the bisection method, while (2.54) is generally obtained via interpolation because in a simulation environment the problem of orbit kinematics can be independently solved before the problem of geolocation.

Furthermore, considering that the only orbital parameter which depends on time t is the true anomaly ν, it is possible to write $\mathbf{x}_\mathrm{S} = \mathbf{x}_\mathrm{S}\left(\nu\right) = \mathbf{x}_\mathrm{S}\left(\nu\left(t\right)\right)$.

In order to figure out how to use operatively the (2.47), 5 instants of time of interest have to be considered:

- The instant of time of signal emission represented in satellite clock $\tau_{\mathrm{S,e}}$;
- The instant of time of signal reception represented in satellite clock $\tau_{\mathrm{S,r}}$;

— The instant of time of signal emission represented in emitter clock $\tau_{\mathrm{E,e}}$;
— The instant of time of signal reception represented in emitter clock $\tau_{\mathrm{E,r}}$;
— The instant of time of synchronization of the two clocks τ_0.

In terms of proper time τ, the Newtonian evaluation of the time delay $\Delta\tau_{\mathrm{n}}$, obtained in (2.23), is evaluated considering the instant of emission with the emitter clock $\tau_{\mathrm{E,e}}$ and the instant of reception with the satellite clock $\tau_{\mathrm{S,r}}$, as shown in (2.55).

$$\Delta\tau_{\mathrm{n}} = \tau_{\mathrm{S,r}} - \tau_{\mathrm{E,e}} \tag{2.55}$$

With a relativistic approach, the evaluation of instants of time must be done with the same clock. Considering the clock on the emitter as reference, (2.56) is obtained, where the interval of time $\Delta\tau_{\mathrm{r}}$ represents the value of the relativistic delay, the interval of time $\Delta\tau_{\mathrm{n}}$ is the value of Newtonian delay and $\Delta\tau_{\mathrm{rc}}$ is the relativistic correction (2.41).

$$\begin{aligned}\Delta\tau_{\mathrm{r}} &= \tau_{\mathrm{E,r}} - \tau_{\mathrm{E,e}} = \tau_{\mathrm{E,r}} - \tau_{\mathrm{E,e}} + \tau_{\mathrm{S,r}} - \tau_{\mathrm{S,r}} \\ &= \Delta\tau_{\mathrm{n}} + \tau_{\mathrm{E,r}} - \tau_{\mathrm{S,r}} = \Delta\tau_{\mathrm{n}} + \Delta\tau_{\mathrm{rc}}\end{aligned} \tag{2.56}$$

In the relativistic version of the algorithm for time delay $\Delta\tau_{\mathrm{r}}$, the modification of Newtonian algorithm is quite straightforward, because there is only an additive contribution $\Delta\tau_{\mathrm{rc}}$ to the Newtonian time delay $\Delta\tau_{\mathrm{n}}$, which can be calculated from (2.45) and (2.46), obtaining the result in (2.57):

$$\begin{gathered}\Delta\tau_{\mathrm{r}} = \Delta\tau_{\mathrm{n}} + \Delta\tau_{\mathrm{rc}} = \frac{\left\|\mathbf{x}_{\mathrm{S}}\left(\tau_{\mathrm{S,r}}\right) - \mathbf{x}_{\mathrm{S}}\left(\tau_{\mathrm{E,e}}\right)\right\|}{\left\|\bar{\mathbf{v}}_{\mathrm{S}}\left(\Delta\tau_{\mathrm{n}}\right)\right\|} \\ +\frac{2e\sqrt{\mu a}}{c^2}\left(\sin\left(E\left(\tau_0\right)\right) - \sin\left(E\left(\tau_{\mathrm{E,r}}\right)\right)\right) + \frac{1}{c^2}\left(\frac{\mu}{r_{\mathrm{E}}} - \frac{3\mu}{2a} + \frac{v_{\mathrm{E}}^2}{2}\right)\left(\tau_{\mathrm{E,r}} - \tau_0\right)\end{gathered} \tag{2.57}$$

In particular, considering the emitter clock as reference, the correction $\Delta\tau_{\mathrm{rc}}$ is as shown in (2.58).

$$\begin{aligned}\Delta\tau_{\mathrm{rc}} = {} & \frac{2e_{\mathrm{S}}\sqrt{\mu_\oplus a_{\mathrm{S}}}}{c^2}\left(\sin\left(E_{\mathrm{S}}\left(\tau_0\right)\right) - \sin\left(E_{\mathrm{S}}\left(\tau_{\mathrm{E,r}}\right)\right)\right) \\ & +\frac{1}{c^2}\left(\frac{\mu_\oplus}{r_{\mathrm{E}}} - \frac{3\mu_\oplus}{2a_{\mathrm{S}}} + \frac{v_{\mathrm{E}}^2}{2}\right)\left(\tau_{\mathrm{E,r}} - \tau_0\right)\end{aligned} \tag{2.58}$$

The relativistic version of the algorithm for the calculation of the relativistic time delay $\Delta\tau_{\mathrm{rel}}$ is represented in the algorithm in Fig. 2.17.

2.3.2 Order of Magnitude Analysis for Relativistic Effects

Equation (2.57) has many terms and, depending on the geometry, they have a different relative weight on the final result.

```
set $\tau_0$                                                        ▷ Clock synchronization instant of time
set $\tau_{\mathrm{E,e}}$                                           ▷ Emission instant of time
load $a$, $e$, $i$, $\omega$, $\Omega$, $\nu(\tau_{\mathrm{E,e}})$  ▷ Satellite position
load $\Lambda_{\mathrm{E}}(\tau_{\mathrm{E,e}}), \lambda_{\mathrm{E}}(\tau_{\mathrm{E,e}})$  ▷ Emitter position
initialize $(\Delta_{\mathrm{S}})_0 = +\infty$, $\kappa = f(\tau_0)$, $(\Delta\tau_{\mathrm{r}})_0 = 0$
while $(\Delta_{\mathrm{S}})_{\mathrm{k}} \geq \theta_{\mathrm{S}}$ do
    $(d)_{\mathrm{k}} \leftarrow \left\| \mathbf{x}_{\mathrm{S}}\left((\nu)_{\mathrm{k-1}}\right) - \mathbf{x}_{\mathrm{E}}(\tau_{\mathrm{E,e}}) \right\|$  ▷ Distance
    $(\Delta\tau_{\mathrm{n}})_{\mathrm{k}} \leftarrow (d)_{\mathrm{k}} / c$  ▷ Newtonian delay
    $(\Delta\tau_{\mathrm{rc}})_{\mathrm{k}} \leftarrow f\left(\tau_{\mathrm{E,e}} + (\Delta\tau_{\mathrm{r}})_{\mathrm{k-1}}, \kappa\right)$  ▷ Correction
    $(\Delta\tau_{\mathrm{r}})_{\mathrm{k}} \leftarrow (\Delta\tau_{\mathrm{n}})_{\mathrm{k}} + (\Delta\tau_{\mathrm{rc}})_{\mathrm{k}}$  ▷ Relativistic delay
    $(\Delta\nu)_{\mathrm{k}} \leftarrow f\left(e, (\Delta\tau_{\mathrm{r}})_{\mathrm{k}}\right)$  ▷ Calculated iteratively
    $(\nu)_{\mathrm{k}} \leftarrow \nu(\tau_{\mathrm{E,e}}) + (\Delta\nu)_{\mathrm{k}}$  ▷ Update true anomaly
    $(\Delta_{\mathrm{S}})_{\mathrm{k}} \leftarrow \left\| \mathbf{x}_{\mathrm{S}}\left((\nu)_{\mathrm{k}}\right) - \mathbf{x}_{\mathrm{S}}\left((\nu)_{\mathrm{k-1}}\right) \right\|$  ▷ Condition
end while
$e_\lambda \leftarrow \Omega_\oplus \Delta\tau_{\mathrm{r}}$  ▷ Longitude error (angle)
$d_\lambda \leftarrow e_\lambda R_\oplus(\Lambda_{\mathrm{E}}) \cos(\Lambda_{\mathrm{E}})$  ▷ Longitude error (distance)
return $e_\lambda, d_\lambda$
```

Figure 2.17: Relativistic version of algorithm of simulation.

The first term is $\Delta\tau_{\mathrm{n}}$. Considering (2.53), it is possible to write (2.59).

$$\Delta\tau_{\mathrm{n}} = \frac{\left\| \mathbf{x}_{\mathrm{S}}(\tau_{\mathrm{S,r}}) - \mathbf{x}_{\mathrm{E}}(\tau_{\mathrm{E,e}}) \right\|}{c} \sim \frac{a - R_\oplus}{c} \tag{2.59}$$

Considering $a - R_\oplus$ ranging from $3 \cdot 10^5$ m for satellites in LEO to $3.6 \cdot 10^7$ m for satellites in GEO, the order of magnitude of $\Delta\tau_{\mathrm{n}}$ is $10^{-3} \sim 10^{-1}$ s.

The second contribution of (2.57) is a periodic term due to sine function. The order of magnitude of the peak of its amplitude is shown in (2.60).

$$\sup_{e \in [0,1[} \left\{ \max_{E \in [0,2\pi]} \left\{ \frac{2e\sqrt{\mu_\oplus a}}{c^2} \sin(E) \right\} \right\} = \sup_{e \in [0,1[} \left\{ \frac{2e\sqrt{\mu_\oplus a}}{c^2} \right\} = \frac{2\sqrt{\mu_\oplus}\sqrt{a}}{c^2} \tag{2.60}$$

Considering a ranging from 10^6 to 10^7, the order of magnitude of the periodic term could be upon $10^{-3} \sim 10^{-2}$ s.

Other terms in (2.57) are those related to potential energy μ/r, time delay v^2/c^2 and clock synchronization τ_0.

Considering $r_{\mathrm{E}} = R_\oplus(\Lambda_{\mathrm{E}})$, the term related to the potential energy of the emitter is about $10^{-9} \cdot \Delta\tau_{\mathrm{sync}}$ s, where $\Delta\tau_{\mathrm{d}} = (\tau_{\mathrm{E,r}} - \tau_0)$ is the interval of time of desynchronization.

The term that depends on the potential energy of the satellite is about $10^{-9} \cdot \Delta\tau_{\mathrm{d}} \sim 10^{-8} \cdot \Delta\tau_{\mathrm{d}}$ s.

Considering $\mathbf{v}_{\mathrm{E}} = \mathbf{\Omega}_{\mathrm{E}} \times \mathbf{r}_{\mathrm{E}}$, where $\mathbf{r}_{\mathrm{E}}$ is the position vector of the emitter and $\mathbf{\Omega}_E$ is the angular speed vector of the emitter equal to $\mathbf{\Omega}_{\mathrm{E}} = \Omega_\oplus \left.\mathbf{u}_z\right|_{\mathrm{ECI}}$ in which $\mathbf{u}_z|_{\mathrm{ECI}}$ is the unit vector along z direction in ECI reference frame, then $v_{\mathrm{E}} = \Omega_{\oplus} r_{\mathrm{E}} \cos(\Lambda_{\mathrm{E}}) = \Omega_{\oplus} R_{\oplus}(\Lambda_{\mathrm{E}}) \cos(\Lambda_{\mathrm{E}})$. Due to the presence of the cosine of the geodetic latitude, this contribution is expected to be null at poles of the Earth and maximum at the Equator: in this latter case, the maximum value is expressed in (2.61) and it is about $10^{-12} \cdot \Delta\tau_{\mathrm{d}}$ s.

$$\begin{aligned} \max_{\Lambda_{\mathrm{E}} \in [-\pi,\pi]} \left\{ \frac{v_{\mathrm{E}}^2}{2c^2} \Delta\tau_{\mathrm{d}} \right\} &= \max_{\Lambda_{\mathrm{E}} \in [-\pi,\pi]} \left\{ \frac{\Omega_{\oplus}^2 R_{\oplus}^2(\Lambda_{\mathrm{E}}) \cos^2(\Lambda_{\mathrm{E}})}{2c^2} \Delta\tau_{\mathrm{d}} \right\} \\ &= \frac{\Omega_{\oplus}^2 R_{\oplus}^2(0)}{2c^2} \Delta\tau_{\mathrm{d}} \end{aligned} \tag{2.61}$$

Assuming a reasonable level of synchronization on the Earth, i.e. $\Delta\tau_{\mathrm{d}} \leq 1$ s, then the only significant value of the relativistic correction is the one due to eccentricity of the orbit e, as evaluated in (2.60).

2.3.3 Worst Case Prediction for Relativistic Effects

In order to simulate a realistic scenario of interest for the relativistic correction on time delay in (2.57), the contributions of its terms have to be further expressed considering the information available at the moment of the reception of the signal.

Considering ECI as reference coordinate system, the magnitude of the position of the emitter r_{E} can be obtained considering (2.62), where $(x_{\mathrm{E}}|_{\mathrm{ECI}}, y_{\mathrm{E}}|_{\mathrm{ECI}}, z_{\mathrm{E}}|_{\mathrm{ECI}})$ are the coordinates of the emitter in ECI.

$$r_{\mathrm{E}} = \sqrt{x_{\mathrm{E}}|_{\mathrm{ECI}}^2 + y_{\mathrm{E}}|_{\mathrm{ECI}}^2 + z_{\mathrm{E}}|_{\mathrm{ECI}}^2} \tag{2.62}$$

Since the emitter is supposed to be fixed on the surface of the Earth, the magnitude of the velocity vector v_{E} is null in the LLH and ECEF reference coordinate systems. Its value in the ECI can be obtained considering that in this reference coordinate system the Earth is rotating, so also the emitter experiences a velocity expressed as in (2.63).

$$v_{\mathrm{E}} = \Omega_{\oplus} r_{\mathrm{E}} \cos(\Lambda_{\mathrm{E}}) \tag{2.63}$$

Choosing an instant of synchronization such that $\tau_{\mathrm{E,r}} \neq \tau_0$ and denoting with $\Delta\tau_{\mathrm{d}} = \tau_{\mathrm{E,r}} - \tau_0$ the interval of time of desynchronization, the sinusoidal difference of the eccentric anomaly E in (2.57) can be manipulated as shown in (2.64).

$$\begin{aligned} \sin(E_{\mathrm{S}}(\tau_0)) - \sin(E_{\mathrm{S}}(\tau_{\mathrm{E,r}})) &= \sin(E_{\mathrm{S}}(\tau_0 + \tau_{\mathrm{E,r}} - \tau_{\mathrm{E,r}})) - \sin(E_{\mathrm{S}}(\tau_{\mathrm{E,r}})) \\ &= \sin(E_{\mathrm{S}}(\tau_{\mathrm{E,r}} - \Delta\tau_{\mathrm{d}})) - \sin(E_{\mathrm{S}}(\tau_{\mathrm{E,r}})) \\ &= \sin(E_{\mathrm{S}}(\tau_{\mathrm{E,r}}) - \Delta E_{\mathrm{S}}) - \sin(E_{\mathrm{S}}(\tau_{\mathrm{E,r}})) \end{aligned} \tag{2.64}$$

Considering the mathematical identity $\sin(\alpha - \beta) = \sin(\alpha)\cos(\beta) - \cos(\alpha)\sin(\beta)$, the (2.64) can be rewritten as in (2.65).

$$\begin{gathered}\sin\left(E_{\mathrm{S}}\left(\tau_0\right)\right)-\sin\left(E_{\mathrm{S}}\left(\tau_{\mathrm{E,r}}\right)\right)=\sin\left(E_{\mathrm{S}}\left(\tau_{\mathrm{E,r}}\right)-\Delta E_{\mathrm{S}}\right)-\sin\left(E_{\mathrm{S}}\left(\tau_{\mathrm{E,r}}\right)\right)\\ =\sin\left(E_{\mathrm{S}}\left(\tau_{\mathrm{E,r}}\right)\right)\cos\left(\Delta E_{\mathrm{S}}\right)-\cos\left(E_{\mathrm{S}}\left(\tau_{\mathrm{E,r}}\right)\right)\sin\left(\Delta E_{\mathrm{S}}\right)-\sin\left(E_{\mathrm{S}}\left(\tau_{\mathrm{E,r}}\right)\right)\end{gathered}\tag{2.65}$$

Considering furthermore that, generally, the interval of desynchronization is much smaller compared to the period of the orbit of the satellite T_{S}, so $\Delta\tau_{\mathrm{d}} \ll T_{\mathrm{S}}$, then also the variation of the mean anomaly of the satellite ΔM_{S} and the variation of the eccentric anomaly of the satellite ΔE_{S} due to the desynchronization are small, so $\Delta M_{\mathrm{S}} \ll 2\pi$ and $\Delta E_{\mathrm{S}} \ll 2\pi$.

Under the assumption of small angles, then $\cos\left(\Delta E_{\mathrm{S}}\right) \to 1$ and $\sin\left(\Delta E_{\mathrm{S}}\right) \to \Delta E_{\mathrm{S}}$, so (2.65) can be rewritten as in (2.66).

$$\begin{gathered}\sin\left(E_{\mathrm{S}}\left(\tau_0\right)\right)-\sin\left(E_{\mathrm{S}}\left(\tau_{\mathrm{E,r}}\right)\right)\\ =\sin\left(E_{\mathrm{S}}\left(\tau_{\mathrm{E,r}}\right)\right)\cos\left(\Delta E_{\mathrm{S}}\right)-\cos\left(E_{\mathrm{S}}\left(\tau_{\mathrm{E,r}}\right)\right)\sin\left(\Delta E_{\mathrm{S}}\right)-\sin\left(E_{\mathrm{S}}\left(\tau_{\mathrm{E,r}}\right)\right)\\ \cong\sin\left(E_{\mathrm{S}}\left(\tau_{\mathrm{E,r}}\right)\right)1-\cos\left(E_{\mathrm{S}}\left(\tau_{\mathrm{E,r}}\right)\right)\Delta E_{\mathrm{S}}-\sin\left(E_{\mathrm{S}}\left(\tau_{\mathrm{E,r}}\right)\right)\\ =-\Delta E_{\mathrm{S}}\cos\left(E_{\mathrm{S}}\left(\tau_{\mathrm{E,r}}\right)\right)\end{gathered}\tag{2.66}$$

The expression [2] that connects the mean anomaly of the satellite M_{S} and the eccentric anomaly of the satellite E_{S} is reported in (2.67).

$$M_{\mathrm{S}}=E_{\mathrm{S}}-e_{\mathrm{S}}\sin\left(E_{\mathrm{S}}\right)\tag{2.67}$$

The difference in the mean anomaly is then expressed as in (2.68).

$$\Delta M_{\mathrm{S}}=\Delta E_{\mathrm{S}}-e_{\mathrm{S}}\left(\sin\left(E_{\mathrm{S}}\left(\tau_0\right)\right)-\sin\left(E_{\mathrm{S}}\left(\tau_{\mathrm{E,r}}\right)\right)\right)\tag{2.68}$$

Considering again the reasonable hypothesis of small angles, (2.68) can be expressed as in (2.69).

$$\Delta M_{\mathrm{S}}\cong\Delta E_{\mathrm{S}}-e_{\mathrm{S}}\Delta E_{\mathrm{S}}\cos\left(\tau_{\mathrm{E,r}}\right)=\Delta E_{\mathrm{S}}\left(1-e_{\mathrm{S}}\cos\left(\tau_{\mathrm{E,r}}\right)\right)\tag{2.69}$$

Excluding the case where both $e_{\mathrm{S}}=1$ (i.e., a parabolic orbit) and $\cos\left(\tau_{\mathrm{E,r}}\right)=1$, the (2.70) can be obtained.

$$\Delta E_{\mathrm{S}}=\frac{\Delta M_{\mathrm{S}}}{1-e_{\mathrm{S}}\cos\left(\tau_{\mathrm{E,r}}\right)}\tag{2.70}$$

The value of the relativistic effects depends on the value of $\cos\left(\tau_{\mathrm{E,r}}\right)$. Considering that on its orbit the satellite experiences all the values of the eccentric anomaly from 0 to 2π, it can be reasonable to consider a conservative hypothesis which is representative of the worst case: $\cos\left(\tau_{\mathrm{E,r}}\right)=1$. Assuming this hypothesis, the value of the sinusoidal contribution to the time delay in (2.66) with the expression obtained in (2.70) can be formulated as in (2.71).

$$\begin{aligned}\sin\left(E_{\mathrm{S}}\left(\tau_0\right)\right)-\sin\left(E_{\mathrm{S}}\left(\tau_{\mathrm{E,r}}\right)\right)&\cong-\Delta E_{\mathrm{S}}\cos\left(E_{\mathrm{S}}\left(\tau_{\mathrm{E,r}}\right)\right)\\&=-\frac{\Delta M_{\mathrm{S}}}{1-e_{\mathrm{S}}\cos\left(\tau_{\mathrm{E,r}}\right)}\cos\left(E_{\mathrm{S}}\left(\tau_{\mathrm{E,r}}\right)\right)\leq-\frac{\Delta M_{\mathrm{S}}}{1-e_{\mathrm{S}}}\end{aligned}\tag{2.71}$$

The mean anomaly is a convenient transformation of geometry [2], because the angular position of the satellite is assigned on an equivalent circular orbit on which there is a simple linear dependence over time, as shown in (2.72), where $\tau|_0$ is a convenient starting time of reference and Ω_{S} is representative of the mean angular motion of the satellite[2].

$$M_{\mathrm{S}}=M_{\mathrm{S}}\left(\tau|_0\right)+\Omega_{\mathrm{S}}\left(\tau-\tau|_0\right)\tag{2.72}$$

From (2.72), the difference in the mean anomaly ΔM_{S} over an interval of time $\Delta\tau_{\mathrm{d}}$ is equal to $\Delta M_{\mathrm{S}}=\Omega_{\mathrm{S}}\Delta\tau_{\mathrm{d}}$.

By the definition of mean motion over an auxiliary circular orbit, the angular velocity is the ratio between the circumference over $\Omega_{\mathrm{S}}=2\pi/T_{\mathrm{S}}$. Furthermore, considering [2] that the value of the period for an elliptic orbit is $T_{\mathrm{S}}=2\pi\sqrt{a_{\mathrm{S}}^3/\mu_\oplus}$, the value of the difference of the mean anomaly ΔM_{S} is given in (2.73).

$$\Delta M_{\mathrm{S}}=\Omega_{\mathrm{S}}\Delta\tau_{\mathrm{d}}=\frac{2\pi}{T_{\mathrm{S}}}\Delta\tau_{\mathrm{d}}=\sqrt{\frac{\mu_\oplus}{a_{\mathrm{S}}^3}}\Delta\tau_{\mathrm{d}}\tag{2.73}$$

Substituting the value of (2.73) into (2.71), (2.74) is obtained.

$$\sin\left(E_{\mathrm{S}}\left(\tau_0\right)\right)-\sin\left(E_{\mathrm{S}}\left(\tau_{\mathrm{E,r}}\right)\right)\leq-\frac{\Delta M_{\mathrm{S}}}{1-e_{\mathrm{S}}}=-\sqrt{\frac{\mu_\oplus}{a_{\mathrm{S}}^3}}\frac{\Delta\tau_{\mathrm{d}}}{1-e_{\mathrm{S}}}\tag{2.74}$$

The expression in (2.74) is important because firstly it transforms the sinusoidal contribution of the eccentric anomaly E_{S} into two alternatives parameters a_{S} and e_{S} related to the shape of the orbit, and secondly it shows that this contribution depends only on the shape of the orbit and not on its orientation into the space, determined by the set of angles i_{S}, ω_{S}, and Ω_{S}.

Finally, substituting the expressions obtained in (2.63) and (2.74) in the relativistic correction obtained in (2.57), the conservative upper limit $\Delta\tau'_{\mathrm{rc}}$ in (2.75) is obtained, where it is interesting to observe that this conservative quantity has a linear dependence on the desynchronization time interval $\Delta\tau_{\mathrm{d}}$.

---

[2] In many textbooks the mean angular motion is denoted with the letter n. In this section Ω_{S} has been introduced to avoid confusion with the refractive index, which is also commonly denoted by n.

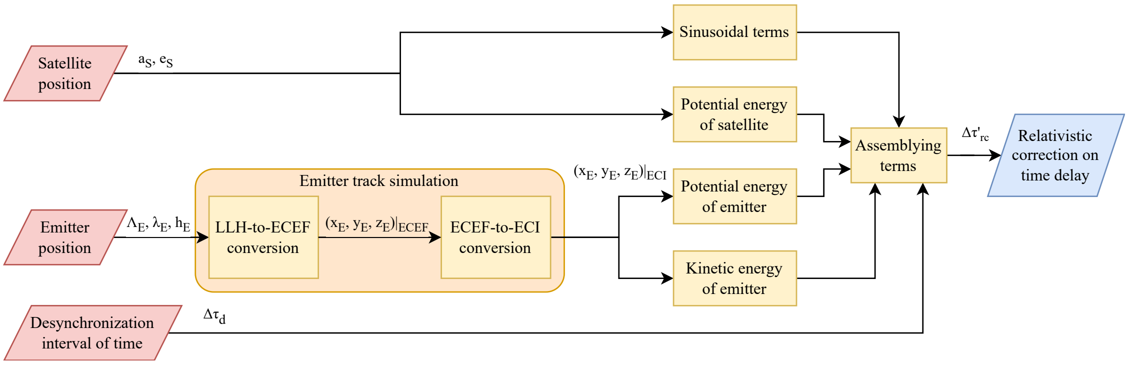

Figure 2.18: Block diagram for the calculation of approximate relativistic correction on time delay $\Delta\tau'_{\mathrm{rc}}$ from desynchronization interval of time $\Delta\tau_{\mathrm{d}}$, satellite orbit shape (semi-major axis a_{S} and eccentricity e_{S}) and the emitter position $\mathbf{x}_{\mathrm{E}}$.

$$\begin{gathered}\Delta\tau_{\mathrm{rc}} \leq \frac{2e_{\mathrm{S}}\sqrt{\mu_{\oplus}a_{\mathrm{S}}}}{c^2}\left(-\sqrt{\frac{\mu_{\oplus}}{a_{\mathrm{S}}^3}}\frac{\Delta\tau_{\mathrm{d}}}{1-e_{\mathrm{S}}}\right)\\ +\frac{\Delta\tau_{\mathrm{d}}}{c^2}\left(\frac{\mu_{\oplus}}{r_{\mathrm{E}}}-\frac{3\mu_{\oplus}}{2a_{\mathrm{S}}}+\frac{\left(\Omega_{\oplus}\cos{(\Lambda_{\mathrm{E}})}r_{\mathrm{E}}\right)^2}{2}\right)=\Delta\tau'_{\mathrm{rc}}\end{gathered} \tag{2.75}$$

2.3.4 Simulation of Relativistic Correction on Time Delay

The right hand of the expression in (2.75), which represents the conservative upper limit $\Delta\tau'_{\mathrm{rc}}$ of the relativistic correction on time delay, could be further expanded with an explicit formulation of r_{E} as a function of latitude and longitude. This fact leads to the possibility to investigate this contribution of error with the same approach considered for the Newtonian contribution.

In the right hand of (2.75) there are four contributions with different energetic meaning:

- The sinusoidal terms which depend on the shape of the orbit, so the semi-major axis a_{S} and eccentricity e_{S};
- Potential energy of the satellite, which also depends on the value of semi-major axis a_{S};
- Potential energy of the emitter, which depends on the value of the position of the emitter $r_{\mathrm{E}} = \|\mathbf{x}_{\mathrm{E}}\|$;
- Kinetic energy of the emitter, which depends on the value of the velocity of the emitter $\|\mathbf{v}_{\mathrm{E}}\| = \|\boldsymbol{\Omega}_{\mathrm{E}} \times \mathbf{r}_{\mathrm{E}}\|$.

Inspecting the four listed terms, the first two of them depend on the state of the satellite and other two depend on the state of the emitter, so a logical scheme of computation in Fig. 2.18 can be depicted.

Simulations have been conducted in MATLAB environment with these set of ranges:

- Geodetic latitude of the emitter $\Lambda_{\mathrm{E}} \in [-15°, 15°]$;
- Longitude of the emitter $\lambda_{\mathrm{E}} \in [-15°, 15°]$;
- Height at perigee $h_{\mathrm{S,p}} \in [300 \text{ km}, 11250 \text{ km}]$; corresponding values of semi-major axis of the orbit $a_{\mathrm{S}}(h_{\mathrm{S,p}}, e_{\mathrm{S}}) \in [6671 \text{ km}, 44052.5 \text{ km}]$ resulted from models in (1.4) and (1.5);
- Eccentricity of the orbit $e_{\mathrm{S}} \in [0.0, 0.6]$;

For every set of ranges 7 evenly spaced samples have been considered for a total of 2401 simulations.

The maximum value of the relativistic correction on time delay $\Delta\tau'_{\mathrm{rc}}$ is $1.69077 \cdot 10^{-8}$ s, the minimum value is $1.49705 \cdot 10^{-8}$ s, and the mean value is $1.61182 \cdot 10^{-8}$ s.

A comparison of the distribution of values of $\Delta\tau'_{\mathrm{rc}}$ over $\Delta\tau_{\mathrm{n}}$ is reported in Fig. 2.19 in form of histogram of the simulations conducted.

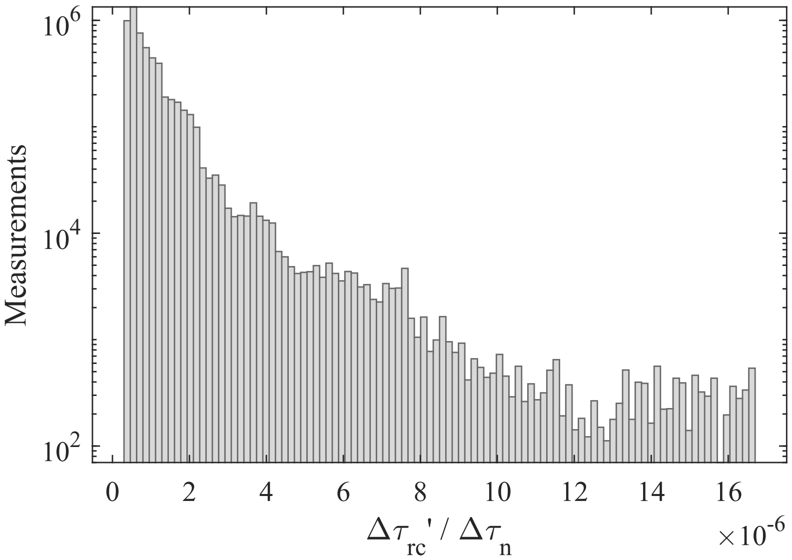

Figure 2.19: The histogram of distribution of the ratio $\Delta\tau'_{\mathrm{rc}}/\Delta\tau_{\mathrm{n}}$ considering all the simulation performed.

In Fig. 2.20 there is the shape of $\Delta\tau'_{\mathrm{rc}}$ as function of the geodetic latitude of the emitter Λ_{E}. From the simulations conducted by the author, the longitude of the emitter λ_{E} has not a particular trend to report.

In Fig. 2.21 there is the shape of $\Delta\tau'_{\mathrm{rc}}$ as function of the size and shape of the orbit: a_{S} and e_{S}.

In (2.76) is presented an approximation in form of Taylor polynomial of the correction on time delay $\Delta\tau'_{\mathrm{rc}}$ obtained in (2.75). However, considering that $\Delta\tau_{\mathrm{d}}$ is a multiplicative factor and in order consider it separately the coefficients of the polynomial in (2.76) are written in a manner that $\Delta\tau_{\mathrm{d}} = 1$. Furthermore, considering the variables in (2.75) it can be noticed that there is a dependence only

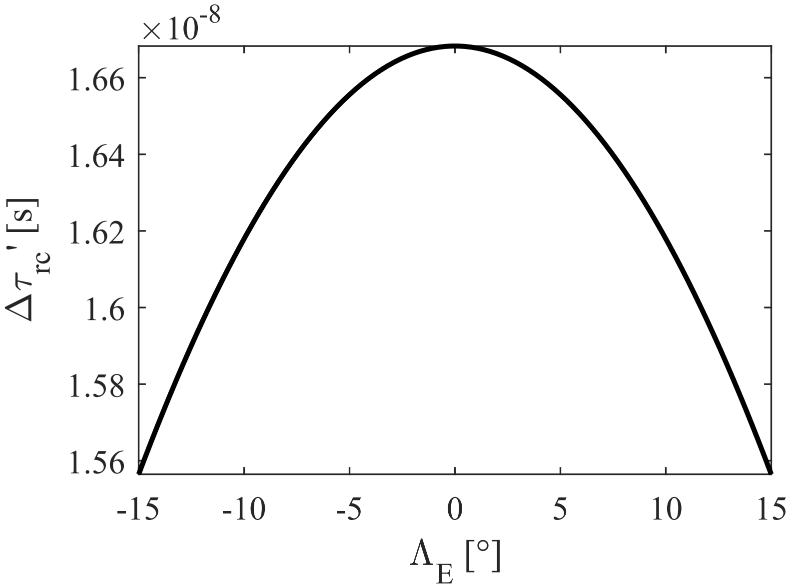

Figure 2.20: Shape of relativistic correction on time delay $\Delta\tau'_{\mathrm{rc}}$ as function of emitter geodetic latitude Λ_{E} in the point ($\lambda_{\mathrm{E}} = 0°$, $a_{\mathrm{S}} = 1735.143$ km, $e_{\mathrm{S}} = 0.3$.

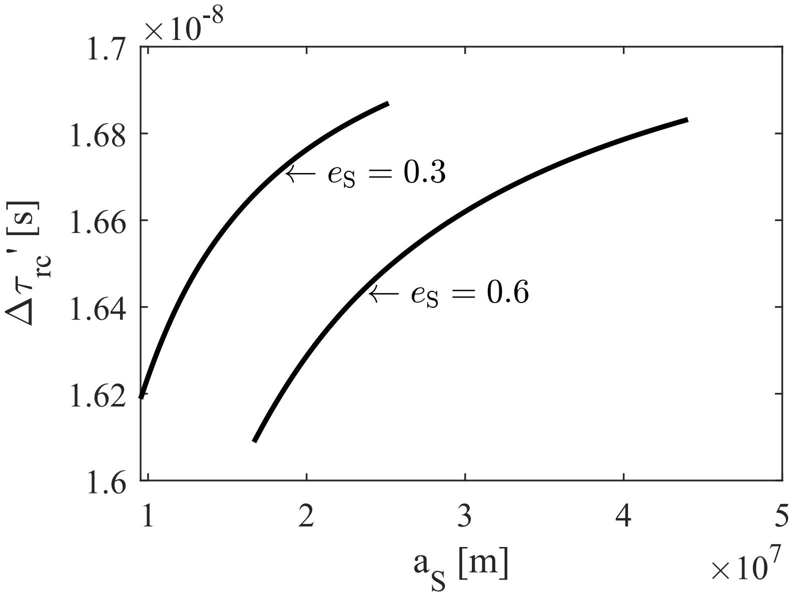

Figure 2.21: Shape of relativistic correction on time delay $\Delta\tau'_{\mathrm{rc}}$ as function of size a_{S} and shape e_{S} of the orbit in the point ($\Lambda_{\mathrm{E}} = 0°$, $\lambda_{\mathrm{E}} = 0°$).

Table 2.4: Coefficients of relativistic correction on time delay $\Delta\tau'_{\mathrm{rc}}$.

Coef.	**Value**	**Meas. unit**	**Coef.**	**Value**	**Meas. unit**
k_{rc}	$1.58371 \cdot 10^{-8}$	s	$k_{\mathrm{rc},1}$	$-5.06093 \cdot 10^{-22}$	$\mathrm{s} \cdot \mathrm{rad}^{-1}$
$k_{\mathrm{rc},2}$	$-3.46914 \cdot 10^{-10}$	$\mathrm{s} \cdot \mathrm{rad}^{-1}$	$k_{\mathrm{rc},3}$	$7.81534 \cdot 10^{-17}$	$\mathrm{s} \cdot \mathrm{m}^{-1}$
$k_{\mathrm{rc},4}$	$-7.13983 \cdot 10^{-10}$	s	$k_{\mathrm{rc},11}$	$-1.62134 \cdot 10^{-23}$	$\mathrm{s} \cdot \mathrm{rad}^{-2}$
$k_{\mathrm{rc},12}, k_{\mathrm{rc},21}$	$-2.20334 \cdot 10^{-22}$	$\mathrm{s} \cdot \mathrm{rad}^{-2}$	$k_{\mathrm{rc},13}, k_{\mathrm{rc},31}$	$4.46673 \cdot 10^{-29}$	$\mathrm{s} \cdot \mathrm{rad}^{-1} \cdot \mathrm{m}^{-1}$
$k_{\mathrm{rc},14}, k_{\mathrm{rc},41}$	$-3.12521 \cdot 10^{-23}$	$\mathrm{s} \cdot \mathrm{rad}^{-1}$	$k_{\mathrm{rc},22}$	$5.03747 \cdot 10^{-22}$	$\mathrm{s} \cdot \mathrm{rad}^{-2}$
$k_{\mathrm{rc},23}, k_{\mathrm{rc},32}$	$1.11802 \cdot 10^{-17}$	$\mathrm{s} \cdot \mathrm{rad}^{-1} \cdot \mathrm{m}^{-1}$	$k_{\mathrm{rc},24}, k_{\mathrm{rc},42}$	$-3.24668 \cdot 10^{-10}$	$\mathrm{s} \cdot \mathrm{rad}^{-1}$
$k_{\mathrm{rc},33}$	$-1.070256 \cdot 10^{-24}$	$\mathrm{s} \cdot \mathrm{m}^{-2}$	$k_{\mathrm{rc},34}, k_{\mathrm{rc},43}$	$1.23281 \cdot 10^{-17}$	$\mathrm{s} \cdot \mathrm{m}^{-1}$
$k_{\mathrm{rc},44}$	$-8.84099 \cdot 10^{-10}$	s			

on the satellite shape of the orbit (i.e., semi-major axis and eccentricity) and not a dependence on its orientation into the space.

$$\begin{aligned}\Delta\tau'_{\mathrm{rc}}\big|_{\Delta\tau_{\mathrm{d}}=1} &\simeq \tau_{\mathrm{rc},0} + (\mathbf{x}-\mathbf{x}_0)^{\mathsf{T}}\, D\tau'_{\mathrm{rc}} + \frac{1}{2}\,(\mathbf{x}-\mathbf{x}_0)^{\mathsf{T}}\, D^2\tau'_{\mathrm{rc}}\,(\mathbf{x}-\mathbf{x}_0)\\ &= \tau_{\mathrm{rc},0} + \sum_{k_1=1}^{4} \frac{\partial\tau'_{\mathrm{rc}}}{\partial x_{k_1}}\,(x_{k_1}-x_{k_1,0})\\ &+\frac{1}{2}\sum_{k_1=1}^{4}\sum_{k_2=1}^{4}\frac{\partial^2\tau'_{\mathrm{rc}}}{\partial x_{k_1}\partial x_{k_2}}\,(x_{k_1}-x_{k_1,0})\,(x_{k_2}-x_{k_2,0})\end{aligned} \tag{2.76}$$

For (2.76) the variables are $(x_1, x_2, x_3, x_4) = (\Lambda_{\mathrm{E}}, \lambda_{\mathrm{E}}, a_{\mathrm{S}}, e_{\mathrm{S}},)$.

The expressions of the constant term $\tau'_{\mathrm{rc},0}$, the gradient $D\tau'_{\mathrm{rc}}$, and the Hessian matrix $D^2\tau'_{\mathrm{rc}}$ of the polynomial model in (2.76) are reported in (2.77), (2.78), and (2.79).

$$\tau'_{\mathrm{rc},0} = k_{\mathrm{rc}} \tag{2.77}$$

$$D\tau'_{\mathrm{rc}} = (k_{\mathrm{rc},1}, k_{\mathrm{rc},2}, k_{\mathrm{rc},3}, k_{\mathrm{rc},4})^{\mathsf{T}} \tag{2.78}$$

$$D^2\tau'_{\mathrm{rc}} = \begin{bmatrix} k_{\mathrm{rc},11}, k_{\mathrm{rc},12}, k_{\mathrm{rc},13}, k_{\mathrm{rc},14}\\ k_{\mathrm{rc},21}, k_{\mathrm{rc},22}, k_{\mathrm{rc},23}, k_{\mathrm{rc},24}\\ k_{\mathrm{rc},31}, k_{\mathrm{rc},32}, k_{\mathrm{rc},33}, k_{\mathrm{rc},34}\\ k_{\mathrm{rc},41}, k_{\mathrm{rc},42}, k_{\mathrm{rc},43}, k_{\mathrm{rc},44}\end{bmatrix} \tag{2.79}$$

The values of the coefficients of the polynomial model are reported in Table 2.4.

From analytical considerations in the worst case scenario for relativistic effects only the size and the shape of the orbit, represented by the semi-major a_{S} axis and eccentricity e_{S}, and the position of the emitter — expressed in terms of geodetic latitude Λ_{E} and longitude λ_{E} — have an impact. The effect of time clock synchronization resulted in a linear dependence.

2.4 Atmospheric Effects

This section summarises models, methods, and results in the published article of the author [6].

2.4.1 Influence of Atmosphere on Time Delay

The time delay considered in (2.23) and also its extension with the relativistic correction shown in (2.57) have a constant speed of propagation $c = c_0$, which is the speed of light in vacuum.

The Earth is surrounded by its atmosphere, which induces a local change in the propagation speed through the refraction index n.

In particular, when the refraction index is taken into account, the speed of propagation becomes $c\,(n) = c_0/n$.

The dependence of the Newtonian delay is $\Delta t \propto 1/c$, while its relativistic correction is $\Delta\tau_{\mathrm{rc}} \propto 1/c^2$.

Substituting the value of the speed of propagation in an infinitesimal interval of time dt (2.23), the (2.80) is obtained.

$$dt = n\frac{ds}{c_0} \tag{2.80}$$

The value of the Newtonian time delay with atmospheric effects Δt_{a} is the result of an integral: on the left side from the instant of emission to the instant of reception, on the right side from the position of the emitter E to the position of the satellite S through a curved path $\gamma\,(\mathbf{x}_{\mathrm{E}}, \mathbf{x}_{\mathrm{S}})$, as shown in (2.81).

$$\Delta t_{\mathrm{a}} = \int_{t_e}^{t_r} dt = \int_{\gamma(\mathbf{x}_{\mathrm{E}},\mathbf{x}_{\mathrm{S}})} n\frac{ds}{c_0} = \frac{1}{c_0}\int_{\gamma(\mathbf{x}_{\mathrm{E}},\mathbf{x}_{\mathrm{S}})} nds \tag{2.81}$$

It can be demonstrated [32] that the error due to the increase in the path length is of the order of $(n-1)^2$ while the error due to the change in the propagation speed is of the order of $n-1$. This common approximation, $n - 1 \ll (n-1)^2$, appears reasonable considering that for the particular case of air in the atmosphere as the medium of propagation $n-1$ has a maximum value of the order of magnitude of 10^{-4} (obtained on the surface of the Earth), so $(n-1)^2$ is 10^{-8}.

Considering the negligible effect of a curved path, the value of the integral in (2.81) can be approximated to its value on a line segment, as shown in (2.82). The subscript l in Δt_{l} indicates that the integral is calculated on a line segment.

$$\Delta t_{\mathrm{a}} = \frac{1}{c_0}\int_{\gamma(\mathbf{x}_{\mathrm{E}},\mathbf{x}_{\mathrm{S}})} nds \cong \frac{1}{c_0}\int_{\mathbf{x}_{\mathrm{E}}}^{\mathbf{x}_{\mathrm{S}}} nds = \Delta t_{\mathrm{l}} \tag{2.82}$$

For comparison, the value of the delay without atmospheric effects (i.e., in vacuum) Δt_{v} in integral form is reported in (2.83). In this case, the curve on which the integral is calculated is always a line segment from the emitter position and the satellite position, because the bending of the waves is a consequence of the presence of a medium.

$$\Delta t_{\mathrm{v}} = \frac{1}{c_0} \int_{\mathbf{x}_{\mathrm{E}}}^{\mathbf{x}_{\mathrm{S}}} ds \tag{2.83}$$

From the difference between (2.82) and (2.83) it is possible to write an atmospheric correction on the time delay Δt_{ac} as shown in (2.84).

$$\begin{aligned}\Delta t_{\mathrm{ac}} = \Delta t_{\mathrm{a}} - \Delta t_{\mathrm{v}} \cong \Delta t_{\mathrm{l}} - \Delta t_{\mathrm{v}} &= \frac{1}{c_0} \int_{\mathbf{x}_{\mathrm{E}}}^{\mathbf{x}_{\mathrm{S}}} n ds - \frac{1}{c_0} \int_{\mathbf{x}_{\mathrm{E}}}^{\mathbf{x}_{\mathrm{S}}} ds \\ &= \frac{1}{c_0} \int_{\mathbf{x}_{\mathrm{E}}}^{\mathbf{x}_{\mathrm{S}}} (n-1)\, ds\end{aligned} \tag{2.84}$$

The reader can observe that the value of delay in vacuum derived in this subsection is the same delay in Newtonian mechanics, so $\Delta t_{\mathrm{v}} = \Delta t_{\mathrm{n}}$. The idea is to obtain an additive correction on the Newtonian delay due to the atmospheric presence: $\Delta t_{\mathrm{a}} \cong \Delta t_{\mathrm{n}} + \Delta t_{\mathrm{ac}}$.

In geometric optics, a relationship has been found between the refraction index n and the density ρ. Starting from works with liquids [33], the Gladstone-Dale relationship has also been proposed and validated for mixtures of gases [34], as shown in (2.85), where K is a constant of proportionality that depends on the value of the wavelength.

$$n(\rho) = 1 + K\rho \tag{2.85}$$

In general, since the values of the refraction index n vary on small values of decimal places, around an order of magnitude of 10^{-6}, an intermediate variable of convenience, called radio refractivity N, is introduced, as shown in (2.86).

$$n = 1 + 10^{-6} N \tag{2.86}$$

Substituting (2.86) into (2.84), (2.87) is obtained.

$$\Delta t_{\mathrm{ac}} \cong \frac{1}{c_0} \int_{\mathbf{x}_{\mathrm{E}}}^{\mathbf{x}_{\mathrm{S}}} (n-1)\, ds = \frac{10^{-6}}{c_0} \int_{\mathbf{x}_{\mathrm{E}}}^{\mathbf{x}_{\mathrm{S}}} N ds \tag{2.87}$$

Considering that for a gas (and mixtures of gases such as the atmosphere) there is a physical relationship among density ρ, pressure p, and temperature T, the radio refractivity N can be expressed as a function of thermodynamic variables. To date, one of the most common models for moist air, also suggested by the ITU (International Communication Union) guidelines on the design of satellite payloads [35], is the Smith-Weintraub relationship reported in (2.88), in which p_{t} is the total pressure and p_{w} is the water vapour partial pressure.

$$N = 77.6\frac{p_\mathrm{t}}{T} + 72\frac{p_\mathrm{w}}{T} + 3.75 \cdot 10^5\frac{p_\mathrm{w}}{T^2} \tag{2.88}$$

The main convenience of the model is that it is independent of the frequency and has been demonstrated to be valid with an accuracy of 0.5 percent on the value of the radio refractivity N, which means an accuracy of the order of $0.5 \cdot 10^{-8}$ on the value of the refractivity n in the following ranges: temperature range $T \in [-50, 40]$°C, total pressure $p_\mathrm{t} \in [400, 1100]$ hPa and water pressure $p_\mathrm{w} \in [0, 30]$ hPa.

Over time many profiles have been proposed for the values of thermodynamic variables in the atmosphere with respect to the value of height h and the integral in (2.87) is solved considering (2.88), and the set of three profiles $T = T(h)$, $p_\mathrm{t} = p_\mathrm{t}(h)$, and $p_\mathrm{w} = p_\mathrm{w}(h)$. A set of suggested profiles can be found among the ITU recommendations [36].

The analytical expression of the integral (2.87) with (2.88) is not trivial, especially with complicated thermodynamic profiles.

There exist attempts to obtain these types of solutions in simpler cases: an example of this exercise can be found in [32], [37] using a simpler exponential model of radio refractivity, as shown in (2.89), where N_0 represents the value of radio refractivity on the surface of the Earth and $H_\oplus$ is the effective height of the planet.

$$N = N_0 \cdot e^{-\frac{(h-h_0)}{H_\oplus}} \tag{2.89}$$

The definition of effective height, also known as scale height, is reproduced in (2.90), where R is the specific universal gas constant equal to 287.05 J/(kg · K), $T_\oplus$ is the mean atmospheric temperature (equal to 250 K), and g_m is the value of the gravitational acceleration constant measured in the centre of the vertical column of air.

$$H_\oplus = \frac{RT_\oplus}{g_\mathrm{m}} \tag{2.90}$$

There are many models for g_m: in general, it depends on the value of the latitude Λ and the height h. A comparison of the models for the propagation problems of signals in the atmosphere is in [38]. A first-level approximation for evaluative purposes considers a constant value of g_m, which leads to a constant value also for $H_\oplus$.

The analytical integration of (2.87) with an exponential model (2.89) and constant values of N_0 and $H_\oplus$ is calculated in [32] and reported in (2.91).

$$\Delta t_\mathrm{ac} \cong \frac{10^{-6}}{c_0}\int_{\mathbf{x}_\mathrm{E}}^{\mathbf{x}_\mathrm{S}} N ds = \frac{10^{-6}}{c_0}\frac{H_\oplus N_0 \sqrt{\pi}\chi e^{\chi^2}}{\sin(\beta)}\left(1 - \mathrm{erf}(\chi)\right) \tag{2.91}$$

To date, the most recent and suggested values by the ITU recommendations [36] are $N_0 = 315$ and $H_\oplus = 7530$ m and have been considered in the simulations of this work.

In (2.91) β is the elevation angle calculated from the ground plane to the emitter-satellite direction and χ is defined in (2.92).

$$\chi = \tan(\beta)\sqrt{\frac{r_\mathrm{E}}{2H_\oplus}} \tag{2.92}$$

The error function of χ is reported in (2.93).

$$\mathrm{erf}(\chi) = \frac{2}{\sqrt{\pi}}\int_0^\chi e^{-x^2}dx \tag{2.93}$$

From the experience of the author, (2.91) has numerical difficulties to converge for high values of elevations ($\beta > 15°$). A further approximated version, also suggested in [32] and reported in (2.94), does not suffer this inconvenience.

$$\Delta t_{\mathrm{ac},2} \cong \frac{10^{-6}}{c_0}\frac{H_\oplus N_0}{\sin(\beta)} \tag{2.94}$$

Considering the plane of the local horizon, as shown in Fig. 2.22, the elevation angle β can be calculated from the dot product between $\overrightarrow{EO}$ and $\overrightarrow{ES}$, as shown in (2.95).

$$\cos\left(\beta + \frac{\pi}{2}\right) = \frac{\overrightarrow{EO}}{\left\|\overrightarrow{EO}\right\|} \cdot \frac{\overrightarrow{ES}}{\left\|\overrightarrow{ES}\right\|} \tag{2.95}$$

Considering $\overrightarrow{EO} = -\mathbf{x}_\mathrm{E}$ and $\overrightarrow{ES} = \mathbf{x}_\mathrm{S} - \mathbf{x}_\mathrm{E}$, (2.96) can be written.

$$\beta = \arccos\left(\frac{-\mathbf{x}_\mathrm{E}}{\|-\mathbf{x}_\mathrm{E}\|} \cdot \frac{\mathbf{x}_\mathrm{S} - \mathbf{x}_\mathrm{E}}{\|\mathbf{x}_\mathrm{S} - \mathbf{x}_\mathrm{E}\|}\right) - \frac{\pi}{2} \tag{2.96}$$

2.4.2 Simulation of Atmospheric Contribution on Time Delay

A logical scheme of computation of atmospheric time delay is depicted in Fig. 2.23.

Simulations in MATLAB environment have been performed considering the same number of values and ranges of other contributions.

The maximum value of the atmospheric correction on time delay Δt_ac is $2.25221 \cdot 10^{-6}$ s, the minimum value is $7.86174 \cdot 10^{-9}$ s, and the mean value is $3.05441 \cdot 10^{-8}$ s.

A comparison of the distribution of values of Δt_ac over Δt_n is reported in Fig. 2.24 in form of histogram of the simulations conducted.

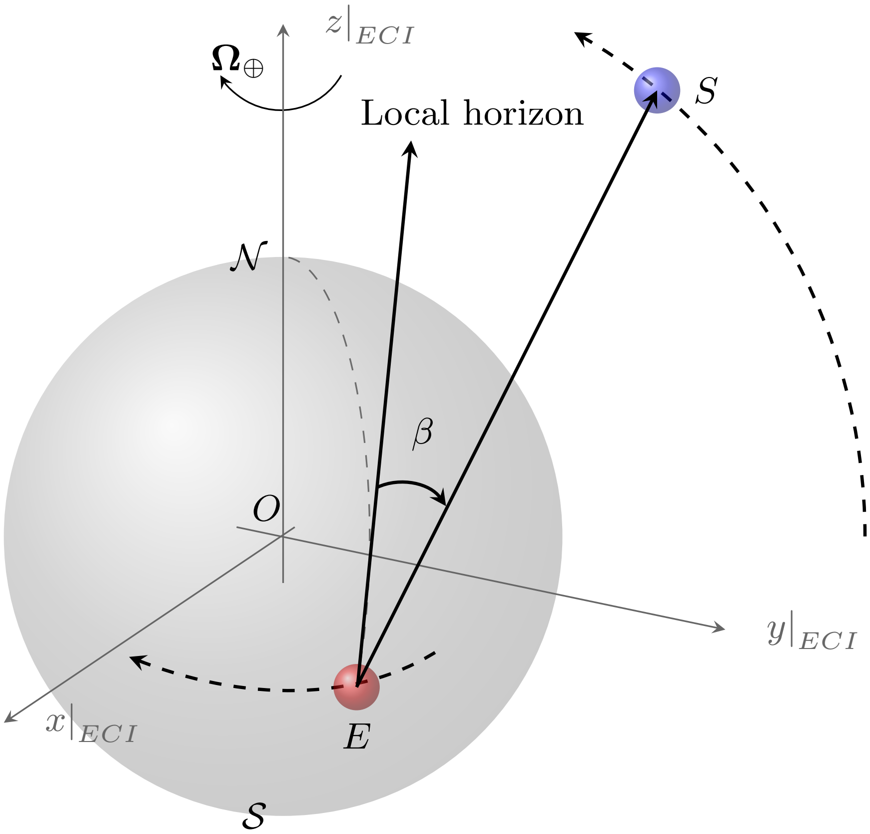

Figure 2.22: Representation of the elevation angle β. By definition it is the angle between the plane of local horizon and emitter-satellite direction $\overrightarrow{ES}/\left\|\overrightarrow{ES}\right\|$.

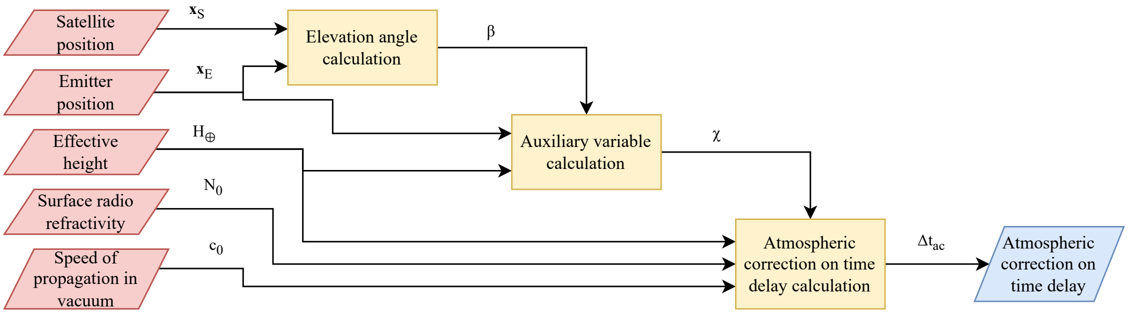

Figure 2.23: Block diagram for the calculation of approximate atmospheric correction on time delay Δt_{a} from satellite position $\mathbf{x}_{\mathrm{S}}$, emitter position $\mathbf{x}_{\mathrm{E}}$, effective height of the Earth $H_\oplus$, radio refractivity on the surface of the Earth N_0, and speed of propagation in vacuum c_0.

In Fig. 2.25 there the shape of Δt_{ac} as function of the position of the emitter on the surface of the Earth (represented by its geodetic latitude Λ_{E} and longitude

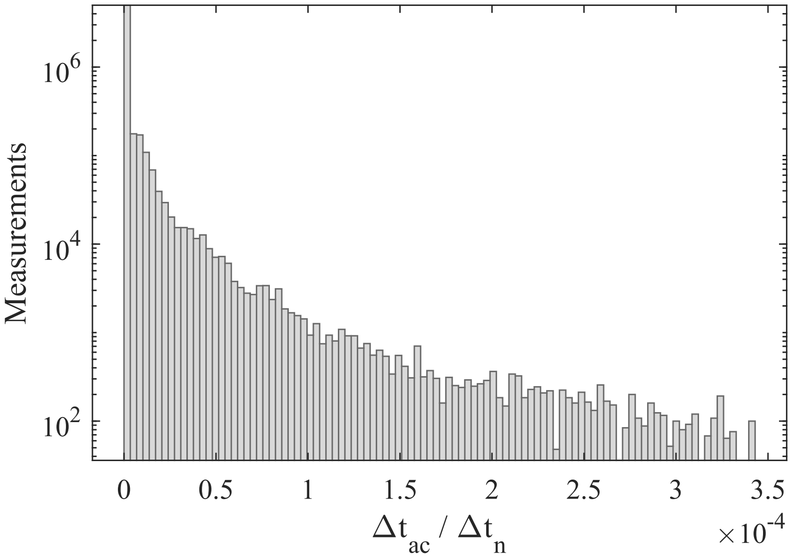

Figure 2.24: The histogram of distribution of the ratio $\Delta t_{\mathrm{ac}}/\Delta t_{\mathrm{n}}$ considering all the simulation performed.

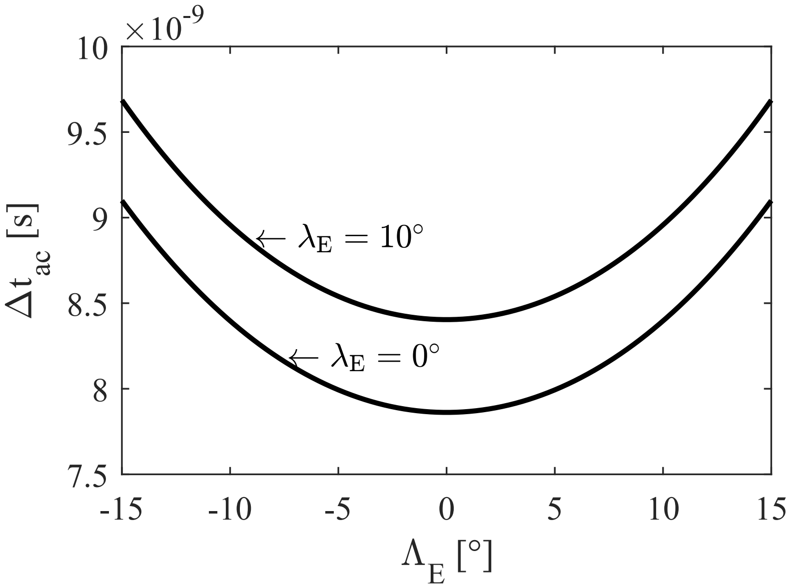

Figure 2.25: Shape of atmospheric correction on time delay Δt_{ac} as function of emitter position on the surface of the Earth, geodetic latitude Λ_{E} and longitude λ_{E}, in the point ($a = 1735.143$ km, $e = 0.3$, $i = 90°$, $\Omega = 0°$, $\omega = 0°$, $\nu = 0°$).

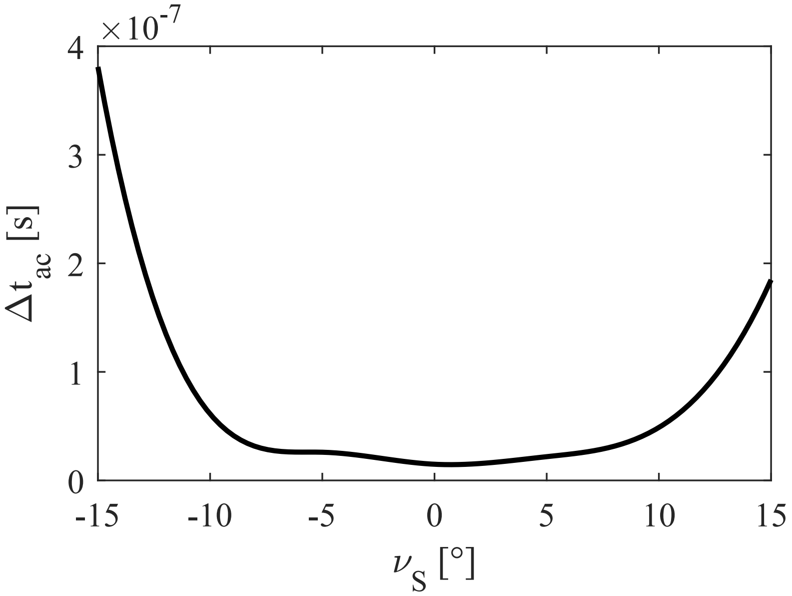

Figure 2.26: Shape of atmospheric correction on time delay Δt_{ac} as function of satellite position on its orbit ν_{S} in the point ($\Lambda_{\mathrm{E}} = 0°$, $\lambda_{\mathrm{E}} = 0°$, $a = 1735.143$ km, $e = 0.3$, $i = 90°$, $\Omega = 0°$, $\omega = 0°$).

λ_{E}).

In Fig. 2.26 there is the shape of Δt_{ac} as function of satellite position on its orbit ν_{S}.

Data gathered in simulation have been fitted in a polynomial model for the atmospheric contribution on time delay Δt_{ac}, as reported in (2.97).

$$\begin{aligned}\Delta t_{\mathrm{ac}} \simeq= t_{\mathrm{ac},0} + (\mathbf{x}-\mathbf{x}_0)^{\mathsf{T}} Dt_{\mathrm{ac}} + \frac{1}{2}(\mathbf{x}-\mathbf{x}_0)^{\mathsf{T}} D^2 t_{\mathrm{ac}} (\mathbf{x}-\mathbf{x}_0) \\ = t_{\mathrm{ac},0} + \sum_{k_1=1}^{8} \frac{\partial t_{\mathrm{ac}}}{\partial x_{k_1}} (x_{k_1} - x_{k_1,0}) \\ + \frac{1}{2} \sum_{k_1=1}^{8} \sum_{k_2=1}^{8} \frac{\partial^2 t_{\mathrm{ac}}}{\partial x_{k_1} \partial x_{k_2}} (x_{k_1} - x_{k_1,0})(x_{k_2} - x_{k_2,0})\end{aligned} \tag{2.97}$$

The variables of the polynomial model in (2.97) are $(x_1, x_2, x_3, x_4, x_5, x_6, x_7, x_8) = (\Lambda_{\mathrm{E}}, \lambda_{\mathrm{E}}, a_{\mathrm{S}}, e_{\mathrm{S}}, i_{\mathrm{S}}, \omega_{\mathrm{S}}, \Omega_{\mathrm{S}}, \nu_{\mathrm{S}})$.

The expressions of the constant term $t_{\mathrm{ac},0}$, gradient Dt_{ac}, and Hessian matrix $D^2 t_{\mathrm{ac}}$ of the polynomial model in (2.97) are reported in (2.98), (2.99), and (2.100).

$$t_{\mathrm{ac},0} = k_{\mathrm{ac}} \tag{2.98}$$

$$Dt_{\mathrm{ac}} = (k_{\mathrm{ac},1}, k_{\mathrm{ac},2}, \ldots, k_{\mathrm{ac},8})^{\mathsf{T}} \tag{2.99}$$

$$D^2 t_{\mathrm{ac}} = \begin{bmatrix} k_{\mathrm{ac},11} & k_{\mathrm{ac},12} & \cdots & k_{\mathrm{ac},18} \\ k_{\mathrm{ac},21} & k_{\mathrm{ac},22} & \cdots & k_{\mathrm{ac},28} \\ \vdots & \vdots & \ddots & \vdots \\ k_{\mathrm{ac},81} & k_{\mathrm{ac},82} & \cdots & k_{\mathrm{ac},88} \end{bmatrix} \tag{2.100}$$

The values of the coefficients of the polynomial model are reported in Table 2.5.

The effects of the presence of the atmosphere are highly dependent on the profile of radio refractivity N which depends on thermodynamic variables such as density ρ, pressure p, and temperature T: for a coarse prediction of the performances of a system or for comparison of multiple systems an exponential model can be used. For real-time corrections of measurements more sophisticated seasonal profiles or, if possible, data locally gathered from meteorological stations are suggested.

Table 2.5: Coefficients of atmospheric correction on time delay Δt_{ac}.

Coef.	**Value**	**Meas. unit**	**Coef.**	**Value**	**Meas. unit**
k_{ac}	$9.01449 \cdot 10^{-9}$	s	$k_{\mathrm{ac},1}$	$-3.13139 \cdot 10^{-10}$	$\mathrm{s} \cdot \mathrm{rad}^{-1}$
$k_{\mathrm{ac},2}$	$6.65171 \cdot 10^{-10}$	$\mathrm{s} \cdot \mathrm{rad}^{-1}$	$k_{\mathrm{ac},3}$	$1.16857 \cdot 10^{-16}$	$\mathrm{s} \cdot \mathrm{m}^{-1}$
$k_{\mathrm{ac},4}$	$-6.28134 \cdot 10^{-9}$	s	$k_{\mathrm{ac},5}$	$-6.65171 \cdot 10^{-10}$	$\mathrm{s} \cdot \mathrm{rad}^{-1}$
$k_{\mathrm{ac},6}$	$6.63238 \cdot 10^{-9}$	$\mathrm{s} \cdot \mathrm{rad}^{-1}$	$k_{\mathrm{ac},7}$	$2.95664 \cdot 10^{-8}$	$\mathrm{s} \cdot \mathrm{rad}^{-1}$
$k_{\mathrm{ac},8}$	$5.80115 \cdot 10^{-12}$	$\mathrm{s} \cdot \mathrm{rad}^{-1}$	$k_{\mathrm{ac},11}$	$-1.29480 \cdot 10^{-8}$	$\mathrm{s} \cdot \mathrm{rad}^{-2}$
$k_{\mathrm{ac},12}, k_{\mathrm{ac},21}$	$-2.96908 \cdot 10^{-21}$	$\mathrm{s} \cdot \mathrm{rad}^{-2}$	$k_{\mathrm{ac},13}, k_{\mathrm{ac},31}$	$1.87375 \cdot 10^{-17}$	$\mathrm{s} \cdot \mathrm{rad}^{-1} \cdot \mathrm{m}^{-1}$
$k_{\mathrm{ac},14}, k_{\mathrm{ac},41}$	$-1.43590 \cdot 10^{-10}$	$\mathrm{s} \cdot \mathrm{rad}^{-1}$	$k_{\mathrm{ac},15}, k_{\mathrm{ac},51}$	$-1.76968 \cdot 10^{-21}$	$\mathrm{s} \cdot \mathrm{rad}^{-2}$
$k_{\mathrm{ac},16}, k_{\mathrm{ac},61}$	$9.86776 \cdot 10^{-21}$	$\mathrm{s} \cdot \mathrm{rad}^{-2}$	$k_{\mathrm{ac},17}, k_{\mathrm{ac},71}$	$1.32101 \cdot 10^{-21}$	$\mathrm{s} \cdot \mathrm{rad}^{-2}$
$k_{\mathrm{ac},18}, k_{\mathrm{ac},81}$	$4.56059 \cdot 10^{-11}$	$\mathrm{s} \cdot \mathrm{rad}^{-2}$	$k_{\mathrm{ac},22}$	$-2.18421 \cdot 10^{-8}$	$\mathrm{s} \cdot \mathrm{rad}^{-2}$
$k_{\mathrm{ac},23}, k_{\mathrm{ac},32}$	$-6.45861 \cdot 10^{-17}$	$\mathrm{s} \cdot \mathrm{rad}^{-1} \cdot \mathrm{m}^{-1}$	$k_{\mathrm{ac},24}, k_{\mathrm{ac},42}$	$1.87555 \cdot 10^{-9}$	$\mathrm{s} \cdot \mathrm{rad}^{-1}$
$k_{\mathrm{ac},25}, k_{\mathrm{ac},52}$	$7.56642 \cdot 10^{-8}$	$\mathrm{s} \cdot \mathrm{rad}^{-2}$	$k_{\mathrm{ac},26}, k_{\mathrm{ac},62}$	$-1.96788 \cdot 10^{-21}$	$\mathrm{s} \cdot \mathrm{rad}^{-2}$
$k_{\mathrm{ac},27}, k_{\mathrm{ac},72}$	$-3.01418 \cdot 10^{-21}$	$\mathrm{s} \cdot \mathrm{rad}^{-2}$	$k_{\mathrm{ac},28}, k_{\mathrm{ac},82}$	$-1.35098 \cdot 10^{-24}$	$\mathrm{s} \cdot \mathrm{rad}^{-2}$
$k_{\mathrm{ac},33}$	$4.66904 \cdot 10^{-24}$	$\mathrm{s} \cdot \mathrm{m}^{-2}$	$k_{\mathrm{ac},34}, k_{\mathrm{ac},43}$	$-3.04319 \cdot 10^{-16}$	$\mathrm{s} \cdot \mathrm{m}^{-1}$
$k_{\mathrm{ac},35}, k_{\mathrm{ac},53}$	$6.45861 \cdot 10^{-17}$	$\mathrm{s} \cdot \mathrm{rad}^{-1} \cdot \mathrm{m}^{-1}$	$k_{\mathrm{ac},36}, k_{\mathrm{ac},63}$	$-1.28766 \cdot 10^{-16}$	$\mathrm{s} \cdot \mathrm{rad}^{-1} \cdot \mathrm{m}^{-1}$
$k_{\mathrm{ac},37}, k_{\mathrm{ac},73}$	$1.54908 \cdot 10^{-16}$	$\mathrm{s} \cdot \mathrm{rad}^{-1} \cdot \mathrm{m}^{-1}$	$k_{\mathrm{ac},38}, k_{\mathrm{ac},83}$	$-8.84284 \cdot 10^{-21}$	$\mathrm{s} \cdot \mathrm{rad}^{-1} \cdot \mathrm{m}^{-1}$
$k_{\mathrm{ac},44}$	$9.48557 \cdot 10^{-9}$	s	$k_{\mathrm{ac},45}, k_{\mathrm{ac},54}$	$-1.87555 \cdot 10^{-9}$	$\mathrm{s} \cdot \mathrm{rad}^{-1}$
$k_{\mathrm{ac},46}, k_{\mathrm{ac},64}$	$3.73931 \cdot 10^{-9}$	$\mathrm{s} \cdot \mathrm{rad}^{-1}$	$k_{\mathrm{ac},47}, k_{\mathrm{ac},74}$	$-4.49845 \cdot 10^{-9}$	$\mathrm{s} \cdot \mathrm{rad}^{-1}$
$k_{\mathrm{ac},48}, k_{\mathrm{ac},84}$	$-1.87768 \cdot 10^{-11}$	$\mathrm{s} \cdot \mathrm{rad}^{-1}$	$k_{\mathrm{ac},55}$	$-2.18421 \cdot 10^{-8}$	$\mathrm{s} \cdot \mathrm{rad}^{-2}$
$k_{\mathrm{ac},56}, k_{\mathrm{ac},65}$	$1.69622 \cdot 10^{-20}$	$\mathrm{s} \cdot \mathrm{rad}^{-2}$	$k_{\mathrm{ac},57}, k_{\mathrm{ac},75}$	$-2.87348 \cdot 10^{-21}$	$\mathrm{s} \cdot \mathrm{rad}^{-2}$
$k_{\mathrm{ac},58}, k_{\mathrm{ac},85}$	$5.31258 \cdot 10^{-24}$	$\mathrm{s} \cdot \mathrm{rad}^{-2}$	$k_{\mathrm{ac},66}$	$-1.13392 \cdot 10^{-9}$	$\mathrm{s} \cdot \mathrm{rad}^{-2}$
$k_{\mathrm{ac},67}, k_{\mathrm{ac},76}$	$-1.55567 \cdot 10^{-8}$	$\mathrm{s} \cdot \mathrm{rad}^{-2}$	$k_{\mathrm{ac},68}, k_{\mathrm{ac},86}$	$-1.14117 \cdot 10^{-23}$	$\mathrm{s} \cdot \mathrm{rad}^{-2}$
$k_{\mathrm{ac},77}$	$-1.39193 \cdot 10^{-7}$	$\mathrm{s} \cdot \mathrm{rad}^{-2}$	$k_{\mathrm{ac},78}, k_{\mathrm{ac},87}$	$-1.69046 \cdot 10^{-24}$	$\mathrm{s} \cdot \mathrm{rad}^{-2}$
$k_{\mathrm{ac},88}$	$-1.54438 \cdot 10^{-14}$	$\mathrm{s} \cdot \mathrm{rad}^{-2}$			

2.5 On the Bending of Electromagnetic Waves

The main approach and models developed in this section are unpublished and must be considered as preliminary results to be verified. At the time of writing, a dedicated journal paper with provisional details in [39] is in preparation for a submission in Dec. 2025. Conditioned on its acceptance, this work is expected to occur during the year 2026.

The main literature on the topic can be found in [40] for satellite tracking activities, in [41] for range and range-rate measurements, in [42] for the effects troposphere and ionosphere upon measurements of range, range-rate and elevation angle, in [43] for the arrival angle of the ray at the ground, and in [44] for the apparent boresight angle on slant paths.

This section wants to give to the reader an elegant overview of the models behind the phenomenon of the bending of the electromagnetic waves, which can happen because of a gravitational field or because of the propagation in a medium with varying refractive index.

The model written here follows the approach in [45], which is based on the equation of geodesics and Christoffel symbols. In this section the convention on repeated indices is adopted.

The geodesic equation is reported in (2.101), where u, v, and w are the indices associated to each dimension, τ is the time, and Γ^{u}_{vw} is the Christoffel symbol of second kind.

$$\frac{d^2x^u}{d\tau^2} + \Gamma^u_{vw}\frac{dx^v}{d\tau}\frac{dx^w}{d\tau} = 0 \tag{2.101}$$

The equation of geodesics (2.101) can be used to describe the path of a photon in a space-time with the properties described by the Christoffel symbols.

The definition of the Christoffel symbol of second kind Γ^u_{vw} is reported in (2.102), where $\Gamma_{s,vw}$ is the Christoffel symbol of first kind and g^{us} is contravariant version of the metric tensor.

$$\Gamma^u_{vw} = g^{us}\Gamma_{s,vw} \tag{2.102}$$

The Christoffel symbols of first kind is reported in (2.103).

$$\Gamma_{u,vw} = \frac{1}{2}\left(\frac{\partial g_{uv}}{\partial x^w} + \frac{\partial g_{uw}}{\partial x^v} - \frac{\partial g_{vw}}{\partial x^u}\right) \tag{2.103}$$

Substituting the (2.103) in (2.102), the (2.104) is obtained

$$\Gamma^u_{vw} = \frac{1}{2}g^{us}\left(\frac{\partial g_{sv}}{\partial x^w} + \frac{\partial g_{sw}}{\partial x^v} - \frac{\partial g_{vw}}{\partial x^s}\right) \tag{2.104}$$

Writing the sum from 1 to 3 for the geodesics equation (2.101), the (2.105) is obtained.

$$\frac{d^2x^u}{d\tau^2} + \sum_{v=1}^{3}\sum_{w=1}^{3}\left(\Gamma^u_{vw}\frac{dx^v}{d\tau}\frac{dx^w}{d\tau}\right) = 0 \qquad u = 1,2,3 \tag{2.105}$$

And substituting Christoffel symbols (2.104) in (2.105), the (2.106) is obtained.

$$\frac{d^2x^u}{d\tau^2} + \sum_{v=1}^{3}\sum_{w=1}^{3}\left(\sum_{s=1}^{3}\left(\frac{1}{2}g^{us}\left(\frac{\partial g_{sv}}{\partial x^w} + \frac{\partial g_{sw}}{\partial x^v} - \frac{\partial g_{vw}}{\partial x^s}\right)\right)\frac{dx^v}{d\tau}\frac{dx^w}{d\tau}\right) = 0, \qquad u = 1,2,3. \tag{2.106}$$

The space-time metric tensor g is a mathematical object that describes the geometry of space-time connecting the infinitesimal interval of time $d\tau$ to the infinitesimal interval of space ds as reported in (2.107).

$$(d\tau)^2 = g_{uv}dx^u dx^v. \tag{2.107}$$

With (2.107) two problems can be formulated: one is about geometrical optics, which considers the propagation of a photon in a medium with varying refractive index n; and a second problem about the propagation in a gravitational field.

For the propagation in the atmosphere, which is a medium with a profile of refractive index n, the connection (2.107) is in the form

$$d\tau = \frac{n}{c} ds \tag{2.108}$$

or equivalently

$$(d\tau)^2 = \left(\frac{n}{c}\right)^2 \left((dx)^2 + (dy)^2 + (dz)^2\right)^2 . \tag{2.109}$$

To write (2.108) and (2.109) the following hypothesis on the metric tensor g has been done

$$g_{ij} = \left(\frac{n\,(x, y, z)}{c}\right)^2 \delta_{ij} \tag{2.110}$$

or equivalently

$$g_{ij} = \begin{cases} \left(\dfrac{n\,(x, y, z)}{c}\right)^2 & \text{if } i = j \\ 0 & \text{if } i \neq j \end{cases} \tag{2.111}$$

The matrix-based expression of the covariant form of the tensor is reported in (2.112), while in (2.113) there is its contravariant counterpart.

$$g_{i,j} = \begin{bmatrix} \left(\dfrac{n\,(x, y, z)}{c}\right)^2 & 0 & 0 \\ 0 & \left(\dfrac{n\,(x, y, z)}{c}\right)^2 & 0 \\ 0 & 0 & \left(\dfrac{n\,(x, y, z)}{c}\right)^2 \end{bmatrix} \tag{2.112}$$

$$g^{i,j} = \begin{bmatrix} \left(\dfrac{c}{n\,(x, y, z)}\right)^2 & 0 & 0 \\ 0 & \left(\dfrac{c}{n\,(x, y, z)}\right)^2 & 0 \\ 0 & 0 & \left(\dfrac{c}{n\,(x, y, z)}\right)^2 \end{bmatrix} \tag{2.113}$$

When the propagation is within a gravitational field, then the Schwarzschild metrics is the reference model, as in (2.39), here repeated in (2.114) for convenience.

$$ds^2 = -\left(1 - \frac{2GM}{c^2 r}\right)^{-1} dr^2 - r^2 d\theta^2 - r^2 \sin^2(\theta) d\phi^2 + c^2 \left(1 - \frac{2GM}{c^2 r}\right) dt^2 \tag{2.114}$$

In this case, the covariant version of the tensor g is as in (2.115); the metric tensor follows this order of the terms: time τ, radial coordinate r, polar angle θ, and azimuthal angle ϕ.

$$g_{i,j}=\begin{bmatrix}\left(1-\frac{2GM}{c^2r}\right) & 0 & 0 & 0\\ 0 & -\left(1-\frac{2GM}{c^2r}\right)^{-1} & 0 & 0\\ 0 & 0 & -r^2 & 0\\ 0 & 0 & 0 & -r^2\sin^2(\theta)\end{bmatrix} \tag{2.115}$$

There are two versions of the Schwarzschild equation and they differ because of the signs of the terms in (τ, r, θ, ϕ) , the one reported here has signature $(+,-,-,-)$ for the variables and it is the Landau-Lifshitz convention, commonly adopted for relativistic mechanics. The other convention, named Lorentian convention, adopts the signature $(-,+,+,+)$ and is used for problems involving particle physics.

For the propagation of a photon in the gravitational field both the signatures can be adopted, because the photon follows the null geodetics path $ds^2 = 0$.

2.5.1 On the Bending of Electromagnetic Waves in Atmosphere

Considering that the metric tensor (2.112) is diagonal, then the summation over the index s in (2.106) is as in (2.116).

$$\Gamma^u_{vw} = g^{us}\Gamma_{s,vw} = g^{uu}\Gamma_{u,vw} \tag{2.116}$$

From the (2.116), the (2.106) can be rewritten as in (2.117), where summation has been omitted for mute indices v and w.

$$\frac{d^2x^u}{d\tau^2}+\frac{1}{2}g^{uu}\left(\frac{\partial g_{uv}}{\partial x^w}+\frac{\partial g_{uw}}{\partial x^v}-\frac{\partial g_{vw}}{\partial x^u}\right)\frac{dx^v}{d\tau}\frac{dx^w}{d\tau}=0, \qquad u=1,2,3 \tag{2.117}$$

It can be noticed that in (2.117), given two indices i and j, the derivatives of the metric tensor g_{ij} is always with respect to the third indices k and it can be computed as in (2.118).

$$\frac{\partial g_{ij}}{\partial x^k}=\frac{\partial\left(\left(\frac{n}{c}\right)^2\delta_{ij}\right)}{\partial x^k}=\frac{1}{c^2}\frac{\partial n^2}{\partial x^k}\delta_{ij}=\frac{2n}{c^2}\frac{\partial n}{\partial x^k}\delta_{ij} \tag{2.118}$$

Substituting the values of the metric tensor g and its derivatives, the (2.117) becomes as in (2.119).

$$\frac{d^2x^u}{d\tau^2}+\frac{1}{2}\left(\frac{c}{n}\right)^2\frac{2n}{c^2}\left(\frac{\partial n}{\partial x^w}\delta_{uv}+\frac{\partial n}{\partial x^v}\delta_{uw}-\frac{\partial n}{\partial x^u}\delta_{vw}\right)\frac{dx^v}{d\tau}\frac{dx^w}{d\tau}=0, \qquad u=1,2,3 \tag{2.119}$$

Writing the sums for indices v and w, the (2.119) becomes as in (2.120) or, separating the sums, as in (2.121).

$$\frac{d^2x^u}{d\tau^2}+\frac{1}{n}\sum_{v=1}^{3}\sum_{w=1}^{3}\left(\left(\frac{\partial n}{\partial x^w}\delta_{uv}+\frac{\partial n}{\partial x^v}\delta_{uw}-\frac{\partial n}{\partial x^u}\delta_{vw}\right)\frac{dx^v}{d\tau}\frac{dx^w}{d\tau}\right)=0, \qquad u=1,2,3 \tag{2.120}$$

$$\begin{gathered}\frac{d^2x^u}{d\tau^2}+\frac{1}{n}\sum_{v=1}^{3}\sum_{w=1}^{3}\left(\frac{\partial n}{\partial x^w}\delta_{uv}\frac{dx^v}{d\tau}\frac{dx^w}{d\tau}\right)+\frac{1}{n}\sum_{v=1}^{3}\sum_{w=1}^{3}\left(\frac{\partial n}{\partial x^v}\delta_{uw}\frac{dx^v}{d\tau}\frac{dx^w}{d\tau}\right)\\ -\frac{1}{n}\sum_{v=1}^{3}\sum_{w=1}^{3}\left(\frac{\partial n}{\partial x^u}\delta_{vw}\frac{dx^v}{d\tau}\frac{dx^w}{d\tau}\right)=0, \qquad u=1,2,3\end{gathered} \tag{2.121}$$

The first couple of sums in (2.121) have nonzero terms if $v=u$, then it can be simplified as in (2.122).

$$\sum_{v=1}^{3}\sum_{w=1}^{3}\left(\frac{\partial n}{\partial x^w}\delta_{uv}\frac{dx^v}{d\tau}\frac{dx^w}{d\tau}\right)=\sum_{w=1}^{3}\left(\frac{\partial n}{\partial x^w}\frac{dx^u}{d\tau}\frac{dx^w}{d\tau}\right)=\frac{dx^u}{d\tau}\sum_{w=1}^{3}\left(\frac{\partial n}{\partial x^w}\frac{dx^w}{d\tau}\right) \tag{2.122}$$

The second couple of sums in (2.121) have nonzero terms if $w=u$, then it can be simplified as in (2.123).

$$\sum_{v=1}^{3}\sum_{w=1}^{3}\left(\frac{\partial n}{\partial x^v}\delta_{uw}\frac{dx^v}{d\tau}\frac{dx^w}{d\tau}\right)=\sum_{v=1}^{3}\left(\frac{\partial n}{\partial x^v}\frac{dx^v}{d\tau}\frac{dx^u}{d\tau}\right)=\frac{dx^u}{d\tau}\sum_{v=1}^{3}\left(\frac{\partial n}{\partial x^v}\frac{dx^v}{d\tau}\right) \tag{2.123}$$

The third couple of sums in (2.121) have nonzero terms if $v=w=i$, then it can be simplified as in (2.124).

$$\begin{aligned}\sum_{v=1}^{3}\sum_{w=1}^{3}\left(\frac{\partial n}{\partial x^u}\delta_{vw}\frac{dx^v}{d\tau}\frac{dx^w}{d\tau}\right)&=\sum_{i=1}^{3}\left(\frac{\partial n}{\partial x^u}\frac{dx^i}{d\tau}\frac{dx^i}{d\tau}\right)=\frac{\partial n}{\partial x^u}\sum_{i=1}^{3}\left(\frac{dx^i}{d\tau}\right)^2\\ &=\frac{\partial n}{\partial x^u}\left(\left(\frac{dx^u}{d\tau}\right)^2+\left(\frac{dx^v}{d\tau}\right)^2+\left(\frac{dx^w}{d\tau}\right)^2\right)\end{aligned} \tag{2.124}$$

Replacing (2.122), (2.123), and (2.124) into (2.121), the (2.125) is obtained.

$$\begin{gathered}\frac{d^2x^u}{d\tau^2}+\frac{1}{n}\frac{dx^u}{d\tau}\sum_{w=1}^{3}\left(\frac{\partial n}{\partial x^w}\frac{dx^w}{d\tau}\right)+\frac{1}{n}\frac{dx^u}{d\tau}\sum_{v=1}^{3}\left(\frac{\partial n}{\partial x^v}\frac{dx^v}{d\tau}\right)\\ -\frac{1}{n}\frac{\partial n}{\partial x^u}\left(\left(\frac{dx^u}{d\tau}\right)^2+\left(\frac{dx^v}{d\tau}\right)^2+\left(\frac{dx^w}{d\tau}\right)^2\right)=0, \qquad u=1,2,3\end{gathered} \tag{2.125}$$

Expanding the sums, (2.125) becomes as in (2.126).

$$\begin{aligned}&\frac{d^2x^u}{d\tau^2}+\frac{1}{n}\left(\frac{\partial n}{\partial x^u}\left(\frac{dx^u}{d\tau}\right)^2-\frac{\partial n}{\partial x^u}\left(\frac{dx^v}{d\tau}\right)^2-\frac{\partial n}{\partial x^u}\left(\frac{dx^w}{d\tau}\right)^2\right.\\&\quad\left.+2\frac{\partial n}{\partial x^v}\frac{dx^u}{d\tau}\frac{dx^v}{d\tau}+2\frac{\partial n}{\partial x^w}\frac{dx^u}{d\tau}\frac{dx^w}{d\tau}\right)=0,\qquad u=1{,}2{,}3\end{aligned}\tag{2.126}$$

Compacting the notation considering (2.127), the system of equation in (2.128) is obtained.

$$\begin{aligned}\ddot{x}&=\frac{d^2x^u}{d\tau^2},\quad &\ddot{y}&=\frac{d^2x^v}{d\tau^2},\quad &\ddot{z}&=\frac{d^2x^w}{d\tau^2},\\\dot{x}&=\frac{dx^u}{d\tau},\quad &\dot{y}&=\frac{dx^v}{d\tau},\quad &\dot{z}&=\frac{dx^w}{d\tau}\\n_x&=\frac{\partial n}{\partial x^u},\quad &n_y&=\frac{\partial n}{\partial x^v},\quad &n_z&=\frac{\partial n}{\partial x^w}\end{aligned}\tag{2.127}$$

$$\begin{cases}\ddot{x}+\frac{1}{n}\left(n_x\dot{x}\dot{x}-n_x\dot{y}\dot{y}-n_x\dot{z}\dot{z}+2n_y\dot{x}\dot{y}+2n_z\dot{x}\dot{z}\right)=0\\\ddot{y}+\frac{1}{n}\left(n_y\dot{y}\dot{y}-n_y\dot{x}\dot{x}-n_y\dot{z}\dot{z}+2n_x\dot{y}\dot{x}+2n_z\dot{y}\dot{z}\right)=0\\\ddot{z}+\frac{1}{n}\left(n_z\dot{z}\dot{z}-n_z\dot{x}\dot{x}-n_z\dot{y}\dot{y}+2n_x\dot{z}\dot{x}+2n_y\dot{z}\dot{y}\right)=0\end{cases}\tag{2.128}$$

To solve the system in (2.128), initial conditions and a field of the refraction index n are needed.

To complete the model, two additional quantities need to be considered: the arrival surface and the interval of time Δt employed for the integration of the equations.

Depending on their roles, two problems can be formulated:

- If the arrival surface is known, then it can be used as boundary condition and the problem becomes a Boundary Value Problem (BVP). In this case the interval of time is an additional unknown.

- If the interval of time is known from external considerations, then it is possible to solve the problem as an Initial Value Problem (IVP). In this case the point of arrival of the photon is the unknown that is calculated.

Here, the second strategy is considered. The evaluation of the time delay Δt has to be considered as a priori knowledge to be calculated as presented in the previous subsections with different levels of detail: a Newtonian approach [27], a relativistic approach [28], and considering the slowdown due to the presence of the atmosphere [6]..

In order to solve the problem in (2.128), initial conditions are needed on the values of the position and velocity for the spatial coordinates at the instant of time $\tau = 0$ and in the following denoted with the subscript 0, as reported in (2.129).

$$\begin{cases} x\left(\tau = 0\right) = x_0 \\ y\left(\tau = 0\right) = y_0 \\ z\left(\tau = 0\right) = z_0 \\ \dot{x}\left(\tau = 0\right) = \dot{x}_0 \\ \dot{y}\left(\tau = 0\right) = \dot{y}_0 \\ \dot{z}\left(\tau = 0\right) = \dot{z}_0 \end{cases} \tag{2.129}$$

The values of the coordinates $\mathbf{x}_0 = \left(x_0, y_0, z_0\right)^{\mathrm{T}}$ define the initial starting point of the propagation of the photon, while the $\dot{\mathbf{x}}_0 = \left(\dot{x}_0, \dot{y}_0, \dot{z}_0\right)^{\mathrm{T}}$ define the initial velocity.

The physical situation is the propagation from the emitter of signal $\mathbf{x}_{\mathrm{E}}$ to the satellite platform $\mathbf{x}_{\mathrm{S}}$. However, considering that the point of view of the study is the reception by satellite platform, and considering that it is of interest the backward reconstruction of the path of the photon, the initial point is set to the satellite platform $\mathbf{x}_{\mathrm{S}}$ where the back-propagation is supposed to happen.

This means also that the equations (2.128) need to be rewritten with a transformation on time $\tau \to -\tau$. Luckily, the equations of geodesics are invariant, because τ can be viewed as an affine parameter, so the orientation of the curve can be changed without changing its orientation.

In this case, it is possible to assume the satellite platform as the initial position $\mathbf{x}_{\mathrm{S}} = \mathbf{x}_0 = \left(x_0, y_0, z_0\right)^{\mathrm{T}}$

Furthermore, it can be noticed that for the magnitude of initial velocity $\dot{\mathbf{x}}_0$, the expression in (2.130) is valid.

$$\left\|\dot{\mathbf{x}}_0\right\| = \sqrt{\left(\dot{x}_0\right)^2 + \left(\dot{y}_0\right)^2 + \left(\dot{z}_0\right)^2} = c \tag{2.130}$$

Considering that for a payload with AOA technology the measurement is a measurements of direction, then it is possible to say that the initial direction of the propagation is the one detected by the AOA measurement, defined in (3.1); with this established, (2.131) follows.

$$\dot{\mathbf{x}}_0 \parallel \mathbf{v}_{\mathrm{LOB}} \tag{2.131}$$

Combining the information on the magnitude of the initial velocity in (2.130) and the information on its direction in (2.131), it follows that the initial velocity $\dot{\mathbf{x}}_0$ vector must be the one defined in (2.132).

$$\dot{\mathbf{x}}_0 = c\mathbf{v}_{\mathrm{LOB}} \tag{2.132}$$

The components of the initial conditions for the back-propagation are summarized in (2.133).

$$\begin{cases} x\left(\tau=0\right)=x_0=x_{\mathrm{S}} \\ y\left(\tau=0\right)=y_0=y_{\mathrm{S}} \\ z\left(\tau=0\right)=z_0=z_{\mathrm{S}} \\ \dot{x}\left(\tau=0\right)=\dot{x}_0=c\dfrac{\left(\hat{x}_{\mathrm{E}}-x_{\mathrm{S}}\right)}{\sqrt{\left(\hat{x}_{\mathrm{E}}-x_{\mathrm{S}}\right)^2+\left(\hat{y}_{\mathrm{E}}-y_{\mathrm{S}}\right)^2+\left(\hat{z}_{\mathrm{E}}-z_{\mathrm{S}}\right)^2}} \\ \dot{y}\left(\tau=0\right)=\dot{y}_0=c\dfrac{\left(\hat{y}_{\mathrm{E}}-y_{\mathrm{S}}\right)}{\sqrt{\left(\hat{x}_{\mathrm{E}}-x_{\mathrm{S}}\right)^2+\left(\hat{y}_{\mathrm{E}}-y_{\mathrm{S}}\right)^2+\left(\hat{z}_{\mathrm{E}}-z_{\mathrm{S}}\right)^2}} \\ \dot{z}\left(\tau=0\right)=\dot{z}_0=c\dfrac{\left(\hat{z}_{\mathrm{E}}-z_{\mathrm{S}}\right)}{\sqrt{\left(\hat{x}_{\mathrm{E}}-x_{\mathrm{S}}\right)^2+\left(\hat{y}_{\mathrm{E}}-y_{\mathrm{S}}\right)^2+\left(\hat{z}_{\mathrm{E}}-z_{\mathrm{S}}\right)^2}} \end{cases} \tag{2.133}$$

2.5.2 Numerical Implementation of the Equations

This section is intended to report to the reader a possible simulation approach for the problem defined in (2.128), with conditions defined in (2.133), and a model of the refraction index in (2.86) and (2.88).

The simulations are conducted in MATLAB 2024a environment with academic license.

The problem with differential equations in (2.128) is an Initial Value Problem (IVP), which can be solved within the more general set of methods based on the mass matrix formulation.

In particular, it is possible to define the problem as in (2.134), where $\mathbf{q}$ is the vector of the state variables, $\mathbf{M}$ is the mass matrix, and t is the time.

$$\mathbf{M}\left(t,\mathbf{q}\right)\dot{\mathbf{q}}=f\left(t,\mathbf{q}\right) \tag{2.134}$$

Generally, two choices are possible: $\mathbf{q}=\left(q_1,q_2,q_3,q_4,q_5,q_6\right)^{\mathrm{T}}=\left(x,y,z,\dot{x},\dot{y},\dot{z}\right)^{\mathrm{T}}$ and $\mathbf{q}=\left(q_1,q_2,q_3,q_4,q_5,q_6\right)^{\mathrm{T}}=\left(x,\dot{x},y,\dot{y},z,\dot{z}\right)^{\mathrm{T}}$, which differ only for the ordering of the elements.

Following the convention $\mathbf{q}=\left(q_1,q_2,q_3,q_4,q_5,q_6\right)^{\mathrm{T}}=\left(x,y,z,\dot{x},\dot{y},\dot{z}\right)^{\mathrm{T}}$, it results the relationships in (2.135).

$$\begin{cases} \dot{q}_1 = q_4 \\ \dot{q}_2 = q_5 \\ \dot{q}_3 = q_6 \\ \dot{q}_4 = f\left(\dot{q}_1, \dot{q}_2, \dot{q}_3\right) = f\left(q_4, q_5, q_6\right) \\ \dot{q}_5 = f\left(\dot{q}_1, \dot{q}_2, \dot{q}_3\right) = f\left(q_4, q_5, q_6\right) \\ \dot{q}_6 = f\left(\dot{q}_1, \dot{q}_2, \dot{q}_3\right) = f\left(q_4, q_5, q_6\right) \end{cases} \tag{2.135}$$

With the choice of state variables as in (2.135), it results that the mass matrix **M** does not depend on time and, in particular, it has constant unitary values, so the problem can be written as in (2.136).

$$\begin{bmatrix} 1 & 0 & 0 & 0 & 0 & 0 \\ 0 & 1 & 0 & 0 & 0 & 0 \\ 0 & 0 & 1 & 0 & 0 & 0 \\ 0 & 0 & 0 & 1 & 0 & 0 \\ 0 & 0 & 0 & 0 & 1 & 0 \\ 0 & 0 & 0 & 0 & 0 & 1 \end{bmatrix} \begin{pmatrix} \dot{q}_1 \\ \dot{q}_2 \\ \dot{q}_3 \\ \dot{q}_4 \\ \dot{q}_5 \\ \dot{q}_6 \end{pmatrix} = \begin{pmatrix} q_4 \\ q_5 \\ q_6 \\ f\left(q_4, q_5, q_6\right) \\ f\left(q_4, q_5, q_6\right) \\ f\left(q_4, q_5, q_6\right) \end{pmatrix} \tag{2.136}$$

The solution of the equations has been obtained considering different numerical schemes, ranging from the simple trapezoidal rule to higher order sophisticated implementations of Runge-Kutta schemes: details and comparison of the methods are reported in the following subsections.

The derivatives of the refractive index n in a given point $\mathbf{x}$ have been coded considering a set of first-order central-difference scheme, as shown in (2.137) and (2.138).

$$\begin{aligned} \frac{\partial n}{\partial x} &\approx \frac{n\left(\mathbf{x} + \Delta\mathbf{x}_1\right) - n\left(\mathbf{x} - \Delta\mathbf{x}_1\right)}{2\Delta x} \\ \frac{\partial n}{\partial y} &\approx \frac{n\left(\mathbf{x} + \Delta\mathbf{x}_2\right) - n\left(\mathbf{x} - \Delta\mathbf{x}_2\right)}{2\Delta y} \\ \frac{\partial n}{\partial z} &\approx \frac{n\left(\mathbf{x} + \Delta\mathbf{x}_3\right) - n\left(\mathbf{x} - \Delta\mathbf{x}_3\right)}{2\Delta z} \end{aligned} \tag{2.137}$$

$$\begin{aligned}
\Delta\mathbf{x}_1 &= \begin{pmatrix}\Delta x\\0\\0\end{pmatrix}\\
\Delta\mathbf{x}_2 &= \begin{pmatrix}0\\\Delta y\\0\end{pmatrix}\\
\Delta\mathbf{x}_3 &= \begin{pmatrix}0\\0\\\Delta z\end{pmatrix}\\
\Delta x &= \Delta y = \Delta z
\end{aligned} \tag{2.138}$$

In this study, higher order schemes for the derivatives of the refractive index n have not been investigated.

The results of the numerical integration are compared with straight propagation without atmosphere, which is supposed to happen in an interval of time Δt as in (2.139).

$$\Delta t = \frac{\|\hat{\mathbf{x}}_{\mathrm{E}} - \mathbf{x}_{\mathrm{S}}\|}{c} \tag{2.139}$$

The interval of time Δt has been used to terminate the integration of the equations in (2.128) with conditions in (2.133). In particular, given $\hat{\mathbf{x}}_{\mathrm{E,b}}$ the result of the integration, which is the new estimation of the position of the emitter of signal taking into account the effect of the bending of the electromagnetic waves, two main quantities are calculated: the linear error e_{d} defined as the distance between the two estimations (2.140), and the angular error ϕ_{d}, defined as in (2.141).

$$e_{\mathrm{d}} = \|\hat{\mathbf{x}}_{\mathrm{E,b}} - \hat{\mathbf{x}}_{\mathrm{E}}\| \tag{2.140}$$

$$\phi_{\mathrm{d}} = \arctan\left(\frac{\|\hat{\mathbf{x}}_{\mathrm{E,b}} - \hat{\mathbf{x}}_{\mathrm{E}}\|}{\|\hat{\mathbf{x}}_{\mathrm{S}} - \hat{\mathbf{x}}_{\mathrm{E}}\|}\right) \tag{2.141}$$

The evaluation of ϕ_{d} in (2.141) is valid as long as $\|\hat{\mathbf{x}}_{\mathrm{E,b}} - \hat{\mathbf{x}}_{\mathrm{E}}\| \ll \|\mathbf{x}_{\mathrm{S}} - \mathbf{x}_{\mathrm{E}}\|$ and $\|\hat{\mathbf{x}}_{\mathrm{E,b}} - \hat{\mathbf{x}}_{\mathrm{E}}\| \ll \|\mathbf{x}_{\mathrm{S}} - \hat{\mathbf{x}}_{\mathrm{E,b}}\|$ and assuming $\angle E \to \pi/2$ and $\angle E_{\mathrm{b}} \to \pi/2$. Then it is possible to say that $\|\hat{\mathbf{x}}_{\mathrm{E,b}} - \hat{\mathbf{x}}_{\mathrm{E}}\| = \sin(\phi_{\mathrm{d}})$ and $\|\mathbf{x}_{\mathrm{S}} - \mathbf{x}_{\mathrm{E}}\| = \cos(\phi_{\mathrm{d}})$, with the arctangent coming from their ratio[3].

---

[3] In theory, the most correct way to evaluate the angular error is

$$\phi_{\mathrm{d}} = \cos\left(\frac{(\mathbf{x}_{\mathrm{S}} - \mathbf{x}_{\mathrm{E}})}{\|\mathbf{x}_{\mathrm{S}} - \mathbf{x}_{\mathrm{E}}\|} \cdot \frac{(\mathbf{x}_{\mathrm{S}} - \hat{\mathbf{x}}_{\mathrm{E,b}})}{\|\mathbf{x}_{\mathrm{S}} - \hat{\mathbf{x}}_{\mathrm{E,b}}\|}\right) \tag{2.142}$$

.

The simulations presented in this section were performed before this illumination.

Fig. 2.27 shows the simulative workflow to calculate the linear error e_d and angular error ϕ_d.

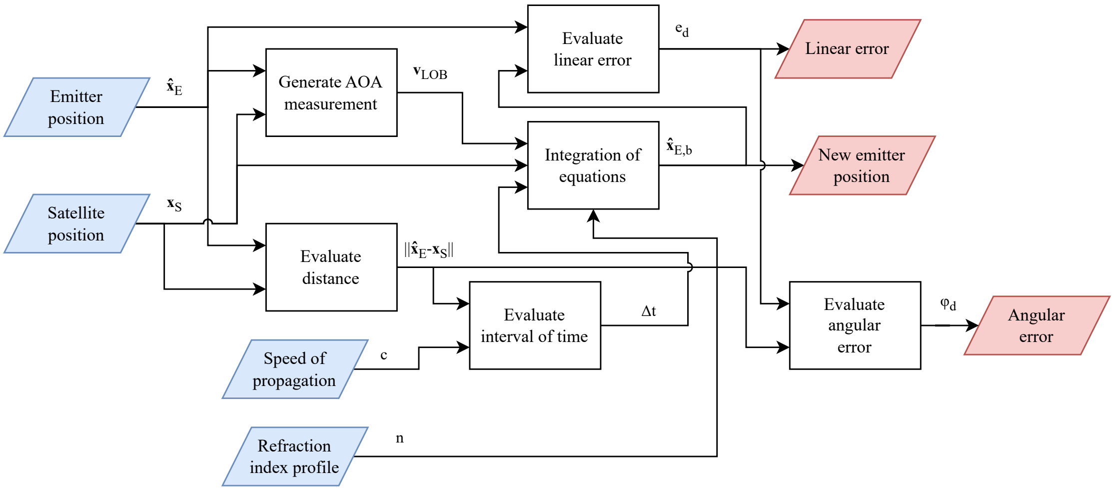

Figure 2.27: Workflow to simulate the bending of the electromagnetic waves and to calculate the linear error e_d and angular error ϕ_d.

In Fig. 2.28 is reported a possible scheme of onboard estimation of the linear error e_d and angular error ϕ_d considering only the available information onboard the satellite system.

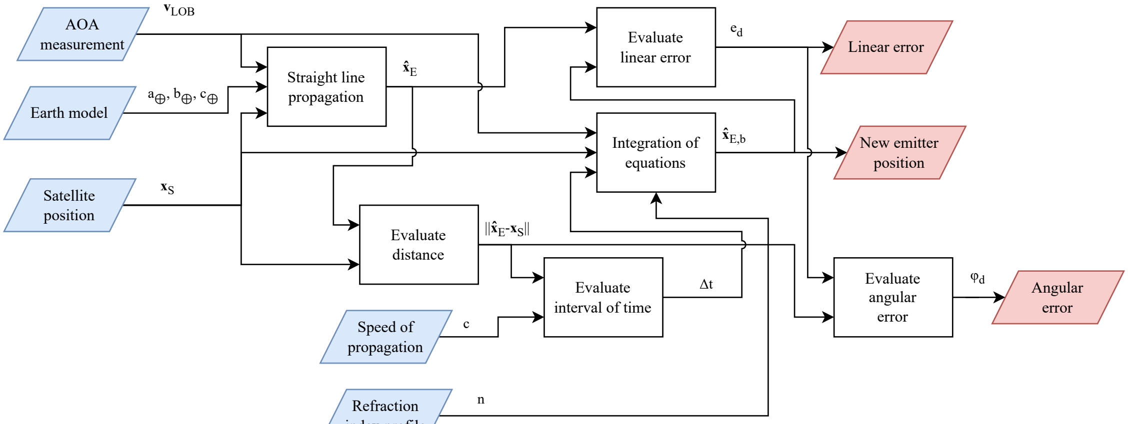

Figure 2.28: Workflow for onboard estimation of the linear error e_d and angular error ϕ_d due to the bending of the electromagnetic waves.

In order to employ the scheme in Fig. 2.28, straight line propagation must be performed solving the geometric problem of the intersection of the ellipsoid of the Earth and the Line of Bearing (AOA measurement), as shown in (1.20).

The linear error e_d can be of interest to have an idea of the error of geolocation in the position of the emitter of signal on the surface of the Earth.

The angular error ϕ_d can be used for a first-level scheme of compensation, to be performed onboard of the satellite.

The evaluation in Fig. 2.28 can be used to compensate the contribution of the error due to the bending of electromagnetic waves for satellite payloads involving AOA measurements.

In the evaluation of the interval of time of integration Δt, the approach considered in this study involved a Newtonian mechanics and constant propagation of the signal c. This implementation can be useful for performance analysis (i.e., to compare $\hat{\mathbf{x}}_{\mathrm{E,b}}$ and $\hat{\mathbf{x}}_\mathrm{E}$) and to build a first-level schemes of compensation. Real implementations and evaluations must take into account second order effects due to the corrections on time delay Δt with relativistic mechanics and slowdown due to the atmosphere.

The author want to warn the reader that the phenomenon related to the apparent shift in the longitude of the emitter of signal due to the rotation of the Earth has to be considered. Furthermore, another phenomenon to be considered is the presence of turbulence, supposed to be absent in this study.

A comprehensive model which considers all the effects together, i.e. bending of electromagnetic waves, shift in longitude, relativistic effects, slowdown, and turbulence is left for future studies.

2.5.3 Working Solvers

To check what are the possible working solvers, analyses are conducted in a test case consisting in an emitter of signal placed in $\Lambda = 0°$, $\lambda = 0°$, and $h_\mathrm{E} = 0$ m and a satellite with the following data $h_\mathrm{S} = 500$ km, $e = 0$, $i = 90°$, $\Omega = 0°$, and $\omega = 0°$.

The value of the true anomaly ν has been selected considering the possibility to check different relative configurations; three cases are considered: a Nadir angle of $\delta_\mathrm{N} = 0°$ (corresponding to a true anomaly $\nu = 0°$ for a satellite in $h_\mathrm{S} = 500$ km), a Nadir angle of $\delta_\mathrm{N} = 20°$ (corresponding to a true anomaly $\nu = 1.510463225225310°$ for a satellite in $h_\mathrm{S} = 500$ km), and a Nadir angle of $\delta_\mathrm{N} = 40°$ (corresponding to a true anomaly $\nu = 3.415176409675859°$ for a satellite in $h_\mathrm{S} = 500$ km).

All the three testing cases do not violate the Line of Sight condition with respect to the surface of the Earth.

For this first explorative analysis, used to check the working solvers, the default settings for the tolerances have been considered with values of $T_\mathrm{a} = 10^{-6}$ for the absolute tolerance and $T_\mathrm{r} = 10^{-3}$ for the relative tolerance.

Available solvers are the following:

`ode23t` trapezoidal rule using a free interpolant;
`ode23tb` implicit Runge-Kutta formula with a trapezoidal rule step as its first stage and a backward differentiation formula of order 2 as its second stage;
`ode23` Runge-Kutta (2,3) pair;
`ode45` Runge-Kutta (4,5) pair;

`ode78` Runge-Kutta 8(7) pair with a 7th-order continuous extension;
`ode89` Runge-Kutta 9(8) pair with a 8th-order continuous extension;
`ode113` Variable-step, variable-order (VSVO) solver of orders 1 to 13;
`ode15s` Variable-step, variable-order (VSVO) solver based on the numerical differentiation formulas (NDFs) of orders 1 to 5;
`ode23s` modified Rosenbrock formula of order 2;
`cvodesNonstiff` Variable-step, variable-order (VSVO) solver using Adams-Moulton formulas, with the order varying between 1 and 12;
`cvodesStiff` Variable-step, variable-order (VSVO) solver using Backward Differentiation Formulas (BDFs) in fixed-leading coefficient form, with order varying between 1 and 5. Supports sensitivity analysis;
`idas` Variable-order, variable-coefficient solver using Backward Differentiation Formulas (BDFs) in fixed-leading coefficient form, with order varying between 1 and 5.

Results are reported in Tab. 2.6.

Table 2.6: Comparison of numerical solvers.

Solver	Does it work?
`ode15s`	Yes
`ode23t`	Yes
`idas`	Yes
`ode23tb`	Yes (with a warning)
`ode23`	Yes (with a warning)
`ode45`	Yes (with a warning)
`ode78`	Yes (with a warning)
`ode89`	Yes (with a warning)
`ode113`	Yes (with a warning)
`ode23s`	No (to check with further investigations)
`cvodesNonstiff`	No
`cvodesStiff`	No

In particular, the warning raised by the software when `ode23`, `ode45`, `ode78`, `ode89`, `ode113`, and `ode23tb` are employed is related to the possibility that the mass matrix could be singular. However, as written in 2.5.2, the mass matrix is an identity matrix, so this concern can be neglected; these set of solvers are suitable for the problem as formulated in this study and, from the experience of the author, the results are proven to be correct.

The solvers `cvodesNonstiff` and `cvodesStiff` do not work because they do not support problems formulated with a mass matrix.

The solver `ode23s` gave an unexpected behaviour and the software refused to execute this particular solver: from the documentation of MATLAB 2024a, the solver should support constant mass matrices. The author suggest further investigations on the possibility of employing this solver.

2.5.4 Influence of Absolute and Relative Tolerances

This subsection is intended to explore the influence of the absolute and relative tolerances on the solution and on the number of points generated for the spatial mesh.

Simulations conducted in this battery of tests are related to an emitter of signal placed in $\Lambda = 0°$, $\lambda = 0°$, and $h_{\mathrm{E}} = 0$ m and a satellite with the following data $h_{\mathrm{S}} = 500$ km, $e = 0$, $i = 90°$, $\Omega = 0°$, and $\omega = 0°$, and $\nu = 3.415176409675859°$ (corresponding to a satellite with a Nadir angle of $\delta_{\mathrm{N}} = 40°$ with respect to the emitter).

In Tab. 2.7 results in terms of number of points of the mesh N_{m} and angular error ϕ_{d} are reported for the solver `ode23t`; similar results are obtained for other solvers.

Table 2.7: Influence of absolute and relative tolerances.

Tolerances	N_{m}	ϕ_{d} [rad]
$T_{\mathrm{a}} = 10^{-6}$, $T_{\mathrm{r}} = 10^{-6}$	22	$6.853520463316711 \cdot 10^{-6}$
$T_{\mathrm{a}} = 10^{-9}$, $T_{\mathrm{r}} = 10^{-6}$	22	$6.853520463316711 \cdot 10^{-6}$
$T_{\mathrm{a}} = 10^{-12}$, $T_{\mathrm{r}} = 10^{-6}$	22	$6.853520463316711 \cdot 10^{-6}$
$T_{\mathrm{a}} = 10^{-6}$, $T_{\mathrm{r}} = 10^{-9}$	180	$6.426127670874709 \cdot 10^{-6}$
$T_{\mathrm{a}} = 10^{-9}$, $T_{\mathrm{r}} = 10^{-9}$	186	$6.426122204283874 \cdot 10^{-6}$
$T_{\mathrm{a}} = 10^{-12}$, $T_{\mathrm{r}} = 10^{-9}$	186	$6.426122204283874 \cdot 10^{-6}$
$T_{\mathrm{a}} = 10^{-6}$, $T_{\mathrm{r}} = 10^{-12}$	1709	$6.422979493908077 \cdot 10^{-6}$
$T_{\mathrm{a}} = 10^{-9}$, $T_{\mathrm{r}} = 10^{-12}$	1776	$6.422964494131494 \cdot 10^{-6}$
$T_{\mathrm{a}} = 10^{-12}$, $T_{\mathrm{r}} = 10^{-12}$	1856	$6.422964434470021 \cdot 10^{-6}$

From the results, it can be observed that the relative tolerance T_{r} has a high impact on both the value of the solution and mesh size; smaller values of the absolute tolerance T_{a}, compared to the default value of 10^{-6}, appear to be quite negligible and non-influent for this class of problems.

In particular, reducing the relative tolerance from T_{r} from 10^{-6} to 10^{-9} the precision appears to be guaranteed on the order of 10^{-5} rad, while increasing the relative tolerance from 10^{-9} to 10^{-12} the precision is guaranteed on the order of 10^{-8} rad.

Consequently, it is observed an increase on the number of points of an order of magnitude every time the relative tolerance is reduced by a factor of 10^{-3}.

2.5.5 A Comparison of the Solvers

A comparison of the most common solvers has been done considering as reference scenario the one composed of an emitter of signal placed in $\Lambda = 0°$, $\lambda = 0°$, and

$h_\mathrm{E} = 0$ m and a satellite with the following data $h_\mathrm{S} = 500$ km, $e = 0$, $i = 90°$, $\Omega = 0°$, and $\omega = 0°$, and $\nu = 3.415176409675859°$ (corresponding to a satellite with a Nadir angle of $\delta_\mathrm{N} = 40°$ with respect to the emitter).

For this campaign of tests, the tolerances are set to $T_\mathrm{a} = 10^{-12}$ and $T_\mathrm{r} = 10^{-12}$.

The results are reported in Tab. 2.8.

Table 2.8: Comparison of performances of the numerical solvers.

Solver	Execution time [s]	N_m	ϕ_d [rad]
`ode23t`	6.5693	1856	$6.422964434470021 \cdot 10^{-6}$
`ode45`	3.5699	605	$6.422945220467921 \cdot 10^{-6}$
`ode89`	64.1575	8737	$6.422945626840114 \cdot 10^{-6}$
`idas`	6.0099	616	$6.422952614808874 \cdot 10^{-6}$
`ode15s`	3.3534	498	$6.422949427427175 \cdot 10^{-6}$

The comparison of the solver shows first of all an agreement among the values of the solution up to the order of magnitude of 10^{-10} rad for the selected tolerances.

Furthermore, to solve this class of problems, it can be seen that the most efficient methods, both in terms of time and number of points on the mesh, are the VSVO `ode15s` or Runge-Kutta of medium order (4,5) pair `ode45`.

To meet the requirements of the tolerances, higher order Runge-Kutta, such as `ode89`, appear computationally too heavy both in terms of time and in terms of sampled points of the domain, without a significant change in the value of the solution and, therefore, are not suggested.

2.5.6 Validation of the Method

To validate the implementation of the equations, a comparison with existing data in the literature has been performed. To the knowledge of the author, there are not many public sources of similar solved problems available to the public.

In [46] a class of problems involving satellites in LEO are solved with an approximated method and considered as comparison for the validation.

The comparison is reported in Tab. 2.9 considering `ode15s` solver with tolerances of $T_\mathrm{a} = 10^{-12}$ and $T_\mathrm{r} = 10^{-12}$.

The test case considered an emitter of signal on the surface of the Earth with coordinates $\Lambda = 0°$, $\lambda = 0°$, and $h_\mathrm{E} = 0$ m and a satellite with the following data $h_\mathrm{S} = 500$ km, $e = 0$, $i = 90°$, $\Omega = 0°$, and $\omega = 0°$.

To compare the values with the data from the literature in [46], the values of true anomaly are calculated considering the application of Carnot theorem and following the geometrical problem described by the set of equations in (2.143) obtaining $\nu = 0.734366516798866°$ for an apparent Nadir angle of $\delta_\mathrm{N} = 10°$, $\nu = 1.510463225225310°$ for an apparent Nadir angle of $\delta_\mathrm{N} = 20°$, $\nu = 2.379363437096807°$ for an apparent Nadir angle of $\delta_\mathrm{N} = 30°$, $\nu = 3.415176409675859°$ for an apparent

Nadir angle of $\delta_{\mathrm{N}} = 40°$, $\nu = 4.740696107886172°$ for an apparent Nadir angle of $\delta_{\mathrm{N}} = 50°$, and $\nu = 6.364426723781293°$ for an apparent Nadir angle of $\delta_{\mathrm{N}} = 59°$.

$$\begin{gathered}\gamma = \pi - \delta_{\mathrm{N}} \\ d = \frac{1}{2}\left(2R_{\oplus}\cos(\gamma) \pm \sqrt{\left(2R_{\oplus}\cos(\gamma)\right)^2 + 4\left(r^2 - R_{\oplus}^2\right)}\right) \\ \nu = \arccos\left(\frac{R_{\oplus}^2 + r^2 - d^2}{2R_{\oplus}r}\right)\end{gathered} \tag{2.143}$$

In particular, among the two solutions given by the second equation in (2.143), the positive one must be considered.

Table 2.9: Validation of the numerical implementation of the equations.

δ_{N} [°]	ϕ_{d} [rad], current study	ϕ_{d} [rad], from [46]
10	$4.890481212616621 \cdot 10^{-6}$	$0.9 \cdot 10^{-6}$
20	$5.142346822696230 \cdot 10^{-6}$	$1.9 \cdot 10^{-6}$
30	$5.616022433064997 \cdot 10^{-6}$	$3.1 \cdot 10^{-6}$
40	$6.422949427427175 \cdot 10^{-6}$	$4.7 \cdot 10^{-6}$
50	$7.817958668548581 \cdot 10^{-6}$	$7.3 \cdot 10^{-6}$
59	$10.114674474882712 \cdot 10^{-6}$	$13.1 \cdot 10^{-6}$

The discrepancies in the lower and in the higher values between the two methods can be justified with the following points: the formulation of the angular error ϕ_{d}, which considers a right triangle $\triangle SE\hat{E}_{\mathrm{b}}$ with a right angle in E; an a priori fixed knowledge on the value of the time delay from the emitter E to the satellite S; the orientation of the target surface (i.e., the Earth) is neglected and assumed to be always perpendicular with respect to the direction of the signal.

2.5.7 Simulations

This subsection is intended to give a sensitivity analysis for a satellite in a circular orbit in LEO varying the main orbital parameters.

For a satellite in LEO the eccentricity is $e = 0$, the semi-major axis becomes coincident to the orbit radius $a = r$, while the argument of perigee becomes a meaningless quantity, conventionally posed to $\omega = 0$.

The simulations considered an emitter of signal on the surface of the Earth with coordinates $\Lambda = 0°$, $\lambda = 0°$, and $h_{\mathrm{E}} = 0$ m.

Fig. 2.29 and Fig. 2.30 show the values of the linear error e_{d} and angular error ϕ_{d} varying the radius of the orbit r and the true anomaly ν. Other parameters have been set to inclination $i = 90°$ and right ascension of the ascending node $\Omega = 2°$.

Fig. 2.31 and Fig. 2.32 show the values of the linear error e_{d} and angular error ϕ_{d} varying the inclination of the orbit i and the true anomaly ν. Other parameters

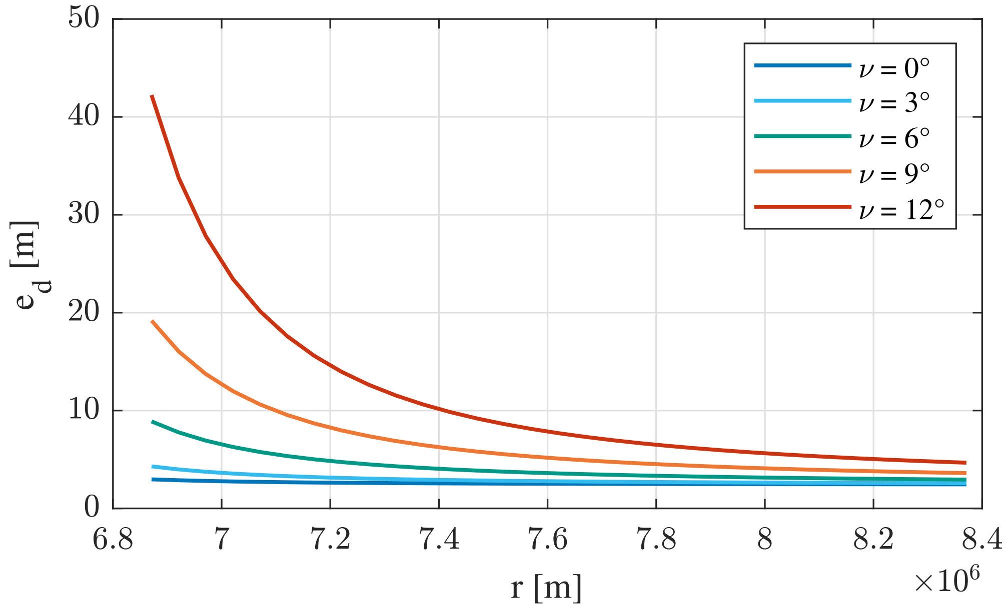

Figure 2.29: Values of the linear error e_d varying the radius of the orbit r and the true anomaly ν.

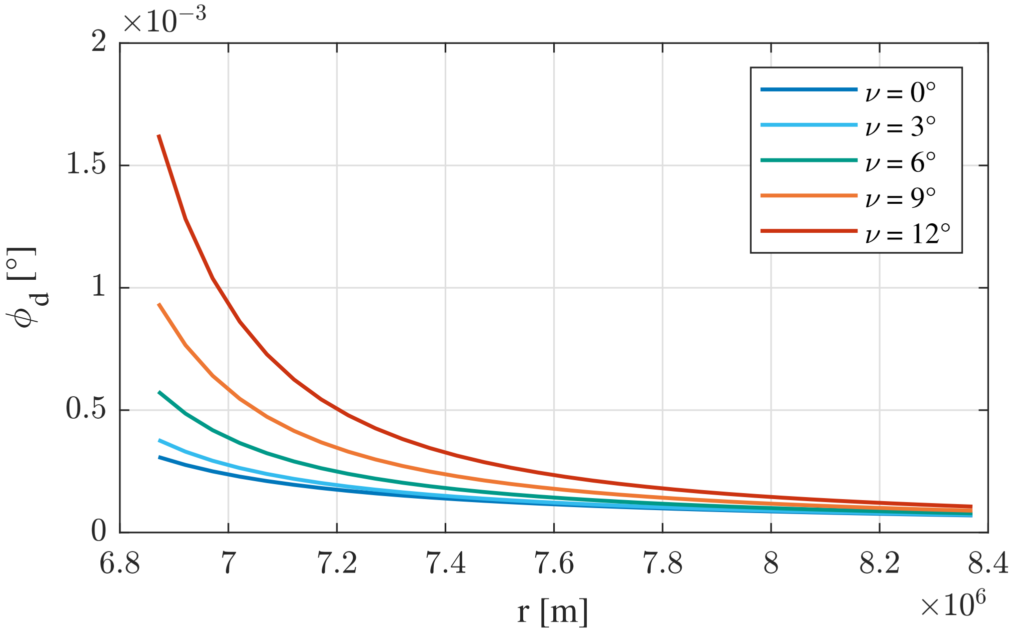

Figure 2.30: Values of the angular error ϕ_d varying the radius of the orbit r and the true anomaly ν.

have been set to orbit radius $r = 6871$ km (corresponding to a satellite at a height of 500 km) and right ascension of the ascending node $\Omega = 2°$.

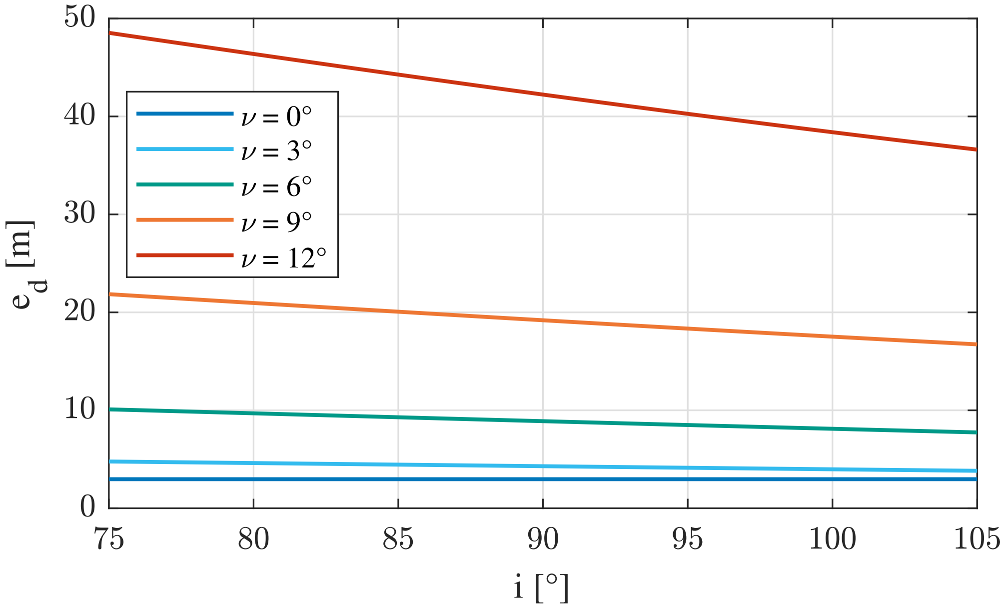

Figure 2.31: Values of the linear error e_d varying the inclination of the orbit r and the true anomaly ν.

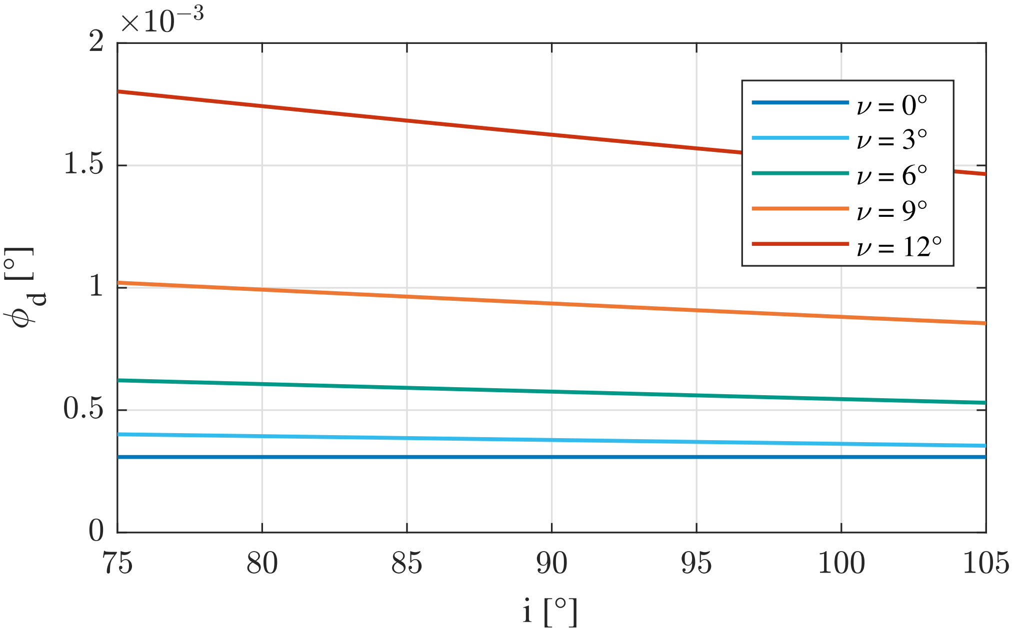

Figure 2.32: Values of the angular error ϕ_d varying the inclination of the orbit i and the true anomaly ν.

Fig. 2.33 and Fig. 2.34 show the values of the linear error e_{d} and angular error ϕ_{d} varying the right ascension of the ascending node of the orbit Ω and the true anomaly ν. Other parameters have been set to orbit radius $r = 6871$ km (corresponding to a satellite at a height of 500 km) and inclination $i = 0°$.

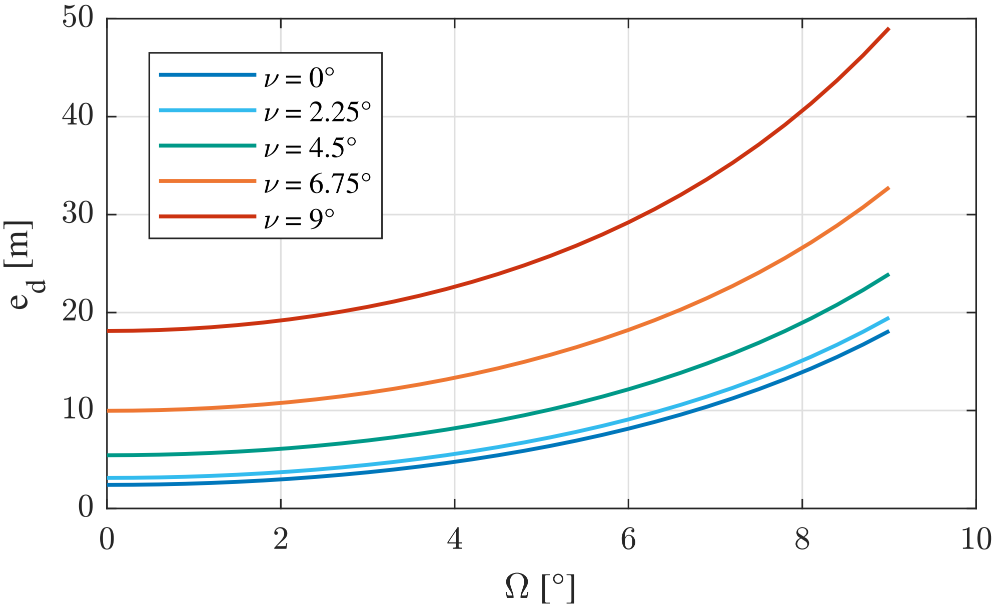

Figure 2.33: Values of the linear error e_{d} varying the right ascension of the ascending node of the orbit Ω and the true anomaly ν.

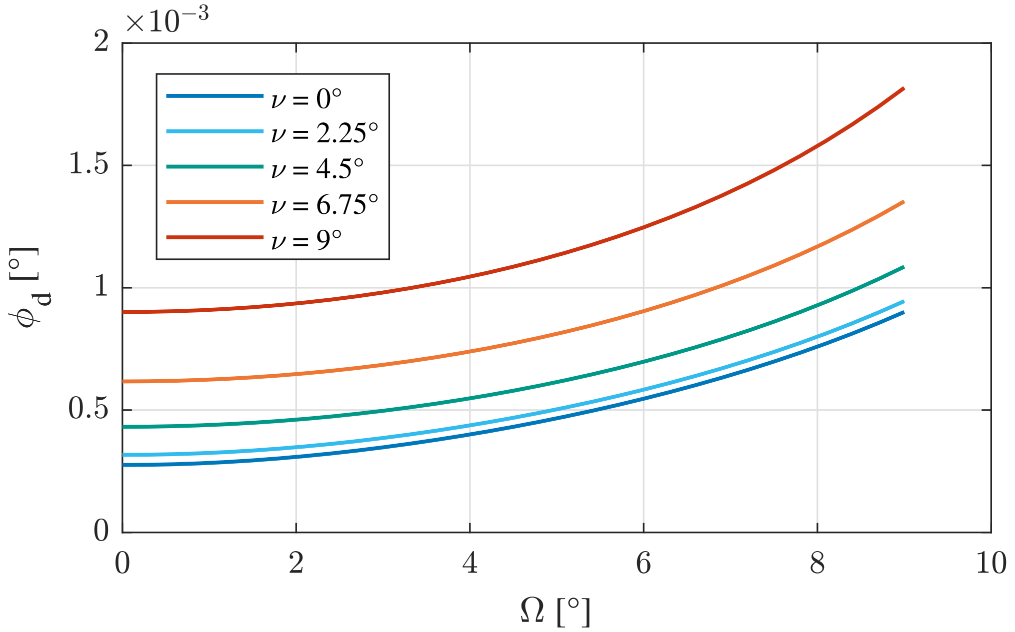

Figure 2.34: Values of the angular error ϕ_d varying the right ascension of the ascending node of the orbit Ω and the true anomaly ν.

2.6 Beam Wander

The set of activities and results presented in this section is unpublished[4] and must be considered in the context of didactic and formative experiences, complementary to all the other topics.

Among all optical phenomena, the study of the optics through atmosphere involves these phenomena: transmission, absorption, emission, refraction, and reflection. In general, the influence of the atmosphere happens through the interaction between the light and different molecular species and small particles like aerosols, water droplets, and ice particles [47]. The atmosphere is a fluid composed of gases and particles, and a useful macroscopic model to describe its composition and properties is the so-called *standard atmosphere*, which assumes that the gases are uniformly mixed with an homogeneous distribution. The main molecular constituents are N_2 (78.1 %) and O_2 (20.9 %) with traces of H_2O, CO_2, CH_4, N_2O, CO, and O_3. The propagation of the optical radiation is affected by the presence of aerosols (dust, haze) and water in the form of ice crystals or cloud droplets.

Phenomena related to the turbulence are connected to the fluctuations of refractive index. In particular, considering the visible and near-infrared spectrum, these fluctuations are due to the mixing of air at different temperatures. In the far-infrared spectrum, the fluctuations due to humidity have a contribution too. The variation of the path of the photon due to the influence of the turbulence is denoted as beam wander. The main interest and application are in space-optical communication with collimated lasers between a ground station (denoted in the following by G) and a satellite S. However, the phenomenon can be of interest also for electromagnetic waves taking into account some differences between the two cases.

The beam wander is a macroscopic manifestation of wavefront fluctuations induced by turbulence. When an electromagnetic wave passes through a medium with a variable refractive index (i.e., the atmosphere), the wavefront experiences a tilt (change in the slope of the wavefront), a variable curvature, and frequency aberrations. The beam wander is the result of low-frequency tilt of the wavefront. This means that the turbulence introduces small inclinations of the wavefront, and these inclinations cause the beam to be deflected laterally.

The beam wander angular variance can be modeled [48] as in (2.144), where D is the aperture diameter, F is the focal length, C_n^2 is the refraction index structure parameter, and H is the local height of the satellite.

---

[4] At the moment of writing, the submission of these results is not planned because there exist similar works on the topic; however, if it is not excluded to be happening in the future if these kind of parametric investigations become of interest.

$$\sigma_{\mathrm{BW}}^2 = 2.92 D^{-\frac{1}{3}} \int_0^H C_{\mathrm{n}}^2 (h) \frac{\left(1 - \frac{z(h)}{H}\right)^2}{\left|\frac{z(h)}{F}\right|^{\frac{1}{3}}} dh \tag{2.144}$$

$z(h)$ is a function of the height h and, for a spherical Earth, it can be calculated as in (2.145), where γ is the Zenith angle and $R_\oplus$ is the radius of the Earth.

$$z(h) = -R_\oplus \cos(\gamma) + \sqrt{R_\oplus^2 \cos^2(\gamma) + 2 R_\oplus h + h^2} \tag{2.145}$$

For preliminary evaluative studies, the assumption of collimated beam can be considered[5], which means that $F \to \infty$, so the (2.144) becomes as in (2.146).

$$\sigma_{\mathrm{BW}}^2 = 2.92 D^{-\frac{1}{3}} \int_0^H C_{\mathrm{n}}^2 (h) \left(1 - \frac{z(h)}{H}\right)^2 dh \tag{2.146}$$

To model the refractive index structure parameter C_{n}^2, the Hufnagel-Valley model [49] has been considered and reported in (2.147), in which v_{RMS} is the Root Mean Square (RMS) of the velocity of the wind in the atmosphere.

$$C_{\mathrm{n}}^2 (h, v_{\mathrm{RMS}}) = 0.00594 \left(\frac{v_{\mathrm{RMS}}}{27}\right)^2 \left(\frac{h}{10^5}\right)^{10} e^{\frac{-h}{1000}} + 2.7 \cdot 10^{-16} e^{\frac{-h}{1500}} + A e^{\frac{-h}{100}} \tag{2.147}$$

When $A = 1.7 \cdot 10^{-14}$ m/s$^{-2/3}$ and $v_{\mathrm{RMS}} = 21$ m/s, the model is denoted as H-V 7/5. For preliminary studies the aperture diameter D can be assumed as a varying parameter[6]. The Zenith angle can be calculated from geometrical considerations: given the positions of the ground station $\mathbf{x}_{\mathrm{G}}$ and the satellite $\mathbf{x}_{\mathrm{S}}$, it can be calculated as in (2.148).

$$\gamma = \arccos\left(\frac{\mathbf{x}_{\mathrm{G}}}{\|\mathbf{x}_{\mathrm{G}}\|} \cdot \frac{\mathbf{x}_{\mathrm{S}} - \mathbf{x}_{\mathrm{G}}}{\|\mathbf{x}_{\mathrm{S}} - \mathbf{x}_{\mathrm{G}}\|}\right) \tag{2.148}$$

---

[5] The assumption $F \to \infty$ is legit for optical rays and lasers employed in space communication technology, but a plane wave has a perfectly flat wavefront and parallel rays. In this case the curvature of the wavefront is zero and the radius of curvature tends to infinity. Therefore, it is possible to say that an 'equivalent focal length' is also infinite. An ideal plane wave can be considered as a beam with $F \to \infty$. It is a mathematical model of convenience, even if not physically realizable over infinite extensions. If a wavefront were perfectly flat, there would be no tilt, but in reality, turbulence introduces local curvature and inclinations, so the beam is never a 'perfect plane wave'.

[6] An ideal plane wave has an infinite equivalent aperture; in reality, the atmosphere still introduces tilt and wander. A generic electromagnetic wave has no intrinsic aperture, but an equivalent aperture can be defined as its transverse extension.

A MATLAB code has been written to predict the phenomenon of beam wander; the workflow of the simulative code is reported in Fig. 2.35. Results of parametric simulations are in Fig. 2.36, Fig. 2.37, and Fig. 2.38.

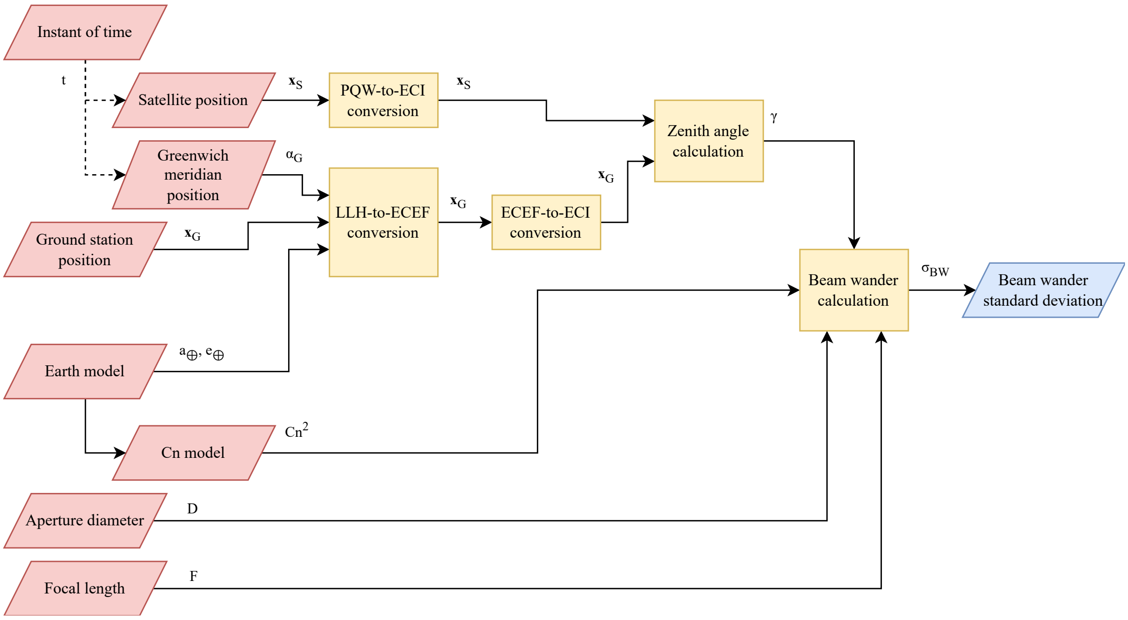

Figure 2.35: Scheme of computation of the beam wander standard deviation.

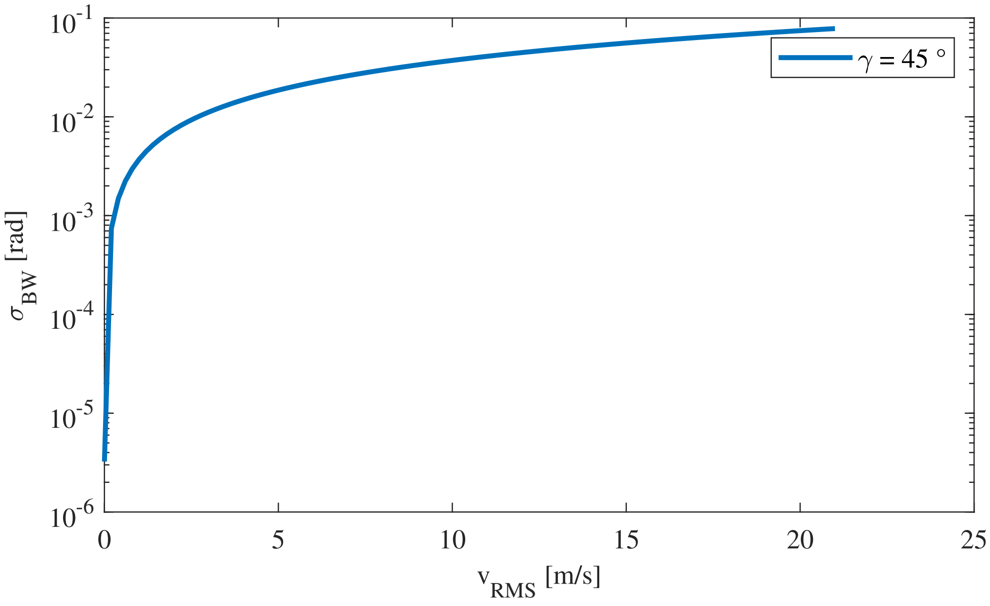

Figure 2.36: Values of beam wander standard deviation varying the velocity of the wind v_{RMS}. Satellite height $h_{\mathrm{S}} = 500$ km, aperture diameter $D = 0.2$ m, Zenith angle $\gamma = 45°$.

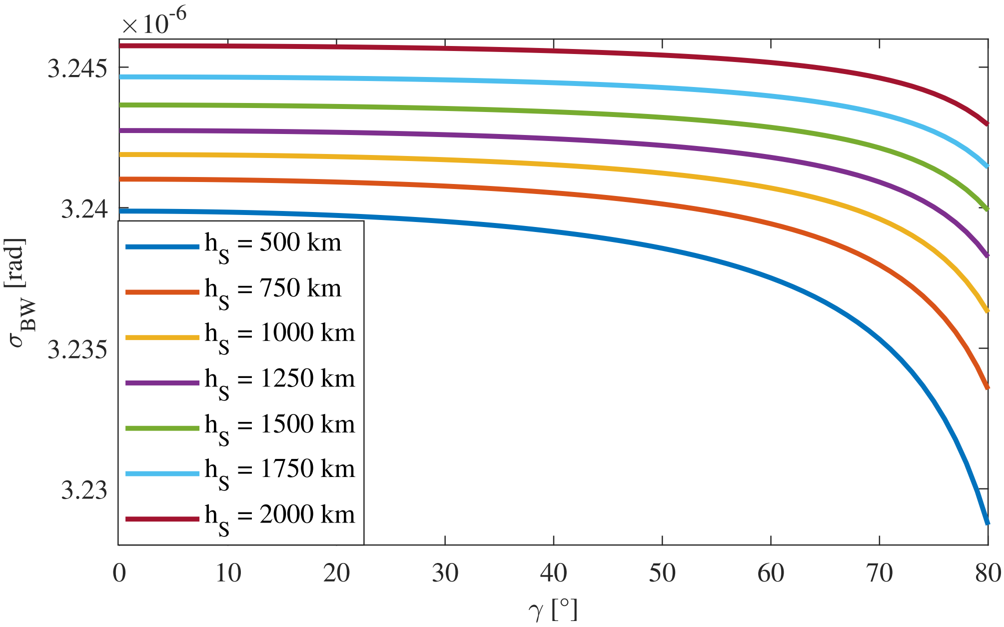

Figure 2.37: Values of beam wander standard deviation varying both the Zenith angle γ and the satellite height h_S. Aperture diameter $D = 0.2$ m, wind speed $v_\mathrm{RMS} = 0$ m/s.

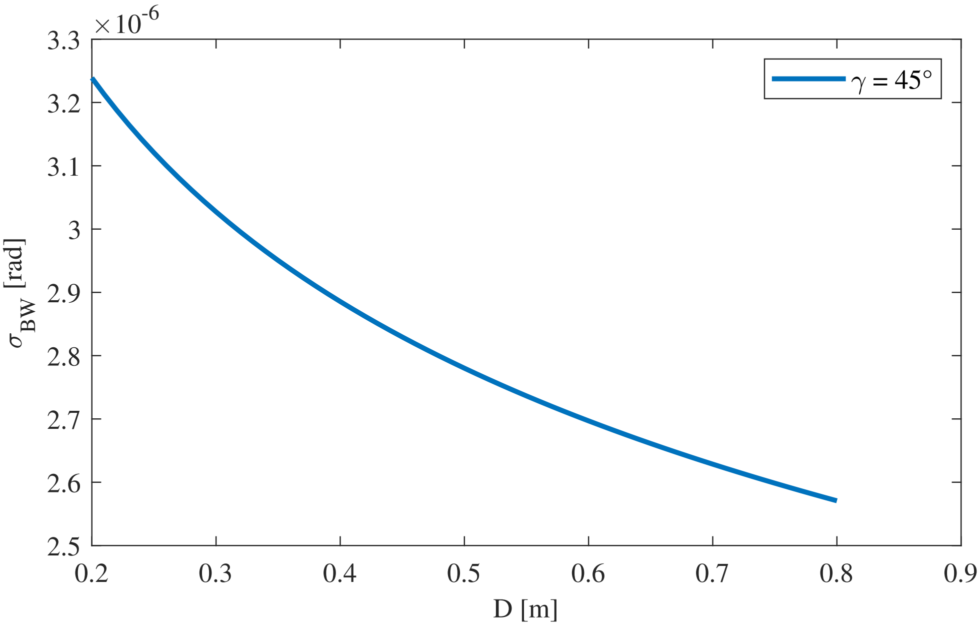

Figure 2.38: Values of beam wander standard deviation varying the aperture D. Satellite height $h_\mathrm{S} = 500$ km, Zenith angle $\gamma = 45°$, wind speed $v_\mathrm{RMS} = 0$ m/s.

Chapter 3

Influence of the Attitude Subsystem

In recent years, the widespread adoption of nanosatellites and picosatellites adhering to the CubeSat standard have steered research efforts toward the progressive miniaturization of the subsystems comprising the ADCS. The task of an ADCS is the estimation of the attitude of the satellite (attitude determination) and the control of its orientation and angular velocity according to the mission requirements [50] [51] [52].

Recent trends are on aggressive miniaturization of Micro-Electro-Mechanical Systems (MEMS) sensors [53], with exemplary emerging technologies on fiber-optic gyroscopes, silicon-photonics, and micro-gyroscopes under development [54] [55]. Furthermore, to present days, lightweight filters can run on resource-constrained processors with minimal latency, enabling real-time multi-sensor fusion and fine attitude control [56].

This chapter introduces the reader to the influence of ADCS on the measurement performed by the payload based on arrays of antennas. In particular, three main studies have been conducted: firstly, in Sec. 3.1 the propagation of the error in the attitude is evaluated and quantified through Monte Carlo simulations varying the position of the emitter and the orbital parameters; then in Sec. 3.2 changes in attitude are analysed to check if it possible to develop a strategy of identification of the set of cases in which the measurement diverges through the clustering of the attitude state; in the end, in Sec. 3.3 a strategy based on tri-axial arrays for the prevention and the compensation of the divergence of the dispersion of the errors is proposed.

3.1 Direct and Indirect Effects

The main approach and models developed in this section are extracted from the work of the author [57]: at the time of writing, this paper is submitted for a journal and it is ‘under review’. Conditioned on its acceptance, this work is expected to be published towards the end of 2025 or the beginning of 2026.

A synthetic presentation of the author for cross antenna arrays has been given in [58].

The main goal is to model and evaluate the influence of the errors in the ADCS on the performance of the payload in case of Nadir pointing. Starting from the mathematical modelling, two effects have been identified: a direct effect on the value of the measurement, and an indirect effect on their dispersion. The methodology involves Monte Carlo simulations varying the relative configuration between the signal emitter and the satellite platform in terms of orbital parameters. The results are on main trends and the full statistical characterization of the distribution of the errors of the payload for Azimuth and Elevation angles, and Cramér-Rao lower bound. Insights on emerging cases of the divergence of measurement for configurations of alignments are also presented and discussed.

3.1.1 Propagation of Attitude Error and Approach to Simulation

A measurement obtained through a payload composed of cross array of antennas in a plane is a measurement of the direction from the emitter of the signal E to the satellite S. This measurement is denoted by the LOB and can be mathematically described as a unit vector $\mathbf{u}_{\mathrm{LOB}}$, as shown in (3.1).

$$\mathbf{u}_{\mathrm{LOB}} = \frac{\mathbf{x}_{\mathrm{E}} - \mathbf{x}_{\mathrm{S}}}{\|\mathbf{x}_{\mathrm{E}} - \mathbf{x}_{\mathrm{S}}\|} \tag{3.1}$$

More in particular, a linear array of antennas aligned in a certain direction $\mathbf{u}_{\mathrm{Ar}}$ can perform a measurement of a broadside angle ζ, which is defined as the angle between the LOB, $\mathbf{u}_{\mathrm{LOB}}$, and the direction $\mathbf{u}_{\mathrm{Ar}}$ on which the elements of the antenna array are aligned, so $\cos(\zeta) = \mathbf{u}_{\mathrm{LOB}} \cdot \mathbf{u}_{\mathrm{Ar}}$.

Denoting by A a local orthogonal coordinate system for the payload with axes $(x_{\mathrm{A}}, y_{\mathrm{A}}, z_{\mathrm{A}})$ and by $\mathbf{u}_{\mathrm{Ar,x}}|_{\mathrm{A}}$, $\mathbf{u}_{\mathrm{Ar,y}}|_{\mathrm{A}}$, the two unit vectors aligned along x_{A} and y_{A} axes, the broadside angles ζ_{x} and ζ_{y} can be defined through (3.2), where $\mathbf{u}_{\mathrm{LOB}}|_{\mathrm{A}}$ is the representation of the LOB (3.1) in the local A coordinate system on the payload.

$$\begin{cases} \cos(\zeta_{\mathrm{x}}) = \mathbf{u}_{\mathrm{LOB}}|_{\mathrm{A}} \cdot \mathbf{u}_{\mathrm{Ar,x}}|_{\mathrm{A}} \\ \cos(\zeta_{\mathrm{y}}) = \mathbf{u}_{\mathrm{LOB}}|_{\mathrm{A}} \cdot \mathbf{u}_{\mathrm{Ar,y}}|_{\mathrm{A}} \end{cases} \tag{3.2}$$

Fixed a certain cartesian coordinate system, the LOB can be also represented in a local spherical coordinate system built from it through two angles [59, 60, 61]. Two possible angles are the Azimuth angle (in the following with subscript Az) and Elevation angle (in the following with subscript El), which are denoted by α_{Az} and α_{El} respectively.

In this study, the representation of the LOB in a local spherical coordinate system in terms of Azimuth angle α_{Az} and Elevation angle α_{El} follows the convention in (3.3).

$$\begin{cases} \dfrac{x_{\mathrm{E}}|_{\mathrm{A}} - x_{\mathrm{S}}|_{\mathrm{A}}}{\|\mathbf{x}_{\mathrm{E}}|_{\mathrm{A}} - \mathbf{x}_{\mathrm{S}}|_{\mathrm{A}}\|} = \cos(\alpha_{\mathrm{Az}})\cos(\alpha_{\mathrm{El}}) \\ \dfrac{y_{\mathrm{E}}|_{\mathrm{A}} - y_{\mathrm{S}}|_{\mathrm{A}}}{\|\mathbf{x}_{\mathrm{E}}|_{\mathrm{A}} - \mathbf{x}_{\mathrm{S}}|_{\mathrm{A}}\|} = \sin(\alpha_{\mathrm{Az}})\cos(\alpha_{\mathrm{El}}) \\ \dfrac{z_{\mathrm{E}}|_{\mathrm{A}} - z_{\mathrm{S}}|_{\mathrm{A}}}{\|\mathbf{x}_{\mathrm{E}}|_{\mathrm{A}} - \mathbf{x}_{\mathrm{S}}|_{\mathrm{A}}\|} = \sin(\alpha_{\mathrm{El}}) \end{cases} \tag{3.3}$$

Equivalently, given $d_{\mathrm{x}}|_{\mathrm{A}} = x_{\mathrm{E}}|_{\mathrm{A}} - x_{\mathrm{S}}|_{\mathrm{A}}$, $d_{\mathrm{y}}|_{\mathrm{A}} = y_{\mathrm{E}}|_{\mathrm{A}} - y_{\mathrm{S}}|_{\mathrm{A}}$, and $d_{\mathrm{z}}|_{\mathrm{A}} = z_{\mathrm{E}}|_{\mathrm{A}} - z_{\mathrm{S}}|_{\mathrm{A}}$, the Azimuth angle α_{Az} and Elevation angle α_{El} can be expressed from (3.3) as in (3.4).

$$\begin{cases} \alpha_{\mathrm{Az}} = \operatorname{atan2}\big(d_{\mathrm{y}}|_{\mathrm{A}}\,,\, d_{\mathrm{x}}|_{\mathrm{A}}\big) \\ \alpha_{\mathrm{El}} = \operatorname{atan2}\left(d_{\mathrm{z}}|_{\mathrm{A}}\,,\, \sqrt{\left(d_{\mathrm{x}}|_{\mathrm{A}}\right)^2 + \left(d_{\mathrm{y}}|_{\mathrm{A}}\right)^2}\right) \end{cases} \tag{3.4}$$

Combining the expression of unit vectors of the linear arrays in coordinate system A, $\mathbf{u}_{\mathrm{Ar,x}}|_{\mathrm{A}} = (1{,}0{,}0)^{\mathrm{T}}$ and $\mathbf{u}_{\mathrm{Ar,y}}|_{\mathrm{A}} = (0{,}1{,}0)^{\mathrm{T}}$, with the expression of the components of LOB in (3.3), the dot product in (3.2) leads to the expressions shown in (3.5).

$$\begin{cases} \cos(\zeta_{\mathrm{x}}) = \mathbf{u}_{\mathrm{LOB}}|_{\mathrm{A}} \cdot \mathbf{u}_{\mathrm{Ar,x}}|_{\mathrm{A}} = \begin{pmatrix} \cos(\alpha_{\mathrm{Az}})\cos(\alpha_{\mathrm{El}}) \\ \sin(\alpha_{\mathrm{Az}})\cos(\alpha_{\mathrm{El}}) \\ \sin(\alpha_{\mathrm{El}}) \end{pmatrix} \cdot \begin{pmatrix} 1 \\ 0 \\ 0 \end{pmatrix} = \cos(\alpha_{\mathrm{Az}})\cos(\alpha_{\mathrm{El}}) \\ \cos(\zeta_{\mathrm{y}}) = \mathbf{u}_{\mathrm{LOB}}|_{\mathrm{A}} \cdot \mathbf{u}_{\mathrm{Ar,y}}|_{\mathrm{A}} = \begin{pmatrix} \cos(\alpha_{\mathrm{Az}})\cos(\alpha_{\mathrm{El}}) \\ \sin(\alpha_{\mathrm{Az}})\cos(\alpha_{\mathrm{El}}) \\ \sin(\alpha_{\mathrm{El}}) \end{pmatrix} \cdot \begin{pmatrix} 0 \\ 1 \\ 0 \end{pmatrix} = \sin(\alpha_{\mathrm{Az}})\cos(\alpha_{\mathrm{El}}) \end{cases} \tag{3.5}$$

Substituting the expressions for Azimuth angle α_{Az} and Elevation angle α_{El} written in (3.4) into (3.5), the expressions in (3.6) for broadside angles ζ_{x} and ζ_{y} are obtained.

$$\begin{cases} \zeta_{\mathrm{x}} = \arccos\left(\cos\left(\operatorname{atan2}\big(d_{\mathrm{y}}|_{\mathrm{A}}\,,\, d_{\mathrm{x}}|_{\mathrm{A}}\big)\right)\,\cos\left(\operatorname{atan2}\left(d_{\mathrm{z}}|_{\mathrm{A}}\,,\, \sqrt{\left(d_{\mathrm{x}}|_{\mathrm{A}}\right)^2 + \left(d_{\mathrm{y}}|_{\mathrm{A}}\right)^2}\right)\right)\right) \\ \zeta_{\mathrm{y}} = \arccos\left(\sin\left(\operatorname{atan2}\big(d_{\mathrm{y}}|_{\mathrm{A}}\,,\, d_{\mathrm{x}}|_{\mathrm{A}}\big)\right)\,\cos\left(\operatorname{atan2}\left(d_{\mathrm{z}}|_{\mathrm{A}}\,,\, \sqrt{\left(d_{\mathrm{x}}|_{\mathrm{A}}\right)^2 + \left(d_{\mathrm{y}}|_{\mathrm{A}}\right)^2}\right)\right)\right) \end{cases} \tag{3.6}$$

To describe the attitude of a satellite S, two further coordinate systems are needed: the ORF and the BRF, denoted by B.

The conversion from ECI to ORF is shown in (1.14).

Data conversion from ORF to BRF occurs through (1.15) with the aid of the matrices of rotation on the attitude angles of roll θ_1, pitch θ_2, and yaw θ_3.

Both payload data and attitude data have to be expressed in body coordinate system; for simplicity, in this study, the mounting parameters are supposed to be known and their influence is neglected.

Considering the expressions in (3.4) and (3.6) together with (1.8), (1.1), (1.6), (1.9), (1.11), (1.2), (1.14), (1.15), and (1.17), the functional dependencies in (3.7) can be written: they denote a direct influence of the attitude angles roll θ_1, pitch θ_2, and yaw θ_3 on the angles of Azimuth α_{Az} and Elevation α_{El}.

$$\begin{aligned} \alpha_{\mathrm{Az}} &= f\left(\Lambda, \lambda, h, a, e, i, \Omega, \omega, \nu, \theta_1, \theta_2, \theta_3\right) \\ \alpha_{\mathrm{El}} &= f\left(\Lambda, \lambda, h, a, e, i, \Omega, \omega, \nu, \theta_1, \theta_2, \theta_3\right) \end{aligned} \tag{3.7}$$

The dependencies in (3.7) mean that changes (in absolute value or as an error contribution) in attitude angles produce a direct change in the value of payload measurement.

In (3.8) the prediction of the variances through the CRLB $\sigma^2_{\hat{\zeta}_{\mathrm{x}}}$ and $\sigma^2_{\hat{\zeta}_{\mathrm{y}}}$ for linear arrays along x_{A} and y_{A} directions are reported. In particular, M_{x} and M_{y} are, respectively, the number of array elements along the two directions, L_{x} and L_{y} the total lengths of the arrays.

$$\begin{cases} \sigma^2_{\hat{\zeta}_{\mathrm{x}}} = \dfrac{12}{(2\pi)^2 SNR \frac{(M_{\mathrm{x}}+1)}{(M_{\mathrm{x}}-1)} M_{\mathrm{x}} \left(\frac{fL_{\mathrm{x}}}{c}\right)^2 \sin^2\left(\zeta_{\mathrm{x}}\right)} \\ \sigma^2_{\hat{\zeta}_{\mathrm{y}}} = \dfrac{12}{(2\pi)^2 SNR \frac{(M_{\mathrm{y}}+1)}{(M_{\mathrm{y}}-1)} M_{\mathrm{y}} \left(\frac{fL_{\mathrm{y}}}{c}\right)^2 \sin^2\left(\zeta_{\mathrm{y}}\right)} \end{cases} \tag{3.8}$$

The functional dependencies of the broadside angles with respect to the attitude angles of roll θ_1, pitch θ_2, and yaw θ_3 can be written for the expressions (3.8) on the standard deviations of the broadside angles $\sigma^2_{\hat{\zeta}_{\mathrm{x}}}$ and $\sigma^2_{\hat{\zeta}_{\mathrm{y}}}$ as shown in (3.9).

$$\begin{aligned} \sigma_{\hat{\zeta}_{\mathrm{x}}} &= f\left(\Lambda, \lambda, h, a, e, i, \Omega, \omega, \nu, \theta_1, \theta_2, \theta_3\right) \\ \sigma_{\hat{\zeta}_{\mathrm{y}}} &= f\left(\Lambda, \lambda, h, a, e, i, \Omega, \omega, \nu, \theta_1, \theta_2, \theta_3\right) \end{aligned} \tag{3.9}$$

In summary, the expressions in (3.9) mean that a change in the attitude angles produces a change in the variance of the payload measurement. An error in the attitude angles propagates as an error contribution to the variance of the payload measurement.

The purpose of this study is to evaluate the effect of the propagation of an error in the attitude to the payload measurement, both in a direct way as in (3.7) and in an indirect way as in (3.9).

For a first level set of evaluations, a possible model for the errors[1] in the attitude angles is to consider a zero-mean Gaussian distribution $\mathcal{N}$ with standard deviations σ_{θ_1}, σ_{θ_2}, and σ_{θ_3}. So the models $\mathrm{d}\theta_1 = \hat{\theta}_1 - \theta_1 \sim \mathcal{N}\left(0, \sigma^2_{\theta_1}\right)$, $\mathrm{d}\theta_2 = \hat{\theta}_2 - \theta_2 \sim \mathcal{N}\left(0, \sigma^2_{\theta_2}\right)$, and $\mathrm{d}\theta_3 = \hat{\theta}_3 - \theta_3 \sim \mathcal{N}\left(0, \sigma^2_{\theta_3}\right)$ are considered.

Considering small values of errors such that $\mathrm{d}\theta_1 \ll 1$, $\mathrm{d}\theta_2 \ll 1$, and $\mathrm{d}\theta_3 \ll 1$, combined with the assumption on the mounting parameters, then the antenna array axes x_{A}, y_{A}, and z_{A} are aligned such that z_{A} is directed toward the center of the Earth, y_{A} is orthogonal to the plane of the orbit, and x_{A} follows the direction of motion of the satellite.

By definition of error, for a true value of Azimuth angle α_{Az} and a true value in Elevation angle α_{El} the quantities in (3.10) are considered. In particular, $\delta\alpha_{\mathrm{Az}}$ denotes the error in Azimuth angle due to an error in the attitude, $\delta\alpha_{\mathrm{El}}$ denotes the same kind of error in Elevation angle, while $\hat{\alpha}_{\mathrm{Az}}$ and $\hat{\alpha}_{\mathrm{El}}$ are their estimations (i.e., true value with error in the attitude).

$$\begin{gathered}
\delta\alpha_{\mathrm{Az}}\left(\theta_1 + \mathrm{d}\theta_1, \theta_2 + \mathrm{d}\theta_2, \theta_3 + \mathrm{d}\theta_3\right) \\
= \left|\alpha_{\mathrm{Az}}\left(\theta_1, \theta_2, \theta_3\right) - \hat{\alpha}_{\mathrm{Az}}\left(\theta_1 + \mathrm{d}\theta_1, \theta_2 + \mathrm{d}\theta_2, \theta_3 + \mathrm{d}\theta_3\right)\right| \\
\delta\alpha_{\mathrm{El}}\left(\theta_1 + \mathrm{d}\theta_1, \theta_2 + \mathrm{d}\theta_2, \theta_3 + \mathrm{d}\theta_3\right) \\
= \left|\alpha_{\mathrm{El}}\left(\theta_1, \theta_2, \theta_3\right) - \hat{\alpha}_{\mathrm{El}}\left(\theta_1 + \mathrm{d}\theta_1, \theta_2 + \mathrm{d}\theta_2, \theta_3 + \mathrm{d}\theta_3\right)\right|
\end{gathered} \tag{3.10}$$

In the same manner, but with an important difference on the meaning of terms, the expressions in (3.11) can be defined on the standard deviations of the broadside angles $\sigma_{\hat{\zeta}_{\mathrm{x}}}$ and $\sigma_{\hat{\zeta}_{\mathrm{y}}}$. In particular, the meaning of the terms is the following: $\sigma_{\hat{\zeta}_{\mathrm{x}}}$ and $\sigma_{\hat{\zeta}_{\mathrm{y}}}$ denote the variance of the payload in the ideal case without an error in the attitude subsystem, while $\hat{\sigma}_{\hat{\zeta}_{\mathrm{x}}}$ and $\hat{\sigma}_{\hat{\zeta}_{\mathrm{y}}}$ denote the values of the variance of the payload when an error in the attitude is considered. Values of $\delta\sigma_{\hat{\zeta}_{\mathrm{x}}}$ and $\delta\sigma_{\hat{\zeta}_{\mathrm{y}}}$ denote the absolute difference between the two cases (without and with error in the attitude).

$$\begin{gathered}
\delta\sigma_{\hat{\zeta}_{\mathrm{x}}}\left(\theta_1 + \mathrm{d}\theta_1, \theta_2 + \mathrm{d}\theta_2, \theta_3 + \mathrm{d}\theta_3\right) \\
= \left|\sigma_{\hat{\zeta}_{\mathrm{x}}}\left(\theta_1, \theta_2, \theta_3\right) - \hat{\sigma}_{\hat{\zeta}_{\mathrm{x}}}\left(\theta_1 + \mathrm{d}\theta_1, \theta_2 + \mathrm{d}\theta_2, \theta_3 + \mathrm{d}\theta_3\right)\right| \\
\delta\sigma_{\hat{\zeta}_{\mathrm{y}}}\left(\theta_1 + \mathrm{d}\theta_1, \theta_2 + \mathrm{d}\theta_2, \theta_3 + \mathrm{d}\theta_3\right) \\
= \left|\sigma_{\hat{\zeta}_{\mathrm{y}}}\left(\theta_1, \theta_2, \theta_3\right) - \hat{\sigma}_{\hat{\zeta}_{\mathrm{y}}}\left(\theta_1 + \mathrm{d}\theta_1, \theta_2 + \mathrm{d}\theta_2, \theta_3 + \mathrm{d}\theta_3\right)\right|
\end{gathered} \tag{3.11}$$

The simulations have considered variations in the dependencies of the expressions in (3.12).

---

[1] In this study, given a true value ϕ and its measured value $\hat{\phi}$, the value $\mathrm{d}\phi = \hat{\phi} - \phi$ denotes a signed value of the error, while $\delta\phi = \left|\phi - \hat{\phi}\right|$ denotes an unsigned value of the error.

$$\begin{aligned}
\delta\alpha_{\mathrm{Az}} &= f\left(\Lambda, \lambda, h, a, e, i, \Omega, \omega, \nu, \theta_1 + \mathrm{d}\theta_1, \theta_2 + \mathrm{d}\theta_2, \theta_3 + \mathrm{d}\theta_3\right)\\
\delta\alpha_{\mathrm{El}} &= f\left(\Lambda, \lambda, h, a, e, i, \Omega, \omega, \nu, \theta_1 + \mathrm{d}\theta_1, \theta_2 + \mathrm{d}\theta_2, \theta_3 + \mathrm{d}\theta_3\right)\\
\delta\sigma_{\hat{\zeta}_{\mathrm{x}}} &= f\left(\Lambda, \lambda, h, a, e, i, \Omega, \omega, \nu, \theta_1 + \mathrm{d}\theta_1, \theta_2 + \mathrm{d}\theta_2, \theta_3 + \mathrm{d}\theta_3\right)\\
\delta\sigma_{\hat{\zeta}_{\mathrm{y}}} &= f\left(\Lambda, \lambda, h, a, e, i, \Omega, \omega, \nu, \theta_1 + \mathrm{d}\theta_1, \theta_2 + \mathrm{d}\theta_2, \theta_3 + \mathrm{d}\theta_3\right)
\end{aligned} \tag{3.12}$$

Considering that, in general, it is assumed that the satellite does not know the position the emitter of the signal, a Nadir pointing is assumed. The Nadir direction is the direction that goes toward the center of the Earth, and, in the context of the study, a Nadir alignment is achieved when the normal of the plane of the antenna arrays $\mathbf{n}_{\mathrm{A}} = \mathbf{x}_{\mathrm{A}} \times \mathbf{y}_{\mathrm{A}}$ is aligned to the Nadir direction, i.e., $(-\mathbf{x}_{\mathrm{S}}/\|\mathbf{x}_{\mathrm{S}}\|) \cdot \mathbf{n}_{\mathrm{A}} = 1$. This means that ADCS has the goal to maintain the angles of roll, pitch and yaw equal to $\theta_1 = 0$, $\theta_2 = 0$, and $\theta_3 = 0$, so the models in (3.12) become as in (3.13).

$$\begin{aligned}
\delta\alpha_{\mathrm{Az}} &= f\left(\Lambda, \lambda, h, a, e, i, \Omega, \omega, \nu, \mathrm{d}\theta_1, \mathrm{d}\theta_2, \mathrm{d}\theta_3\right)\\
\delta\alpha_{\mathrm{El}} &= f\left(\Lambda, \lambda, h, a, e, i, \Omega, \omega, \nu, \mathrm{d}\theta_1, \mathrm{d}\theta_2, \mathrm{d}\theta_3\right)\\
\delta\sigma_{\hat{\zeta}_{\mathrm{x}}} &= f\left(\Lambda, \lambda, h, a, e, i, \Omega, \omega, \nu, \mathrm{d}\theta_1, \mathrm{d}\theta_2, \mathrm{d}\theta_3\right)\\
\delta\sigma_{\hat{\zeta}_{\mathrm{y}}} &= f\left(\Lambda, \lambda, h, a, e, i, \Omega, \omega, \nu, \mathrm{d}\theta_1, \mathrm{d}\theta_2, \mathrm{d}\theta_3\right)
\end{aligned} \tag{3.13}$$

One variable at a time has been analyzed (among $\Lambda, \lambda, h, a, e, i, \Omega, \omega, \nu$) to observe its direct and indirect influence on errors with respect to a reference scenario, which in the following will be denoted with subscript 0.

Denoting with a generic letter χ one of the models of distribution in (3.13), i.e., $\chi \in X = \{\delta\alpha_{\mathrm{Az}}, \delta\alpha_{\mathrm{El}}, \delta\sigma_{\hat{\zeta}_{\mathrm{x}}}, \delta\sigma_{\hat{\zeta}_{\mathrm{y}}}\}$, the following statistics have been considered to characterize each distribution: mean value $\hat{\mu}(\chi)$, quantiles $Q(\chi)$ evaluated at $[25, 75]$ % and $[5, 95]$ %, skewness $s(\chi)$, and kurtosis $k(\chi)$. For skewness and kurtosis unbiased estimators have been considered.

To obtain the distributions in (3.13), the simulations of random variables $\mathrm{d}\theta_1$, $\mathrm{d}\theta_2$, and $\mathrm{d}\theta_3$ are required, and they have been obtained through a Monte Carlo approach. The points of the Gaussian distributions have been generated using a pseudo-random number generator with N_{θ_1} points for roll angle θ_1, N_{θ_2} points for pitch angle, and N_{θ_3} for yaw angle. By hypothesis, it has been considered that the error distributions of the three attitude angles were the same, i.e., $\mathrm{d}\theta_1 = \mathrm{d}\theta_2 = \mathrm{d}\theta_3$ with mean values of $\mu_{\theta_1} = \mu_{\theta_2} = \mu_{\theta_3} = 0$ and variance $\sigma^2_{\theta_1} = \sigma^2_{\theta_2} = \sigma^2_{\theta_3} = \sigma^2$. A value of $\sigma^2 = 10^{-6}$ rad^2 for the errors of each attitude angle has been considered.

Furthermore, the same number of points has been considered for each attitude angle, i.e., $N_{\theta_1} = N_{\theta_2} = N_{\theta_3} = N$. The total number of points in the simulations is then $N_{\mathrm{sim}} = N_{\theta_1} N_{\theta_2} N_{\theta_3} = N^3$.

Given N_{sim} samples $x_1, x_1, \ldots, x_{\mathrm{k}}, \ldots, x_{\mathrm{N_{sim}}}$ of a distribution χ, the estimated mean $\hat{\mu}_{\mathrm{N_{sim}}}$ and the estimated standard deviation $\sigma_{\mathrm{N_{sim}}}$ for the set of samples are defined as in (3.14).

$$\begin{aligned}\hat{\mu}_{\mathrm{N_{sim}}} &= \frac{1}{N_{\mathrm{sim}}}\sum_{k=1}^{N_{\mathrm{sim}}}\left(x_{\mathrm{k}}\right)\\ \hat{\sigma}_{\mathrm{N_{sim}}} &= \sqrt{\frac{1}{N_{\mathrm{sim}}-1}\sum_{k=1}^{N_{\mathrm{sim}}}\left|\hat{\mu}_{\mathrm{N_{sim}}}-x_{\mathrm{k}}\right|^{2}}\end{aligned} \tag{3.14}$$

The choice of the number of points N for each distribution has followed the criterion on the convergence on the mean value of the expressions in (3.10) and (3.11). Considering that if $N_{\mathrm{sim}} \to \infty$, then $\hat{\mu}_{\mathrm{N_{sim}}} \to \mu$ and $\sigma_{\mathrm{N_{sim}}} \to 0$, the criterion in (3.15) has been considered to choose the number of points of the distributions, where C is a constant value.

$$\left|\mu - \hat{\mu}_{\mathrm{N_{sim}}}\right| < \frac{C}{\sqrt{N_{\mathrm{sim}}-1}} \tag{3.15}$$

To achieve a value $\left|\mu - \hat{\mu}_{\mathrm{N_{sim}}}\right|/C < 0.001$ (i.e., <0.1%), a value of $N = 101$ (i.e., a total number of simulated cases of $N_{\mathrm{sim}} = 1030301$) has been considered.

The results are with respect to a reference scenario, denoted by the subscript 0. The default reference scenario used to compare the results obtained in simulations is the one that considers an emitter of signal on the surface of the Earth (i.e., $h_0 = 0$) and a circular orbit with properties of $a_0 = r_{\mathrm{S},0} = 500$ km, $e_0 = 0$, and $i_0 = 90°$. The reference position of the satellite on the orbit is $\Omega_0 = 0°$, $\nu_0 = 0°$. Conventionally, $\omega_0 = 0°$ since it is not defined for circular orbits[2]. The reference position considered for the emitter is $\Lambda_0 = 5°$, $\lambda_0 = 5°$ in order not to have the trivial case of Nadir alignment between the emitter of signal and the satellite.

The number of elements of the antenna arrays resulted in $M_{\mathrm{x}} = M_{\mathrm{y}} = 7$ and it has been calculated from the length of the array $L_{\mathrm{x}} = L_{\mathrm{y}} = 0.334$ m, the spacing distance between consecutive elements $d_{\mathrm{x}} = d_{\mathrm{y}} = c/\left(4f\right)$, and the frequency of the signal $f = 1575.42$ MHz, representative of the use case of spectrum monitoring of jamming signals for GNSS.

The value of Signal-to-Noise ratio SNR has been chosen considering the minimum value required to guarantee probability of detection $p_{\mathrm{D}} = 0.997$ and probability of false alarms $p_{\mathrm{FA}} = 10^{-6}$ for the detector from the ROC (Receiver Operating Characteristic) in the case of a linear detector, a non-fluctuating signal with unknown phase, and Gaussian noise [24]. For simplicity and evaluative purposes, a free-space path loss propagation has been assumed. Phenomena of reflection, refraction, and multipath have been neglected. From ROC models resulted

---

[2] Some authors, e.g. [62], introduce a new quantity to avoid ambiguities: the argument of latitude, defined as $u = \omega + \nu$. For circular orbits it is $u = 0 + \nu = \nu$.

$SNR\left(p_{\text{FA}}, p_{\text{D}}\right) \approx 15$ dB. To take into account non-modeled effects (i.e., propagation in atmosphere), a further increment of 3 dB has been considered as safety margin.

The presentation of the simulations has been divided into three subsections: varying the emitter position in terms of geodetic latitude Λ and longitude λ, while satellite orbit and position are fixed (subsection 3.1.2); varying the satellite position in terms of a, Ω and ν, while the emitter position is fixed (subsection 3.1.3); considering further aspects on the effects of eccentricity e and inclination of the orbit i (subsection 3.1.4).

3.1.2 Simulations for Emitter Position

This subsection presents the results of the simulations that vary the geodetic latitude Λ and longitude λ of the emitter with respect to the reference scenario described in section 3.1.1.

Variations in the emitter height h have been investigated up to 12000 m: however, they have not been presented in this study because it has been noticed that the effect of this variable is negligible in the results compared to the case $h = 0$ m.

In particular, in Figure 3.1, the models in $\delta\alpha_{\text{Az}}\left(\Lambda\right)$ and $\delta\alpha_{\text{El}}\left(\Lambda\right)$ are presented. Figure 3.2 presents the models $\delta\sigma_{\hat{\zeta}_{\text{x}}}\left(\Lambda\right)$ and $\delta\sigma_{\hat{\zeta}_{\text{y}}}\left(\Lambda\right)$. Figure 3.3 presents the models $\delta\alpha_{\text{Az}}$ and $\delta\alpha_{\text{El}}\left(\lambda\right)$. Figure 3.4 presents the models $\delta\sigma_{\hat{\zeta}_{\text{x}}}\left(\lambda\right)$ and $\delta\sigma_{\hat{\zeta}_{\text{y}}}\left(\lambda\right)$.

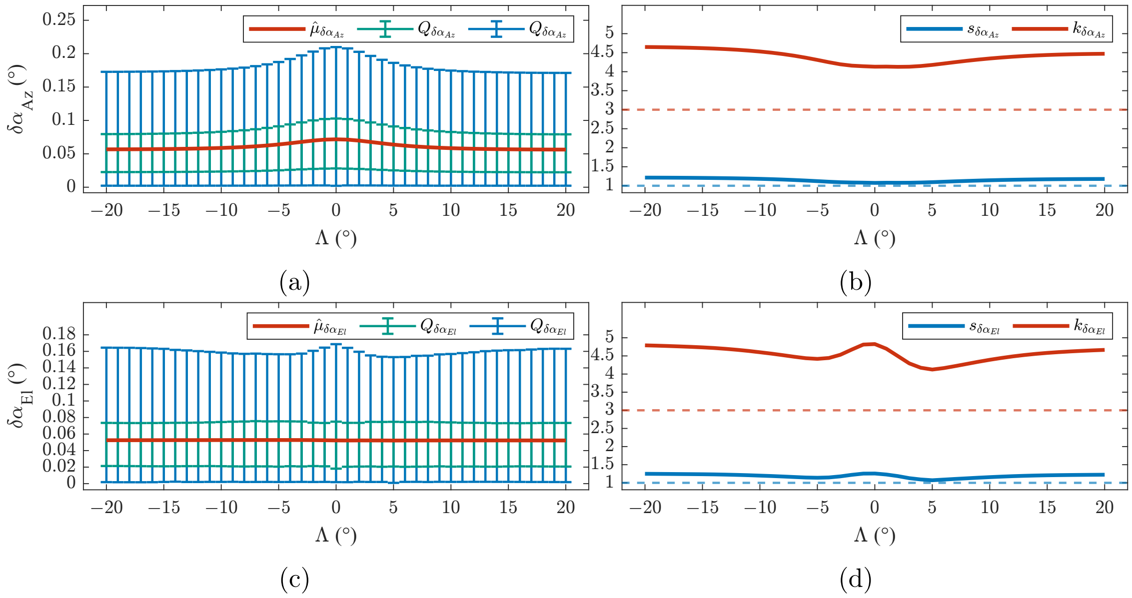

(a) (b)

(c) (d)

Figure 3.1: (a) Trends of the simulated model $\delta\alpha_{\text{Az}}\left(\Lambda\right) = f\left(\Lambda, \lambda_0, r_{\text{S},0}, e_0, i_0, \Omega_0, \nu_0\right)$: mean value and quantiles evaluated at $[25, 75]$ % and $[5, 95]$ %. (b) Trends of skewness and kurtosis for $\delta\alpha_{\text{Az}}\left(\Lambda\right)$. (c) Trends of the simulated model $\delta\alpha_{\text{El}}\left(\Lambda\right) = f\left(\Lambda, \lambda_0, r_{\text{S},0}, e_0, i_0, \Omega_0, \nu_0\right)$: mean value and quantiles evaluated at $[25, 75]$ % and $[5, 95]$ %. (d) Trends of skewness and kurtosis for $\delta\alpha_{\text{El}}\left(\Lambda\right)$.

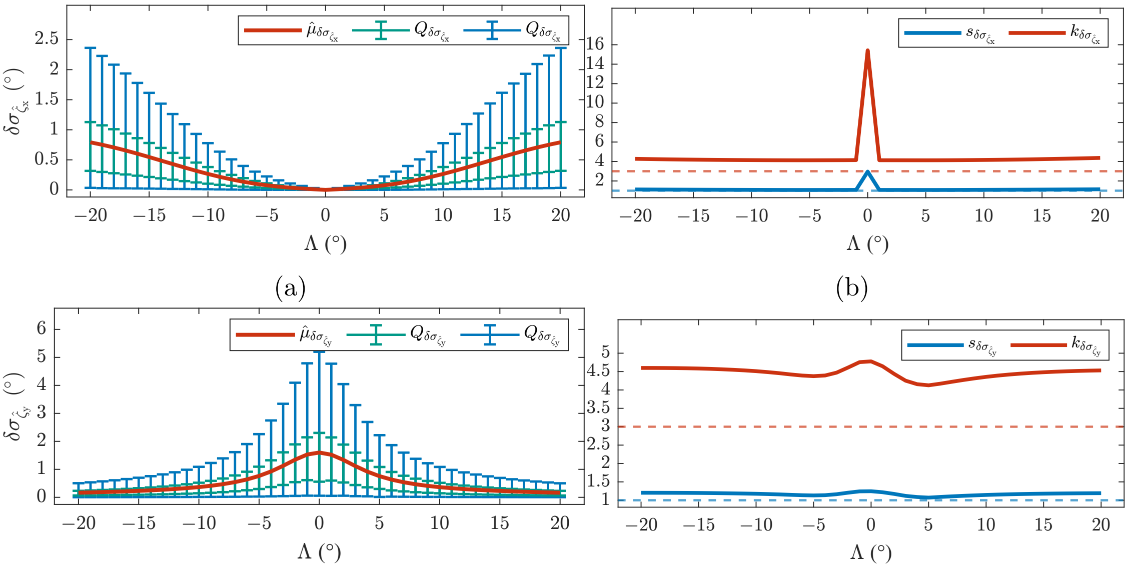

(a) (b)

(c) (d)

Figure 3.2: (a) Trends of the simulated model $\delta\sigma_{\hat{\zeta}_x}(\Lambda) = f(\Lambda, \lambda_0, r_{S,0}, e_0, i_0, \Omega_0, \nu_0)$: mean value and quantiles evaluated at $[25, 75]$ % and $[5, 95]$ %. (b) Trends of skewness and kurtosis for $\delta\sigma_{\hat{\zeta}_x}(\Lambda)$. (c) Trends of the simulated model $\delta\sigma_{\hat{\zeta}_y}(\Lambda) = f(\Lambda, \lambda_0, r_{S,0}, e_0, i_0, \Omega_0, \nu_0)$: mean value and quantiles evaluated at $[25, 75]$ % and $[5, 95]$ %. (d) Trends of skewness and kurtosis for $\delta\sigma_{\hat{\zeta}_y}(\Lambda)$.

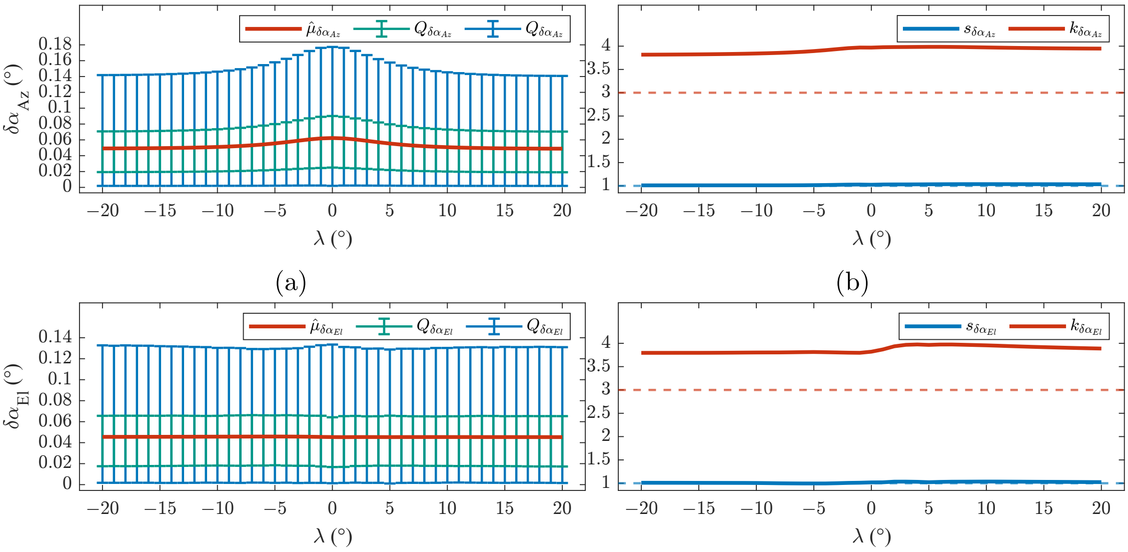

(a) (b)

(c) (d)

Figure 3.3: (a) Trends of the simulated model $\delta\alpha_{\rm Az}(\lambda) = f(\Lambda_0, \lambda, r_{S,0}, e_0, i_0, \Omega_0, \nu_0)$: mean value and quantiles evaluated at $[25, 75]$ % and $[5, 95]$ %. (b) Trends of skewness and kurtosis for $\delta\alpha_{\rm Az}(\lambda)$. (c) Trends of the simulated model $\delta\alpha_{\rm El}(\lambda) = f(\Lambda_0, \lambda, r_{S,0}, e_0, i_0, \Omega_0, \nu_0)$: mean value and quantiles evaluated at $[25, 75]$ % and $[5, 95]$ %. (d) Trends of skewness and kurtosis for $\delta\alpha_{\rm El}(\lambda)$.

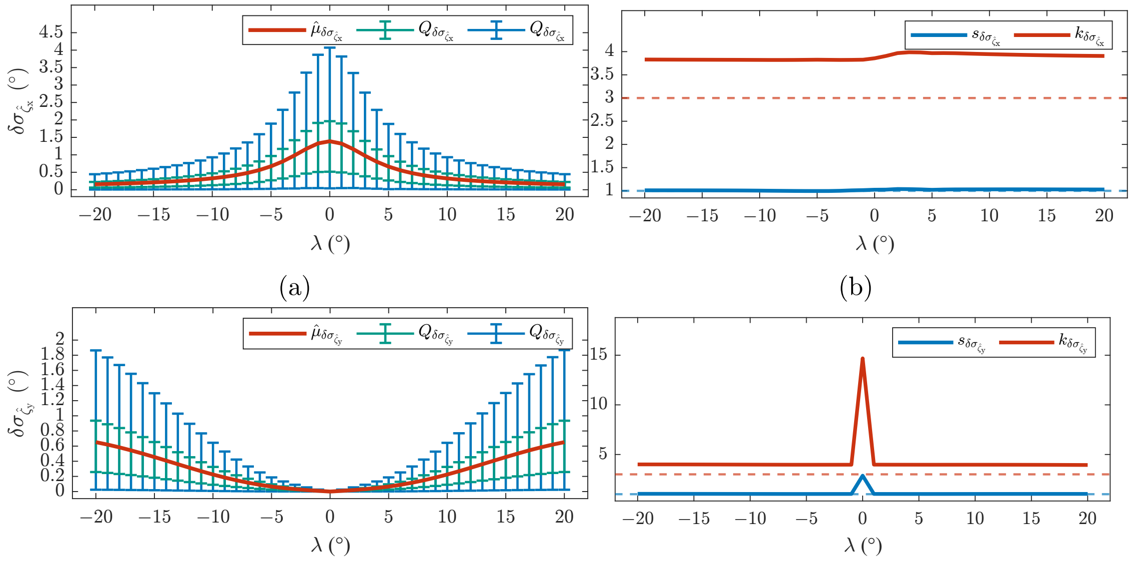

(a) (b) (c) (d)

Figure 3.4: (a) Trends of the simulated model $\delta\sigma_{\hat{\zeta}_{\mathrm{x}}}(\lambda) = f(\Lambda_0, \lambda, r_{\mathrm{S},0}, e_0, i_0, \Omega_0, \nu_0)$: mean value and quantiles evaluated at $[25, 75]$ % and $[5, 95]$ %. (b) Trends of skewness and kurtosis for $\delta\sigma_{\hat{\zeta}_{\mathrm{x}}}(\lambda)$. (c) Trends of the simulated model $\delta\sigma_{\hat{\zeta}_{\mathrm{y}}}(\lambda) = f(\Lambda_0, \lambda, r_{\mathrm{S},0}, e_0, i_0, \Omega_0, \nu_0)$: mean value and quantiles evaluated at $[25, 75]$ % and $[5, 95]$ %. (d) Trends of skewness and kurtosis for $\delta\sigma_{\hat{\zeta}_{\mathrm{y}}}(\lambda)$.

3.1.3 Simulations for Satellite Position

This subsection presents the results of the simulations that vary the orbit radius r_{S}, the right ascension of the ascending node Ω, and the true anomaly ν of the satellite with respect to the reference scenario described in section 3.1.1.

In Figure 3.5, the models $\delta\alpha_{\mathrm{Az}}(r_{\mathrm{S}})$ and $\delta\alpha_{\mathrm{El}}(r_{\mathrm{S}})$ are presented. Figure 3.6 presents the models $\delta\sigma_{\hat{\zeta}_{\mathrm{x}}}(r_{\mathrm{S}})$ and $\delta\sigma_{\hat{\zeta}_{\mathrm{y}}}(r_{\mathrm{S}})$. Figure 3.7 presents the models $\delta\alpha_{\mathrm{Az}}(\Omega)$ and $\delta\alpha_{\mathrm{El}}(\Omega)$. Figure 3.8 presents the models $\delta\sigma_{\hat{\zeta}_{\mathrm{x}}}(\Omega)$ and $\delta\sigma_{\hat{\zeta}_{\mathrm{y}}}(\Omega)$. Figure 3.9 presents the models $\delta\alpha_{\mathrm{Az}}(\nu)$ and $\delta\alpha_{\mathrm{El}}(\nu)$. Figure 3.10 presents the models $\delta\sigma_{\hat{\zeta}_{\mathrm{x}}}(\nu)$ and $\delta\sigma_{\hat{\zeta}_{\mathrm{y}}}(\nu)$.

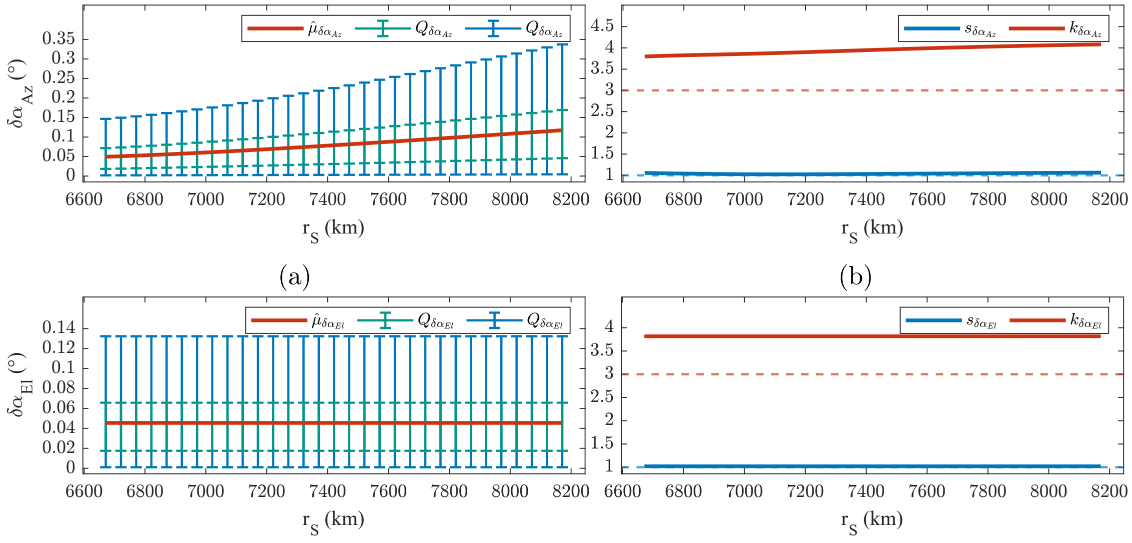

(a) (b)

(c) (d)

Figure 3.5: (a) Trends of the simulated model $\delta\alpha_{\mathrm{Az}}(r_{\mathrm{S}}) = f(\Lambda_0, \lambda_0, r_{\mathrm{S}}, e_0, i_0, \Omega_0, \nu_0)$: mean value and quantiles evaluated at $[25, 75]$ % and $[5, 95]$ %. (b) Trends of skewness and kurtosis for $\delta\alpha_{\mathrm{Az}}(r_{\mathrm{S}})$. (c) Trends of the simulated model $\delta\alpha_{\mathrm{El}}(r_{\mathrm{S}}) = f(\Lambda_0, \lambda_0, r_{\mathrm{S}}, e_0, i_0, \Omega_0, \nu_0)$: mean value and quantiles evaluated at $[25, 75]$ % and $[5, 95]$ %. (d) Trends of skewness and kurtosis for $\delta\alpha_{\mathrm{El}}(r_{\mathrm{S}})$.

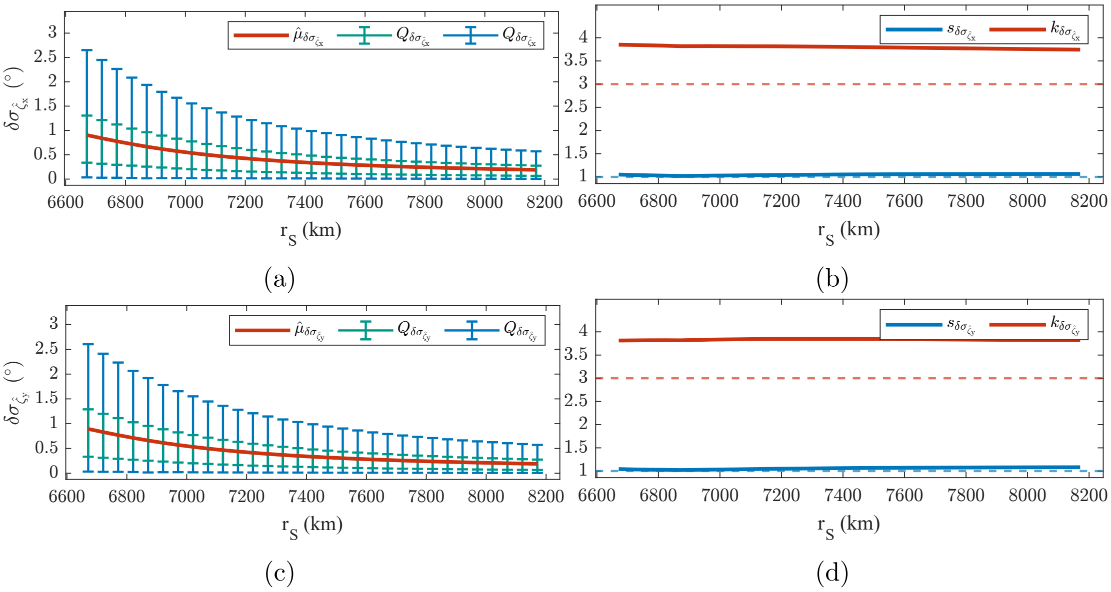

(a) (b)

(c) (d)

Figure 3.6: (a) Trends of the simulated model $\delta\sigma_{\hat{\zeta}_x}(r_S) = f(\Lambda_0, \lambda_0, r_S, e_0, i_0, \Omega_0, \nu_0)$: mean value and quantiles evaluated at [25, 75] % and [5, 95] %. (b) Trends of skewness and kurtosis for $\delta\sigma_{\hat{\zeta}_x}(r_S)$. (c) Trends of the simulated model $\delta\sigma_{\hat{\zeta}_y}(r_S) = f(\Lambda_0, \lambda_0, r_S, e_0, i_0, \Omega_0, \nu_0)$: mean value and quantiles evaluated at [25, 75] % and [5, 95] %. (d) Trends of skewness and kurtosis for $\delta\sigma_{\hat{\zeta}_y}(r_S)$.

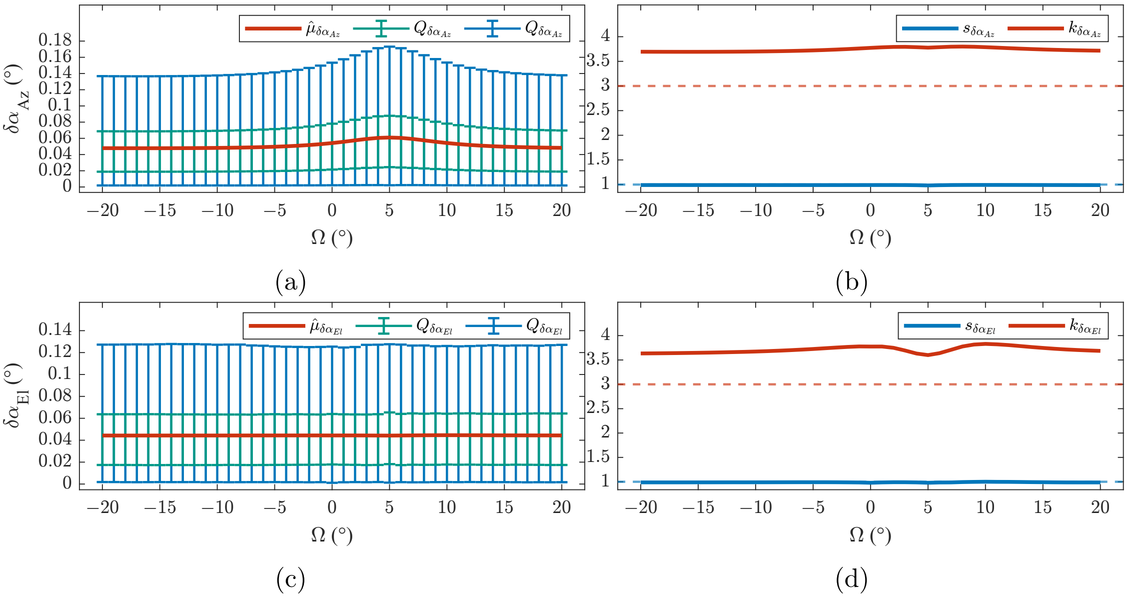

(a) (b)

(c) (d)

Figure 3.7: (a) Trends of the simulated model $\delta\alpha_{\mathrm{Az}}(\Omega) = f(\Lambda_0, \lambda_0, r_{S,0}, e_0, i_0, \Omega, \nu_0)$: mean value and quantiles evaluated at [25, 75] % and [5, 95] %. (b) Trends of skewness and kurtosis for $\delta\alpha_{\mathrm{Az}}(\Omega)$. (c) Trends of the simulated model $\delta\alpha_{\mathrm{El}}(\Omega) = f(\Lambda_0, \lambda_0, r_{S,0}, e_0, i_0, \Omega, \nu_0)$: mean value and quantiles evaluated at [25, 75] % and [5, 95] %. (d) Trends of skewness and kurtosis for $\delta\alpha_{\mathrm{El}}(\Omega)$.

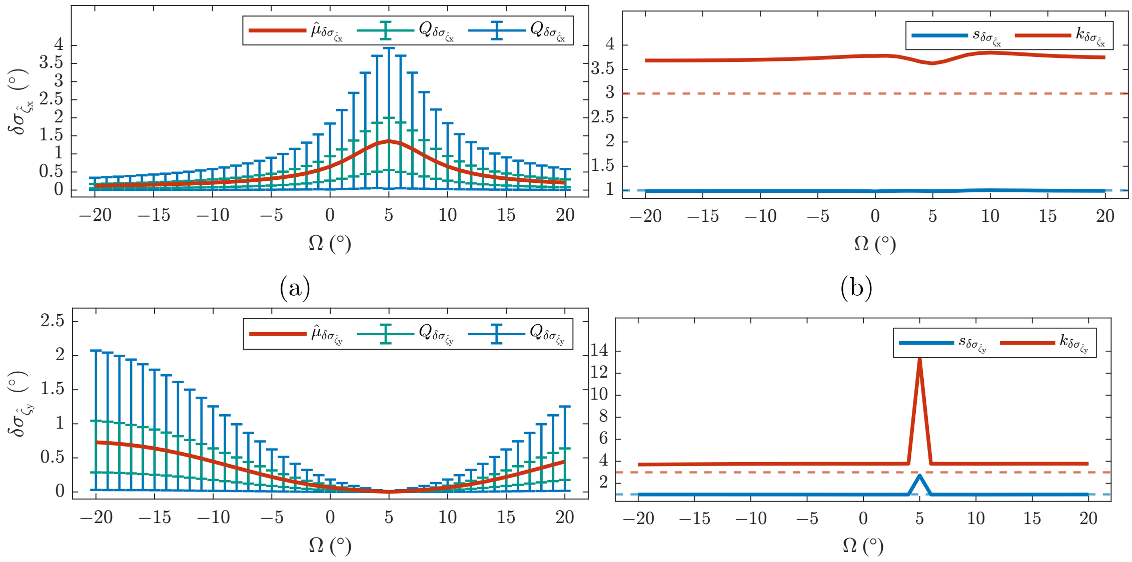

(a) (b)

(c) (d)

Figure 3.8: (a) Trends of the simulated model $\delta\sigma_{\hat{\zeta}_x}(\Omega) = f(\Lambda_0, \lambda_0, r_{S,0}, e_0, i_0, \Omega, \nu_0)$: mean value and quantiles evaluated at $[25, 75]$ % and $[5, 95]$ %. (b) Trends of skewness and kurtosis for $\delta\sigma_{\hat{\zeta}_x}(\Omega)$. (c) Trends of the simulated model $\delta\sigma_{\hat{\zeta}_y}(\Omega) = f(\Lambda_0, \lambda_0, r_{S,0}, e_0, i_0, \Omega, \nu_0)$: mean value and quantiles evaluated at $[25, 75]$ % and $[5, 95]$ %. (d) Trends of skewness and kurtosis for $\delta\sigma_{\hat{\zeta}_y}(\Omega)$.

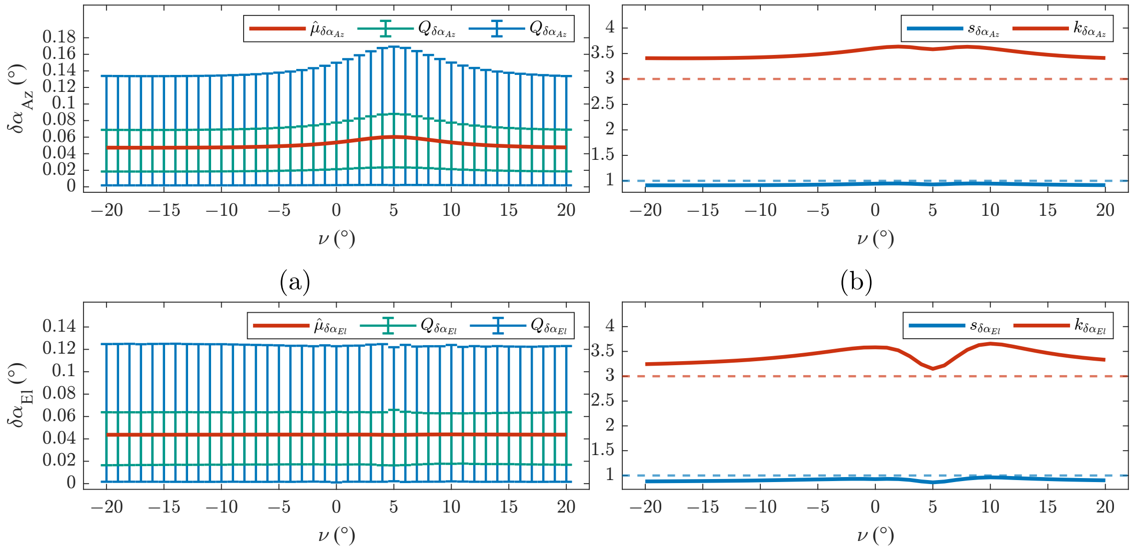

(a) (b)

(c) (d)

Figure 3.9: (a) Trends of the simulated model $\delta\alpha_{\mathrm{Az}}(\nu) = f(\Lambda_0, \lambda_0, r_{S,0}, e_0, i_0, \Omega_0, \nu)$: mean value and quantiles evaluated at $[25, 75]$ % and $[5, 95]$ %. (b) Trends of skewness and kurtosis for $\delta\alpha_{\mathrm{Az}}(\nu)$. (c) Trends of the simulated model $\delta\alpha_{\mathrm{El}}(\nu) = f(\Lambda_0, \lambda_0, r_{S,0}, e_0, i_0, \Omega_0, \nu)$: mean value and quantiles evaluated at $[25, 75]$ % and $[5, 95]$ %. (d) Trends of skewness and kurtosis for $\delta\alpha_{\mathrm{El}}(\nu)$.

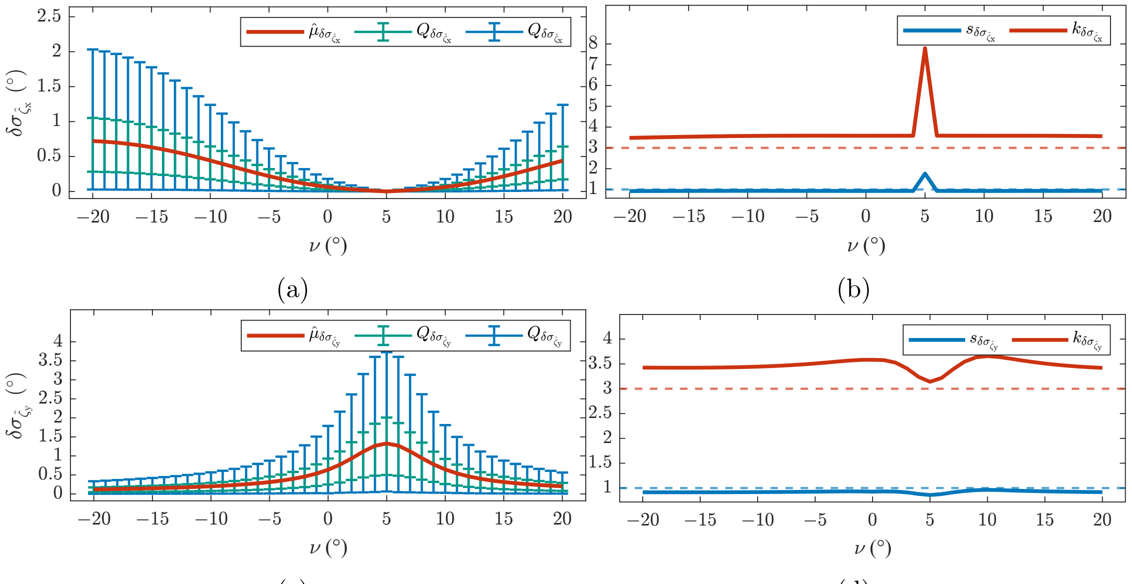

(a) (b)

(c) (d)

Figure 3.10: (a) Trends of the simulated model $\delta\sigma_{\hat{\zeta}_x}(\nu) = f(\Lambda_0, \lambda_0, r_{S,0}, e_0, i_0, \Omega_0, \nu)$: mean value and quantiles evaluated at $[25, 75]$ % and $[5, 95]$ %. (b) Trends of skewness and kurtosis for $\delta\sigma_{\hat{\zeta}_x}(\nu)$. (c) Trends of the simulated model $\delta\sigma_{\hat{\zeta}_y}(\nu) = f(\Lambda_0, \lambda_0, r_{S,0}, e_0, i_0, \Omega_0, \nu)$: mean value and quantiles evaluated at $[25, 75]$ % and $[5, 95]$ %. (d) Trends of skewness and kurtosis for $\delta\sigma_{\hat{\zeta}_y}(\nu)$.

3.1.4 Further Simulations on Eccentricity and Inclination of the Orbit

This subsection presents the results of the simulations that vary the eccentricity of the orbit e and its inclination i with respect to the reference scenario described in Sec. 3.1.1.

Influence of orbit eccentricity e and orbit inclination i on the direct effects (i.e., the quantities $\delta\alpha_{\mathrm{Az}}(e)$, $\delta\alpha_{\mathrm{El}}(e)$, $\delta\alpha_{\mathrm{Az}}(i)$, and $\delta\alpha_{\mathrm{El}}(i)$) are omitted and not presented among the results of the study because they were found to have an almost flat behavior which means that there are no significant changes compared to the reference scenario.

Influence on indirect effects is presented as follows. In Figure 3.11, the models $\delta\sigma_{\hat{\zeta}_{\mathrm{x}}}(e)$ and $\delta\sigma_{\hat{\zeta}_{\mathrm{y}}}(e)$ are presented. Figure 3.12 presents the models $\delta\sigma_{\hat{\zeta}_{\mathrm{x}}}(i)$ and $\delta\sigma_{\hat{\zeta}_{\mathrm{y}}}(i)$.

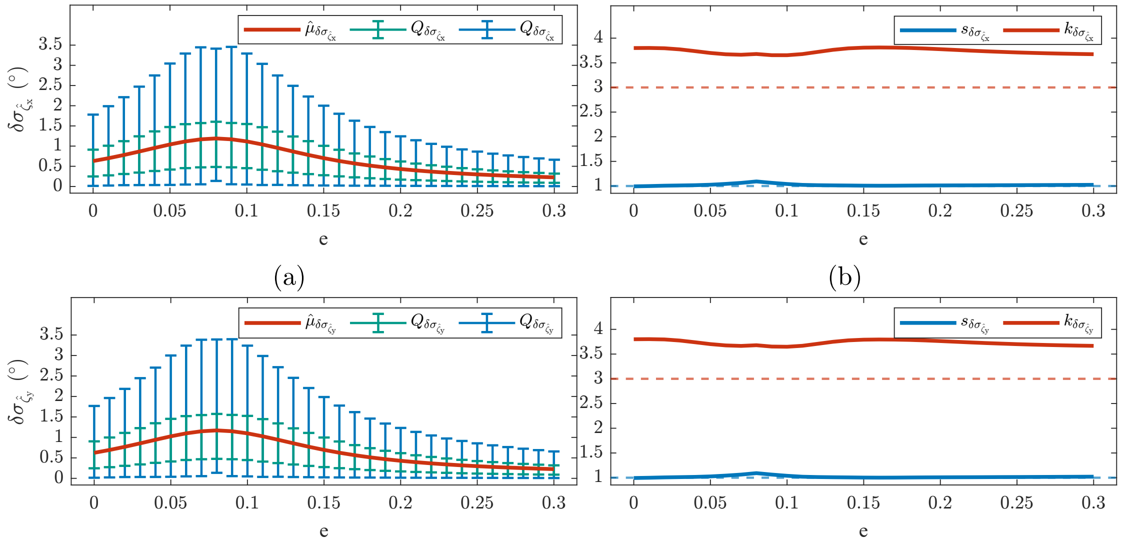

(a) (b)

(c) (d)

Figure 3.11: (a) Trends of the simulated model $\delta\sigma_{\hat{\zeta}_{\mathrm{x}}}(e) = f(\Lambda_0, \lambda_0, r_{\mathrm{S},0}, e, i_0, \Omega_0, \nu_0)$: mean value and quantiles evaluated at $[25, 75]$ % and $[5, 95]$ %. (b) Trends of skewness and kurtosis for $\delta\sigma_{\hat{\zeta}_{\mathrm{x}}}(e)$. (c) Trends of the simulated model $\delta\sigma_{\hat{\zeta}_{\mathrm{y}}}(e) = f(\Lambda_0, \lambda_0, r_{\mathrm{S},0}, e, i_0, \Omega_0, \nu_0)$: mean value and quantiles evaluated at $[25, 75]$ % and $[5, 95]$ %. (d) Trends of skewness and kurtosis for $\delta\sigma_{\hat{\zeta}_{\mathrm{y}}}(e)$.

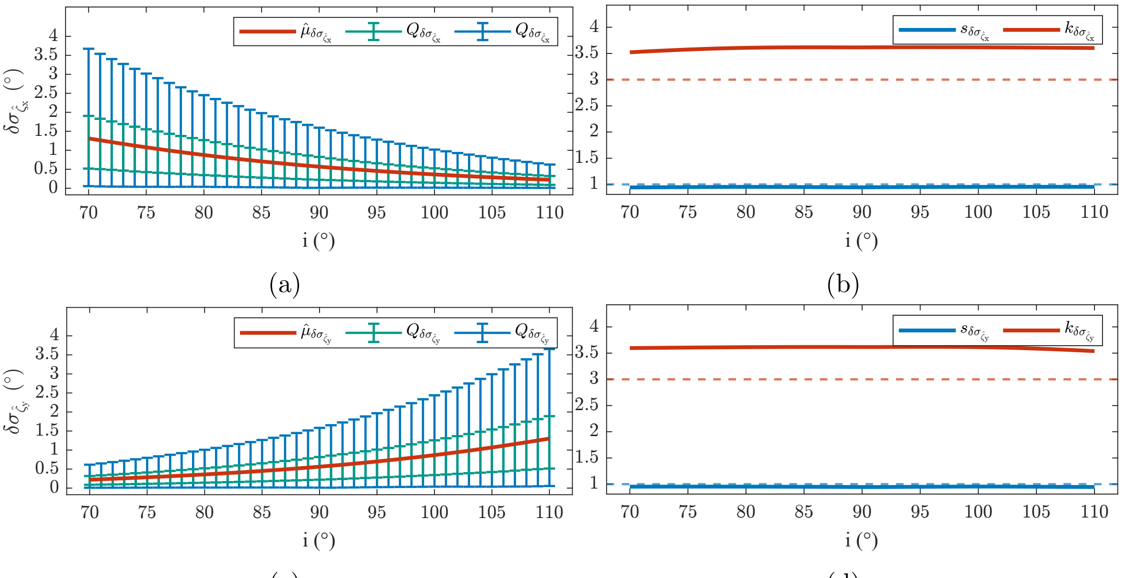

(a) (b)

(c) (d)

Figure 3.12: (a) Trends of the simulated model $\delta\sigma_{\hat{\zeta}_\mathrm{x}}(i) = f(\Lambda_0, \lambda_0, r_{\mathrm{S},0}, e_0, i, \Omega_0, \nu_0)$: mean value and quantiles evaluated at $[25, 75]$ % and $[5, 95]$ %. (b) Trends of skewness and kurtosis for $\delta\sigma_{\hat{\zeta}_\mathrm{x}}(i)$. (c) Trends of the simulated model $\delta\sigma_{\hat{\zeta}_\mathrm{y}}(i) = f(\Lambda_0, \lambda_0, r_{\mathrm{S},0}, e_0, i, \Omega_0, \nu_0)$: mean value and quantiles evaluated at $[25, 75]$ % and $[5, 95]$ %. (d) Trends of skewness and kurtosis for $\delta\sigma_{\hat{\zeta}_\mathrm{y}}(i)$.

3.1.5 Analysis of Results

The analysis of Figure 3.1 (a) reveals that the mean value of $\delta\alpha_{\mathrm{Az}}$ has a maximum when the $\mathbf{y}_{\mathrm{A}}$ axis of the antenna array tends to be aligned along the direction between the satellite and the the emitter, i.e. $\left(\mathbf{x}_{\mathrm{S}}-\mathbf{x}_{\mathrm{E}}\right)/\|\mathbf{x}_{\mathrm{S}}-\mathbf{x}_{\mathrm{E}}\| \cdot \mathbf{y}_{\mathrm{A}}/\|\mathbf{y}_{\mathrm{A}}\| \rightarrow \pm 1$, which happens in $\Lambda = 0°$. For the cases analyzed in the study, the increase is of about $0.05° \sim 0.07°$ in the evaluation of the mean value of the Azimuth error for the analyzed cases of the study. The mean increase in Elevation error due to the variations in latitude in Figure 3.1 (c) appears almost flat with a value of about $0.05°$.

Figures 3.3 (a) (c) reveal also the same behavior for errors in the Azimuth angle, but in this case it is applied to direction $\mathbf{x}_{\mathrm{A}}$: every time an axis of the antenna array tends to be aligned with respect to the satellite-emitter direction (in this case $\mathbf{x}_{\mathrm{A}}$), the direct influence on the error model increases. Also here, the increments are about $0.05° \sim 0.07°$ in the evaluation of the mean value of the Azimuth error, and about $0.05°$ in the evaluation of the mean value of Elevation error.

Figure 3.7 (a) and 3.9 (a) show that changes in the right ascension of the ascending node Ω and in the true anomaly ν can lead to a maximum for the mean value of the error distribution of the Azimuth angle. From a geometric point of view, this happens when $\mathbf{x}_{\mathrm{A}}$ or $\mathbf{y}_{\mathrm{A}}$ tends to have an alignment with respect to the satellite-emitter direction, i.e., $\left(\mathbf{x}_{\mathrm{S}}-\mathbf{x}_{\mathrm{E}}\right)/\|\mathbf{x}_{\mathrm{S}}-\mathbf{x}_{\mathrm{E}}\| \cdot \mathbf{x}_{\mathrm{A}}/\|\mathbf{x}_{\mathrm{A}}\| \rightarrow \pm 1$ or $\left(\mathbf{x}_{\mathrm{S}}-\mathbf{x}_{\mathrm{E}}\right)/\|\mathbf{x}_{\mathrm{S}}-\mathbf{x}_{\mathrm{E}}\| \cdot \mathbf{y}_{\mathrm{A}}/\|\mathbf{y}_{\mathrm{A}}\| \rightarrow \pm 1$. The increments appears to be about $0.4° \sim 0.5°$ for the mean value of the error distribution of the Azimuth and Elevation angle.

Figures 3.2 (c), 3.4 (a), 3.8 (a), and 3.10 (c) present potential cases of divergence in the variance of the bearing angles $\sigma_{\hat{\zeta}_{\mathrm{x}}}$ and $\sigma_{\hat{\zeta}_{\mathrm{y}}}$ that happen in the cases of alignment of one of the axes of the antenna array due to changes in the latitude of the emitter Λ, in the longitude of the emitter λ, in the right ascension of the ascending node of the satellite Ω, and in the true anomaly of the satellite ν respectively. Simultaneously, in Figures 3.2 (a), 3.4 (c), 3.8 (c), and 3.10 (a) there is the realization of the minimum: apparently, in ideal conditions of alignment, the axis orthogonal to the direction of alignment can achieve the minimum of $\sigma_{\hat{\zeta}_{\mathrm{x}}}$ if $\left(\mathbf{x}_{\mathrm{S}}-\mathbf{x}_{\mathrm{E}}\right)/\|\mathbf{x}_{\mathrm{S}}-\mathbf{x}_{\mathrm{E}}\| \cdot \mathbf{x}_{\mathrm{A}}/\|\mathbf{x}_{\mathrm{A}}\| \rightarrow 0$ or the minimum of $\sigma_{\hat{\zeta}_{\mathrm{y}}}$ if $\left(\mathbf{x}_{\mathrm{S}}-\mathbf{x}_{\mathrm{E}}\right)/\|\mathbf{x}_{\mathrm{S}}-\mathbf{x}_{\mathrm{E}}\| \cdot \mathbf{y}_{\mathrm{A}}/\|\mathbf{y}_{\mathrm{A}}\| \rightarrow 0$.

Mathematically, the divergence occurs because when the antenna array along the $\mathbf{x}_{\mathrm{A}}$ direction tends to be aligned along satellite-emitter direction (i.e., $\zeta_x \rightarrow 0$), then, from (3.8) it is $\sigma^2_{\hat{\zeta}_x} \propto 1/\sin^2\left(\zeta_x\right) \rightarrow \infty$. Conversely, the measurement along $\mathbf{y}_{\mathrm{A}}$ presents a minimum in the same case $\delta\sigma_{\hat{\zeta}_y} \propto 1/\sin^2\left(\zeta_y\right) \rightarrow 0$, because $\zeta_y \rightarrow \pi/2$.

The effect of the radius of the orbit r_{S} is evident in Figures 3.5 (a) and 3.6 (a) (c): changes in this variable mainly produces changes in the errors in the Azimuth angle α_{Az} and the variance of the errors in the broadside angles, i.e., $\delta\sigma_{\hat{\zeta}_x}$ and $\delta\sigma_{\hat{\zeta}_y}$.

The same happens with changes in the values of the eccentricity of the orbit e, as shown in Figure 3.11. This means that changes the size of the orbit, in terms of the orbit radius r_S and eccentricity e, can lead to a variation in the estimation of the variance of the errors for the angles of interest.

Figures 3.12 (a) (c) reveal opposite behaviour: positive changes in the inclination of the orbit produce an decrement for the dispersion of the errors in the variance of the x-broadside angle $\delta\sigma_{\hat{\zeta}_x}$ and a contemporary increment for the dispersion of the errors in the y-broadside angle $\delta\sigma_{\hat{\zeta}_y}$. This happens because a change in the inclination of the orbit i indirectly produces a change of the orientation of the antenna arrays, which produces an increase or decrease of these quantities.

The values of skewness are around the unitary value, revealing slightly symmetric distributions for all the quantities of interest. Cases of exception happen in singular cases of alignment and divergence.

The values of kurtosis present an excess of $+0.5 \sim +2.0$ with respect to the reference Gaussian (reference value of 3), revealing that these quantities can be modelled with a distribution more peaked than the Normal distribution.

3.2 Prediction and Clustering of Measurement Divergence

The main approach and models developed in this section are unpublished and must be considered as preliminary results to be verified. At the time of writing, a dedicated journal paper with provisional details in [63] is in preparation for a submission in Dec. 2025. Conditioned on its acceptance, this work is expected to occur during the year 2026.

From the standard deviations $\sigma_{\hat{\zeta}_\mathrm{x}}$ and $\sigma_{\hat{\zeta}_\mathrm{y}}$ it is possible to evaluate the overall standard deviation as in (3.16).

$$\sigma_{\hat{\zeta}} = \sqrt{\sigma^2_{\hat{\zeta}_\mathrm{x}} + \sigma^2_{\hat{\zeta}_\mathrm{y}}} \tag{3.16}$$

Similarly to the considerations made in Sec. 3.1, the functional dependencies of the standard deviation of the broadside angles with respect to the attitude angles of roll θ_1, pitch θ_2, and yaw θ_3, shown in (3.9), can be written for the expression (3.16) related to the standard deviation of the broadside angle $\sigma^2_{\hat{\zeta}}$ as shown in (3.17).

$$\sigma_{\hat{\zeta}} = f\left(\Lambda, \lambda, h, a, e, i, \Omega, \omega, \nu, \theta_1, \theta_2, \theta_3\right) \tag{3.17}$$

In summary, the expressions in (3.17) mean that a change in the attitude angles produces a change in the overall variance of the payload measurement.

3.2.1 Approach to Simulation and Clustering of Cases of Divergence

Fixed a certain relative geometry in terms of position, the study wants to investigate the cases of divergence for (3.16) varying the attitude of the satellite.

Given $\Lambda = \Lambda_0$, $\Lambda = \lambda_0$, $h = h_0$, $a = a_0$, $e = e_0$, $i = i_0$, $\Omega = \Omega_0$, $\omega = \omega_0$, and $\nu = \nu_0$, the expression in (3.18) is simulated varying θ_1, θ_2, and θ_3.

$$\sigma_{\hat{\zeta}}\Big|_{\{\Lambda=\Lambda_0,\lambda=\lambda_0,h=h_0,a=a_0,e=e_0,i=i_0,\Omega=\Omega_0,\omega=\omega_0,\nu=\nu_0\}} : (\theta_1,\theta_2,\theta_3) \to f(\theta_1,\theta_2,\theta_3) \tag{3.18}$$

In particular, the goal is to have a discrete set of samples of the function (3.18) and evaluate what are the subsets of attitude angles for which the function tends to diverge.

Given a number of samples N_{θ_1} for the roll angle, a number of samples N_{θ_2} for the pitch angle, a number of samples N_{θ_3} for the yaw angle, then the total number of simulated cases is $N_\mathrm{t} = N_{\theta_1} N_{\theta_2} N_{\theta_3}$.

Considering that $\theta_1 \in \mathcal{D}_1 = [-\pi, \pi[$, $\theta_2 \in \mathcal{D}_2 =]-\pi/2, \pi/2[$, and $\theta_3 \in \mathcal{D}_3 = [-\pi, \pi[$, it is observed that the measurements of the domains are, respectively, $\mu(\mathcal{D}_1) = 2\pi$, $\mu(\mathcal{D}_2) = \pi$, and $\mu(\mathcal{D}_3) = 2\pi$.

To have evenly spaced samples, the domain $\mathcal{D}_1$ has been subdivided in $N_{\theta_1} = 2N + 1$ points, $\mathcal{D}_2$ in $N_{\theta_2} = N + 1$ points, and $\mathcal{D}_3$ in $N_{\theta_3} = 2N + 1$ points, for a total of $N_\mathrm{t} = N_{\theta_1} N_{\theta_2} N_{\theta_3} = (2N+1)(N+1)(2N+1)$ synthetic samples for the function $\sigma_{\hat{\zeta}}$.

However, considering the periodicity of the domains $\mathcal{D}_1$ and $\mathcal{D}_3$, it results $\theta_1^{(1)} = \theta_1^{(2N+1)}$ and $\theta_3^{(1)} = \theta_3^{(2N+1)}$. This means that the last point for these two variables have to be excluded. Furthermore, for the pitch angle θ_2 is has to be observed that it should be $\theta_2 \neq \pi/2 + k\pi$ with $k \in \mathbb{Z}$, so for the discretization of the domain $\mathcal{D}_2$ the points $\theta_2^{(1)}$ and $\theta_2^{(N+1)}$ have to be excluded too. Considering these two facts, the actual number of points employed for the simulations becomes $N_{\theta_1} = 2N$, $N_{\theta_2} = N - 1$, and $N_{\theta_3} = 2N$, so the total number of points is $N_\mathrm{t} = 4N^2(N-1)$.

The resulting sampled domains are the ones reported in (3.19).

$$\begin{aligned}
\tilde{\mathcal{D}}_1 &= \left\{ \theta_1^{(k)} = \frac{2\pi(k-1)}{2N} - \pi \,\middle|\, k = 1, \ldots, 2N \right\} \\
\tilde{\mathcal{D}}_2 &= \left\{ \theta_2^{(k)} = \frac{\pi k}{N-1} - \frac{\pi}{2} \,\middle|\, k = 1, \ldots, N-1 \right\} \\
\tilde{\mathcal{D}}_3 &= \left\{ \theta_3^{(k)} = \frac{2\pi(k-1)}{2N} - \pi \,\middle|\, k = 1, \ldots, 2N \right\}
\end{aligned} \tag{3.19}$$

From the sampled domains, the Cartesian product $\tilde{\mathcal{D}} = \tilde{\mathcal{D}}_1 \times \tilde{\mathcal{D}}_2 \times \tilde{\mathcal{D}}_3$ can be projected into three grid arrays $\mathcal{T}_1$, $\mathcal{T}_2$, $\mathcal{T}_3$ with repeated elements using a projection operator ξ, as shown formally in (3.20).

$$
\begin{aligned}
\xi_1 &: \tilde{\mathcal{D}} \to \mathcal{T}_1, \quad \xi_1\left(\theta_1^{(k_1)}, \theta_2^{(k_2)}, \theta_3^{(k_3)}\right) = \theta_1^{(k_1)} \\
\xi_2 &: \tilde{\mathcal{D}} \to \mathcal{T}_2, \quad \xi_2\left(\theta_1^{(k_1)}, \theta_2^{(k_2)}, \theta_3^{(k_3)}\right) = \theta_2^{(k_2)} \\
\xi_3 &: \tilde{\mathcal{D}} \to \mathcal{T}_3, \quad \xi_3\left(\theta_1^{(k_1)}, \theta_2^{(k_2)}, \theta_3^{(k_3)}\right) = \theta_3^{(k_3)}
\end{aligned}
\tag{3.20}
$$

In order to evaluate the condition of the divergence, a threshold $\sigma_{\hat{\zeta},\mathrm{d}}$ has been established in the form of $\sigma_{\hat{\zeta}} > \sigma_{\hat{\zeta},\mathrm{d}}$.

With the aid of the threshold, the samples of the function $\sigma_{\hat{\zeta}}$ have been classified assigning a binary value, formally creating the mask function χ_d as shown in (3.21).

$$
\chi_\mathrm{d}(\theta_1, \theta_2, \theta_3) = \begin{cases} 1 & \sigma_{\hat{\zeta}}(\theta_1, \theta_2, \theta_3) > \sigma_{\hat{\zeta},\mathrm{d}} \\ 0 & \sigma_{\hat{\zeta}}(\theta_1, \theta_2, \theta_3) \leq \sigma_{\hat{\zeta},\mathrm{d}} \end{cases} \tag{3.21}
$$

The mask function χ_d is used to filter the projected grid arrays $\mathcal{T}_1$, $\mathcal{T}_2$, and $\mathcal{T}_3$, as shown in (3.22).

$$
\begin{aligned}
\mathcal{T}_1^{\chi_\mathrm{d}} &= \{\mathcal{T}_1(\theta_1, \theta_2, \theta_3) |\, \chi_\mathrm{d}(\theta_1, \theta_2, \theta_3) = 1\} \\
\mathcal{T}_2^{\chi_\mathrm{d}} &= \{\mathcal{T}_2(\theta_1, \theta_2, \theta_3) |\, \chi_\mathrm{d}(\theta_1, \theta_2, \theta_3) = 1\} \\
\mathcal{T}_3^{\chi_\mathrm{d}} &= \{\mathcal{T}_3(\theta_1, \theta_2, \theta_3) |\, \chi_\mathrm{d}(\theta_1, \theta_2, \theta_3) = 1\}
\end{aligned}
\tag{3.22}
$$

The filtering process is considered successful if there exist at least one element of the domain that satisfy the condition on the threshold, so $\mathcal{T}_1^{\chi_\mathrm{d}} \neq \emptyset$, $\mathcal{T}_2^{\chi_\mathrm{d}} \neq \emptyset$, and $\mathcal{T}_3^{\chi_\mathrm{d}} \neq \emptyset$.

Once the grid arrays have been filtered, it is possible to build the matrix of values $\mathcal{T}^{\chi_\mathrm{d}} = [\mathcal{T}_1^{\chi_\mathrm{d}}, \mathcal{T}_2^{\chi_\mathrm{d}}, \mathcal{T}_3^{\chi_\mathrm{d}}]$, concatenating the elements of each set of (3.22).

Each element $(\theta_1, \theta_2, \theta_3) \in \mathcal{T}^{\chi_\mathrm{d}}$ is a point of the domain for which $\sigma_{\hat{\zeta}}(\theta_1, \theta_2, \theta_3) > \sigma_{\hat{\zeta},\mathrm{d}}$ is satisfied. The matrix $\mathcal{T}^{\chi_\mathrm{d}}$ can be employed for the operation of clustering in order to identify the regions in which the divergence of the dispersion of the errors is supposed to happen.

At this point, the clustering operation should be applied on the set of values in $\mathcal{T}^{\chi_\mathrm{d}}$; however, considering that the set of attitude angles are defined in a domain with the shape of a cylindrical manifold with periodicity in the first and third angular dimensions, it is possible that if a cluster is on the border of the domain it is separated and identified as separated clusters.

To avoid this issue, the transformation Φ in (3.23) is considered, which is a projection on a Cartesian space from $\mathcal{D} \subset \mathbb{R}^3$ to $\Phi(\mathcal{D}) \subset \mathbb{R}^6$. In this way, the ends of the linear border are connected in a unitary circumference.

$$
\Phi(\theta_1, \theta_2, \theta_3) = [\sin(\theta_1), \cos(\theta_1), \sin(\theta_2), \cos(\theta_2), \sin(\theta_3), \cos(\theta_3)] \tag{3.23}
$$

The result of the application of Φ to the set of points of $\mathcal{T}^{\chi_\mathrm{d}}$ is denoted with $\mathcal{T}_{\mathrm{Cart}}^{\chi_\mathrm{d}}$.

To identify the clusters and their number, it is possible to evaluate the distances between each pair points of the domain, that are represented in the rows of $\mathcal{T}_{\mathrm{Cart}}^{\chi_{\mathrm{d}}}$. If the distance is sufficiently low, then two points are supposed to belong to the same cluster of points.

This can be done by building a matrix of distances; given $\mathbf{t}_{k_1} = \Phi\left(\theta_1^{(k_1)}, \theta_2^{(k_1)}, \theta_3^{(k_1)}\right)$ and $\mathbf{t}_{k_2} = \Phi\left(\theta_1^{(k_2)}, \theta_2^{(k_2)}, \theta_3^{(k_2)}\right)$ the k_1-th and k_2-th rows of the matrix $\mathcal{T}_{\mathrm{Cart}}^{\chi_{\mathrm{d}}}$, then the distance $d\left(k_1, k_2\right)$ is evaluated as reported in (3.24).

$$d\left(k_1, k_2\right) = \left\|\mathbf{t}_{k_1} - \mathbf{t}_{k_2}\right\| = \left\|\Phi\left(\theta_1^{(k_1)}, \theta_2^{(k_1)}, \theta_3^{(k_1)}\right) - \Phi\left(\theta_1^{(k_2)}, \theta_2^{(k_2)}, \theta_3^{(k_2)}\right)\right\| \tag{3.24}$$

The 2D matrix with distances $d\left(k_1, k_2\right)$ is filtered considering a threshold ε_{d}; the resulting element $d_{\mathrm{A}}\left(k_1, k_2\right)$ matrix of boolean values is reported in (3.25).

$$d_{\mathrm{A}}\left(k_1, k_2\right) = \begin{cases} 1 & d\left(k_1, k_2\right) \leq \varepsilon_{\mathrm{d}} \\ 0 & d\left(k_1, k_2\right) > \varepsilon_{\mathrm{d}} \end{cases} \tag{3.25}$$

The matrix $\mathbf{A} \in \{0{,}1\}^{m \times m}$ composed by the m resulting elements $d_{\mathrm{A}}\left(k_1, k_2\right)$ can be considered as an adjacency boolean matrix of a graph $G\left(\mathbf{A}\right)$: in particular, the value 1 indicates the presence of an edge, the value of 0 denotes the absence of a connection between the points of the domain.

At this point, the clustering is completed counting the number of connected components of the graph $G\left(\mathbf{A}\right)$.

3.2.2 Simulation and Results

The clustering approach described in Sec. 3.2.1 presents three main parameters to manage: a parameter for the number of the points in the domain N, a threshold parameter $\sigma_{\hat{\zeta},\mathrm{d}}$ considered to filter the values of the standard deviation, and the threshold on the distance of the domain ε_{d}.

To check if the proposed strategy works, a scenario of satellite in LEO with slightly off the Nadir alignment is considered; in particular, the following values are considered: $\Lambda_0 = 5°$, $\lambda_0 = 5°$, $h_0 = 0$ m, $a_0 = R_{\oplus} + 500$ km, $e_0 = 0$, $i_0 = 90°$, $\Omega_0 = 0°$, $\omega_0 = 0°$, $\nu_0 = 0°$.

To isolate the results from the influence of the relative position with respect to the Greenwich meridian, an instant of time such that $\alpha_{\mathrm{Gr}}\left(t\right) = 0°$ has been selected.

The simulations considered a frequency of $f = 1575.42$ MHz, $M_{\mathrm{x}} = M_{\mathrm{y}} = 7$ array elements for each direction, and a value of $SNR\left(p_{\mathrm{FA}}, p_{\mathrm{D}}\right) \approx 15$ dB with $+3$ dB as a safety margin.

To determine the value of the threshold $\sigma_{\hat{\zeta},\mathrm{d}}$ of the mask function, it has considered a fixed number of residual values N_{res} after the threshold resulting from on a fixed value of the index $q \in [0,1]$ of the quantile of the distribution of the synthetic data; the threshold, determined as quantile, can be reported as function of the index of the quantile as $\sigma_{\hat{\zeta},\mathrm{d}} = \sigma_{\hat{\zeta},\mathrm{d}}(q)$.

The value of N_{res} has been calculated considering the expected number of groups $\hat{N}_{\mathrm{G}}$, a mean number of points for within each group $\bar{N}_{\mathrm{g}}$, and a multiplicative factor used as safety margin N_{s}. The number of residual points, which formally is equal to the sum of the binary values of the mask function χ_{d}, after the application of the threshold is as in (3.26).

$$N_{\mathrm{res}} = \sum_{\left(\theta_1^{(k_1)},\theta_2^{(k_2)},\theta_3^{(k_3)}\right)\in\hat{\mathcal{D}}} \chi_{\mathrm{d}} = \hat{N}_{\mathrm{G}}\bar{N}_{\mathrm{g}}N_{\mathrm{sf}} \tag{3.26}$$

Given the samples of the domain $\left(\theta_1^{(k_1)},\theta_2^{(k_2)},\theta_3^{(k_3)}\right) \in \hat{\mathcal{D}}$ and the resulting synthetic data $\sigma_{\hat{\zeta}}^{(k_1,k_2,k_3)} = \sigma_{\hat{\zeta}}\left(\theta_1^{(k_1)},\theta_2^{(k_2)},\theta_3^{(k_3)}\right)$, the value of the number of the residual points N_{res} has been used to determine the quantile of such distribution.

Formally, the index q of the quantile $\sigma_{\hat{\zeta},\mathrm{d}}$ is determined by the expression of the cardinality # of the set in (3.27).

$$\#\left\{\left(\theta_1^{(k_1)},\theta_2^{(k_2)},\theta_3^{(k_3)}\right) \in \hat{\mathcal{D}}\middle|\, \sigma_{\hat{\zeta}}^{(k_1,k_2,k_3)} > \sigma_{\hat{\zeta},\mathrm{d}}(q)\right\} = N_{\mathrm{res}} \tag{3.27}$$

The mean number of points for within each group $\bar{N}_{\mathrm{g}}$ can be predicted considering a scaled subset of the total number of points of the domain; for this study an empirical value of $\bar{N}_{\mathrm{g}} = 5\,(N/10)^3$ has been considered, which demonstrated a good scalability varying the resolution of the domain.

Operatively, the reasoning is the following: the index q is such that the number of residual values N_{res} is determined by the difference $N_{\mathrm{t}} - qN_{\mathrm{t}} = N_{\mathrm{res}}$, as reported in (3.28).

$$\begin{aligned} q = \frac{N_{\mathrm{t}} - N_{\mathrm{res}}}{N_{\mathrm{t}}} &= \frac{4N^2(N-1) - \hat{N}_{\mathrm{G}}\bar{N}_{\mathrm{g}}N_{\mathrm{sf}}}{4N^2(N-1)} \\ &= \frac{4N^2(N-1) - \hat{N}_{\mathrm{G}}\left(5\left(\frac{N}{10}\right)^3\right)N_{\mathrm{sf}}}{4N^2(N-1)} \end{aligned} \tag{3.28}$$

It is expected that the order of magnitude for the number of groups is $\hat{N}_{\mathrm{G}} = O(10)$ and a further safety margin of $N_{\mathrm{sf}} = 2$ has been considered for the explorative purposes of the study.

The value of N can be selected considering the desired value of the spacing $\Delta\theta$ between consecutive samples of the attitude angles. Following the hypotheses in Sec. 3.2.1, it results $\Delta\theta = \pi/N$.

The threshold on the distances, resulted in $\varepsilon_{\mathrm{d}} = \sqrt{3}\Delta\theta = \sqrt{3}\pi/N$, has been evaluated considering the minimum chance to connect the samples $\left(\theta_1^{(k_1)}, \theta_2^{(k_2)}, \theta_3^{(k_3)}\right)$ and $\left(\theta_1^{(k_1)} + \Delta\theta, \theta_2^{(k_2)} + \Delta\theta, \theta_3^{(k_3)} + \Delta\theta\right)$.

Simulations have been conducted in MATLAB environment with a value of the resolution employed for the simulation equal to $N = 72$, corresponding to $\Delta\theta = 2.5°$: in this case, the clustering strategy identified 4 groups. The value of the thresholds resulted in $\sigma_{\hat{\zeta},\mathrm{d}} = 0.021838705709797$ rad.

In Figure 3.13 there is a scatter plot of the 4 groups and in Figure 3.14, Figure 3.15, Figure 3.16 its views along θ_1-θ_2 plane, θ_1-θ_3 plane, and θ_2-θ_3 plane.

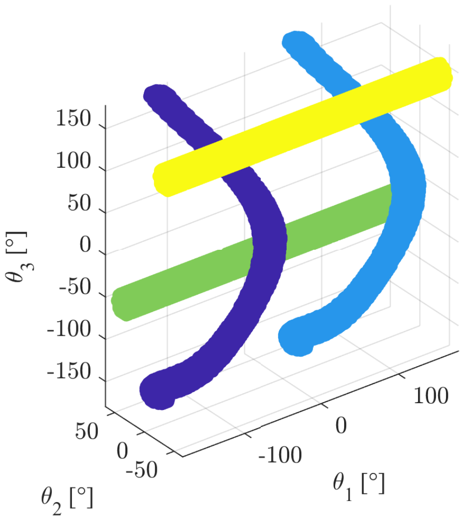

Figure 3.13: Scatter plot of the 4 clusters of attitude angles θ_1, θ_2, θ_3 identified for an AOA receiver.

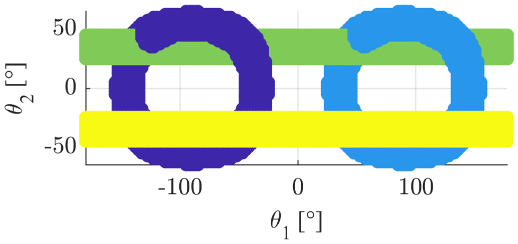

Figure 3.14: View along θ_1-θ_2 plane of the scatter plot of the 4 clusters of attitude angles θ_1, θ_2, θ_3 identified for an AOA receiver.

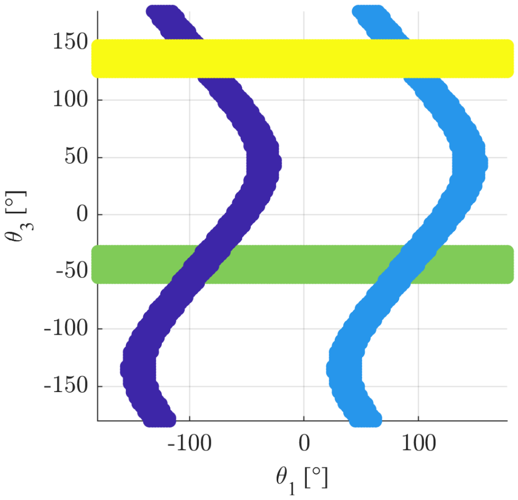

Figure 3.15: View along θ_1-θ_3 plane of the scatter plot of the 4 clusters of attitude angles θ_1, θ_2, θ_3 identified for an AOA receiver.

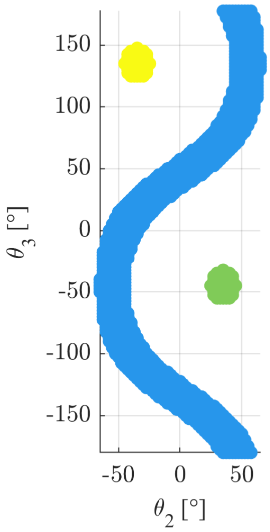

Figure 3.16: View along θ_2-θ_3 plane of the scatter plot of the 4 clusters of attitude angles θ_1, θ_2, θ_3 identified for an AOA receiver.

3.3 Divergence Management with Tri-Axial Arrays of Antennas

The approach and models developed in this section are extracted from the work of the author [64].

The starting point of the study is the problem of the geolocation of the position of a source of an electromagnetic waves $\mathbf{x}_{\mathrm{E}}$ by a satellite platform placed in $\mathbf{x}_{\mathrm{S}}$ with AOA technology [8].

In order to perform this operation, the onboard algorithm must perform the workflow depicted in Fig. 3.17; the operations are based on common representation of data in astrodynamics [2].

Each sensing array calculates its bearing angle ζ_{x}, ζ_{y}, ζ_{z}, which geometrically can be defined as the dot product between the LOB $\mathbf{u}_{\mathrm{LOB}}$ and the unit vectors of the arrays $\mathbf{u}_{\mathrm{Ar,x}}$, $\mathbf{u}_{\mathrm{Ar,y}}$, $\mathbf{u}_{\mathrm{Ar,z}}$ as shown in (3.29).

$$\begin{cases} \cos\left(\zeta_{\mathrm{x}}\right) = \mathbf{u}_{\mathrm{LOB}} \cdot \mathbf{u}_{\mathrm{Ar,x}} \\ \cos\left(\zeta_{\mathrm{y}}\right) = \mathbf{u}_{\mathrm{LOB}} \cdot \mathbf{u}_{\mathrm{Ar,y}} \\ \cos\left(\zeta_{\mathrm{z}}\right) = \mathbf{u}_{\mathrm{LOB}} \cdot \mathbf{u}_{\mathrm{Ar,z}} \end{cases} \tag{3.29}$$

Introducing [59] a local spherical coordinate system $\{x_{\mathrm{A}}, y_{\mathrm{A}}, z_{\mathrm{A}}\}$, it is possible to define the (3.29) in terms of Azimuth angle α_{Az} and Elevation angle α_{El} as shown in (3.30).

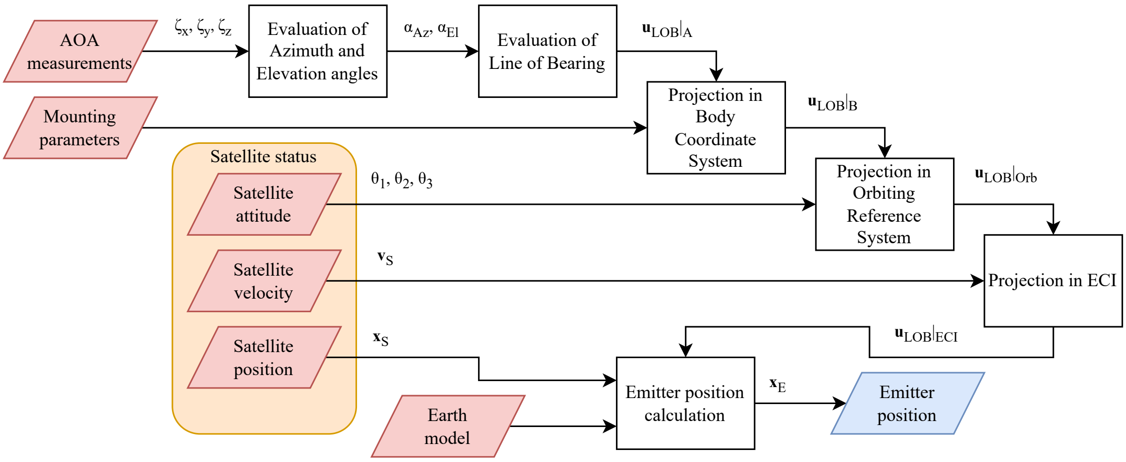

Figure 3.17: Scheme of geolocation of the position an electromagnetic emitter of signal $\mathbf{x}_{\mathrm{E}}$ from a satellite platform placed in $\mathbf{x}_{\mathrm{S}}$.

$$\begin{cases} \cos\left(\zeta_{\mathrm{x}}\right) = \mathbf{u}_{\mathrm{LOB}}\big|_{\mathrm{A}} \cdot \mathbf{u}_{\mathrm{Ar,x}}\big|_{\mathrm{A}} = \begin{pmatrix} \cos\left(\alpha_{\mathrm{Az}}\right)\cos\left(\alpha_{\mathrm{El}}\right) \\ \sin\left(\alpha_{\mathrm{Az}}\right)\cos\left(\alpha_{\mathrm{El}}\right) \\ \sin\left(\alpha_{\mathrm{El}}\right) \end{pmatrix} \cdot \begin{pmatrix} 1 \\ 0 \\ 0 \end{pmatrix} = \cos\left(\alpha_{\mathrm{Az}}\right)\cos\left(\alpha_{\mathrm{El}}\right) \\ \cos\left(\zeta_{\mathrm{y}}\right) = \mathbf{u}_{\mathrm{LOB}}\big|_{\mathrm{A}} \cdot \mathbf{u}_{\mathrm{Ar,y}}\big|_{\mathrm{A}} = \begin{pmatrix} \cos\left(\alpha_{\mathrm{Az}}\right)\cos\left(\alpha_{\mathrm{El}}\right) \\ \sin\left(\alpha_{\mathrm{Az}}\right)\cos\left(\alpha_{\mathrm{El}}\right) \\ \sin\left(\alpha_{\mathrm{El}}\right) \end{pmatrix} \cdot \begin{pmatrix} 0 \\ 1 \\ 0 \end{pmatrix} = \sin\left(\alpha_{\mathrm{Az}}\right)\cos\left(\alpha_{\mathrm{El}}\right) \\ \cos\left(\zeta_{\mathrm{z}}\right) = \mathbf{u}_{\mathrm{LOB}}\big|_{\mathrm{A}} \cdot \mathbf{u}_{\mathrm{Ar,z}}\big|_{\mathrm{A}} = \begin{pmatrix} \cos\left(\alpha_{\mathrm{Az}}\right)\cos\left(\alpha_{\mathrm{El}}\right) \\ \sin\left(\alpha_{\mathrm{Az}}\right)\cos\left(\alpha_{\mathrm{El}}\right) \\ \sin\left(\alpha_{\mathrm{El}}\right) \end{pmatrix} \cdot \begin{pmatrix} 0 \\ 0 \\ 1 \end{pmatrix} = \sin\left(\alpha_{\mathrm{El}}\right) \end{cases} \tag{3.30}$$

A measurement of a broadside angle $\hat{\zeta}$ for a linear antenna array can be unreliable when the variance $\sigma^2_{\hat{\zeta}}$, predicted through the CRLB [22] and reported in (1.50) of Sec. 1.10, diverges.

The divergence condition is $\sigma^2_{\hat{\zeta}} \rightarrow \infty$ which corresponds to $1/\sin^2\left(\zeta\right) \rightarrow \infty$ or, equivalently, to $\sin\left(\zeta\right) \rightarrow 0$ and $\zeta \rightarrow 0 + k\pi$ with $k \in \mathbb{Z}$. Operatively, for models reported in (3.29) and (3.30), the condition of divergence written as $\cos\left(\zeta\right) \rightarrow \pm 1$ is of interest.

Given a certain relative configuration between the satellite position $\mathbf{x}_{\mathrm{S}}$ and emitter position $\mathbf{x}_{\mathrm{E}}$, this divergence can occur because the antenna array axis can be aligned to the LOB because of the satellite attitude, so it is possible to assume $\zeta = \zeta\left(\theta_1, \theta_2, \theta_3\right)$ as a first attempt of abstract model, where $\theta_1, \theta_2, \theta_3$ denote the attitude angles of roll, pitch, and yaw of the satellite.

In particular, when $\hat{\zeta}_{\mathrm{x}}$ results unreliable, then $\cos\left(\hat{\alpha}_{\mathrm{Az}}\right)\cos\left(\hat{\alpha}_{\mathrm{El}}\right) \rightarrow \pm 1$ or, equivalently, $\hat{\alpha}_{\mathrm{Az}} \rightarrow k_1\pi \,\cup\, \hat{\alpha}_{\mathrm{El}} \rightarrow k_2\pi$ with $k_1, k_2 \in \mathbb{Z}$.

When $\hat{\zeta}_{\mathrm{y}}$ results unreliable, then $\sin\left(\hat{\alpha}_{\mathrm{Az}}\right)\cos\left(\hat{\alpha}_{\mathrm{El}}\right) \rightarrow \pm 1$ or, equivalently, $\hat{\alpha}_{\mathrm{Az}} \rightarrow \pi/2 + k_1\pi \,\cup\, \hat{\alpha}_{\mathrm{El}} \rightarrow k_2\pi$ with $k_1, k_2 \in \mathbb{Z}$.

When $\hat{\zeta}_{\mathrm{z}}$ results unreliable, then $\sin\left(\hat{\alpha}_{\mathrm{El}}\right) \rightarrow \pm 1$ or, equivalently, $\hat{\alpha}_{\mathrm{El}} \rightarrow \pi/2 + k\pi$ with $k \in \mathbb{Z}$.

From the representation of data in (3.30) it is possible to conclude that for each pair of broadside angles an estimation of the Azimuth and Elevation angles is possible.

Given the measurements $\hat{\zeta}_{\mathrm{x}}$ and $\hat{\zeta}_{\mathrm{y}}$, the corresponding Azimuth and Elevation angles, denoted here with $\hat{\alpha}_{\mathrm{Az;x-y}}$ and $\hat{\alpha}_{\mathrm{El;x-y}}$ can be estimated through the ones reported in 3.31.

$$\begin{cases} \hat{\alpha}_{\mathrm{Az;x-y}}\left(\hat{\zeta}_{\mathrm{x}}, \hat{\zeta}_{\mathrm{y}}\right) = \mathrm{atan2}\Big(\cos\left(\hat{\zeta}_{\mathrm{y}}\right), \cos\left(\hat{\zeta}_{\mathrm{x}}\right)\Big) \\ \hat{\alpha}_{\mathrm{El;x-y}}\left(\hat{\zeta}_{\mathrm{x}}, \hat{\zeta}_{\mathrm{y}}\right) = \sqrt{\cos^2\left(\hat{\zeta}_{\mathrm{x}}\right) + \cos^2\left(\hat{\zeta}_{\mathrm{y}}\right)} \end{cases} \tag{3.31}$$

Given the measurements $\hat{\zeta}_{\mathrm{x}}$ and $\hat{\zeta}_{\mathrm{z}}$, the corresponding Azimuth and Elevation angles, denoted with $\hat{\alpha}_{\mathrm{Az;x-z}}$ and $\hat{\alpha}_{\mathrm{El;x-z}}$ can be estimated through the ones reported in 3.32.

$$\begin{cases} \hat{\alpha}_{\mathrm{Az;x-z}}\left(\hat{\zeta}_{\mathrm{x}},\hat{\zeta}_{\mathrm{z}}\right) = \arccos\left(\dfrac{\cos\left(\hat{\zeta}_{\mathrm{x}}\right)}{\cos\left(\arcsin\left(\cos\left(\hat{\zeta}_{\mathrm{z}}\right)\right)\right)}\right) \\ \hat{\alpha}_{\mathrm{El;x-z}}\left(\hat{\zeta}_{\mathrm{z}}\right) = \arcsin\left(\cos\left(\hat{\zeta}_{\mathrm{z}}\right)\right) \end{cases} \tag{3.32}$$

Given the measurements $\hat{\zeta}_{\mathrm{y}}$ and $\hat{\zeta}_{\mathrm{z}}$, the corresponding Azimuth and Elevation angles, denoted with $\hat{\alpha}_{\mathrm{Az;y-z}}$ and $\hat{\alpha}_{\mathrm{El;y-z}}$ can be estimated through the ones reported in 3.33.

$$\begin{cases} \hat{\alpha}_{\mathrm{Az;y-z}}\left(\hat{\zeta}_{\mathrm{y}},\hat{\zeta}_{\mathrm{z}}\right) = \arcsin\left(\dfrac{\cos\left(\hat{\zeta}_{\mathrm{y}}\right)}{\cos\left(\arcsin\left(\cos\left(\hat{\zeta}_{\mathrm{z}}\right)\right)\right)}\right) \\ \hat{\alpha}_{\mathrm{El;y-z}}\left(\hat{\zeta}_{\mathrm{z}}\right) = \arcsin\left(\cos\left(\hat{\zeta}_{\mathrm{z}}\right)\right) \end{cases} \tag{3.33}$$

When all the three measurements $\hat{\zeta}_{\mathrm{x}}$, $\hat{\zeta}_{\mathrm{y}}$, $\hat{\zeta}_{\mathrm{z}}$ are reliable, then, in principle, it is possible to fuse all the estimations 3.31, 3.32, and 3.33. For simplicity and demonstrative purposes, in this study a linear model with weights $w_{\mathrm{Az;x-y}}$, $w_{\mathrm{Az;x-z}}$, $w_{\mathrm{Az;y-z}}$, $w_{\mathrm{El;x-y}}$, $w_{\mathrm{El;x-z}}$, and $w_{\mathrm{El;y-z}}$ is assumed, as in (3.34).

$$\begin{cases} \hat{\alpha}_{\mathrm{Az}}\left(\hat{\zeta}_{\mathrm{x}},\hat{\zeta}_{\mathrm{y}},\hat{\zeta}_{\mathrm{z}}\right) = w_{\mathrm{Az;x-y}}\hat{\alpha}_{\mathrm{Az;x-y}}\left(\hat{\zeta}_{\mathrm{x}},\hat{\zeta}_{\mathrm{y}}\right) + w_{\mathrm{Az;x-z}}\hat{\alpha}_{\mathrm{Az;x-z}}\left(\hat{\zeta}_{\mathrm{x}},\hat{\zeta}_{\mathrm{z}}\right) \\ \qquad + w_{\mathrm{Az;y-z}}\hat{\alpha}_{\mathrm{Az;y-z}}\left(\hat{\zeta}_{\mathrm{y}},\hat{\zeta}_{\mathrm{z}}\right) \\ \hat{\alpha}_{\mathrm{El}}\left(\hat{\zeta}_{\mathrm{x}},\hat{\zeta}_{\mathrm{y}},\hat{\zeta}_{\mathrm{z}}\right) = w_{\mathrm{El;x-y}}\hat{\alpha}_{\mathrm{El;x-y}}\left(\hat{\zeta}_{\mathrm{x}},\hat{\zeta}_{\mathrm{y}}\right) + w_{\mathrm{El;x-z}}\hat{\alpha}_{\mathrm{El;x-z}}\left(\hat{\zeta}_{\mathrm{z}}\right) \\ \qquad + w_{\mathrm{El;y-z}}\hat{\alpha}_{\mathrm{El;y-z}}\left(\hat{\zeta}_{\mathrm{z}}\right) \end{cases} \tag{3.34}$$

The set of condition on the weights are reported in (3.35).

$$\begin{cases} w_{\mathrm{Az;x-y}} + w_{\mathrm{Az;x-z}} + w_{\mathrm{Az;y-z}} = 1 \\ w_{\mathrm{El;x-y}} + w_{\mathrm{El;x-z}} + w_{\mathrm{El;y-z}} = 1 \\ 0 \le w_{\mathrm{Az;x-y}} \le 1 \\ 0 \le w_{\mathrm{Az;x-z}} \le 1 \\ 0 \le w_{\mathrm{Az;y-z}} \le 1 \\ 0 \le w_{\mathrm{El;x-y}} \le 1 \\ 0 \le w_{\mathrm{El;x-z}} \le 1 \\ 0 \le w_{\mathrm{El;y-z}} \le 1 \end{cases} \tag{3.35}$$

The reader can notice that $\hat{\alpha}_{\mathrm{El;x-z}}\left(\hat{\zeta}_{\mathrm{z}}\right) = \hat{\alpha}_{\mathrm{El;y-z}}\left(\hat{\zeta}_{\mathrm{z}}\right) = \hat{\alpha}_{\mathrm{El;z}}\left(\hat{\zeta}_{\mathrm{z}}\right)$, so it is possible to consider $w_{\mathrm{El;x-z}} = w_{\mathrm{El;y-z}} = w_{\mathrm{El;z}}$, then the second equation of 3.34 can be rewritten as reported in (3.36).

$$\begin{cases} \hat{\alpha}_{\mathrm{Az}}\left(\hat{\zeta}_{\mathrm{x}}, \hat{\zeta}_{\mathrm{y}}, \hat{\zeta}_{\mathrm{z}}\right) = w_{\mathrm{Az;x-y}}\hat{\alpha}_{\mathrm{Az;x-y}}\left(\hat{\zeta}_{\mathrm{x}}, \hat{\zeta}_{\mathrm{y}}\right) + w_{\mathrm{Az;x-z}}\hat{\alpha}_{\mathrm{Az;x-z}}\left(\hat{\zeta}_{\mathrm{x}}, \hat{\zeta}_{\mathrm{z}}\right) \\ \qquad + w_{\mathrm{Az;y-z}}\hat{\alpha}_{\mathrm{Az;y-z}}\left(\hat{\zeta}_{\mathrm{y}}, \hat{\zeta}_{\mathrm{z}}\right) \\ \hat{\alpha}_{\mathrm{El}}\left(\hat{\zeta}_{\mathrm{x}}, \hat{\zeta}_{\mathrm{y}}, \hat{\zeta}_{\mathrm{z}}\right) = w_{\mathrm{El;x-y}}\hat{\alpha}_{\mathrm{El;x-y}}\left(\hat{\zeta}_{\mathrm{x}}, \hat{\zeta}_{\mathrm{y}}\right) + 2w_{\mathrm{El;z}}\hat{\alpha}_{\mathrm{El;z}}\left(\hat{\zeta}_{\mathrm{z}}\right) \end{cases} \tag{3.36}$$

An architectural representation of the linear fusion strategy of the model (3.34) is reported in Fig. 3.18.

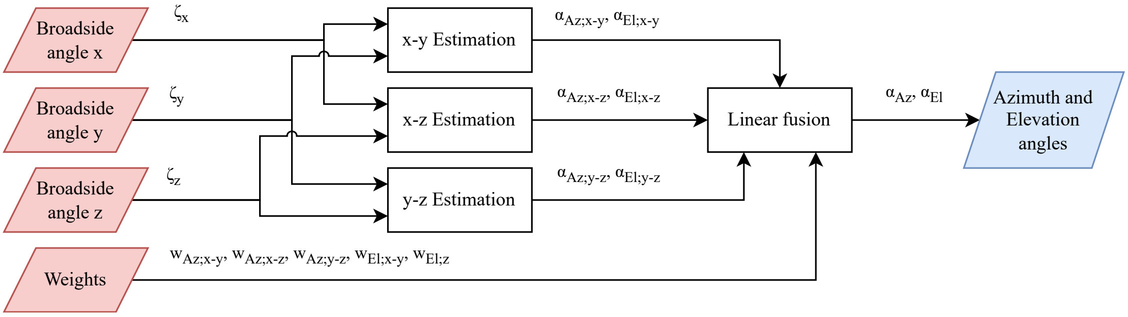

Figure 3.18: Scheme of linear fusion of the measurements with weights for the calculation of Azimuth angle α_{Az} and Elevation angle α_{El}.

Considering that an estimation of Azimuth angle and Elevation angle can be obtained even if one of the three broadside angles is unreliable, then it is possible to develop a simple scheme of reliability analysis with the selection of weights for the fusion of the measurements as reported in Fig. 3.19. More generally, it is also possible to conceive the scheme considering the estimation of the position of the emitter of the signal as additional feedback information: in this latter case, the reliability analysis is performed considering the relative position between the satellite platform and the emitter of signal $\mathbf{x}_{\mathrm{E}} - \mathbf{x}_{\mathrm{S}}$ and the full status of the satellite.

The model shows that for this payload it is possible to predict and overcome the phenomenon of the divergence of the dispersion of the measurement if the current status of the satellite is available. Despite the study is restricted to a linear fusion model, an overall reliable measurement has been obtained and a compensation scheme has been presented. The validation of the method, its simulation and experimental implementation are left for future investigations.

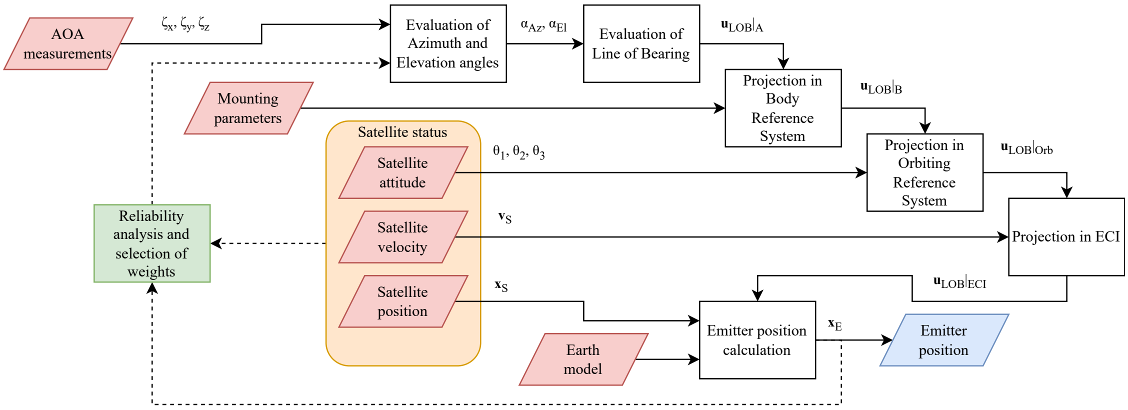

Figure 3.19: Scheme of geolocation of the position an electromagnetic emitter of signal $\mathbf{x}_E$ from a satellite platform placed in $\mathbf{x}_S$ with a scheme of reliability analysis of the measurements and selection of weights for the fusion of the measurements.

Chapter 4

Multi-Satellite Systems

This section explores the topic of multi-satellite systems. The first section 4.1 presents some high-level reasoning and differences of approach between centralized and distributed systems; Sec. 4.2 presents a semi-analytical method developed to calculate the visibility window and the angle of sight considering the relative geometry between the emitter of signal and a satellite platforms: these quantities are of interest because they constitute the main physical and geometrical constraints used to determine when a measurement with multi-satellite system (but they are of interest also for a single platform system) is possible; Sec. 4.3 shows a possible mathematical approach to formulate and solve the problem of optimization of the relative position of a cluster of satellites within a constellation in order with respect to the metrics of Dilution of Precision (DOP); besides the development of the models, in Sec. 4.4 selected campaigns of analysis explored properties of symmetry and antisymmetry for the angles that describe the constellation, changes in orbit radius and latitude of the emitter, influence of SNR in an exemplary case of cross antenna array, and what happens if the receivers are different in terms of size and number of antenna elements in an exemplary case of planar antenna array.

4.1 Centralized and Distributed Architectures

When multiple measurements from different satellite platforms are available it is important to develop a strategy to fuse the measurements.

Given a set $I = \{S_1, S_2, \dots, S_\mathrm{k}, \dots, S_\mathrm{n}\}$ of satellite platforms with the possibility to obtain $\mathbf{v}_{\mathrm{LOB},1}, \mathbf{v}_{\mathrm{LOB},2}, \dots, \mathbf{v}_{\mathrm{LOB,k}}, \dots, \mathbf{v}_{\mathrm{LOB,n}}$, in principle, two alternative approaches are possible.

The first one is a centralized architecture in which all the satellites communicate with a single reference 'node'. The reference node can be another satellite indicated with S_c, with a role of chief, or a ground station, indicated with G.

This first kind of architecture, represented in Fig. 4.1, is simple and conceptually involves the following consecutive steps:

Step 1: each k-th satellite S_{k} performs its measurement $\mathbf{v}_{\mathrm{LOB,k}}$;

Step 2: each satellite S_{k} sends its measurement $\mathbf{v}_{\mathrm{LOB,k}}$ to the chief satellite S_{c} (or to the ground station G);

Step 3: the chief satellite S_{c} (or the ground station G) performs the fusion of the collected measurements obtaining the estimated position of the emitter $\hat{\mathbf{x}}_{\mathrm{E}}$;

Step 4: if the measurement is performed by a chief satellite S_{c}, then it sends the estimated position of the emitter $\hat{\mathbf{x}}_{\mathrm{E}}$ to the ground station G, where the user is supposed to be. If there is not a chief satellite and the elaboration of the information is performed in the ground station G, then this step does not happen, because the estimation is already available to the user.

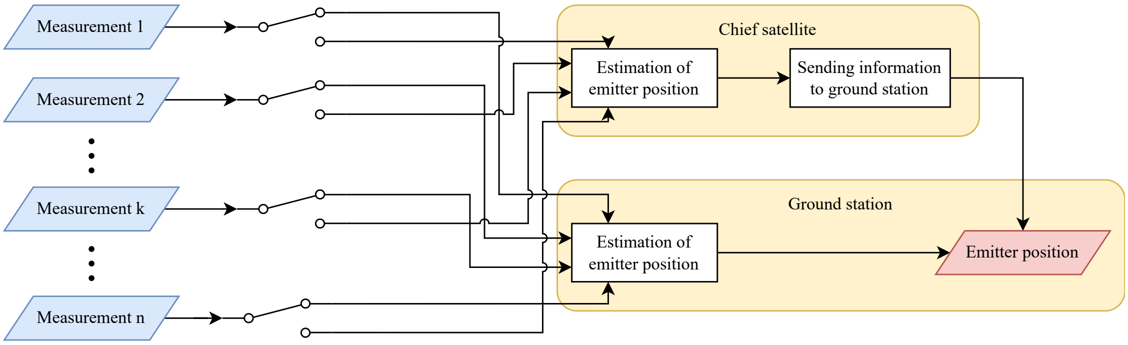

Figure 4.1: Centralized architecture for multi-satellite system.

The second strategy is a distributed solution, in which there is not a chief or a reference ground station to perform the measurements. In that case, the first conceptual steps are the following:

Step 1: each k-th satellite S_{k} performs its measurement $\mathbf{v}_{\mathrm{LOB,k}}$;

Step 4: each k-th satellite S_{k} sends its measurement $\mathbf{v}_{\mathrm{LOB,k}}$ to a subset $I^* \subseteq I \setminus \{S_{\mathrm{k}}\}$ of satellites of the same constellation, where in particular $I \neq \emptyset$; in other terms, the information is sent to at least one different satellite;

Step 3: each k-th satellite S_{k} performs its local estimation $\hat{\mathbf{x}}_{\mathrm{E,k}}$;

Step 4: each k-th satellite S_{k} sends its local estimation $\hat{\mathbf{x}}_{\mathrm{E,k}}$ to the other satellites to obtain the consensus $\hat{\mathbf{x}}_{\mathrm{E}}$;

Step 4: the obtained consensus $\hat{\mathbf{x}}_{\mathrm{E}}$ is sent to the user in the ground station G.

Compared to the centralized strategy, the distributed solution has two main difficulties: among the satellites a communication network should be designed and a convergent algorithm of consensus should be adopted.

Possible networks to be adopted are: ‘all-to-all’, a regular graph, and ‘gossip’.

An ‘all-to-all’ net means that all the satellites send the information to all the satellites.

In a regular graph all the satellites send the information to a fixed and restricted number of satellites; the quality of results and type of operation differ depending on the number of the available measurements.

The bare minimum is a 1-regular-graph, and two solutions are possible. If the graph is not oriented there will be isolated couples of satellites that exchange information, $S_1 \leftrightarrow S_2, S_3 \leftrightarrow S_4, \dots, S_{\mathrm{k}_1} \leftrightarrow S_{\mathrm{k}_2} \dots, S_{\mathrm{n}-1} \leftrightarrow S_{\mathrm{n}}$ with $n = 2m$ and $m \in \mathbb{N}$. If the graph is oriented, then the result of a 1-regular-graph is a directed cycle, $S_1 \to S_2 \to S_3 \to \cdots \to S_{\mathrm{k}_1} \to S_{\mathrm{k}_2} \to \cdots \to S_{\mathrm{n}-1} \to S_{\mathrm{n}} \to S_1$ with $n \in \mathbb{N}$.

With a 1-regular-graph the possible operation is the evaluation of the mean point between the LOBs, or its weighted version.

In a ‘gossip’ strategy each k-th satellite sends the information to a random selection of satellites.

The selection of the particular topology of communication strategy of consensus with the evaluation of its performance are beyond the purposes of this thesis and are left for future investigations.

4.2 Angle of Sight and Visibility Window

The approach and models developed in this section are extracted from the work of the author [65]: at the moment of writing this paper is ‘submitted’ and under review; the presentation, provided its acceptance, is expected to happen in May 2026 at RadarConf’26 conference.

This section proposes a semi-analytical method to evaluate two quantities of interest in mission planning: the angle of sight and the visibility window.

The two quantities are calculated for a single satellite platform S with respect to an emitter of signal E on the surface of the Earth.

In order to evaluate the corresponding angle of sight and the visibility window, the starting point is to define the portion of the orbit in which the satellite has a direct Line of Sight (LOS) with the emitter.

Formally, this can be evaluated considering the constraint determined by the plane π_{c}, which is the set of points that has a zero angle of elevation with respect to the position of the emitter $\mathbf{x}_{\mathrm{E}}$, and its intersection with the orbit of the satellite γ_{S}, which is supposed to lay on the orbital plane π_{o}, so $\gamma_{\mathrm{S}} \in \pi_{\mathrm{o}}$.

Assuming $\pi_{\mathrm{c}} \nparallel \pi_{\mathrm{o}}$, then it is possible to say that π_{c} divides in two parts the orbit, here denoted as $\gamma_{\mathrm{S},1}$ and $\gamma_{\mathrm{S},2}$. It results $\gamma_{\mathrm{S},1} \cup \gamma_{\mathrm{S},2} = \gamma_{\mathrm{S}}$.

Formally, the set of points of intersection I between the orbit γ_{S} and the constraint plane π_{c} is defined as in (4.1).

$$I = \left\{\mathbf{x} \in \mathbb{R}^3 | \pi_{\mathrm{c}} \cap \gamma_{\mathrm{S}}\right\} \tag{4.1}$$

Possible cases are: I has two distinct points, $I = \{\mathbf{x}_{\mathrm{I},1}, \mathbf{x}_{\mathrm{I},2}\}$; I has two coincident points, $I = \{\mathbf{x}_{\mathrm{I}}\}$; the set I is void, $I = \emptyset$. For this study, the third case is not considered, while the second case is considered as a particular case of the first one as $\mathbf{x}_{\mathrm{I}} = \mathbf{x}_{\mathrm{I},1} = \mathbf{x}_{\mathrm{I},2}$.

Equivalently, it is also possible to consider the definition in (4.2), where $l = (\pi_{\mathrm{c}} \cap \pi_{\mathrm{o}})$ is an auxiliary line introduced to reduce the dimensionality of the operation of intersection within the definition of the set I.

$$I = \left\{\mathbf{x} \in \mathbb{R}^3 | \left(\pi_{\mathrm{c}} \cap \pi_{\mathrm{o}}\right) \cap \gamma_{\mathrm{S}}\right\} = \left\{\mathbf{x} \in \mathbb{R}^3 | l \cap \gamma_{\mathrm{S}}\right\} \tag{4.2}$$

The set I is the intersection between an ellipse (i.e., the satellite orbit γ_{S}) and the tangent line l obtained from the zero-elevation condition.

Given a representation $\pi_{\mathrm{c}} : a_{\mathrm{c,x}}x + a_{\mathrm{c,y}}y + a_{\mathrm{c,z}}z + a_{\mathrm{c},0} = 0$, then π_{c} is the set of points in which the unitary normal vector to the plane is $\mathbf{n}_{\mathrm{c}} = \left(n_{\mathrm{x,c}}, n_{\mathrm{y,c}}, n_{\mathrm{z,c}}\right)^{\mathrm{T}} = \left(a_{\mathrm{c,x}}, a_{\mathrm{c,y}}, a_{\mathrm{c,z}}\right)^{\mathrm{T}}$.

Given a representation of the coordinates of the emitter of signal in geodetic latitude, longitude, and height, $\mathbf{x}_{\mathrm{E}}|_{\mathrm{LLH}} = (\Lambda, \lambda, h)^{\mathrm{T}}$, then the components of the normal vector to the Earth's surface plane can be calculated as in (4.3).

$$\mathbf{n}_{\mathrm{c}} = \lim_{\Delta h \to 0} \left(\frac{\mathbf{x}_{\mathrm{E}}(h + \Delta h) - \mathbf{x}_{\mathrm{E}}(h)}{\left\|\mathbf{x}_{\mathrm{E}}(h + \Delta h) - \mathbf{x}_{\mathrm{E}}(h)\right\|} \right) = \frac{\mathbf{x}_{\mathrm{E}}^{\prime}(h)}{\left\|\mathbf{x}_{\mathrm{E}}^{\prime}(h)\right\|} \tag{4.3}$$

Denoting with $s_\alpha = \sin(\alpha)$ and $c_\alpha = \cos(\alpha)$ the sine and cosine functions to compact the notation, then the representation of $\mathbf{x}_{\mathrm{E}}$ in Earth-Centered Inertial (ECI) coordinate system is as in (4.4), where $a_\oplus$ and $e_\oplus$ are the semi-major axis and the eccentricity of the ellipsoidal model of the Earth and α_{Gr} is the position of the Greenwich meridian[1].

$$\begin{cases} x_{\mathrm{E}}|_{\mathrm{ECI}} = c_{\alpha_{\mathrm{Gr}}} \left(\left(\dfrac{a_\oplus}{1 - e_\oplus^2 s_\Lambda} + h \right) c_\Lambda c_\lambda \right) - s_{\alpha_{\mathrm{Gr}}} \left(\left(\dfrac{a_\oplus}{1 - e_\oplus^2 s_\Lambda} + h \right) c_\Lambda s_\lambda \right) \\ y_{\mathrm{E}}|_{\mathrm{ECI}} = s_{\alpha_{\mathrm{Gr}}} \left(\left(\dfrac{a_\oplus}{1 - e_\oplus^2 s_\Lambda} + h \right) c_\Lambda c_\lambda \right) + c_{\alpha_{\mathrm{Gr}}} \left(\left(\dfrac{a_\oplus}{1 - e_\oplus^2 s_\Lambda} + h \right) c_\Lambda s_\lambda \right) \\ z_{\mathrm{E}}|_{\mathrm{ECI}} = \left(\dfrac{a_\oplus}{1 - e_\oplus^2 s_\Lambda} \left(1 - e_\oplus^2\right) + h \right) s_\Lambda \end{cases} \tag{4.4}$$

---

[1] To pass from LLH to ECI, an intermediate coordinate system Earth-Centered Earth-Fixed (ECEF) is considered [4].

A possible model for the parameters of Earth's ellipsoid, i.e. $a_\oplus$ and $e_\oplus$, is WGS84 [5].

Performing the derivation of (4.4) with respect to the height of the emitter h, the (4.5) are obtained.

$$\begin{cases} \dfrac{\partial\, x_\mathrm{E}|_\mathrm{ECI}}{\partial h} = c_{\alpha_\mathrm{Gr}} c_\Lambda c_\lambda - s_{\alpha_\mathrm{Gr}} c_\Lambda s_\lambda \\ \dfrac{\partial\, y_\mathrm{E}|_\mathrm{ECI}}{\partial h} = s_{\alpha_\mathrm{Gr}} c_\Lambda c_\lambda + c_{\alpha_\mathrm{Gr}} c_\Lambda s_\lambda \\ \dfrac{\partial\, z_\mathrm{E}|_\mathrm{ECI}}{\partial h} = s_\Lambda \end{cases} \tag{4.5}$$

It can be demonstrated that $\left\|\mathbf{x}'_\mathrm{E}(h)\right\| = 1$, so the normal vector $\mathbf{n}_\mathrm{c}$ is as in (4.6).

$$\mathbf{n}_\mathrm{c}|_\mathrm{ECI} = \begin{pmatrix} c_{\alpha_\mathrm{Gr}} c_\Lambda c_\lambda - s_{\alpha_\mathrm{Gr}} c_\Lambda s_\lambda \\ s_{\alpha_\mathrm{Gr}} c_\Lambda c_\lambda + c_{\alpha_\mathrm{Gr}} c_\Lambda s_\lambda \\ s_\Lambda \end{pmatrix} \tag{4.6}$$

The value of $a_{\mathrm{c},0}$ can be obtained considering that $\mathbf{x}_\mathrm{E} \in \pi_\mathrm{c}$, so its value is as in (4.7).

$$a_{\mathrm{c},0} = -\left(a_{\mathrm{c,x}}\, x_\mathrm{E}|_\mathrm{ECI} + a_{\mathrm{c,y}}\, y_\mathrm{E}|_\mathrm{ECI} + a_{\mathrm{c,z}}\, z_\mathrm{E}|_\mathrm{ECI}\right) \tag{4.7}$$

In this study, only a single representative point of interest for the emitter of signal is considered; in general, during the passage of the satellite S over an emitter of signal E, the estimation of the position of the emitter of signal includes an error in terms of longitude shift due to the rotation of the Earth: in general, this kind of evaluation requires an iterative approach, as shown in Ch. 2.

A similar representation can be assumed for the orbital plane $\pi_\mathrm{o} : a_{\mathrm{o,x}}x + a_{\mathrm{o,y}}y + a_{\mathrm{o,z}}z + a_{\mathrm{o},0} = 0$, then the unitary normal vector to the plane is $\mathbf{n}_\mathrm{o} = \left(n_{\mathrm{x,o}}, n_{\mathrm{y,o}}, n_{\mathrm{z,o}}\right)^\mathrm{T} = \left(a_{\mathrm{o,x}}, a_{\mathrm{o,y}}, a_{\mathrm{o,z}}\right)^\mathrm{T}$.

Conventionally, it is expected that the satellite orbit is represented trough the orbital parameters in PQW. In this representation it is $\mathbf{n}_\mathrm{o}|_\mathrm{PQW} = (0,0,1)^\mathrm{T}$.

The conversion from PQW to ECI is as in (4.8).

$$\mathbf{n}_\mathrm{o}|_\mathrm{ECI} = \mathbf{R}_{(\Omega,3)}\mathbf{R}_{(i,1)}\mathbf{R}_{(\omega,3)}\ \mathbf{n}_\mathrm{o}|_\mathrm{PQW} \tag{4.8}$$

Performing the operations in (4.8), the (4.9) is obtained.

$$\mathbf{n}_\mathrm{o}|_\mathrm{ECI} = \begin{pmatrix} s_\Omega s_i \\ -c_\Omega s_i \\ c_i \end{pmatrix} \tag{4.9}$$

The value of $a_{\mathrm{o},0}$ can be obtained observing that the satellite position belongs to the orbital plane $\mathbf{x}_\mathrm{S} \in \pi_\mathrm{o}$.

Performing the rotations in (1.2), the value of $a_{\mathrm{o},0}$ can be obtained from (4.10).

$$a_{\mathrm{o},0} = -\left(a_{\mathrm{o,x}}\, x_{\mathrm{S}}|_{\mathrm{ECI}} + a_{\mathrm{o,y}}\, y_{\mathrm{S}}|_{\mathrm{ECI}} + a_{\mathrm{o,z}}\, z_{\mathrm{S}}|_{\mathrm{ECI}}\right) \tag{4.10}$$

Considering a parametric representation for the line l as function of the linear parameter t_{l}, as in (4.11),

$$l: \begin{cases} x = x_{\mathrm{l},0} + v_{\mathrm{l,x}} t_{\mathrm{l}} \\ y = y_{\mathrm{l},0} + v_{\mathrm{l,y}} t_{\mathrm{l}} \qquad t_{\mathrm{l}} \in \mathbb{R}, \\ z = z_{\mathrm{l},0} + v_{\mathrm{l,z}} t_{\mathrm{l}} \end{cases} \tag{4.11}$$

then the direction vector $\mathbf{v}_{\mathrm{l}} = (v_{\mathrm{l,x}}, v_{\mathrm{l,y}}, v_{\mathrm{l,z}})^T$ can be calculated as $\mathbf{v}_{\mathrm{l}} = \mathbf{n}_{\mathrm{c}} \times \mathbf{n}_{\mathrm{o}}$, as reported in (4.12).

$$\begin{aligned} v_{\mathrm{l,x}} &= n_{\mathrm{c,y}} n_{\mathrm{o,z}} - n_{\mathrm{c,z}} n_{\mathrm{o,y}} = s_{\alpha_{\mathrm{Gr}}} c_{\Lambda} c_{\lambda} c_i + c_{\alpha_{\mathrm{Gr}}} c_{\Lambda} c_i + s_{\Lambda} c_{\Omega} s_i \\ v_{\mathrm{l,y}} &= -n_{\mathrm{c,x}} n_{\mathrm{o,z}} + n_{\mathrm{c,z}} n_{\mathrm{o,x}} = c_{\alpha_{\mathrm{Gr}}} c_{\Lambda} c_{\lambda} c_i - s_{\alpha_{\mathrm{Gr}}} c_{\Lambda} s_{\lambda} c_i - s_{\Lambda} s_{\Omega} s_i \\ v_{\mathrm{l,z}} &= n_{\mathrm{c,x}} n_{\mathrm{o,y}} - n_{\mathrm{c,y}} n_{\mathrm{o,x}} = -c_{\alpha_{\mathrm{Gr}}} c_{\Lambda} c_{\lambda} c_{\Omega} s_i + s_{\alpha_{\mathrm{Gr}}} c_{\Lambda} s_{\lambda} c_{\Omega} s_i + s_{\alpha_{\mathrm{Gr}}} c_{\Lambda} c_{\lambda} s_{\Omega} s_i \\ &\qquad + c_{\alpha_{\mathrm{Gr}}} c_{\Lambda} s_{\lambda} s_{\Omega} s_i \end{aligned} \tag{4.12}$$

The components of the point on the line $(x_{\mathrm{l},0}, y_{\mathrm{l},0}, z_{\mathrm{l},0})^{\mathrm{T}}$ can be obtained considering the system of equations in (4.13).

$$l: \begin{cases} \pi_{\mathrm{c}} : a_{\mathrm{c,x}} x + a_{\mathrm{c,y}} y + a_{\mathrm{c,z}} z + a_{\mathrm{c},0} = 0 \\ \pi_{\mathrm{o}} : a_{\mathrm{o,x}} x + a_{\mathrm{o,y}} y + a_{\mathrm{o,z}} z + a_{\mathrm{o},0} = 0 \end{cases} \tag{4.13}$$

Choosing $z_{\mathrm{l},0} = 0$, then the result is as in (4.14).

$$\begin{cases} x_{\mathrm{l},0} = \dfrac{-n_{\mathrm{y,c}} a_{\mathrm{o},0} + n_{\mathrm{y,o}} a_{\mathrm{c},0}}{n_{\mathrm{x,o}} n_{\mathrm{y,c}} - n_{\mathrm{y,o}} n_{\mathrm{x,c}}} \\ y_{\mathrm{l},0} = \dfrac{n_{\mathrm{x,c}} a_{\mathrm{o},0} - n_{\mathrm{x,o}} a_{\mathrm{c},0}}{n_{\mathrm{x,o}} n_{\mathrm{y,c}} - n_{\mathrm{y,o}} n_{\mathrm{x,c}}} \\ z_{\mathrm{l},0} = 0 \end{cases} \tag{4.14}$$

Also the elliptic orbit γ_{S} can be expressed in parametric form, as in (4.15), where a and e are the semi-major axis and the eccentricity of the orbit, the point $\mathbf{x}_{\gamma,0} = (x_{\gamma,0}, y_{\gamma,0}, z_{\gamma,0})^{\mathrm{T}}$ represents the centre of the ellipse, and the values s_{t_γ} and c_{t_γ} are the sine and cosine of the angular parameter t_γ.

$$\gamma_{\mathrm{S}}: \begin{cases} x = x_{\gamma,0} + a u_{\gamma,\mathrm{x}} c_{\mathrm{t}_\gamma} + a\sqrt{1-e^2}\, v_{\gamma,\mathrm{x}} s_{\mathrm{t}_\gamma} \\ y = y_{\gamma,0} + a u_{\gamma,\mathrm{y}} c_{\mathrm{t}_\gamma} + a\sqrt{1-e^2}\, v_{\gamma,\mathrm{y}} s_{\mathrm{t}_\gamma} \qquad t_\gamma \in [0,2\pi], \\ z = z_{\gamma,0} + a u_{\gamma,\mathrm{z}} c_{\mathrm{t}_\gamma} + a\sqrt{1-e^2}\, v_{\gamma,\mathrm{z}} s_{\mathrm{t}_\gamma} \end{cases} \tag{4.15}$$

The vectors $\mathbf{u}_\gamma = (u_{\gamma,\mathrm{x}}, u_{\gamma,\mathrm{y}}, u_{\gamma,\mathrm{z}})^T$ and $\mathbf{v}_\gamma = (v_{\gamma,\mathrm{x}}, v_{\gamma,\mathrm{y}}, v_{\gamma,\mathrm{z}})^T$ are two non-parallel vectors in the plane of the orbit, formally described by the set of conditions in (4.16).

$$\begin{cases} \mathbf{u}_\gamma \in \pi_\mathrm{o} \\ \mathbf{v}_\gamma \in \pi_\mathrm{o} \\ \mathbf{u}_\gamma \nparallel \mathbf{v}_\gamma \\ \mathbf{u}_\gamma \cdot \mathbf{n}_\mathrm{o} = 0 \\ \mathbf{v}_\gamma \cdot \mathbf{n}_\mathrm{o} = 0 \end{cases} \tag{4.16}$$

The (4.16) has 6 unknowns and 4 degrees of freedom; a possible solution is $\mathbf{u}_\gamma|_\mathrm{PQW} = (1,0,0)^\mathrm{T}$ and $\mathbf{v}_\gamma|_\mathrm{PQW} = (0,1,0)^\mathrm{T}$ with representation in ECI is as in (4.17) and in (4.18).

$$\mathbf{u}_\gamma|_\mathrm{ECI} = \mathbf{R}_{(\Omega,3)}\mathbf{R}_{(i,1)}\mathbf{R}_{(\omega,3)}\ \mathbf{u}_\gamma|_\mathrm{PQW} = \begin{pmatrix} c_\Omega c_\omega - s_\Omega c_i s_\omega \\ s_\Omega c_\omega + c_\Omega c_i s_\omega \\ s_i s_\omega \end{pmatrix} \tag{4.17}$$

$$\mathbf{v}_\gamma|_\mathrm{ECI} = \mathbf{R}_{(\Omega,3)}\mathbf{R}_{(i,1)}\mathbf{R}_{(\omega,3)}\ \mathbf{v}_\gamma|_\mathrm{PQW} = \begin{pmatrix} -c_\Omega s_\omega - s_\Omega c_i c_\omega \\ -s_\Omega s_\omega + c_\Omega c_i c_\omega \\ s_i c_\omega \end{pmatrix} \tag{4.18}$$

The centre of the ellipse $\mathbf{x}_{\gamma,0}$ can be derived considering that it is the mean point of the two foci F_1 and F_2. Assuming that the position of the Earth $\mathbf{x}_\oplus$ is in F_1, then $\mathbf{x}_{\mathrm{F}_1} = \mathbf{x}_\oplus$ and $\mathbf{x}_{\mathrm{F}_2} = \mathbf{x}_{\mathrm{F}_1} - 2ea\mathbf{a} = \mathbf{x}_\oplus - 2ea\mathbf{a}$, where $\mathbf{a}$ is the unitary vector of the line of the apsides.

Representing the positions ECI, then $\mathbf{x}_\oplus|_\mathrm{ECI} = \mathbf{0}$, obtaining $\mathbf{x}_{\mathrm{F}_2}|_\mathrm{ECI} = -2ea\ \mathbf{a}|_\mathrm{ECI}$.

The centre of the ellipse $\mathbf{x}_{\gamma,0}$ can be calculated as in (4.19).

$$\mathbf{x}_{\gamma,0}|_\mathrm{ECI} = \frac{\mathbf{x}_{\mathrm{F}_2}|_\mathrm{ECI} + \mathbf{x}_{\mathrm{F}_1}|_\mathrm{ECI}}{2} = -ea\ \mathbf{a}|_\mathrm{ECI} \tag{4.19}$$

The unitary vector of the line of apsides in PQW is represented as $\mathbf{a}|_\mathrm{PQW} = (1,0,0)^\mathrm{T}$, then its representation in ECI is as in (4.20).

$$\mathbf{a}|_\mathrm{ECI} = \mathbf{R}_{(\Omega,3)}\mathbf{R}_{(i,1)}\mathbf{R}_{(\omega,3)}\ \mathbf{a}|_\mathrm{PQW} = \begin{pmatrix} c_\Omega c_\omega - s_\Omega c_i s_\omega \\ s_\Omega c_\omega + c_\Omega c_i s_\omega \\ s_i s_\omega \end{pmatrix} \tag{4.20}$$

At this point, everything is set up to express the system of equations that can lead to the solution; in particular, the intersection between the line l and the orbit γ_S is performed equating the expressions in (4.11) and (4.15), obtaining the system of equations in (4.21).

$$\begin{cases} x_{\gamma,0} + au_{\gamma,\mathrm{x}}c_{\mathrm{t}_\gamma} + a\sqrt{1-e^2}v_{\gamma,\mathrm{x}}s_{\mathrm{t}_\gamma} = x_{\mathrm{l},0} + v_{\mathrm{l,x}}t_{\mathrm{l}} \\ y_{\gamma,0} + au_{\gamma,\mathrm{y}}c_{\mathrm{t}_\gamma} + a\sqrt{1-e^2}v_{\gamma,\mathrm{y}}s_{\mathrm{t}_\gamma} = y_{\mathrm{l},0} + v_{\mathrm{l,y}}t_{\mathrm{l}} \\ z_{\gamma,0} + au_{\gamma,\mathrm{z}}c_{\mathrm{t}_\gamma} + a\sqrt{1-e^2}v_{\gamma,\mathrm{z}}s_{\mathrm{t}_\gamma} = z_{\mathrm{l},0} + v_{\mathrm{l,z}}t_{\mathrm{l}} \end{cases} \quad t_\gamma \in [0,2\pi]\,, t_{\mathrm{l}} \in \mathbb{R} \tag{4.21}$$

The system in (4.21) has three transcendental equations with two unknown t_γ and t_{l}, this means that it is is overdetermined and two equations are sufficient to determine the solutions. Depending on the geometry, possible solutions can give up to two values for the linear parameter $t_{\mathrm{l},1}$ and $t_{\mathrm{l},2}$ and up to two values with periodicity for the angular parameter $t_{\gamma,1} + 2k\pi$ and $t_{\gamma,1} + 2k\pi$ with $k \in \mathbb{Z}$.

Once the values of the angular parameter are known, then the true anomalies ν_1 and ν_2 can be retrieved with the aid of (4.22).

$$\tan(\nu) = \frac{a\sqrt{1-e^2}s_{\mathrm{t}_\gamma}}{a\left(c_{\mathrm{t}_\gamma} - e\right)} = \frac{\sqrt{1-e^2}s_{\mathrm{t}_\gamma}}{c_{\mathrm{t}_\gamma} - e} \tag{4.22}$$

From the calculation of the true anomalies ν_1 and ν_2 obtained in (4.22), it is possible to evaluate the angle of sight $\Delta\nu$ as in (4.23), where $\hat{\nu}_1 = (\nu_1 \mod 2\pi)$ and $\hat{\nu}_2 = (\nu_2 \mod 2\pi)$ are the normalized angles of the true anomalies, so $\hat{\nu}_1 \in [0,2\pi[$ and $\hat{\nu}_2 \in [0,2\pi[$.

$$\Delta\nu = \min\left(|\hat{\nu}_2 - \hat{\nu}_1|, 2\pi - |\hat{\nu}_2 - \hat{\nu}_1|\right) \tag{4.23}$$

From values of true anomaly, then the eccentric anomalies E_1 and E_2 can be obtained from (4.24).

$$E = \operatorname{arctan2}\left(\sqrt{1-e^2}s_{\hat{\nu}}, e + c_{\hat{\nu}}\right) \tag{4.24}$$

When (4.24) is employed, the use of atan2 leads to $E \in]-\pi,\pi]$; the obtained values of E_1 and E_2 have to be normalized as $\hat{E}_1 = (E_1 \mod 2\pi)$ and $\hat{E}_2 = (E_2 \mod 2\pi)$ in order to have $\hat{E}_1 \in [0,2\pi[$ and $\hat{E}_2 \in [0,2\pi[$.

Once the normalized eccentric anomalies $\hat{E}_1$ and $\hat{E}_2$ have been obtained, then the mean anomalies M_1 and M_2 are obtained from the classic relationship in (4.25).

$$M = \hat{E} - es_{\hat{\mathrm{E}}} \tag{4.25}$$

Since $\hat{E} \in [0,2\pi[$, then $M \in [0,2\pi[$ follows, so it is not necessary to normalize the values of M_1 and M_2. At this point, it is possible to retrieve the minimum difference of the instants of time t_1 and t_2 associated to the passage of the satellite in ν_1 and ν_2 with the aid of (4.26), where t is the current time, τ is the time of pericenter, and T is the period of the orbit, calculated as $T = 2\pi\sqrt{a^3/\mu_\oplus}$; in particular, $\mu_\oplus$ is the standard gravitational parameter of the Earth.

$$t - \tau = \frac{MT}{2\pi} \tag{4.26}$$

The visibility window Δt_v can be obtained as in (4.27), where ΔM is calculated as in (4.28).

$$\Delta t_\mathrm{v} = \Delta M \frac{T}{2\pi} \tag{4.27}$$

$$\Delta M = \min\left(|M_2 - M_1|, 2\pi - |M_2 - M_1|\right) \tag{4.28}$$

The normalization in (4.28) is necessary because having $M_1 \in [0,2\pi[$ and $M_2 \in [0,2\pi[$ do not imply that $M_2 - M_1 \in [0,2\pi[$ and $M_1 - M_2 \in [0,2\pi[$.

The method proposed is completely analytical and every passage can be solved without numerical aids, with the only exception of the solution of the system of equations in (4.21).

4.2.1 Choice of Initial Conditions

This system in (4.21) is composed of equations with a linear term in t_l and trigonometric functions of t_γ; the strategies of resolution are generally iterative and based on multivariate Newton-Raphson algorithm or its variants [66].

In order to solve the system numerically and obtain the two different solutions, the choice of initial conditions is important.

It can be observed that for a spherical Earth and circular orbit and in the case of a Zenith passage over the emitter, the maximum interval of true anomaly of visibility is as in (4.29).

$$\max\left(\Delta\nu_\mathrm{v}\right) = 2\arccos\left(\frac{R_\oplus}{r}\right) \tag{4.29}$$

This means that, given an arbitrary configuration with a satellite in a certain orbit with radius r, the two different linear parameters $t_{\mathrm{l},1}$ and $t_{\mathrm{l},2}$ are within the intervals reported in (4.30).

$$\begin{gathered} 0 \le t_{\mathrm{l},1} \le r\arccos\left(\max\Delta\nu_\mathrm{v}\right) \\ -r\arccos\left(\max\Delta\nu_\mathrm{v}\right) \le t_{\mathrm{l},2} \le 0 \end{gathered} \tag{4.30}$$

Assuming a completely unknown passage of the satellite over the emitter, a good choice of attempt for the initial values of the linear parameter $t_{\mathrm{l},1,\mathrm{Init}}$ and $t_{\mathrm{l},2,\mathrm{Init}}$ can be the half points reported in (4.31).

$$\begin{aligned} t_{\mathrm{l},1,\mathrm{Init}} &= \frac{1}{2} r\arccos\left(\max\left(\Delta\nu_\mathrm{v}\right)\right) \\ t_{\mathrm{l},2,\mathrm{Init}} &= -\frac{1}{2} r\arccos\left(\max\left(\Delta\nu_\mathrm{v}\right)\right) \end{aligned} \tag{4.31}$$

Consequently, the parameter t_γ related to the ellipse can be obtained observed that the equations reported in (4.21) are in the form $A+Bc_{\mathrm{t}_\gamma}+Cs_{\mathrm{t}_\gamma}=0$. Assuming the transformation $Dc_\beta = B$ and $Ds_\beta = C$, the equation will be in the form $A+Dc_\beta c_{\mathrm{t}_\gamma}+Ds_\beta s_{\mathrm{t}_\gamma}=0$. Exploiting the identity $c_\beta c_{\mathrm{t}_\gamma}+s_\beta s_{\mathrm{t}_\gamma}=c_{(\mathrm{t}_\gamma-\beta)}$, then the equation can be written in the form $A+Dc_{(\mathrm{t}_\gamma-\beta)}=0$. In particular, depending on the choice $j=\{1{,}2{,}3\}$ of the equation, A can be one of the following

$$A^{(j)}\left(t_{\mathrm{l},k,\mathrm{Init}}\right)=\begin{cases} x_{0,\gamma}-x_{0,\mathrm{l}}-v_{\mathrm{l,x}}t_{\mathrm{l},k,\mathrm{Init}} & j=1,k=1{,}2\\ y_{0,\gamma}-y_{0,\mathrm{l}}-v_{\mathrm{l,y}}t_{\mathrm{l},k,\mathrm{Init}} & j=2,k=1{,}2\\ z_{0,\gamma}-z_{0,\mathrm{l}}-v_{\mathrm{l,z}}t_{\mathrm{l},k,\mathrm{Init}} & j=3,k=1{,}2\end{cases}, \tag{4.32}$$

B can be one of the following

$$B^{(j)}=\begin{cases} au_{\gamma,\mathrm{x}} & j=1\\ au_{\gamma,\mathrm{y}} & j=3\\ au_{\gamma,\mathrm{z}} & j=3\end{cases}, \tag{4.33}$$

and C can be one of the following

$$C^{(j)}=\begin{cases} a\sqrt{1-e^2}v_{\gamma,\mathrm{x}} & j=1\\ a\sqrt{1-e^2}v_{\gamma,\mathrm{y}} & j=2\\ a\sqrt{1-e^2}v_{\gamma,\mathrm{z}} & j=3\end{cases}. \tag{4.34}$$

Given $D^{(j)}=\sqrt{\left(B^{(j)}\right)^2+\left(C^{(j)}\right)^2}$ and $\beta^{(j)}=\arccos\left(B^{(j)}/D^{(j)}\right)$, the parameters $t^{(j)}_{\gamma,1,\mathrm{Init}}$ and $t^{(j)}_{\gamma,2,\mathrm{Init}}$ can be obtained as in (4.35).

$$t^{(j)}_{\gamma,k,\mathrm{Init}}=\beta^{(j)}+\arccos\left(\frac{A^{(j)}\left(t_{l,k,\mathrm{Init}}\right)}{D^{(j)}}\right)\quad k=1{,}2 \tag{4.35}$$

In particular, it is important to check that $t^{(j)}_{\gamma,1,\mathrm{Init}}\neq t^{(j)}_{\gamma,2,\mathrm{Init}}$. If this does not happen, it is because of the choice of the equation represented by the index j; in particular, the reader must pay attention that in the selected equation j, the two solutions differ because of the value of the linear parameter $t_{l,k,\mathrm{Init}}$ in the expression of $A^{(j)}$ in (4.32). The issue does not happen if in the selected equation the value of $v_{\mathrm{l,x}}$, $v_{\mathrm{l,y}}$, or $v_{\mathrm{l,z}}$ is non-zero. To avoid the issue, it is suggested to select the component j that has the highest value in modulus, as shown in (4.36).

$$j=\underset{\mathrm{m}\in\{\mathrm{x,y,z}\}}{\arg\max}\left(\left|v_{\mathrm{l,m}}\right|\right) \tag{4.36}$$

From the experience of the author, this approach to the choice of the initial guess for the iterations converges to two different solutions.

4.2.2 Solving the System of Equations

After the determination of initial guesses as shown in Sec. 4.2.1, the system of equations can be solved with multivariate Newton-Raphson method or any equivalent method.

The system (4.21) has three equations and two unknowns; it is overdetermined, and two equations are actually sufficient to retrieve the solutions. To compact the notation, the two selected equations are written in the general form $\mathbf{F}\left(t_\gamma, t_\mathrm{l}\right) = \left[f_1\left(t_\gamma, t_\mathrm{l}\right), f_2\left(t_\gamma, t_\mathrm{l}\right)\right]^\mathrm{T} = [0,0]^\mathrm{T}$. The Jacobian $\mathbf{J}$ can be calculated as in (4.37).

$$\mathbf{J}\left(t_\gamma, t_\mathrm{l}\right) = \begin{bmatrix} \frac{\partial f_1(t_\gamma,t_\mathrm{l})}{\partial t_\gamma} & \frac{\partial f_1(t_\gamma,t_\mathrm{l})}{\partial t_\mathrm{l}} \\ \frac{\partial f_2(t_\gamma,t_\mathrm{l})}{\partial t_\gamma} & \frac{\partial f_2(t_\gamma,t_\mathrm{l})}{\partial t_\mathrm{l}} \end{bmatrix} \tag{4.37}$$

The solution can be retrieved iterating the steps from n to $n+1$ as in (4.38).

$$\begin{bmatrix} \left(t_\gamma\right)_{n+1} \\ \left(t_\mathrm{l}\right)_{n+1} \end{bmatrix} = \begin{bmatrix} \left(t_\gamma\right)_{n} \\ \left(t_\mathrm{l}\right)_{n} \end{bmatrix} - \mathbf{J}^{-1}\left(\left(t_\gamma\right)_n, \left(t_\mathrm{l}\right)_n\right)\mathbf{F}\left(\left(t_\gamma\right)_n, \left(t_\mathrm{l}\right)_n\right) \tag{4.38}$$

To check the convergence, the stopping criteria are based on the two conditions reported in (4.39) with $\varepsilon_\mathrm{F} \ll 1$ for residuals and $\varepsilon_\mathrm{t} \ll 1$ for the increment $\left(\Delta\mathbf{t}\right)_{n+1} = \mathbf{t}_{n+1} - \mathbf{t}_n$.

$$\begin{gathered} \left\|\mathbf{F}\left(\left(t_\gamma\right)_n, \left(t_\mathrm{l}\right)_n\right)\right\|^2 \leq \varepsilon_\mathrm{F} \\ \left\|\left(\Delta\mathbf{t}\right)_{n+1}\right\| \leq \varepsilon_\mathrm{t} \end{gathered} \tag{4.39}$$

The feasibility and correctness of the method have been checked with simulations in MATLAB environment using `fsolve` with `trust-region`.

The first check has been done considering a well-known trivial case of an emitter of signal in $\Lambda = 0°$, $\lambda = 0°$, and $h = 0$ m and a satellite in LEO with values of $a = R_\oplus + 500000$ km, $e = 0$, $i = 90°$, $\Omega = 0°$, and $\omega = 0°$; assuming $\varepsilon_\mathrm{F} = 10^{-24}$ and $\varepsilon_\mathrm{t} = 10^{-24}$, the method converged giving an angle of sight of $\Delta\nu = 43.9858°$ and visibility window of $\Delta t_\mathrm{v} = 692.549$ s as expected.

Example of values of residuals and increments are reported in Fig. 4.2 for the solution $t_{\mathrm{l},2}$ and $t_{\gamma,2}$. Similar values have been obtained for $t_{\mathrm{l},1}$ and $t_{\gamma,1}$.

From Fig. 4.2 results that $\|\mathbf{F}\|$ limits the convergence in the first three iterations, then in the subsequent iterations $\|(\Delta\mathbf{t})\|$ has more impact, meaning that both the stopping criteria ε_F and ε_t are important to achieve the convergence.

Other two tests have been conducted varying the orbit size in terms of a and the right ascension of the ascending node Ω.

The first test considered an emitter of signal in $\Lambda = 41.108852°$, $\lambda = 16.878680°$, and $h = 0$ m and a satellite in LEO with values of $e = 0.001$, $i = 90°$, $\Omega = 15°$, and $\omega = 45°$ the method converged to the solutions in Tab. 4.1.

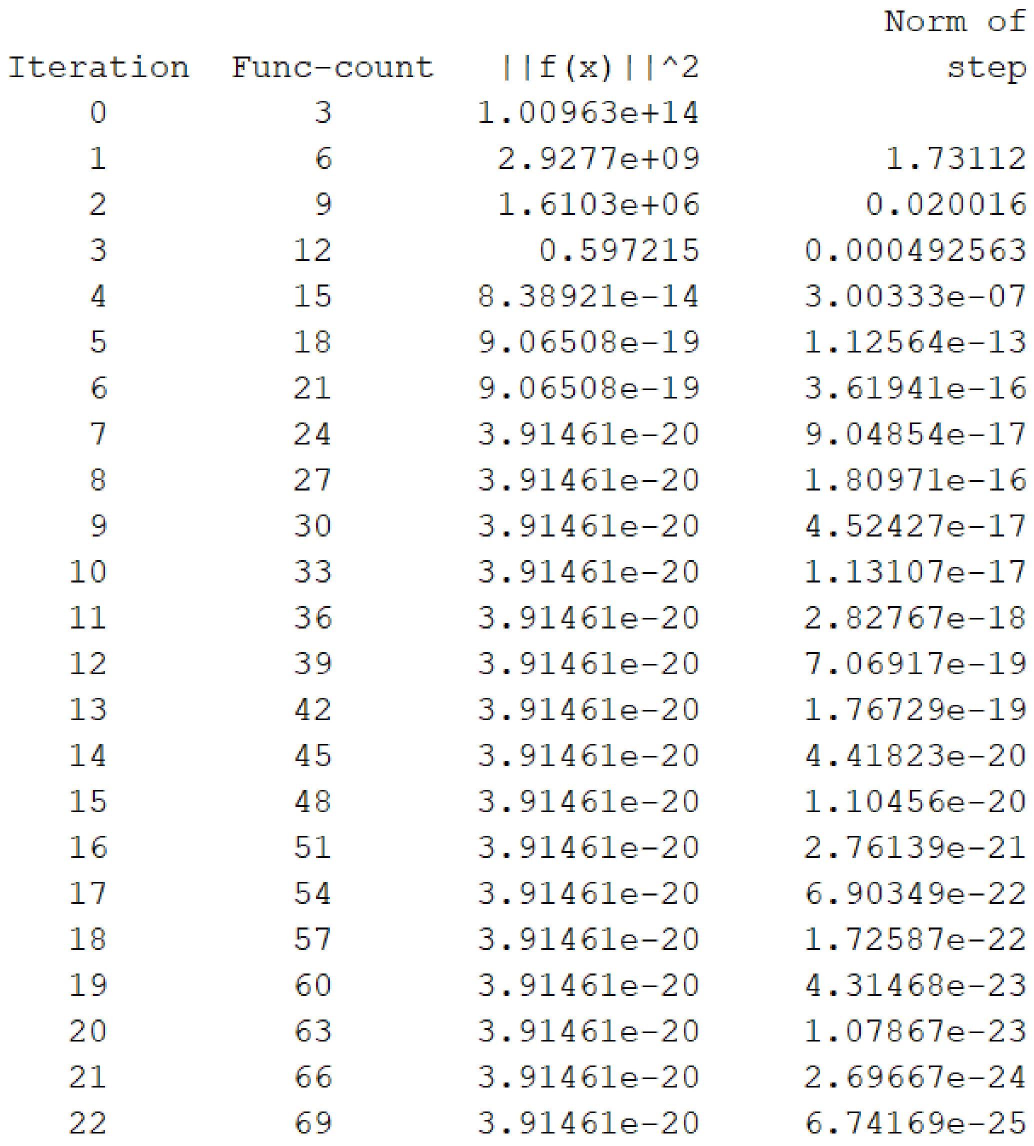

```
                                              Norm of
 Iteration  Func-count    ||f(x)||^2           step
     0           3       1.00963e+14
     1           6        2.9277e+09          1.73112
     2           9        1.6103e+06         0.020016
     3          12          0.597215      0.000492563
     4          15       8.38921e-14      3.00333e-07
     5          18       9.06508e-19      1.12564e-13
     6          21       9.06508e-19      3.61941e-16
     7          24       3.91461e-20      9.04854e-17
     8          27       3.91461e-20      1.80971e-16
     9          30       3.91461e-20      4.52427e-17
    10          33       3.91461e-20      1.13107e-17
    11          36       3.91461e-20      2.82767e-18
    12          39       3.91461e-20      7.06917e-19
    13          42       3.91461e-20      1.76729e-19
    14          45       3.91461e-20      4.41823e-20
    15          48       3.91461e-20      1.10456e-20
    16          51       3.91461e-20      2.76139e-21
    17          54       3.91461e-20      6.90349e-22
    18          57       3.91461e-20      1.72587e-22
    19          60       3.91461e-20      4.31468e-23
    20          63       3.91461e-20      1.07867e-23
    21          66       3.91461e-20      2.69667e-24
    22          69       3.91461e-20      6.74169e-25
```

Figure 4.2: Values of residuals $\|\mathbf{F}\|^2$ and increments $\|(\Delta \mathbf{t})\|$, indicated as $\|f(x)\|^2$ and 'norm of step', respectively, in the MATLAB environment.

Table 4.1: Values of angle of sight $\Delta\nu$ and visibility window Δt_{v} with respect to the semi-major axis of the orbit a.

a [km]	$\Delta\nu$ [°]	Δt_{v} [s]
$R_{\oplus} + 400$	46.178	711.25
$R_{\oplus} + 800$	50.764	852.18
$R_{\oplus} + 1200$	54.581	993.98
$R_{\oplus} + 1600$	57.855	1138.2
$R_{\oplus} + 2000$	60.710	1285.4

The second test considered an emitter of signal in $\Lambda = 40.452730°$, $\lambda = -3.726092°$, and $h = 0$ m and a satellite in LEO with values of $a = R_{\oplus} + 500000$ km, $e = 0.003$, $i = 90°$, and $\omega = 40°$ the method converged to the solutions in Tab. 4.2.

Table 4.2: Values of angle of sight $\Delta\nu$ and visibility window Δt_{v} with respect to the right ascension of the ascending node Ω.

Ω [°]	$\Delta\nu$ [°]	Δt_{v} [s]
0	47.536	748.45
10	45.257	712.57
20	38.377	604.24
30	23.248	366.04
33	13.004	204.74
35	0.025791	0.40607

.

4.3 Optimization of Satellite Constellations

Part of this section is extracted from the published works of the author [67], [68], [69], [70], and [23].

4.3.1 Dilution of Precision

In satellite systems for geolocation purposes, the variance of the error estimation has two main sources: the error on the single measurement, which depends mainly on the frequency of the signal itself, on the SNR and on the particular characteristics of receiver (e.g., number of antennas and their distribution into the space); the error due to the distribution of the receivers in the space, also known as DOP.

A common strategy of compensations of the variance in a noisy measurement is though multiple measurements. In satellite systems this can be achieved through multiple measurements over time with a single receiver or with multiple measurements performed by multiple satellite platforms.

The second strategy is obviously expensive compared to the first one, because there is not only the need of realization of other satellite platforms, but also their management and maintenance. So the addition of a new satellite in a constellation used for geolocation purposes is a strategy employed only when the first possibility is already evaluated and exploited.

The second source of error has a geometric origin and it is known as DOP, which arises from the spatial distribution of receivers in space. The minimization of the DOP enhances the overall precision of the geolocation system and improves the services that rely on satellite-based geolocation. The optimization of the spatial distribution of satellites in constellations started in the context of Global GNSS [71] [72], although for these kind of systems the measurement is based on Time of Arrival (TOA).

In addition to GNSS studies, some works have focused on terrestrial wireless systems exploring fixed geometries in a plane (e.g., triangular, squared and hexagonal distributions, [73]) as well as optimal geometrical distributions of receivers in two dimensions [74], [75]. Other studies have derived closed-form solutions for estimation errors [76], developed closed-form estimators for hybrid measurements (i.e., combining AOA with other techniques), and explored the simultaneous localization of multiple emitters [77].

Recent mathematical analyses, driven by the availability of different GNSS systems, have focused on determining how many satellites minimize the DOP for GNSS systems [78], [79], on reducing computational costs [80], and on developing approximate solutions using artificial intelligence in non-line-of-sight conditions [81].

In this section, the signal emitter is denoted with E, while satellites are indicated with $S_1, S_2, \ldots, S_\mathrm{k}, \ldots, S_\mathrm{n}$, where n is the total number of satellites.

Given two satellites S_{k_1} and S_{k_2} a quantity of interest, useful to describe the relative geometry of the constellation, is the spacing angle $\gamma_{\mathrm{k}_1,\mathrm{k}_2} = \angle S_{\mathrm{k}_1} E S_{\mathrm{k}_2}$ between the satellite S_{k_1} and S_{k_1} with respect to the emitter position E, which can be calculated as in (4.40).

$$\gamma_{\mathrm{k}_1,\mathrm{k}_2} = \arccos\left(\frac{\overrightarrow{ES_{\mathrm{k}_1}}}{\left\|\overrightarrow{ES_{\mathrm{k}_1}}\right\|} \cdot \frac{\overrightarrow{ES_{\mathrm{k}_2}}}{\left\|\overrightarrow{ES_{\mathrm{k}_2}}\right\|} \right) \tag{4.40}$$

Given n satellite platforms with n AOA receivers, it is possible to obtain $\mathbf{v}_{\mathrm{LOB},1}, \mathbf{v}_{\mathrm{LOB},2}, \ldots, \mathbf{v}_{\mathrm{LOB,k}}, \ldots, \mathbf{v}_{\mathrm{LOB,n}}$ measurements.

In general, for a system of satellites composed of platforms equipped with AOA receivers, at least two non-parallel LOB are needed to perform the geolocation. The LOBs can come from at least two non-aligned platforms, i.e., given two LOBS $\mathbf{v}_{\mathrm{LOB,k}_1}$ and $\mathbf{v}_{\mathrm{LOB,k}_2}$, they satisfy the condition $\mathbf{v}_{\mathrm{LOB,k}_1} \nparallel \mathbf{v}_{\mathrm{LOB,k}_2}$.

This section considers the single measurement for each satellite platform; then the intersection of the LOBs obtained in a certain instant of time can reveal the unknown position of the emitter $\mathbf{x}_\mathrm{E}$.

Considering that the measurements are affected by errors, the estimation of the position is generally done through the least squares method.

Representing the LOB in a spherical coordinate system, the single LOB can be defined by a unitary radius (which is not relevant) and a set of two angles, generally denoted by azimuth angle and polar angle (or Zenith angle) [59].

In general, if the coordinate system is the one fixed on the satellite receiver, the two set of angles are denoted by Azimuth angle (in the following with subscript Az) and Elevation angle (in the following with subscript El). The representation of these angles is not unique in literature, with different conventions depending on the reference directions used to calculate them. Details on these representations can be found in [60], [61].

In order to perform the measurement in every direction, at least two elements per orthogonal direction are necessary; the measurement is then obtained through the difference in phase of the impinging electromagnetic wave. In this case, it is possible to have two measured angles: Azimuth angle α_{Az} and Elevation angle α_{El}.

In this section the representation of the Azimuth angle $\alpha_{\mathrm{Az,k}}$ and the Elevation angle $\alpha_{\mathrm{El,k}}$ for the k-th satellite considered in this study is the one reported in (4.41).

$$\begin{cases} \alpha_{\mathrm{Az,k}} = \operatorname{atan2}(y_{\mathrm{E}} - y_{\mathrm{S_k}}, x_{\mathrm{E}} - x_{\mathrm{S_k}}) \quad k = 1,2,\dots,n \\ \alpha_{\mathrm{El,k}} = \operatorname{atan2}\left(\sqrt{(x_{\mathrm{E}} - x_{\mathrm{S_k}})^2 + (y_{\mathrm{E}} - y_{\mathrm{S_k}})^2}, z_{\mathrm{E}} - z_{\mathrm{S_k}}\right) \quad k = 1,2,\dots,n \end{cases} \tag{4.41}$$

Considering (4.41), and given n AOA receivers, the number of possible independent AOA measurement equations in a certain instant of time is $N_{\mathrm{AOA}} = 2n$.

From the measurement equations (4.41) it is possible to write the calculate the DOP.

The DOP is calculated considering the square root of the trace of the inverse of the Fisher Information Matrix $\mathbf{F}$, as shown in (4.42).

$$DOP = \sqrt{Tr\left(\mathbf{F^{-1}}\right)} \tag{4.42}$$

Depending on the variables considered for the problem, the matrix $\mathbf{F}$ can be a 2×2 matrix for 2D spatial problems, a 3×3 matrix for 3D spatial problems, and a 4×4 matrix for 3D space-time problems.

For this section, the Position Dilution of Precision $PDOP$ is considered, which takes into account the three spatial coordinates. Therefore, $\mathbf{F}$ is a 3×3 matrix, as shown in (4.43).

$$PDOP = \sqrt{Tr\left(\mathbf{F}_{3\times 3}^{-1}\right)} \tag{4.43}$$

A common decomposition for the Fisher Information Matrix $\mathbf{F}$ is as shown in (4.44).

$$\mathbf{F} = \mathbf{H}^{\mathrm{T}}\mathbf{C^{-1}}\mathbf{H} \tag{4.44}$$

In particular, $\mathbf{C}$ is the Covariance Matrix and $\mathbf{H}$ is the geometric design matrix. For this study, the geometric design matrix is composed by the set of derivatives of the equations of measurements with respect to the position coordinates of the emitter $(x_{\mathrm{E}}, y_{\mathrm{E}}, z_{\mathrm{E}})$, as shown in (4.45).

$$
\mathbf{H} = \begin{pmatrix}
\frac{\partial \alpha_{\mathrm{Az,1}}}{\partial x_{\mathrm{E}}} & \frac{\partial \alpha_{\mathrm{Az,1}}}{\partial y_{\mathrm{E}}} & \frac{\partial \alpha_{\mathrm{Az,1}}}{\partial z_{\mathrm{E}}} \\
\frac{\partial \alpha_{\mathrm{El,1}}}{\partial x_{\mathrm{E}}} & \frac{\partial \alpha_{\mathrm{El,1}}}{\partial y_{\mathrm{E}}} & \frac{\partial \alpha_{\mathrm{El,1}}}{\partial z_{\mathrm{E}}} \\
\frac{\partial \alpha_{\mathrm{Az,2}}}{\partial x_{\mathrm{E}}} & \frac{\partial \alpha_{\mathrm{Az,2}}}{\partial y_{\mathrm{E}}} & \frac{\partial \alpha_{\mathrm{Az,2}}}{\partial z_{\mathrm{E}}} \\
\frac{\partial \alpha_{\mathrm{El,2}}}{\partial x_{\mathrm{E}}} & \frac{\partial \alpha_{\mathrm{El,2}}}{\partial y_{\mathrm{E}}} & \frac{\partial \alpha_{\mathrm{El,2}}}{\partial z_{\mathrm{E}}} \\
\vdots & \vdots & \vdots \\
\frac{\partial \alpha_{\mathrm{Az,k}}}{\partial x_{\mathrm{E}}} & \frac{\partial \alpha_{\mathrm{Az,k}}}{\partial y_{\mathrm{E}}} & \frac{\partial \alpha_{\mathrm{Az,k}}}{\partial z_{\mathrm{E}}} \\
\frac{\partial \alpha_{\mathrm{El,k}}}{\partial x_{\mathrm{E}}} & \frac{\partial \alpha_{\mathrm{El,k}}}{\partial y_{\mathrm{E}}} & \frac{\partial \alpha_{\mathrm{El,k}}}{\partial z_{\mathrm{E}}} \\
\vdots & \vdots & \vdots \\
\frac{\partial \alpha_{\mathrm{Az,n}}}{\partial x_{\mathrm{E}}} & \frac{\partial \alpha_{\mathrm{Az,n}}}{\partial y_{\mathrm{E}}} & \frac{\partial \alpha_{\mathrm{Az,n}}}{\partial z_{\mathrm{E}}} \\
\frac{\partial \alpha_{\mathrm{El,n}}}{\partial x_{\mathrm{E}}} & \frac{\partial \alpha_{\mathrm{El,n}}}{\partial y_{\mathrm{E}}} & \frac{\partial \alpha_{\mathrm{El,n}}}{\partial z_{\mathrm{E}}}
\end{pmatrix} \tag{4.45}
$$

The elements of the Covariance matrix $\mathbf{C}$ are constituted by the covariance between each pair of measurements. In particular, for this context, it is supposed that the measurement errors are Gaussian and independent. Under these hypothesis, the Covariance matrix $\mathbf{C}$ is diagonal, with variances on the main diagonal, calculated as CRLB of Sec. 1.10. In particular, the construction of the Covariance matrix $\mathbf{C}$ has to follow the same order of construction of the geometric design matrix $\mathbf{H}$. Considering the ordering of equations in (4.45).

$$
\begin{split}
\mathbf{C} = \mathrm{diag}\Big(&\sigma^2_{\mathrm{AOA},\hat{\alpha}_{\mathrm{Az,1}}}, \sigma^2_{\mathrm{AOA},\hat{\alpha}_{\mathrm{El,1}}}, \sigma^2_{\mathrm{AOA},\hat{\alpha}_{\mathrm{Az,2}}}, \sigma^2_{\mathrm{AOA},\hat{\alpha}_{\mathrm{El,2}}}, \dots, \\
&\sigma^2_{\mathrm{AOA},\hat{\alpha}_{\mathrm{Az,k}}}, \sigma^2_{\mathrm{AOA},\hat{\alpha}_{\mathrm{El,k}}}, \dots, \sigma^2_{\mathrm{AOA},\hat{\alpha}_{\mathrm{Az,n}}}, \sigma^2_{\mathrm{AOA},\hat{\alpha}_{\mathrm{El,n}}}\Big)
\end{split} \tag{4.46}
$$

4.3.2 Derivatives for AOA Measurement Equations

Before the evaluation of derivatives it is observed that

$$
\begin{aligned}
\frac{\partial \left(\mathrm{atan2}(x,y)\right)}{\partial x} &= \frac{\partial \left(\arctan\left(\frac{x}{y}\right)\right)}{\partial x} \\
\frac{\partial \left(\mathrm{atan2}(x,y)\right)}{\partial y} &= \frac{\partial \left(\arctan\left(\frac{x}{y}\right)\right)}{\partial y}.
\end{aligned} \tag{4.47}
$$

Here are reported the derivatives for AOA equations (4.41). In (4.48) there is the derivative of the Azimuth angle $\alpha_{\mathrm{Az,k}}$ with respect to the variable x_{E}.

$$\begin{aligned}\frac{\partial \alpha_{\mathrm{Az,k}}}{\partial x_{\mathrm{E}}} &= \frac{\partial \left(\arctan\left(\frac{y_{\mathrm{E}}-y_{\mathrm{S_k}}}{x_{\mathrm{E}}-x_{\mathrm{S_k}}}\right)\right)}{\partial x_{\mathrm{E}}} = \frac{1}{1+\left(\frac{y_{\mathrm{E}}-y_{\mathrm{S_k}}}{x_{\mathrm{E}}-x_{\mathrm{S_k}}}\right)^2}\frac{\partial \left(\frac{y_{\mathrm{E}}-y_{\mathrm{S_k}}}{x_{\mathrm{E}}-x_{\mathrm{S_k}}}\right)}{\partial x_{\mathrm{E}}} \\ &= \frac{\left(y_{\mathrm{E}}-y_{\mathrm{S_k}}\right)}{1+\left(\frac{y_{\mathrm{E}}-y_{\mathrm{S_k}}}{x_{\mathrm{E}}-x_{\mathrm{S_k}}}\right)^2}\frac{\partial \left(\frac{1}{x_{\mathrm{E}}-x_{\mathrm{S_k}}}\right)}{\partial x_{\mathrm{E}}} = \frac{\left(y_{\mathrm{E}}-y_{\mathrm{S_k}}\right)}{1+\left(\frac{y_{\mathrm{E}}-y_{\mathrm{S_k}}}{x_{\mathrm{E}}-x_{\mathrm{S_k}}}\right)^2}\left(\frac{-1}{\left(x_{\mathrm{E}}-x_{\mathrm{S_k}}\right)^2}\right) \\ &= \frac{-\left(y_{\mathrm{E}}-y_{\mathrm{S_k}}\right)}{\left(x_{\mathrm{E}}-x_{\mathrm{S_k}}\right)^2+\left(y_{\mathrm{E}}-y_{\mathrm{S_k}}\right)^2}\end{aligned} \tag{4.48}$$

In (4.49) there is the derivative of the Azimuth angle $\alpha_{\mathrm{Az,k}}$ with respect to the variable y_{E}.

$$\begin{aligned}\frac{\partial \alpha_{\mathrm{Az,k}}}{\partial y_{\mathrm{E}}} &= \frac{\partial \left(\arctan\left(\frac{y_{\mathrm{E}}-y_{\mathrm{S_k}}}{x_{\mathrm{E}}-x_{\mathrm{S_k}}}\right)\right)}{\partial y_{\mathrm{E}}} = \frac{1}{1+\left(\frac{y_{\mathrm{E}}-y_{\mathrm{S_k}}}{x_{\mathrm{E}}-x_{\mathrm{S_k}}}\right)^2}\frac{\partial \left(\frac{y_{\mathrm{E}}-y_{\mathrm{S_k}}}{x_{\mathrm{E}}-x_{\mathrm{S_k}}}\right)}{\partial y_{\mathrm{E}}} \\ &= \frac{1}{1+\left(\frac{y_{\mathrm{E}}-y_{\mathrm{S_k}}}{x_{\mathrm{E}}-x_{\mathrm{S_k}}}\right)^2}\frac{1}{\left(x_{\mathrm{E}}-x_{\mathrm{S_k}}\right)}\frac{\partial \left(y_{\mathrm{E}}-y_{\mathrm{S_k}}\right)}{\partial y_{\mathrm{E}}} = \frac{1}{1+\left(\frac{y_{\mathrm{E}}-y_{\mathrm{S_k}}}{x_{\mathrm{E}}-x_{\mathrm{S_k}}}\right)^2}\frac{1}{\left(x_{\mathrm{E}}-x_{\mathrm{S_k}}\right)} \\ &= \frac{\left(x_{\mathrm{E}}-x_{\mathrm{S_k}}\right)}{\left(x_{\mathrm{E}}-x_{\mathrm{S_k}}\right)^2+\left(y_{\mathrm{E}}-y_{\mathrm{S_k}}\right)^2}\end{aligned} \tag{4.49}$$

In (4.50) there is the derivative of the Azimuth angle $\alpha_{\mathrm{Az,k}}$ with respect to the variable z_{E}.

$$\frac{\partial \alpha_{\mathrm{Az,k}}}{\partial z_{\mathrm{E}}} = \frac{\partial \left(\arctan\left(\frac{y_{\mathrm{E}}-y_{\mathrm{S_k}}}{x_{\mathrm{E}}-x_{\mathrm{S_k}}}\right)\right)}{\partial z_{\mathrm{E}}} = 0 \tag{4.50}$$

In (4.51) there is the derivative of the Azimuth angle $\alpha_{\mathrm{El,k}}$ with respect to the variable x_{E}.

$$
\begin{aligned}
\frac{\partial \alpha_{\mathrm{El,k}}}{\partial x_{\mathrm{E}}} &= \frac{\partial\left(\arctan\left(\frac{\sqrt{\left(x_{\mathrm{E}}-x_{\mathrm{S_k}}\right)^2+\left(y_{\mathrm{E}}-y_{\mathrm{S_k}}\right)^2}}{z_{\mathrm{E}}-z_{\mathrm{S_k}}}\right)\right)}{\partial x_{\mathrm{El,k}}} \\
&= \frac{1}{1+\left(\frac{\sqrt{\left(x_{\mathrm{E}}-x_{\mathrm{S_k}}\right)^2+\left(y_{\mathrm{E}}-y_{\mathrm{S_k}}\right)^2}}{z_{\mathrm{E}}-z_{\mathrm{S_k}}}\right)^2} \frac{\partial\left(\frac{\sqrt{\left(x_{\mathrm{E}}-x_{\mathrm{S_k}}\right)^2+\left(y_{\mathrm{E}}-y_{\mathrm{S_k}}\right)^2}}{z_{\mathrm{E}}-z_{\mathrm{S_k}}}\right)}{\partial x_{\mathrm{E}}} \\
&= \frac{\left(z_{\mathrm{E}}-z_{\mathrm{S_k}}\right)^2}{\left(z_{\mathrm{E}}-z_{\mathrm{S_k}}\right)^2+\left(x_{\mathrm{E}}-x_{\mathrm{S_k}}\right)^2+\left(y_{\mathrm{E}}-y_{\mathrm{S_k}}\right)^2} \frac{\partial\left(\frac{\sqrt{\left(x_{\mathrm{E}}-x_{\mathrm{S_k}}\right)^2+\left(y_{\mathrm{E}}-y_{\mathrm{S_k}}\right)^2}}{z_{\mathrm{E}}-z_{\mathrm{S_k}}}\right)}{\partial x_{\mathrm{E}}} \qquad (4.51) \\
&= \frac{\left(z_{\mathrm{E}}-z_{\mathrm{S_k}}\right)\frac{\partial\left(\sqrt{\left(x_{\mathrm{E}}-x_{\mathrm{S_k}}\right)^2+\left(y_{\mathrm{E}}-y_{\mathrm{S_k}}\right)^2}\right)}{\partial x_{\mathrm{E}}}}{\left(z_{\mathrm{E}}-z_{\mathrm{S_k}}\right)^2+\left(x_{\mathrm{E}}-x_{\mathrm{S_k}}\right)^2+\left(y_{\mathrm{E}}-y_{\mathrm{S_k}}\right)^2} \\
&= \frac{1}{2}\frac{\left(z_{\mathrm{E}}-z_{\mathrm{S_k}}\right)\left(\left(x_{\mathrm{E}}-x_{\mathrm{S_k}}\right)^2+\left(y_{\mathrm{E}}-y_{\mathrm{S_k}}\right)^2\right)^{\frac{-1}{2}}\frac{\partial\left(\left(x_{\mathrm{E}}-x_{\mathrm{S_k}}\right)^2\right)}{\partial x_{\mathrm{E}}}}{\left(z_{\mathrm{E}}-z_{\mathrm{S_k}}\right)^2+\left(x_{\mathrm{E}}-x_{\mathrm{S_k}}\right)^2+\left(y_{\mathrm{E}}-y_{\mathrm{S_k}}\right)^2} \\
&= \frac{\left(z_{\mathrm{E}}-z_{\mathrm{S_k}}\right)\left(\left(x_{\mathrm{E}}-x_{\mathrm{S_k}}\right)^2+\left(y_{\mathrm{E}}-y_{\mathrm{S_k}}\right)^2\right)^{\frac{-1}{2}}\left(x_{\mathrm{E}}-x_{\mathrm{S_k}}\right)}{\left(z_{\mathrm{E}}-z_{\mathrm{S_k}}\right)^2+\left(x_{\mathrm{E}}-x_{\mathrm{S_k}}\right)^2+\left(y_{\mathrm{E}}-y_{\mathrm{S_k}}\right)^2}
\end{aligned}
$$

In (4.52) there is the derivative of the Azimuth angle $\alpha_{\mathrm{El,k}}$ with respect to the variable y_{E}.

$$
\begin{aligned}
\frac{\partial \alpha_{\mathrm{El,k}}}{\partial y_{\mathrm{E}}} &= \frac{\partial \left(\arctan \left(\frac{\sqrt{\left(x_{\mathrm{E}} - x_{\mathrm{S_k}}\right)^2 + \left(y_{\mathrm{E}} - y_{\mathrm{S_k}}\right)^2}}{z_{\mathrm{E}} - z_{\mathrm{S_k}}} \right) \right)}{\partial y_{\mathrm{El,k}}} \\
&= \frac{1}{1 + \left(\frac{\sqrt{\left(x_{\mathrm{E}} - x_{\mathrm{S_k}}\right)^2 + \left(y_{\mathrm{E}} - y_{\mathrm{S_k}}\right)^2}}{z_{\mathrm{E}} - z_{\mathrm{S_k}}} \right)^2} \frac{\partial \left(\frac{\sqrt{\left(x_{\mathrm{E}} - x_{\mathrm{S_k}}\right)^2 + \left(y_{\mathrm{E}} - y_{\mathrm{S_k}}\right)^2}}{z_{\mathrm{E}} - z_{\mathrm{S_k}}} \right)}{\partial y_{\mathrm{E}}} \\
&= \frac{\left(z_{\mathrm{E}} - z_{\mathrm{S_k}}\right)^2}{\left(z_{\mathrm{E}} - z_{\mathrm{S_k}}\right)^2 + \left(x_{\mathrm{E}} - x_{\mathrm{S_k}}\right)^2 + \left(y_{\mathrm{E}} - y_{\mathrm{S_k}}\right)^2} \frac{\partial \left(\frac{\sqrt{\left(x_{\mathrm{E}} - x_{\mathrm{S_k}}\right)^2 + \left(y_{\mathrm{E}} - y_{\mathrm{S_k}}\right)^2}}{z_{\mathrm{E}} - z_{\mathrm{S_k}}} \right)}{\partial y_{\mathrm{E}}} \qquad (4.52) \\
&= \frac{\left(z_{\mathrm{E}} - z_{\mathrm{S_k}}\right) \frac{\partial \left(\sqrt{\left(x_{\mathrm{E}} - x_{\mathrm{S_k}}\right)^2 + \left(y_{\mathrm{E}} - y_{\mathrm{S_k}}\right)^2} \right)}{\partial y_{\mathrm{E}}}}{\left(z_{\mathrm{E}} - z_{\mathrm{S_k}}\right)^2 + \left(x_{\mathrm{E}} - x_{\mathrm{S_k}}\right)^2 + \left(y_{\mathrm{E}} - y_{\mathrm{S_k}}\right)^2} \\
&= \frac{1}{2} \frac{\left(z_{\mathrm{E}} - z_{\mathrm{S_k}}\right) \left(\left(x_{\mathrm{E}} - x_{\mathrm{S_k}}\right)^2 + \left(y_{\mathrm{E}} - y_{\mathrm{S_k}}\right)^2 \right)^{\frac{-1}{2}} \frac{\partial \left(\left(y_{\mathrm{E}} - y_{\mathrm{S_k}}\right)^2 \right)}{\partial y_{\mathrm{E}}}}{\left(z_{\mathrm{E}} - z_{\mathrm{S_k}}\right)^2 + \left(x_{\mathrm{E}} - x_{\mathrm{S_k}}\right)^2 + \left(y_{\mathrm{E}} - y_{\mathrm{S_k}}\right)^2} \\
&= \frac{\left(z_{\mathrm{E}} - z_{\mathrm{S_k}}\right) \left(\left(x_{\mathrm{E}} - x_{\mathrm{S_k}}\right)^2 + \left(y_{\mathrm{E}} - y_{\mathrm{S_k}}\right)^2 \right)^{\frac{-1}{2}} \left(y_{\mathrm{E}} - y_{\mathrm{S_k}}\right)}{\left(z_{\mathrm{E}} - z_{\mathrm{S_k}}\right)^2 + \left(x_{\mathrm{E}} - x_{\mathrm{S_k}}\right)^2 + \left(y_{\mathrm{E}} - y_{\mathrm{S_k}}\right)^2}
\end{aligned}
$$

In (4.53) there is the derivative of the Azimuth angle $\alpha_{\mathrm{El,k}}$ with respect to the variable z_{E}.

$$
\begin{aligned}
\frac{\partial \alpha_{\mathrm{El,k}}}{\partial z_{\mathrm{E}}} &= \frac{\partial \left(\arctan \left(\frac{\sqrt{\left(x_{\mathrm{E}}-x_{\mathrm{S_k}}\right)^2+\left(y_{\mathrm{E}}-y_{\mathrm{S_k}}\right)^2}}{z_{\mathrm{E}}-z_{\mathrm{S_k}}} \right) \right)}{\partial z_{\mathrm{El,k}}} \\
&= \frac{1}{1+\left(\frac{\sqrt{\left(x_{\mathrm{E}}-x_{\mathrm{S_k}}\right)^2+\left(y_{\mathrm{E}}-y_{\mathrm{S_k}}\right)^2}}{z_{\mathrm{E}}-z_{\mathrm{S_k}}} \right)^2} \frac{\partial \left(\frac{\sqrt{\left(x_{\mathrm{E}}-x_{\mathrm{S_k}}\right)^2+\left(y_{\mathrm{E}}-y_{\mathrm{S_k}}\right)^2}}{z_{\mathrm{E}}-z_{\mathrm{S_k}}} \right)}{\partial z_{\mathrm{E}}} \\
&= \frac{\sqrt{\left(x_{\mathrm{E}}-x_{\mathrm{S_k}}\right)^2+\left(y_{\mathrm{E}}-y_{\mathrm{S_k}}\right)^2}}{1+\left(\frac{\sqrt{\left(x_{\mathrm{E}}-x_{\mathrm{S_k}}\right)^2+\left(y_{\mathrm{E}}-y_{\mathrm{S_k}}\right)^2}}{z_{\mathrm{E}}-z_{\mathrm{S_k}}} \right)^2} \frac{\partial \left(\frac{1}{z_{\mathrm{E}}-z_{\mathrm{S_k}}} \right)}{\partial z_{\mathrm{E}}} \\
&= \frac{\sqrt{\left(x_{\mathrm{E}}-x_{\mathrm{S_k}}\right)^2+\left(y_{\mathrm{E}}-y_{\mathrm{S_k}}\right)^2}}{1+\left(\frac{\sqrt{\left(x_{\mathrm{E}}-x_{\mathrm{S_k}}\right)^2+\left(y_{\mathrm{E}}-y_{\mathrm{S_k}}\right)^2}}{z_{\mathrm{E}}-z_{\mathrm{S_k}}} \right)^2} \left(\frac{-1}{\left(z_{\mathrm{E}}-z_{\mathrm{S_k}}\right)^2} \right) \\
&= \frac{\left(z_{\mathrm{E}}-z_{\mathrm{S_k}}\right)^2 \sqrt{\left(x_{\mathrm{E}}-x_{\mathrm{S_k}}\right)^2+\left(y_{\mathrm{E}}-y_{\mathrm{S_k}}\right)^2}}{\left(z_{\mathrm{E}}-z_{\mathrm{S_k}}\right)^2+\left(x_{\mathrm{E}}-x_{\mathrm{S_k}}\right)^2+\left(y_{\mathrm{E}}-y_{\mathrm{S_k}}\right)^2} \left(\frac{-1}{\left(z_{\mathrm{E}}-z_{\mathrm{S_k}}\right)^2} \right) \\
&= \frac{-\sqrt{\left(x_{\mathrm{E}}-x_{\mathrm{S_k}}\right)^2+\left(y_{\mathrm{E}}-y_{\mathrm{S_k}}\right)^2}}{\left(z_{\mathrm{E}}-z_{\mathrm{S_k}}\right)^2+\left(x_{\mathrm{E}}-x_{\mathrm{S_k}}\right)^2+\left(y_{\mathrm{E}}-y_{\mathrm{S_k}}\right)^2}
\end{aligned}
\tag{4.53}
$$

4.3.3 Optimization Problem

It is assumed that the problem of detection is already solved, so the cluster of satellites already have a coarse estimation of the position of the emitter. Furthermore, it is assumed that operative mode of the satellites is in tracking stage, so the orientation of the satellite is such that to set the desired attitude that aligns the broadside direction of the array to the direction of the detected emitter in order to perform the accurate location estimation. In particular, from a geometrical point of view, this alignment means that, if the payload is made up of two arrays of antennas, the normal to the axes points toward the emitter of the signal.

Hypothesis 1 — $\zeta_{\mathrm{x,1}} = \zeta_{\mathrm{x,2}} = \cdots = \zeta_{\mathrm{x,k}} = \cdots = \zeta_{\mathrm{x,n}} = \pi/2$ and $\zeta_{\mathrm{y,1}} = \zeta_{\mathrm{y,2}} = \cdots = \zeta_{\mathrm{y,k}} = \cdots = \zeta_{\mathrm{y,n}} = \pi/2$.

It is assumed that every satellite has the same AOA receiver in terms of size and number of elements.

Hypothesis 2 — ($\mathbf{H}_2$): $L_{\mathrm{x,1}} = L_{\mathrm{x,2}} = \cdots = L_{\mathrm{x,k}} = \cdots = L_{\mathrm{x,n}} = L_{\mathrm{x}}$, $L_{\mathrm{y,1}} = L_{\mathrm{y,2}} = \cdots = L_{\mathrm{y,k}} = \cdots = L_{\mathrm{y,n}} = L_{\mathrm{y}}$, $M_{\mathrm{x,1}} = M_{\mathrm{x,2}} = \cdots = M_{\mathrm{x,k}} = \cdots = M_{\mathrm{x,n}} = M_{\mathrm{x}}$, and $M_{\mathrm{y,1}} = M_{\mathrm{y,2}} = \cdots = M_{\mathrm{y,k}} = \cdots = M_{\mathrm{y,n}} = M_{\mathrm{y}}$.

Furthermore, it is assumed that in both the arrays the size and number of elements are the same.

Hypothesis 3 — ($\mathbf{H}_3$): $L_\mathrm{x} = L_\mathrm{y}$ and $M_\mathrm{x} = M_\mathrm{y}$.

Every satellite is deployed on a circular orbit; this means that the eccentricities are 0, the argument of perigee is undefined, and the semi-major axis a is equal to the radius of the orbit r. Furthermore, the argument of perigee ω becomes a meaningless quantity and conventionally posed to 0.

Hypothesis 4 — ($\mathbf{H}_4$): $e_1 = e_2 = \cdots = e_\mathrm{k} = \cdots = e_\mathrm{n} = 0$, $a_1 = r_1$, $a_2 = r_2$, $\dots$, $a_\mathrm{k} = r_\mathrm{k}$, $\dots$, $a_\mathrm{n} = r_\mathrm{n}$, $\omega_1 + \nu_1 = \nu_1$, $\omega_2 + \nu_2 = \nu_2$, $\dots$, $\omega_\mathrm{k} + \nu_\mathrm{k} = \nu_\mathrm{k}$, $\dots$, $\omega_\mathrm{n} + \nu_\mathrm{n} = \nu_\mathrm{n}$.

The inclination of the orbit is such that the satellites perform an Earth scanning mission in a polar orbit.

Hypothesis 5 — ($\mathbf{H}_5$): $i_1 = i_2 = \cdots = i_\mathrm{k} = \cdots = i_\mathrm{n} = \pi/2$.

The emitter of the signal is on the surface of the Earth.

Hypothesis 6 — ($\mathbf{H}_6$): $h = 0$.

Every satellite has the same orbital period: combined with hypothesis ($\mathbf{H}_4$), this means that all the satellite orbits have the same orbit radius.

Hypothesis 7 — ($\mathbf{H}_7$): $r_1 = r_2 = \cdots = r_\mathrm{k} = \cdots = r_\mathrm{n} = r$.

The Position Dilution of Precision (PDOP) is assumed as objective function, which has the functional dependence in (4.54).

$$PDOP = f\left(\Lambda, \lambda, \Omega_1, \Omega_2, \dots, \Omega_\mathrm{k}, \dots \Omega_\mathrm{n}, \nu_1, \nu_1, \dots, \nu_\mathrm{k}, \dots, \nu_\mathrm{n}, r\right) \tag{4.54}$$

In particular, the orbit radius r is supposed to be a fixed mission parameter, while a value of $\Lambda = 0$ is chosen for the latitude, in order to observe the maximum variation of PDOP: since it has been assumed that the orbits are polar with $i = \pi/2$, then at latitudes $\Lambda \to \pm\pi/2$ all the satellites have to pass on the Zenith direction of the poles.

Also a convenient value of the longitude $\lambda = 0$ of the emitter position has been considered: fixed a certain epoch t, so also the position of the Greenwich meridian $\alpha_\mathrm{GR}(t)$, from a relative perspective in the geometry of interest, which has an inclination of $i = \pi/2$, every change in the value of the longitude λ corresponds to a possible a variation in the RAAN Ω; considering that this is an evaluative study on the relative position among the satellites performances (i.e., the results are on differences in the right ascension of the ascending nodes), the value of the longitude λ can be eliminated among all variables. However, it is recalled to the reader that the actual values are of interest in real missions or in the development of realistic software simulators that take into account the selected time epoch.

Considering these simplifications and choosing the set of angles of the right ascension of the ascending node $\Omega_1, \Omega_2, \dots, \Omega_\mathrm{k}, \dots, \Omega_\mathrm{n}$ and the set of angles of the true anomaly $\nu_1, \nu_2, \dots, \nu_\mathrm{k}, \dots, \nu_\mathrm{n}$ are as variables of the problem, the model in (4.55) is considered as the objective function.

$$PDOP = f\left(\Omega_{\mathrm{1}}, \Omega_{\mathrm{2}}, \ldots, \Omega_{\mathrm{k}}, \ldots \Omega_{\mathrm{n}}, \nu_{\mathrm{1}}, \nu_{\mathrm{1}}, \ldots, \nu_{\mathrm{k}}, \ldots, \nu_{\mathrm{n}}\right) \tag{4.55}$$

Considering that, by definition, for a k-th satellite $\Omega_{\mathrm{k}} \in [0{,}2\pi]$ and $\nu_{\mathrm{k}} \in [0{,}2\pi]$, then the domain of the problem defined for n satellites is $\mathcal{D} = [0{,}2\pi]^{2n}$.

A consequence of the assumptions made in this subsection is that $\sigma_{\hat{\alpha}_{\mathrm{Az,1}}} = \sigma_{\hat{\alpha}_{\mathrm{Az,2}}} = \cdots = \sigma_{\hat{\alpha}_{\mathrm{Az,k}}} = \cdots = \sigma_{\hat{\alpha}_{\mathrm{Az,n}}} = \sigma_{\hat{\alpha}_{\mathrm{El,1}}} = \sigma_{\hat{\alpha}_{\mathrm{El,2}}} = \cdots = \sigma_{\hat{\alpha}_{\mathrm{El,k}}} = \cdots = \sigma_{\hat{\alpha}_{\mathrm{El,n}}} = \sigma$, so the Covariance Matrix $\mathbf{C}$ can be written as in (4.56), where $\mathbf{I}_{\mathrm{2n}}$ is the identity matrix of dimensions $2n \times 2n$.

$$\mathbf{C} = \sigma^2 \mathbf{I}_{\mathrm{2n}} \tag{4.56}$$

Considering (4.56), it is possible to simplify the expression in (4.44) as in (4.57).

$$\mathbf{F} = \frac{1}{\sigma^2}\mathbf{H}^{\mathrm{T}}\mathbf{H} \tag{4.57}$$

Combining (4.57) and (4.43), the (4.58) is obtained.

$$PDOP = \sqrt{Tr\left(\mathbf{F^{-1}}\right)} = \sigma\sqrt{Tr\left(\left(\mathbf{H}^{\mathrm{T}}\mathbf{H}\right)^{\mathbf{-1}}\right)} \tag{4.58}$$

It is remarked that for some authors, especially in GNSS literature (e.g., [82]), only the geometric part of (4.58) (i.e., the value of the square root which only depends on the Geometric Design Matrix $\mathbf{H}$) is considered for the definition of the DOP, here indicated as $PDOP'$, as shown in (4.59).

$$PDOP' = \frac{PDOP}{\sigma} = \sqrt{Tr\left(\left(\mathbf{H}^{\mathrm{T}}\mathbf{H}\right)^{\mathbf{-1}}\right)} \tag{4.59}$$

The expression in (4.59) leads to the position error σ_{p}, which can be written [83] as shown in (4.60).

$$\sigma_{\mathrm{p}} = PDOP = PDOP'\sigma \tag{4.60}$$

Since the purpose of the study is the minimization of the position error σ_{p} and assuming that $\sigma = \mathrm{const.}$, the particular convention used for the definition of the DOP does not affect the result, because $\min\left(\sigma_{\mathrm{p}}\right) = \min\left(PDOP\right) = \min\left(PDOP'\right)$.

One of the consequences of all the assumptions that lead $\sigma = \mathrm{const.}$ is that the problem of minimization of $PDOP$ (or $PDOP'$) is both independent from array geometry and frequency of the signal.

It is highlighted that assuming $\sigma = \mathrm{const.}$ is a very strong hypothesis that comes from a high-level modelling of the system of satellites and real-case applications must take into account the variations on the standard deviation σ which depends on the actual fine design of the receiver and on SNR.

Another observation is that the value to be optimized considered in model (4.43) is instantaneous and it is related to a single measurement per receiver.

The constraints of the problems are on the positions of the emitter and satellites with respect to the Earth. Trivially, both the actors of the problem can not be inside the surface of the Earth, so $h \geq 0$ and $r \geq R_\oplus$ (equivalently $h_\mathrm{S} \geq 0$). And, secondly, the Line of Sight (LOS) between the emitter and every satellite must be guaranteed.

The LOS is a constraint associated to the visibility of the emitter E by the satellite S_k.

The local horizon of visibility of the emitter can be determined by the set of tangent lines to the surface of the Earth that pass through the emitter. For an emitter above the surface of a spherical Earth, this horizon of visibility is a circumference.

Considering this construction of the horizon, the admissible set of LOBs (AOA measurements) are the ones that do not intersect the spherical cap determined by the surface of the Earth within the circumference determined by the LOS.

As derived in [67], indicating with $\Omega_{\mathrm{k},0}$ and $\nu_{\mathrm{k},0}$ the angular position for the k-th satellite corresponding to the Nadir direction with respect to the emitter position, there exists a maximum angle δ_k for the k-th satellite such that the condition on the satellite angles Ω_k and ν_k is expressed as in (4.61).

$$(\Omega_\mathrm{k} - \Omega_{\mathrm{k},0})^2 + (\nu_\mathrm{k} - \nu_{\mathrm{k},0})^2 \leq \delta_\mathrm{k}^2 \tag{4.61}$$

Considering the Fig. 4.3, this condition can be mathematically formulated considering the right triangle with vertices E, S_k, and the origin $O_\oplus$ of ECI reference system in the centre of the Earth and the right angle in $\angle O_\oplus E S_\mathrm{k} = \pi/2$.

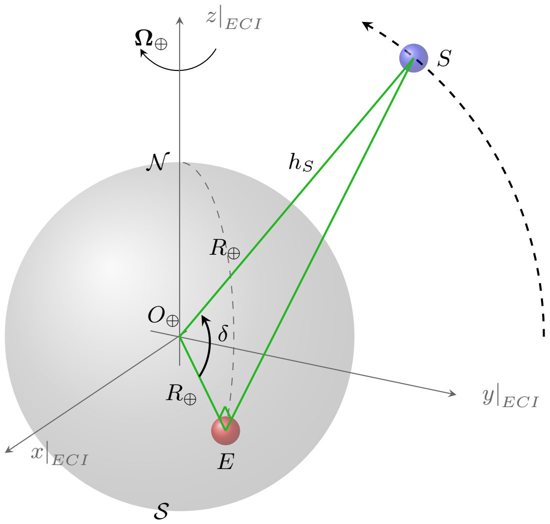

Figure 4.3: Construction of the triangle with vertices $O_\oplus$, E, and S and definition of the constraint angle δ.

The (4.61) is an absolute condition on the k-th satellite. However, considering also that the absolute angle δ_k can be expressed as

$$\delta_\mathrm{k} = \arccos\left(\frac{R_\oplus}{R_\oplus + h_{\mathrm{S_k}}}\right) \tag{4.62}$$

and the assumption that all the satellites have the same orbit radius, the absolute condition (4.61) has the same maximum angle for all the satellites $\delta_1 = \delta_1 = \cdots = \delta_\mathrm{k} = \cdots = \delta_\mathrm{n} = \delta$.

In (4.63) the problem of spatial optimization is reported, with the standard deviation on the position σ_p as objective function and $\Omega_{\mathrm{k},0} = \nu_{\mathrm{k},0} = 0$ for every k-th satellite (i.e., the k-th LOS condition is written with respect to the Nadir alignment between the k-th satellite and the emitter).

$$\begin{cases} \min\limits_{(\Omega_1,\Omega_2,\ldots,\Omega_\mathrm{k},\ldots\Omega_\mathrm{n},\nu_1,\nu_2,\ldots,\nu_\mathrm{k},\ldots,\nu_\mathrm{n})\in\mathcal{D}=[0,2\pi]^{2n}} (\sigma_\mathrm{p}) \\ s.t. \quad \Omega_1^2 + \nu_1^2 \leq \delta^2 \\ s.t. \quad \Omega_2^2 + \nu_2^2 \leq \delta^2 \\ \quad\vdots \\ s.t. \quad \Omega_\mathrm{k}^2 + \nu_\mathrm{k}^2 \leq \delta^2 \\ \quad\vdots \\ s.t. \quad \Omega_\mathrm{n}^2 + \nu_\mathrm{n}^2 \leq \delta^2 \end{cases} \tag{4.63}$$

4.4 Optimization of Clusters of Two Satellites

This section summarizes methods, models and results of the published works of the author [67], [68], [69], and [70].

4.4.1 Problem Definition and Conditions

When two satellites are considered the problem in (4.63) becomes as in (4.64).

$$\begin{cases} \min\limits_{(\Omega_1,\Omega_2,\nu_1,\nu_2)\in[0,2\pi]^4} (\sigma_\mathrm{p}) \\ s.t. \quad \Omega_1^2 + \nu_1^2 \leq \delta^2 \\ s.t. \quad \Omega_2^2 + \nu_2^2 \leq \delta^2 \end{cases} \tag{4.64}$$

Recalling the hypothesis of target pointing and equation in (4.60), with a constant value of σ, representative of the fact that every satellite has the same receiver, the minimum of σ_p occurs for the same set of variables for the minimum of $PDOP$.

The problem in (4.64) can be also expressed in term of differences, as shown in (4.65). In particular, once the angular position of the first satellite is fixed, Ω_1

and ν_1, then the angular position of the second satellite, Ω_2 and ν_2, is calculated considering the difference with respect to the first satellite $\Delta\Omega = \Omega_2 - \Omega_1$ and $\Delta\nu = \nu_2 - \nu_1$.

$$\begin{cases} \displaystyle\min_{(\Delta\Omega,\Delta\nu)\in[0,2\pi]^2} (\sigma_\mathrm{p}) \\ s.t. \quad \Delta\Omega^2 + \Delta\nu^2 \leq \delta_{1,2}^2 \\ \qquad given \quad \Omega_1, \nu_1 \end{cases} \tag{4.65}$$

Problem in (4.64) has four absolute variables $(\Omega_1, \nu_1, \Omega_2, \nu_2)$ and 2 conditions, while problem in (4.65) has 2 relative variables $(\Delta\Omega, \Delta\nu)$ and 1 condition.

Considering the definition of $\Delta\Omega$ and $\Delta\nu$ the relative condition in (4.65) ties together Ω_1, ν_1, Ω_2, ν_2, and $\delta_{1,2}$.

The problem in (4.65) can be considered a particular instance of the problem in (4.64) and it has to be iterated varying the values of Ω_1 and ν_1 (and also the parameters Λ and r), but it is important to remember firstly that both these angles must not violate the LOS condition and also it is important to notice that $\delta_{1,2}$ is a relative condition of the satellite S_2 with respect to satellite S_1.

In this study, a conservative the relationship among the absolute angle δ and its relative $\delta_{1,2}$ is expressed as in (4.66).

$$\delta \geq \delta_{1,2} + \sqrt{(\max|\Omega_1|)^2 + (\max|\nu_1|)^2} \tag{4.66}$$

The meaning of (4.66) is that the maximum displacement of the first satellite S_1 plus the relative displacement of the second satellite S_2 with respect to the first one, expressed by $\delta_{1,2}$, must be lower than or equal to the absolute angular condition δ.

A convenient hypothesis, which is further conservative for simulation purposes, is to consider $\max|\Omega_1| = \max|\nu_1| = \delta_{1,2} = \delta_\mathrm{r}$.

With this assumption, the condition (4.66) become as in (4.67).

$$\delta \geq \delta_\mathrm{r} + \sqrt{\delta_\mathrm{r}^2 + \delta_\mathrm{r}^2} = \delta_\mathrm{r} + \sqrt{2\delta_\mathrm{r}^2} = \delta_\mathrm{r} + \sqrt{2}\delta_\mathrm{r} = \left(1 + \sqrt{2}\right)\delta_\mathrm{r} \tag{4.67}$$

The condition (4.67) can also be expressed as in (4.68).

$$\delta_\mathrm{r} \leq \frac{\delta}{1 + \sqrt{2}} \tag{4.68}$$

From (4.68), the ranges for Ω_1 and ν_1 in which the problem in (4.65) has to be iterated become as in (4.69) and they guarantee the LOS condition in the case of $\Omega_{1,0} = \nu_{1,0} = 0$ (i.e., the LOS condition is written with respect to the Nadir alignment between the first satellite and the emitter).

$$\begin{aligned} \frac{-\delta}{1+\sqrt{2}} \leq \Omega_1 \leq \frac{\delta}{1+\sqrt{2}} \\ \frac{-\delta}{1+\sqrt{2}} \leq \nu_1 \leq \frac{\delta}{1+\sqrt{2}} \end{aligned} \tag{4.69}$$

To generalize the problem and relax the limitations imposed by $\Omega_{1,0} = 0$ and $\nu_{1,0} = 0$, a further consideration can be made on their meaning. It must be observed that the values of Ω_1 and ν_1 are with respect to the value of the latitude Λ and longitude λ of the emitter. In general, the range of interest should be centered on the Nadir direction with respect to the emitter position, so their values have to be corrected considering $\Omega_1 \to \Omega_1 + \lambda$ and $\nu_1 \to \nu_1 + \Lambda$; then (4.69) become as in (4.70).

$$\begin{aligned} \frac{-\delta}{1+\sqrt{2}} \leq \Omega_1 + \lambda \leq \frac{\delta}{1+\sqrt{2}} \\ \frac{-\delta}{1+\sqrt{2}} \leq \nu_1 + \Lambda \leq \frac{\delta}{1+\sqrt{2}} \end{aligned} \tag{4.70}$$

An important observation is that this way of reasoning, which permits to pass directly from the conditions written in terms of $\Omega_{1,0}$ and $\nu_{1,0}$ to Λ and λ, is always valid for a spherical Earth. When an ellipsoidal model is used, the condition on the right ascension of the ascending node Ω_1 in (4.70) is still valid in any case, but the condition on the true anomaly ν_1 needs special attention because of the distinction between the geodetic latitude and geocentric latitude.

Since a variation of the results with respect to the value of the longitude λ is not expected (i.e., because a variation in longitude can be compensated with a shift on the right ascension of the ascending node obtaining the same results), in this study it is assumed $\lambda = 0$.

The value of $\lambda \neq 0$ on the conditions in (4.70) can take place as theoretical completeness or can be of interest in simulators, where the current value of $\alpha_{\mathrm{GR}}(t)$ in a certain time epoch t is of interest.

On the other hand, the variation of results with respect to the latitude Λ is of interest, because with an inclination of $\pi/2$ the trajectories of the orbits tend to converge to the same point in the poles of the Earth.

Another angle that can be considered to characterize the cluster of satellites is is the spacing angle γ defined in (4.40). For two satellites S_1 and S_2, the spacing angle $\gamma_{1,2} = \angle S_1 E S_2$ is as in (4.71). This angle represents the spacing between the satellite S_1 and S_2 with respect to the position of the emitter E, as shown in Fig. 4.4.

$$\gamma_{1,2} = \operatorname{acos}\left(\frac{\overrightarrow{ES_1}}{\left\| \overrightarrow{ES_1} \right\|} \cdot \frac{\overrightarrow{ES_2}}{\left\| \overrightarrow{ES_2} \right\|} \right) \tag{4.71}$$

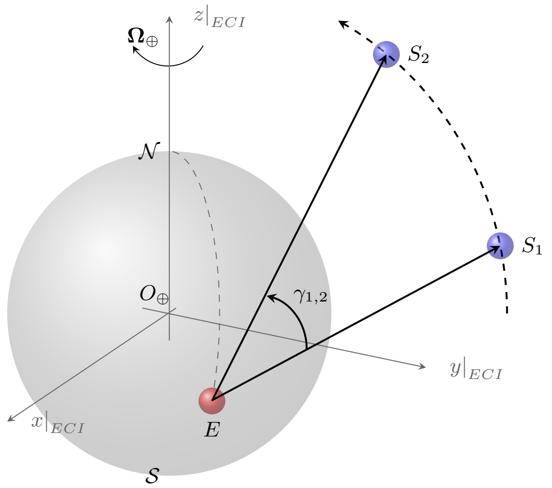

Figure 4.4: Construction of the angle $\gamma_{1,2} = \angle S_1 E S_2$.

4.4.2 Simulation Settings

The simulations of the problem in (4.65) with conditions expressed in (4.66) and (4.70) have been conducted in MATLAB environment with the aid of the Symbolic Math Toolbox and the Optimization Toolbox: the first has been used to write the optimization problem on the objective function (i.e., the PDOP) in terms of symbolic variables, the latter has been used to solve the problem written in terms of symbolic variables and to obtain the optimal solution (i.e., the set of angles of the right ascension of the ascending node and the true anomaly for each satellite).

To solve the problem the interior point algorithm has been chosen; this is because it is mathematically proven that it is able to solve effectively a nonlinear objective function subject to nonlinear inequality constraints converging to an approximate solution defined by the user-defined tolerances; furthermore it always satisfies the boundary conditions at all iterations, and it can recover from possible `NaN` (i.e., not a number) or `Inf` (i.e., infinite) results in every the iteration. As expected, from the conducted campaign of simulations the algorithm demonstrated to be always convergent. Mathematical details of the algorithm can be found in [84].

In particular, considering $\mathbf{x}$ as the solution of the problem, $g(\mathbf{x})$ as the nonlinear objective function, $w_1(\mathbf{x}) \leq 0, w_2(\mathbf{x}) \leq 0, \cdots, w_\mathrm{l}(\mathbf{x}) \leq 0, w_\mathrm{m}(\mathbf{x}) \leq 0$ as the m nonlinear inequality constraint conditions, and $\mathbf{x}_\mathrm{j}$ as the solution calculated at j-th iteration, the tolerances are defined in relative terms: the condition on step tolerance is defined as shown in (4.72), where $T_\mathrm{s} > 0$ is the step tolerance; the optimality condition is defined as shown in (4.73), where $T_\mathrm{o} > 0$ is the optimality tolerance, $\lambda_1 \geq 0, \lambda_2 \geq 0, \cdots, \lambda_\mathrm{l}, \cdots, \lambda_\mathrm{m} \geq 0$ are the Lagrange multipliers, and $\|\cdot\|_\infty$ denotes the infinity norm; the constraint condition is defined as shown in

(4.74), where $T_\mathrm{c} > 0$ is the constraint tolerance.

$$\|\mathbf{x}_\mathrm{j} - \mathbf{x}_\mathrm{j+1}\| < T_\mathrm{s}\left(1 + \|\mathbf{x}_\mathrm{j}\|\right) \tag{4.72}$$

$$\left\|\nabla g\left(\mathbf{x}_\mathrm{j+1}\right) + \sum_{\mathrm{l}=1}^{m}\left(\lambda_\mathrm{l} w_\mathrm{l}\left(\mathbf{x}_\mathrm{j+1}\right)\right)\right\| < T_\mathrm{o}\|\nabla g\left(\mathbf{x}_\mathrm{j+1}\right)\|_\infty \tag{4.73}$$

$$\begin{cases} \|w_1\left(\mathbf{x}_\mathrm{j}\right)\| < T_\mathrm{c} \\ \|w_2\left(\mathbf{x}_\mathrm{j}\right)\| < T_\mathrm{c} \\ \qquad\vdots \\ \|w_l\left(\mathbf{x}_\mathrm{j}\right)\| < T_\mathrm{c} \\ \qquad\vdots \\ \|w_\mathrm{m}\left(\mathbf{x}_\mathrm{j}\right)\| < T_\mathrm{c} \end{cases} \tag{4.74}$$

It is recalled that the left hand of (4.73) is a particular case of the more general Lagrangian of the Karush-Kuhn-Tucker (KKT) conditions [85], that considers both equality and inequality constraints for convex and nonconvex problems; as can be seen from (4.65) the optimization problem that the study aims to solve involves only inequality constraints.

The iterations are stopped or on a certain fixed number (e.g., the default value is 1000) or when one of the conditions on step tolerance (4.72) (i.e., the relative difference in values) or optimality tolerance (4.73) (that is, the values of the first-order derivatives, KKT condition) is met; in this latter case, the constraint tolerance (4.74) is always satisfied.

Details on the numerical implementation of the optimization algorithm, stopping criteria, and the derivation of formulas used for the calculation of tolerances can be found in the MATLAB User Guide for the Optimization Toolbox [86] and the dedicated literature.

For this algorithm the following settings have been considered for the iterations of the solver: a step tolerance of $T_\mathrm{s} = 10^{-15}$, an optimality tolerance of $T_\mathrm{o} = 10^{-12}$, a constraint tolerance of $T_\mathrm{c} = 10^{-12}$, interior point algorithm, scheme of central finite differences,and maximum number of iterations equal to 2400.

The value of maximum number of iterations has been chosen in order to never be reached.

The choice of the settings has been made observing the precision of the solution. In particular, the selected case for these tests is the one with the emitter position in $\Lambda = 30°$, $\lambda = 0°$, and $h = 0$ m. The altitudes of the satellites were in $h_\mathrm{S} = 400$ km, and the angular position of the first satellite was in $\Omega_1 = \delta\left(h_\mathrm{S}\right)/\left(1+\sqrt{2}\right) \approx 8.198361918°$, $\nu_1 = \Lambda - \delta\left(h_\mathrm{S}\right)/\left(1+\sqrt{2}\right) \approx 21.80163808°$. The choice of the first satellite at the border of the constraints has been done to stress the solver not only on the step tolerance T_s and the optimality tolerance T_o, but also on the tolerance related to the constraints T_c.

The selected cases of the tests were on step tolerance T_s, T_o, and T_c from 10^{-3} to 10^{-12}. The results of the tests are for the precision of the numerical figures of solution and they are reported in Table 4.3. For simulations, the step tolerance has been further decreased to $T_\mathrm{s} = 10^{-15}$ because it was observed that it was the main reason that stopped the convergence of the solver.

Even if the numerical convergence analysis has been conducted up to 15 figures and beyond, the solutions have to be considered physically valid up to 7 figures, because the limitation is on the input data: in particular, the mean Earth radius $r_\oplus$ considered in this study is precise up to 7 figures.

Table 4.3: Analysis of precision of the results with different settings of the solver.

Settings $(T_\mathrm{s}, T_\mathrm{o}, T_\mathrm{c})$	**Solution [°]**	**Precision**
$(10^{-3}, 10^{-3}, 10^{-3})$	$\Delta\Omega_1 = 7.7998839497769267836702$1	10^{-5}
	$\Delta\nu_1 = -22.200116050222959529492$1	10^{-6}
	$\gamma_{1,2} = 46.956746998389434111231$8	10^{-5}
$(10^{-6}, 10^{-6}, 10^{-6})$	$\Delta\Omega_1 = 7.7998963997522423596819$9	10^{-7}
	$\Delta\nu_1 = -22.200103600247757640318$0	10^{-8}
	$\gamma_{1,2} = 46.956765090929465600311$2	10^{-8}
$(10^{-9}, 10^{-9}, 10^{-9})$	$\Delta\Omega_1 = 7.7998963070596118996036$2	10^{-10}
	$\Delta\nu_1 = -22.200103692940274413558$7	10^{-11}
	$\gamma_{1,2} = 46.956764956226663798588$6	10^{-10}
$(10^{-12}, 10^{-12}, 10^{-12})$	$\Delta\Omega_1 = 7.7998963074078346835449$3	$< 10^{-40}$
	$\Delta\nu_1 = -22.200103692592165316455$1	$< 10^{-40}$
	$\gamma_{1,2} = 46.956764956732634175296$0	$< 10^{-40}$
$(10^{-15}, 10^{-12}, 10^{-12})$	$\Delta\Omega_1 = 7.7998963074078346835449$3	Reference
	$\Delta\nu_1 = -22.200103692592165316455$1	Reference
	$\gamma_{1,2} = 46.956764956732634175296$0	Reference

4.4.3 Properties of Simmetry and Antisimmetry

The first explorative set of simulations considered an orbit with $h_{\mathrm{S},1} = h_{\mathrm{S},2} = 500$ km. The value of the constraint angle is $\delta = 21.993°$.

The following set of ranges have been considered: $\Omega_1 \in [-9°, 9°]$ and $\nu_1 \in [-9°, 9°]$.

Considering that the maximum angular displacement of S_1 from Nadir pointing can be upon $\sqrt{(\max|\Omega_1|)^2 + (\max|\nu_1|)^2} = \sqrt{9^2 + 9^2} = 12.728°$, then in order to guarantee the condition on δ, the relative condition chosen for the problem has to be $\delta_{1,2} \leq \delta - \sqrt{\max|\Omega_1|^2 + \max|\nu_1|^2}$, so a value of $\delta_{1,2} = 9°$ has been chosen.

A resolution of 0.3° obtained with 61 evenly spaced values for Ω_1 and ν_1 in their ranges have been considered resulting in 3721 instances of the problem in (4.65).

The simulations have been conducted in MATLAB environment with the aid of the Symbolic Math Toolbox and the Optimization Toolbox.

Among the settings and parameters of the optimization solver, the interior point algorithm has been considered for this first study with the scheme of central finite differences, a step tolerance of 10^{-15}, an optimality tolerance of 10^{-9}, and a constraint tolerance of 10^{-9}.

An example of contour of the objective function is presented in Fig. 4.5. In particular, it can be noticed that there are multiple local minima and, in order to select the region where the absolute minimum is, a pre-evaluation of the objective function with a resolution of 0.01° has been considered in order to obtain the best initial point for the algorithm in every instance of the problem.

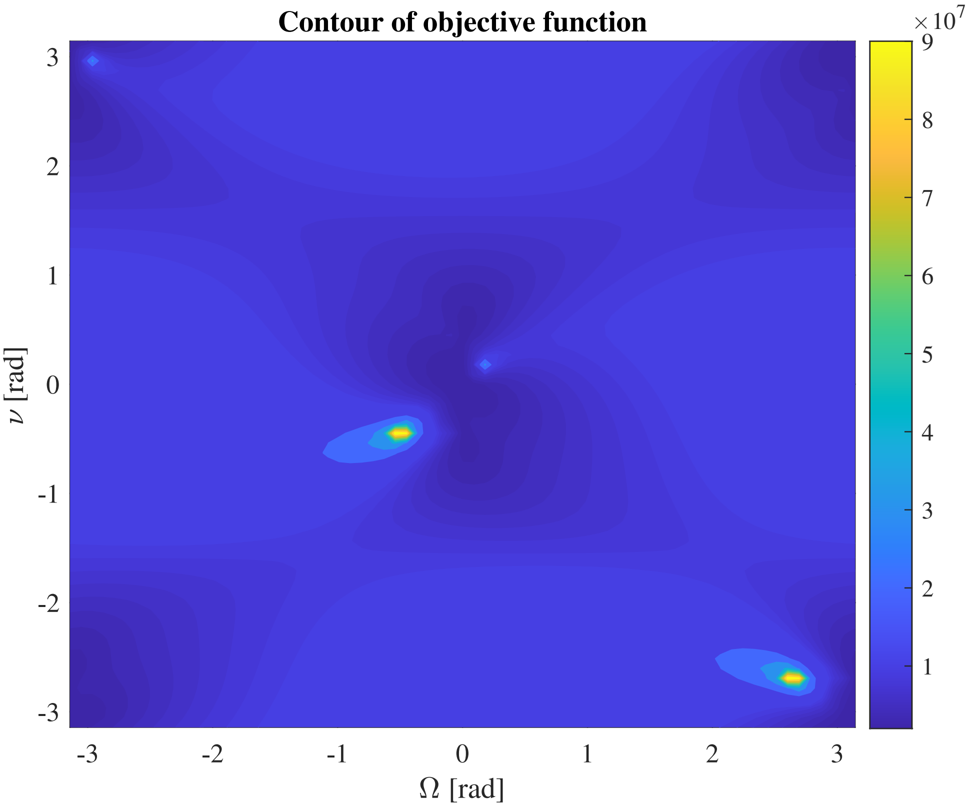

Figure 4.5: Example of contour of the objective function.

Results obtained for $\Delta\Omega$ as function of Ω_1 and ν_1 are in Fig. 4.6, while results for $\Delta\nu$ as function of Ω_1 and ν_1 are in Fig. 4.7.

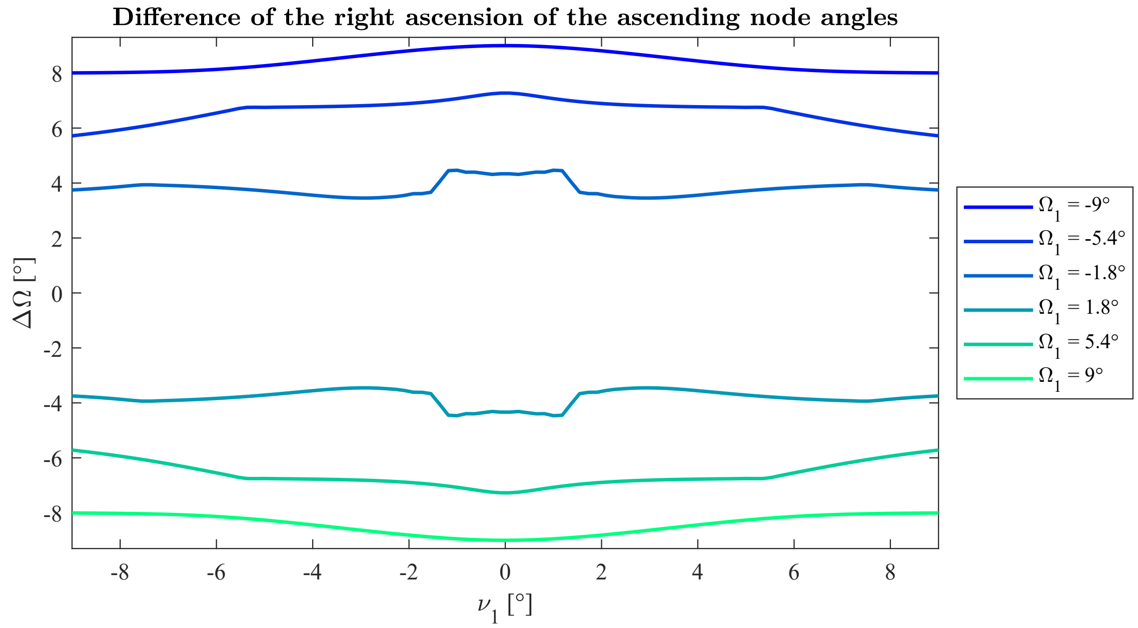

Figure 4.6: Values of $\Delta\Omega$ as function of Ω_1 and ν_1.

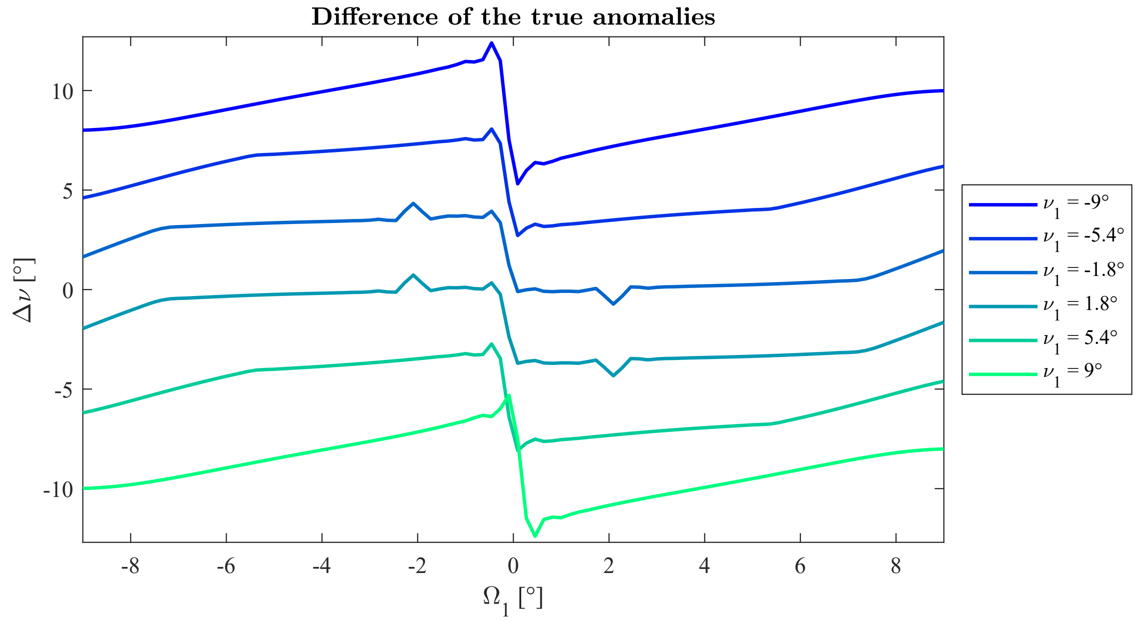

Figure 4.7: Values of $\Delta\nu$ as function of Ω_1 and ν_1.

The values of $\Delta\Omega$ resulted to be symmetric with respect to ν_1, so $\Delta\Omega(\nu_1) = \Delta\Omega(-\nu_1)$ and anti-symmetric with respect to Ω_1, so $\Delta\Omega(\Omega_1) = -\Delta\Omega(-\Omega_1)$.

The values of $\Delta\nu$ resemble the same behavior of anti-symmetry with respect to Ω_1, but shifted by a constant value in the ordinates depending on the value of ν_1, so $\Delta\nu(\Omega_1, \nu_1) = -\Delta\nu(-\Omega_1, \nu_1) + f(\nu_1)$.

From the values obtained in simulations the angle $\gamma_{1,2}$ resulted symmetric as function of both ν_1 and Ω_1, i.e., $\gamma_{1,2}(\Omega_1) = \gamma_{1,2}(-\Omega_1)$ and $\gamma_{1,2}(\nu_1) = \gamma_{1,2}(-\nu_1)$. Since its symmetry and to avoid superposition of curves, only positive values in Ω_1 have been reported in Fig. 4.8.

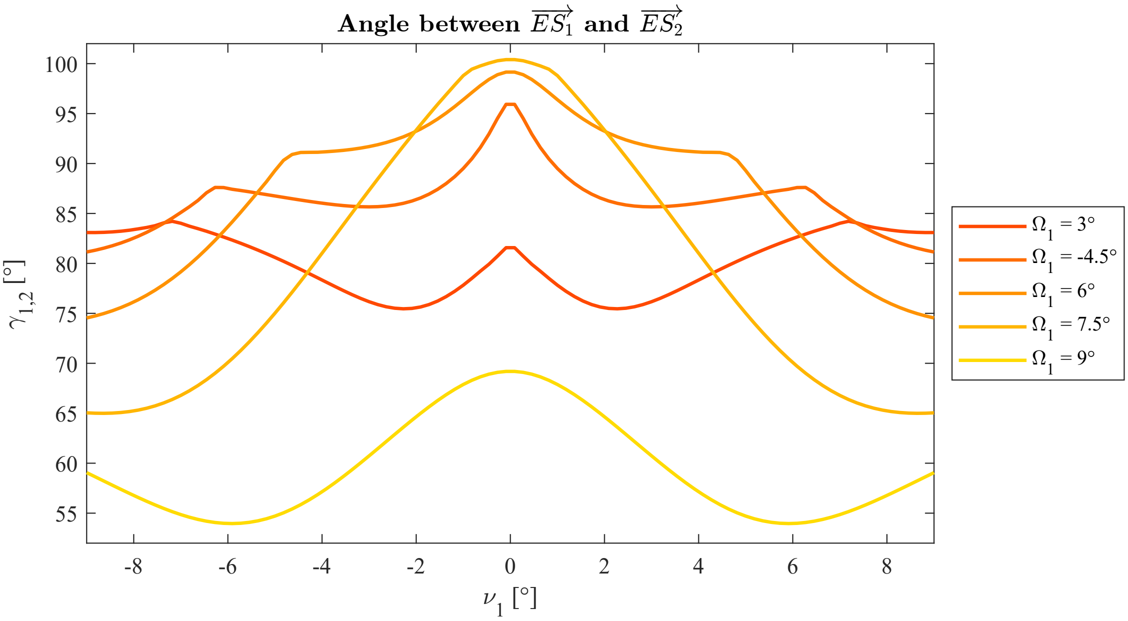

Figure 4.8: Values of $\gamma_{1,2}$ as function of Ω_1 and ν_1.

4.4.4 Changes in Orbit Radius and Emitter Latitude

The second campaign of simulations considered changes in orbit radius and emitter latitude. In particular, 17 evenly spaced values of the latitude of the emitter Λ from -80° to 80° and 9 evenly spaced values of the orbit radius r with h from 400 km to 2000 km have been considered. 14 evenly spaced values have been considered for both Ω_1 and ν_1. The total number of simulated cases is 29988. In all simulated cases the constraints were satisfied and the solution exists. In 28798 cases the solver stopped on the condition on the step tolerance, while in 1190 cases stopped on the optimality tolerance. The maximum number of iterations has never been met.

Fig. 4.9 (a) shows the values of the absolute constraint angle δ and Fig. 4.9 (b) the relative constraint angle δ_{r} with respect to the orbit height of the satellites h_{S}. In particular, it can be noticed that the constraint angle is tighter with lower heights of the orbit.

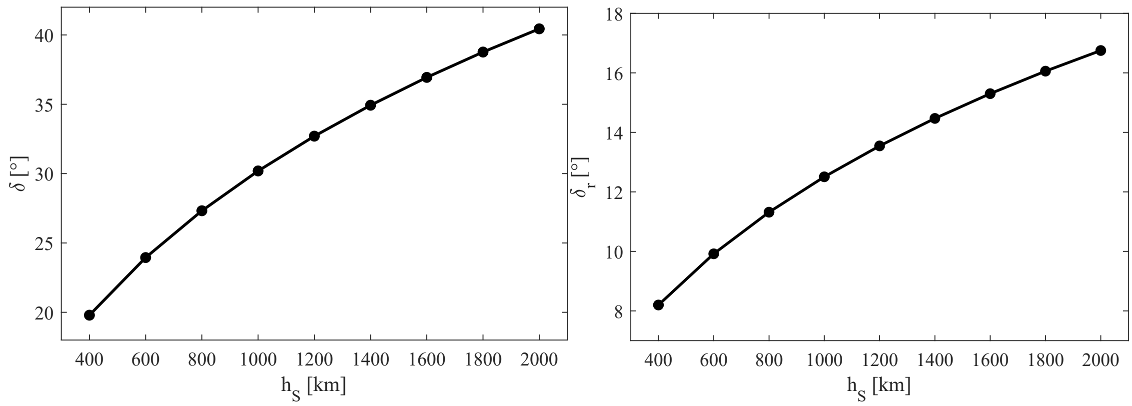

(a) Values of the absolute constraint angle δ with respect to the orbit height of the satellites h_{S}.

(b) Values of the relative constraint angle δ_{r} with respect to the orbit height of the satellites h_{S}.

Figure 4.9: Representation of the values of LOS constraints.

The values are reported also in Table 4.4.

Table 4.4: Values of the absolute condition δ and relative condition δ_{r} for the LOS with respect to the height h_{S} of the satellites S_1 and S_2.

h_{S} [km]	δ [°]	δ_{r} [°]
400	19.7926	8.1984
600	23.9459	9.9187
800	27.3222	11.3172
1000	30.1933	12.5065
1200	32.7011	13.5452
1400	34.9309	14.4689
1600	36.9393	15.3008
1800	38.7661	16.0574
2000	40.4405	16.7510

The values of

$$\begin{aligned}\Delta\Omega &= \Delta\Omega\left(\Omega_1, \nu_1, \Lambda, r\right)\\ \Delta\nu &= \Delta\nu\left(\Omega_1, \nu_1, \Lambda, r\right)\\ \gamma_{1,2} &= \gamma_{1,2}\left(\Omega_1, \nu_1, \Lambda, r\right)\end{aligned} \tag{4.75}$$

are the main results of the study. $\Delta\Omega$ and $\Delta\nu$ are the optima, while $\gamma_{1,2}$ is the spacing angle between the satellites with respect to the emitter. Since they are 4D functions the number of necessary graphical representations on 2D plane for each function is 6.

To take into account that in some representation planes the results are in different ranges with respect to ν_1, because a shift in the latitude of the emitter requires a value of $\nu_{1,0} = \Lambda$ for Nadir alignment, the independent variable ν_1 has been replaced with $\nu_1^{\Lambda} = (\nu_1 - \nu_{1,0}) = (\nu_1 - \Lambda)$, as shown in (4.76), (4.77), and (4.78).

$$\Delta\Omega = \Delta\Omega\left(\Omega_1, \nu_1 - \nu_{1,0}, \Lambda, r\right) = \Delta\Omega\left(\Omega_1, \nu_1 - \Lambda, \Lambda, r\right) = \Delta\Omega\left(\Omega_1, \nu_1^{\Lambda}, \Lambda, r\right) \tag{4.76}$$

$$\Delta\nu = \Delta\nu\left(\Omega_1, \nu_1 - \nu_{1,0}, \Lambda, r\right) = \Delta\nu\left(\Omega_1, \nu_1 - \Lambda, \Lambda, r\right) = \Delta\nu\left(\Omega_1, \nu_1^{\Lambda}, \Lambda, r\right) \tag{4.77}$$

$$\gamma_{1,2} = \gamma_{1,2}\left(\Omega_1, \nu_1 - \nu_{1,0}, \Lambda, r\right) = \gamma_{1,2}\left(\Omega_1, \nu_1 - \Lambda, \Lambda, r\right) = \Delta\gamma_{1,2}\left(\Omega_1, \nu_1^{\Lambda}, \Lambda, r\right) \tag{4.78}$$

In Figs. 4.10, 4.11, and 4.12 the dots are the calculated values obtained by the solver. Among them, the trend lines have been obtained through an interpolation with a Piecewise Cubic Hermite Interpolating Polynomial of 100 points for each curve [87]: the choice of this interpolation method has been made for graphical purposes and it is due to its shape-preserving properties and to avoid as much as possible unwanted oscillations among the values.

In particular, for the function $\Delta\Omega = \Delta\Omega\left(\Omega_1, \nu_1^{\Lambda}, \Lambda, r\right)$ the following functions

$$
\begin{aligned}
\Delta\Omega &= \Delta\Omega\left(\Omega_1, \nu_1^{\Lambda}, \Lambda_*, r_*\right)\\
\Delta\Omega &= \Delta\Omega\left(\Omega_1, \nu_{1,*}^{\Lambda}, \Lambda, r_*\right)\\
\Delta\Omega &= \Delta\Omega\left(\Omega_1, \nu_{1,*}^{\Lambda}, \Lambda_*, r\right)\\
\Delta\Omega &= \Delta\Omega\left(\Omega_{1,*}, \nu_1^{\Lambda}, \Lambda, r_*\right)\\
\Delta\Omega &= \Delta\Omega\left(\Omega_{1,*}, \nu_1^{\Lambda}, \Lambda_*, r\right)\\
\Delta\Omega &= \Delta\Omega\left(\Omega_{1,*}, \nu_{1,*}^{\Lambda}, \Lambda, r\right)
\end{aligned}
\tag{4.79}
$$

have been considered for the representations in Fig. 4.10, where $\Omega_{1,*}$, $\nu_{1,*}^{\Lambda}$, Λ_*, and r_* are fixed values.

For representations of trends, $\Lambda_* = 0°$ has been chosen, and r_* is the one that corresponds to the height $h_{\mathrm{S}_*} = 400$ km.

Because of a jump discontinuity in the result trends in $\Omega_1 = 0$ and $\nu_1^{\Lambda} = 0$, these values were not chosen for $\Omega_{1,*}$ and $\nu_{1,*}^{\Lambda}$. Instead, for $\Omega_{1,*}$ and $\nu_{1,*}^{\Lambda}$ the first positive values in range of simulated values have been considered.

These first positive values depend on how the ranges for Ω_1 and ν_1^{Λ} are defined and spaced in simulation environment; in this study 14 evenly spaced values have been considered, but the ranges depend on the relative condition δ_r. Considering these two facts the first positive values for $\Omega_{1,*}$ and $\nu_{1,*}^{\Lambda}$ depend on the value of the orbit radius r: it vary from $\approx 0.63°$ for $h_{\mathrm{S}_*} = 400$ km to $\approx 1.29°$ for $h_{\mathrm{S}} = 2000$ km.

For the function $\Delta\nu = \Delta\nu\left(\Omega_1, \nu_1^{\Lambda}, \Lambda, r\right)$ the following functions

$$
\begin{aligned}
\Delta\nu &= \Delta\nu\left(\Omega_1, \nu_1^{\Lambda}, \Lambda_*, r_*\right)\\
\Delta\nu &= \Delta\nu\left(\Omega_1, \nu_{1,*}^{\Lambda}, \Lambda, r_*\right)\\
\Delta\nu &= \Delta\nu\left(\Omega_1, \nu_{1,*}^{\Lambda}, \Lambda_*, r\right)\\
\Delta\nu &= \Delta\nu\left(\Omega_{1,*}, \nu_1^{\Lambda}, \Lambda, r_*\right)\\
\Delta\nu &= \Delta\nu\left(\Omega_{1,*}, \nu_1^{\Lambda}, \Lambda_*, r\right)\\
\Delta\nu &= \Delta\nu\left(\Omega_{1,*}, \nu_{1,*}^{\Lambda}, \Lambda, r\right)
\end{aligned}
\tag{4.80}
$$

have been considered for the representations in Fig. 4.11. Same considerations made for $\Delta\Omega$ apply for the values of $\Omega_{1,*}$, $\nu_{1,*}^{\Lambda}$, Λ_*, and r_* in the representation of $\Delta\nu$ function.

For the function $\gamma_{1,2} = \gamma_{1,2}\left(\Omega_1, \nu_1^{\Lambda}, \Lambda, r\right)$ the following functions

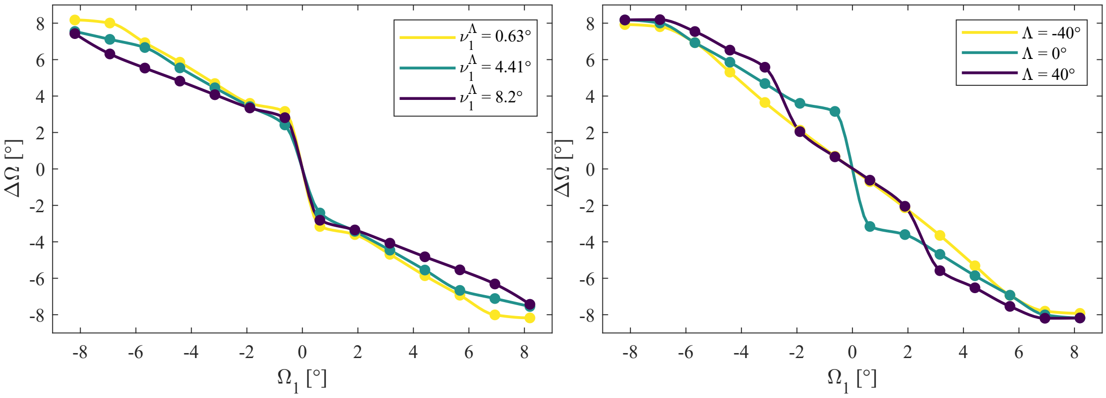

(a) Graphic representation of the function $\Delta\Omega = \Delta\Omega\left(\Omega_1, \nu_1^\Lambda, \Lambda_*, r_*\right)$.

(b) Graphic representation of the function $\Delta\Omega = \Delta\Omega\left(\Omega_1, \nu_{1,*}^\Lambda, \Lambda, r_*\right)$.

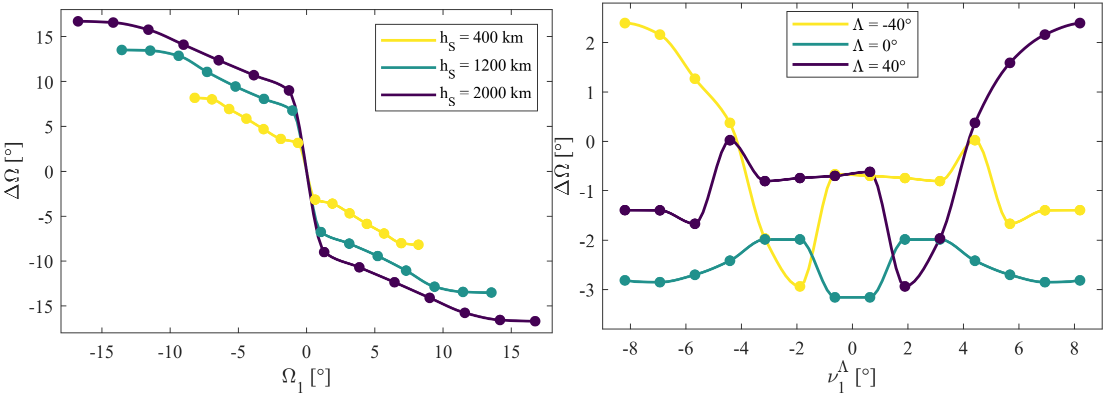

(c) Graphic representation of the function $\Delta\Omega = \Delta\Omega\left(\Omega_1, \nu_{1,*}^\Lambda, \Lambda_*, r\right)$.

(d) Graphic representation of the function $\Delta\Omega = \Delta\Omega\left(\Omega_{1,*}, \nu_1^\Lambda, \Lambda, r_*\right)$.

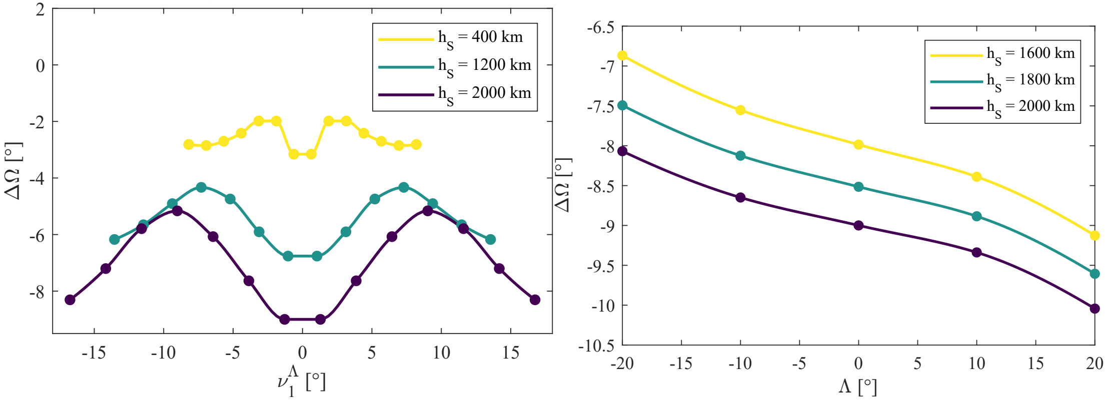

(e) Graphic representation of the function $\Delta\Omega = \Delta\Omega\left(\Omega_{1,*}, \nu_1^\Lambda, \Lambda_*, r\right)$.

(f) Graphic representation of the function $\Delta\Omega = \Delta\Omega\left(\Omega_{1,*}, \nu_{1,*}^\Lambda, \Lambda, r\right)$.

Figure 4.10: Trends of the function $\Delta\Omega = \Delta\Omega\left(\Omega_1, \nu_1^\Lambda, \Lambda, r\right)$ representative of optima of the differences between the values of the right ascension of the ascending node of the two satellites. Dots are results of simulation, lines are interpolated values.

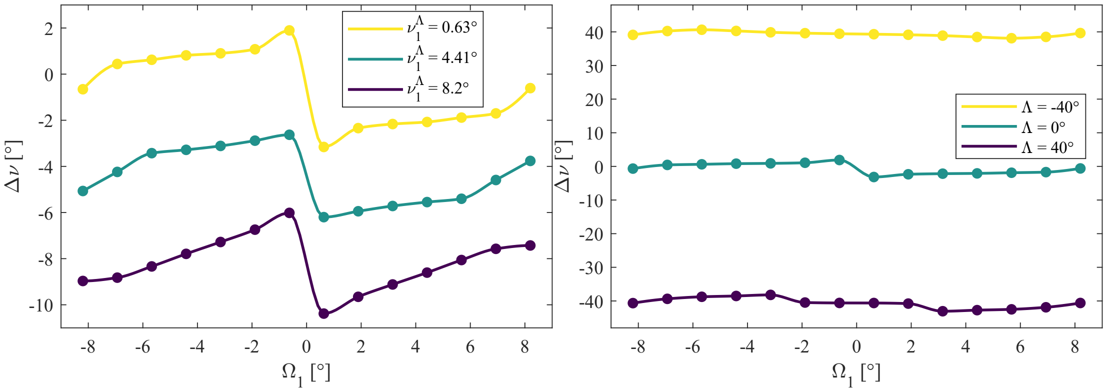

(a) Graphic representation of the function $\Delta\nu = \Delta\nu\left(\Omega_1, \nu_1^\Lambda, \Lambda_*, r_*\right)$.

(b) Graphic representation of the function $\Delta\nu = \Delta\nu\left(\Omega_1, \nu_{1,*}^\Lambda, \Lambda, r_*\right)$.

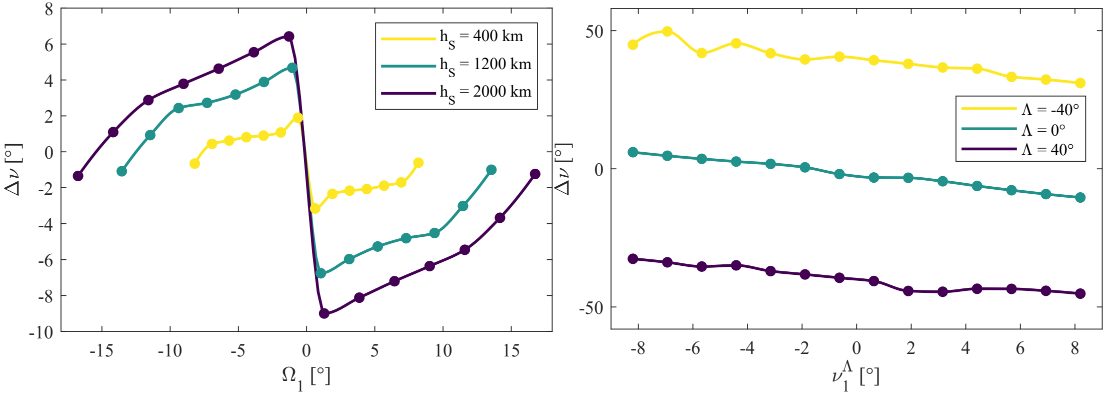

(c) Graphic representation of the function $\Delta\nu = \Delta\nu\left(\Omega_1, \nu_{1,*}^\Lambda, \Lambda_*, r\right)$.

(d) Graphic representation of the function $\Delta\nu = \Delta\nu\left(\Omega_{1,*}, \nu_1^\Lambda, \Lambda, r_*\right)$.

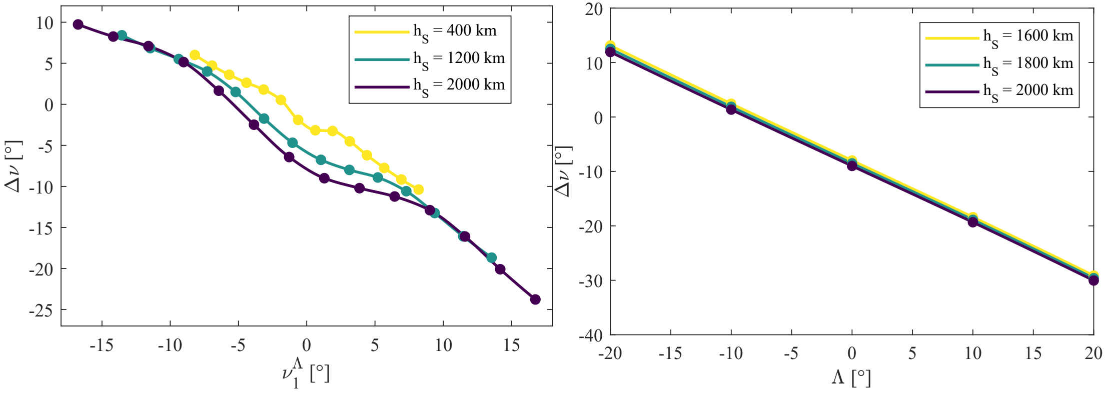

(e) Graphic representation of the function $\Delta\nu = \Delta\nu\left(\Omega_{1,*}, \nu_1^\Lambda, \Lambda_*, r\right)$.

(f) Graphic representation of the function $\Delta\nu = \Delta\nu\left(\Omega_{1,*}, \nu_{1,*}^\Lambda, \Lambda, r\right)$.

Figure 4.11: Trends of the function $\Delta\nu = \Delta\nu\left(\Omega_1, \nu_1^\Lambda, \Lambda, r\right)$ representative of optima of the differences between the values of the true anomaly of the two satellites. Dots are results of simulation, lines are interpolated values.

$$\begin{aligned}\gamma_{1,2} &= \gamma_{1,2}\left(\Omega_1, \nu_1^\Lambda, \Lambda_*, r_*\right)\\ \gamma_{1,2} &= \gamma_{1,2}\left(\Omega_1, \nu_{1,*}^\Lambda, \Lambda, r_*\right)\\ \gamma_{1,2} &= \gamma_{1,2}\left(\Omega_1, \nu_{1,*}^\Lambda, \Lambda_*, r\right)\\ \gamma_{1,2} &= \gamma_{1,2}\left(\Omega_{1,*}, \nu_1^\Lambda, \Lambda, r_*\right)\\ \gamma_{1,2} &= \gamma_{1,2}\left(\Omega_{1,*}, \nu_1^\Lambda, \Lambda_*, r\right)\\ \gamma_{1,2} &= \gamma_{1,2}\left(\Omega_{1,*}, \nu_{1,*}^\Lambda, \Lambda, r\right)\end{aligned} \tag{4.81}$$

have been considered for the representations in Fig. 4.12. Same considerations made for $\Delta\Omega$ apply for the values of $\Omega_{1,*}$, $\nu_{1,*}^\Lambda$, Λ_*, and r_* in the representation of $\gamma_{1,2}$ function.

Once the results have been obtained, their interpretation has been performed.

The first set of functions is the ones in (4.79). From Fig. 4.10 (a), (b), (c), the dependence of $\Delta\Omega$ with respect to the right ascension of the ascending node of the first satellite Ω_1 reveals that it is always decreasing with a possible presence of a jump discontinuity in the value of $\Omega_1 = 0$.

Furthermore, $\Delta\Omega$ appears also anti-symmetric with respect to Ω_1: i.e., $\Delta\Omega\left(\Omega_1\right) = -\Delta\Omega\left(-\Omega_1\right)$. This behavior confirms the prediction of a previous investigation [67], even if it was restricted to a selected instance of the problem.

A possible approximate and linear models for $\Delta\Omega$ with respect to Ω_1 to capture the behaviors of these results are

$$\begin{aligned}&\Delta\Omega\left(\Omega_1, \nu_1^\Lambda, \Lambda_*, r_*\right) \approx -k_{\nu_1,1}\left(\nu_1^\Lambda, \Lambda_*, r_*\right)\Omega_1\\ &+k_{\nu_1,2}\left(\nu_1^\Lambda, \Lambda_*, r_*\right)\operatorname{sgn}\left(\Omega_1\right) + f_{\nu_1}\left(\nu_1^\Lambda, \Lambda_*, r_*\right)\end{aligned} \tag{4.82}$$

with $k_{\nu_1,1}\left(\nu_1^\Lambda, \Lambda_*, r_*\right), k_{\nu_1,2}\left(\nu_1^\Lambda, \Lambda_*, r_*\right) \in \mathbb{R}_{>0}$ as linear coefficients and $f_{\nu_1}\left(\nu_1^\Lambda, \Lambda_*, r_*\right)$ as nonlinear function with minimal effect,

$$\begin{aligned}&\Delta\Omega\left(\Omega_1, \nu_{1,*}^\Lambda, \Lambda, r_*\right) \approx -k_{\Lambda,1}\left(\nu_{1,*}^\Lambda, \Lambda, r_*\right)\Omega_1\\ &+k_{\Lambda,2}\left(\nu_{1,*}^\Lambda, \Lambda, r_*\right)\operatorname{sgn}\left(\Omega_1\right) + f_\Lambda\left(\nu_{1,*}^\Lambda, \Lambda, r_*\right)\end{aligned} \tag{4.83}$$

with $k_{\Lambda,1}\left(\nu_{1,*}^\Lambda, \Lambda, r_*\right), k_{\Lambda,2}\left(\nu_{1,*}^\Lambda, \Lambda, r_*\right) \in \mathbb{R}_{>0}$ as linear coefficients and $f_\Lambda\left(\nu_{1,*}^\Lambda, \Lambda, r_*\right)$ as nonlinear function with minimal effect, and

$$\begin{aligned}&\Delta\Omega\left(\Omega_1, \nu_{1,*}^\Lambda, \Lambda_*, r\right) \approx -k_{r,1}\left(\nu_{1,*}^\Lambda, \Lambda_*, r\right)\Omega_1\\ &+k_{r,2}\left(\nu_{1,*}^\Lambda, \Lambda_*, r\right)\operatorname{sgn}\left(\Omega_1\right) + f_r\left(\nu_{1,*}^\Lambda, \Lambda_*, r\right)\end{aligned} \tag{4.84}$$

with $k_{r,1}\left(\nu_{1,*}^\Lambda, \Lambda_*, r\right), k_{r,2}\left(\nu_{1,*}^\Lambda, \Lambda_*, r\right) \in \mathbb{R}_{>0}$ as linear coefficients and $f_r\left(\nu_{1,*}^\Lambda, \Lambda_*, r\right)$ as nonlinear function with minimal effect.

In Fig. 4.10 (c) it can be noticed also that the function $\Delta\Omega$ with respect to the orbit radius r presents an amplification and a change of scale with respect to Ω_1, so

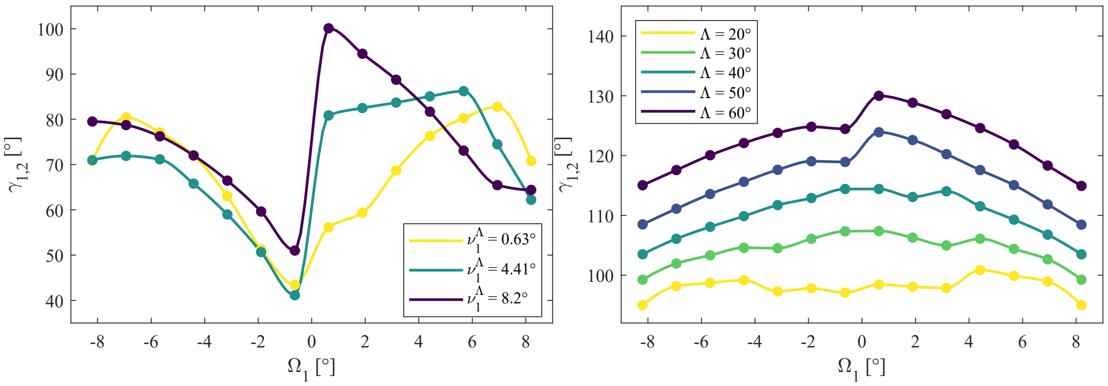

(a) Graphic representation of the function $\gamma_{1,2} = \gamma_{1,2}\left(\Omega_1, \nu_1^\Lambda, \Lambda_*, r_*\right)$.

(b) Graphic representation of the function $\gamma_{1,2} = \gamma_{1,2}\left(\Omega_1, \nu_{1,*}^\Lambda, \Lambda, r_*\right)$.

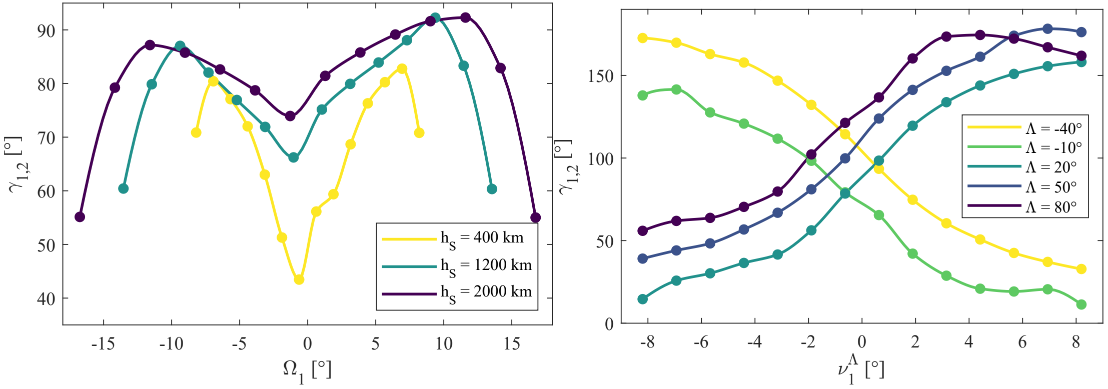

(c) Graphic representation of the function $\gamma_{1,2} = \gamma_{1,2}\left(\Omega_1, \nu_{1,*}^\Lambda, \Lambda_*, r\right)$.

(d) Graphic representation of the function $\gamma_{1,2} = \gamma_{1,2}\left(\Omega_{1,*}, \nu_1^\Lambda, \Lambda, r_*\right)$.

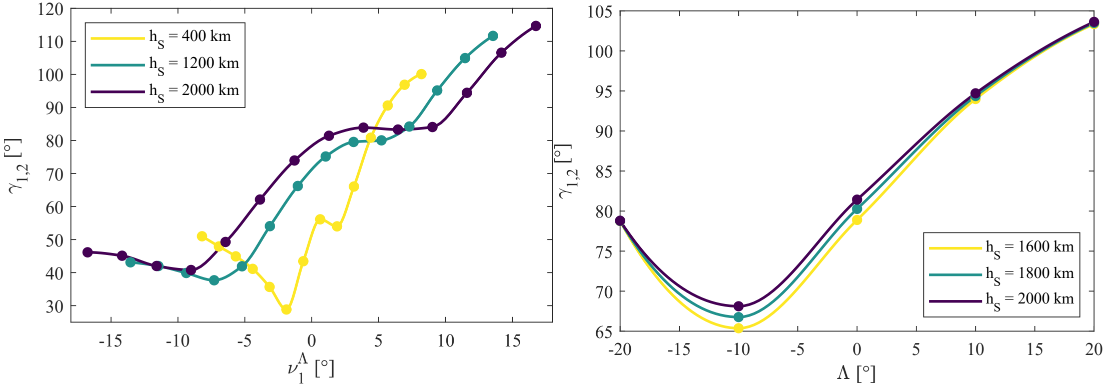

(e) Graphic representation of the function $\gamma_{1,2} = \gamma_{1,2}\left(\Omega_{1,*}, \nu_1^\Lambda, \Lambda_*, r\right)$.

(f) Graphic representation of the function $\gamma_{1,2} = \gamma_{1,2}\left(\Omega_{1,*}, \nu_{1,*}^\Lambda, \Lambda, r\right)$.

Figure 4.12: Trends of the function $\gamma_{1,2} = \gamma_{1,2}\left(\Omega_1, \nu_1^\Lambda, \Lambda, r\right)$ representative of optima of the values of the spacing angle between the two satellites. Dots are results of simulation, lines are interpolated values.

$$\Delta\Omega\left(\Omega_1, \nu_{1,*}^{\Lambda}, \Lambda_*, r\right) \approx -k_1\left(r\right)\Delta\Omega\left(-k_2\left(r\right)\Omega_1, \nu_{1,*}^{\Lambda}, \Lambda_*\right) \tag{4.85}$$

could also be an alternative possible model with $k_1\left(r\right), k_2\left(r\right) \in \mathbb{R}\backslash\{0\}$.

From Fig. 4.10 (a), (d), (e), the dependence of $\Delta\Omega$ with respect to ν_1^{Λ} appears more complicated. In selected cases of [67] it was predicted a symmetric behavior as $\Delta\Omega\left(\nu_1^{\Lambda}\right) = \Delta\Omega\left(-\nu_1^{\Lambda}\right)$, but the extended analysis of this present study reveals that $\Delta\Omega\left(\nu_1^{\Lambda}\right)$ is still symmetric varying the orbit radius r (i.e., h_S)), but it has a more complicated behavior with respect to the latitude of the emitter when $\Lambda \neq 0$, revealing a local minimum and a local maximum, as shown in Fig. 4.10 (d).

From Fig. 4.10 (f), there is a decreasing behavior with respect to the orbit radius r (i.e., the height h_S). This is also evident in Fig. 4.10 (e) and for positive values of Ω_1 in Fig. 4.10 (c), so

$$\begin{cases} \dfrac{\partial\left(\Delta\Omega\right)}{\partial r} > 0 & \Omega_1 > 0 \\ \dfrac{\partial\left(\Delta\Omega\right)}{\partial r} < 0 & \Omega_1 < 0 \end{cases} \tag{4.86}$$

is a possible interpretation of the data.

The second set of functions is the ones reported in (4.80). From Fig. 4.11 (a), (b), (c), the dependence of $\Delta\nu$ with respect to Ω_1 reveals an anti-symmetric behavior, i.e., $\Delta\nu\left(\Omega_1\right) = -\Delta\nu\left(-\Omega_1\right)$.

In addition to anti-symmetry with respect to Ω_1, there is a translation with respect to ν_1^{Λ}, i.e.,

$$\Delta\nu\left(\Omega_1, \nu_1^{\Lambda}, \Lambda_*, r_*\right) \approx -\Delta\nu\left(-\Omega_1, \nu_1^{\Lambda}, \Lambda_*, r_*\right) + k\left(\nu_1^{\Lambda}\right)\mathrm{sgn}\left(\nu_1^{\Lambda}\right) \tag{4.87}$$

with $k\left(\nu_1^{\Lambda}\right) \in \mathbb{R}_{>0}$; the sign function models the mathematical jump.

There is a translation also with respect to Λ, i.e.,

$$\Delta\nu\left(\Omega_1, \nu_{1,*}^{\Lambda}, \Lambda, r_*\right) \approx -\Delta\nu\left(-\Omega_1, \nu_{1,*}^{\Lambda}, \Lambda, r_*\right) + k\left(\Lambda\right)\mathrm{sgn}\left(\Lambda\right) \tag{4.88}$$

with $k\left(\Lambda\right) \in \mathbb{R}_{>0}$.

With respect to the orbit radius r, the function $\Delta\nu$ presents an amplification and a change of scale with respect to ν_1^{Λ}, so

$$\Delta\nu\left(\Omega_1, \nu_{1,*}^{\Lambda}, \Lambda_*, r\right) \approx -k_1\left(r\right)\Delta\nu\left(-k_2\left(r\right)\Omega_1, \nu_{1,*}^{\Lambda}, \Lambda_*\right) \tag{4.89}$$

with $k_1\left(r\right), k_2\left(r\right) \in \mathbb{R}\backslash\{0\}$ is a possible model to interpret the data in Fig. 4.11 (c).

From Fig. 4.11 (b), (d), (f) the behavior of $\Delta\nu$ with respect to the latitude of the emitter Λ is always decreasing, then

$$\frac{\partial\left(\Delta\nu\right)}{\partial\Lambda} < 0 \tag{4.90}$$

in every case.

In Fig. 4.11 (e) the behavior of $\Delta\nu$ with respect to the combined variation of both the orbit radius r and the true anomaly of the first satellite scaled with the actual position of the emitter ν_1^Λ resembles a similar amplification and a change of scale with respect to r of (4.89), but without anti-symmetry as shown in (4.91), where $k_1\left(r\right), k_2\left(r\right) \in \mathbb{R}\backslash\{0\}$.

$$\Delta\nu\left(\Omega_{1,*}, \nu_1^\Lambda, \Lambda_*, r\right) \approx k_1\left(r\right)\Delta\nu\left(\Omega_{1,*}, k_2\left(r\right)\nu_1^\Lambda, \Lambda_*\right) \tag{4.91}$$

Fig. 4.11 (f) shows the decreasing behavior of $\Delta\nu$ with respect to Λ, as stated in (4.90), but it reveals also a minimal (if not negligible) effect of the orbit radius r when Ω_1 and ν_1^Λ are not varying, so $\Delta\nu\left(\Omega_{1,*}, \nu_{1,*}^\Lambda, \Lambda, r\right) \approx \Delta\nu\left(\Omega_{1,*}, \nu_{1,*}^\Lambda, \Lambda\right)$.

The third set of functions is the ones reported in (4.81). From Fig. 4.12 (a), (b), (c), the dependence of $\gamma_{1,2}$ with respect to Ω_1 reveals macroscopic symmetric behavior, but with nonlinear influences due to other variables.

The completely symmetric model predicted in [67], i.e. $\gamma_{1,2}\left(\Omega_1\right) = \gamma_{1,2}\left(-\Omega_1\right)$, obtained in simplified scenarios, must be corrected with nonlinear influences that depend on the actual values of ν_1^Λ, Λ, and r.

Possible additive models could be the ones reported in (4.92), (4.93), and (4.94).

$$\gamma_{1,2}\left(\Omega_1, \nu_1^\Lambda, \Lambda_*, r_*\right) = \gamma_{1,2}\left(-\Omega_1, \nu_1^\Lambda, \Lambda_*, r_*\right) + f\left(\nu_1^\Lambda, \Lambda_*, r_*\right) \tag{4.92}$$

$$\gamma_{1,2}\left(\Omega_1, \nu_{1,*}^\Lambda, \Lambda, r_*\right) = \gamma_{1,2}\left(-\Omega_1, \nu_{1,*}^\Lambda, \Lambda, r_*\right) + f\left(\nu_{1,*}^\Lambda, \Lambda, r_*\right) \tag{4.93}$$

$$\gamma_{1,2}\left(\Omega_1, \nu_{1,*}^\Lambda, \Lambda_*, r\right) = \gamma_{1,2}\left(-\Omega_1, \nu_{1,*}^\Lambda, \Lambda_*, r\right) + f\left(\nu_{1,*}^\Lambda, \Lambda_*, r\right) \tag{4.94}$$

From Fig. 4.12 (a), (d) the behavior of $\gamma_{1,2}$ with respect to the true anomaly of the first satellite ν_1^Λ (translated considering the actual latitude of the emitter) reveals two distinct trends: $\gamma_{1,2}$ is decreasing for negative values of ν_1^Λ and $\gamma_{1,2}$ is increasing for positive values of ν_1^Λ, so

$$\begin{cases} \dfrac{\partial\left(\gamma_{1,2}\right)}{\partial\nu_1^\Lambda} > 0 & \nu_1^\Lambda > 0 \\ \dfrac{\partial\left(\gamma_{1,2}\right)}{\partial\nu_1^\Lambda} < 0 & \nu_1^\Lambda < 0 \end{cases} \tag{4.95}$$

is a possible interpretation of the data.

However, the trends in Fig. 4.12 (a), (d) are related to low altitudes (i.e., h = 400 km); when the value of the altitude becomes higher, the main trend is the increasing one, as shown in Fig. 4.12 (e), revealing a possible multiplicative influence of the orbit radius r. Given two orbit radii $r_{\mathrm{S_A}}$ and $r_{\mathrm{S_B}}$, a possible model is the one shown in (4.96), where $\Delta r_{A,B} = r_{\mathrm{S_B}} - r_{\mathrm{S_A}}$ is the difference of the orbits radii, f is multiplicative function of the orbit radii, and $k \in \mathbb{R}$ is an eventual additive shift. In particular, $f < 0$ for $\nu_1^{\Lambda} < 0$ and $f > 0$ for $\nu_1^{\Lambda} > 0$.

$$\gamma_{1,2}\left(r_{\mathrm{S_B}}\right) \approx f\left(\nu_1^{\Lambda}, \Delta r_{A,B}\right) \gamma_{1,2}\left(r_{\mathrm{S_A}}\right) + k\left(\nu_1^{\Lambda}, \Delta r_{A,B}\right) \tag{4.96}$$

From Fig. 4.12 (b) the behavior of $\gamma_{1,2}$ with respect to Λ, varying Ω_1, but keeping a fixed value of ν_1^{Λ} and orbit radius r, reveals an increase of the spacing angle, i.e., given $\Lambda_{\mathrm{A}} > \Lambda_{\mathrm{B}}$, then

$$\gamma_{1,2}\left(\Omega_1, \nu_{1,*}^{\Lambda}, \Lambda_{\mathrm{A}}, r_*\right) > \gamma_{1,2}\left(\Omega_1, \nu_{1,*}^{\Lambda}, \Lambda_{\mathrm{B}}, r_*\right) \tag{4.97}$$

for every value of Ω_1.

From Fig. 4.12 (d) the behavior of $\gamma_{1,2}$ with respect to Λ, varying ν_1^{Λ}, but keeping a fixed value of Ω_1 and orbit radius r, reveals two trends: $\gamma_{1,2}$ is increasing for $\Lambda > 0$ and it is decreasing for $\Lambda < 0$, so (4.98) can be formulated as a macroscopic level of approximation.

$$\begin{cases} \dfrac{\partial\left(\gamma_{1,2}\right)}{\partial \nu_1^{\Lambda}} \geq 0 & \Lambda > 0 \\ \dfrac{\partial\left(\gamma_{1,2}\right)}{\partial \nu_1^{\Lambda}} \geq 0 & \Lambda < 0 \end{cases} \tag{4.98}$$

Considering also the specular trends Fig. 4.12 (d), the property in (4.99) holds.

$$\gamma_{1,2}\left(\Omega_{1,*}, \nu_1^{\Lambda}, \Lambda, r_*\right) = -\gamma_{1,2}\left(\Omega_{1,*}, \nu_1^{\Lambda}, -\Lambda, r_*\right) \tag{4.99}$$

In the last result of the study, the Fig. 4.12 (f), there is the combined influence of the latitude of the emitter Λ and the orbit radius r when the angular position of the first satellite is fixed and not varying (i.e., $\Omega_1 = \Omega_{1,*}$ and $\nu_1^{\Lambda} = \nu_{1,*}^{\Lambda}$). In particular, The effect of Λ is dominant with a second order trend and a local minimum; instead, the effect of the orbit radius r appears decoupled. Properties in (4.100) hold with $\Lambda_{\mathrm{m}}\left(\Omega_{1,*}, \nu_{1,*}^{\Lambda}\right)$ the value of the minimum which depends on the actual values of Ω_1 and ν_1^{Λ}.

$$\begin{cases} \dfrac{\partial\left(\gamma_{1,2}\right)}{\partial \Lambda} > 0 & \Lambda > \Lambda_{\mathrm{m}}\left(\Omega_{1,*}, \nu_{1,*}^{\Lambda}\right) \\ \dfrac{\partial\left(\gamma_{1,2}\right)}{\partial \Lambda} < 0 & \Lambda < \Lambda_{\mathrm{m}}\left(\Omega_{1,*}, \nu_{1,*}^{\Lambda}\right) \\ \dfrac{\partial^2\left(\gamma_{1,2}\right)}{\partial \Lambda^2} < 0 & \forall \Lambda \in \left(-\dfrac{\pi}{2}, \dfrac{\pi}{2}\right) \\ \dfrac{\partial\left(\gamma_{1,2}\right)}{\partial r} > 0 & \forall \Lambda \in \left(-\dfrac{\pi}{2}, \dfrac{\pi}{2}\right) \end{cases} \tag{4.100}$$

4.4.5 Influence of SNR on Optimum Constellation

By definition [88], the DOP is calculated considering the square root of the trace of the inverse of the Fisher Information Matrix **F**, built from the Geometric Design Matrix **H** and the Covariance Matrix **C**. In particular, the Position Dilution of Precision $PDOP$ has a 3 × 3 Fisher Information Matrix, as shown in (4.43) and reported in (4.101).

$$PDOP = \sqrt{Tr\left(\mathbf{F}_{3\times3}^{-1}\right)} = \sqrt{Tr\left(\left(\mathbf{H}_{4\times3}^{\mathrm{T}}\mathbf{C^{-1}}_{4\times4}\mathbf{H}_{4\times3}\right)^{-1}\right)} \tag{4.101}$$

Considering the assumptions of Gaussian, independent and non-correlated errors in the measurements, the Covariance Matrix is diagonal with values of standard deviations on the main diagonal as shown in (4.46).

This campaign of analysis considers two different cases.

The first case assumes that all the values of the standard deviations are the same for every satellite regardless of the geometrical configuration, so $\sigma_{\hat{\alpha}_{\mathrm{Az},1}} = \sigma_{\hat{\alpha}_{\mathrm{El},1}} = \sigma_{\hat{\alpha}_{\mathrm{Az},2}} = \sigma_{\hat{\alpha}_{\mathrm{El},2}} = \sigma$.

For this first case, (4.101) simplifies as in (4.102).

$$PDOP = \sigma\sqrt{Tr\left(\left(\mathbf{H}_{4\times3}^{\mathrm{T}}\mathbf{H}_{4\times3}\right)^{-1}\right)} \tag{4.102}$$

The second case considers the actual values of the Signal-to-Noise for every satellite, so for satellite S_1 it is assumed $\sigma_{\hat{\alpha}_{\mathrm{Az},1}} = \sigma_{\hat{\alpha}_{\mathrm{El},1}} = \sigma_1\left(SNR_1\right)$, and for satellite S_2 it is considered $\sigma_{\hat{\alpha}_{\mathrm{Az},2}} = \sigma_{\hat{\alpha}_{\mathrm{El},2}} = \sigma_2\left(SNR_2\right)$.

The values of SNR_1 and SNR_2 considered for the simulations are such that they have a certain probability of detection p_{D} and probability of false alarms p_{FA} — in the worst case where the satellites are in the furthest position with respect to the emitter — and they are obtained from the ROC for a linear detector, a non-fluctuating signal with unknown phase, and Gaussian noise. Furthermore, free-space path loss propagation has been assumed for the evaluation of SNR_1 and SNR_2.

The simulations conducted for these comparison have been conducted with the aid of the Optimization Toolbox and the Symbolic Math Toolbox of the MATLAB environment. The following settings have been used for the solver: step tolerance of 10^{-15}, optimality tolerance of 10^{-12}, constraint tolerance of 10^{-12}, interior point algorithm, and scheme of central finite differences.

For the detector it is assumed the probabilities of false alarm $p_{\mathrm{FA}} = 10^{-6}$ and of detection $p_{\mathrm{D}} = 0.997$. The corresponding ROC curve gives a minimum value of $SNR\left(p_{\mathrm{FA}}, p_{\mathrm{D}}\right) \approx 15$ dB. In addition, an increment of 3 dB has been considered as safety margin to take into account neglected effects (i.e., the presence of the atmosphere).

The receiver has $L = 0.334$ m and $M = 7$.

Furthermore, the influence of the actual distance between every satellite and the emitter in a free-space path loss model has been considered for the value of SNR.

For evaluative purposes, the target frequency considered in the study is $f = 1575.42$ MHz, which is associated to the center of L1/E1 band of GNSS services and applications.

The satellites S_1 and S_2 are supposed to be placed on orbits in LEO with heights of 400 km.

The emitter position is placed in geodetic latitude of $\Lambda = 0°$, longitude of $\lambda = 0°$, and height $h_{\mathrm{E}} = 0$ m.

Results of the simulation are in Fig. 4.13 for the function $\Delta\Omega$, Fig. 4.14 for the function $\Delta\nu$, and Fig. 4.15 for the function $\gamma_{1,2}$.

The analysis of the results shows that from a qualitative point of view the trends of the functions $\Delta\Omega$, $\Delta\nu$, and $\gamma_{1,2}$ are the same both in the first case (i.e., without the effect of SNR) and in the second case (i.e., with the effect of SNR).

Results of symmetry and anti-symmetry appears to be same for both the cases. In particular, for the function $\Delta\Omega$ it results $\Delta\Omega\left(\Omega_1, \nu_1\right) = -\Delta\Omega\left(-\Omega_1, -\nu_1\right)$, so symmetric with respect to Ω_1 and anti-symmetric with respect to ν_1. For the function $\Delta\nu$ it results $\Delta\nu\left(\Omega_1, \nu_1\right) = -\Delta\nu\left(-\Omega_1, -\nu_1\right) + f\left(\nu_1\right)$, so anti-symmetric with respect to both Ω_1 and ν_1. However, a shift on the values of the ordinates depending on the value of ν_1 is observed. For the function $\gamma_{1,2}$ it results $\gamma_{1,2}\left(\Omega_1, \nu_1\right) = \gamma_{1,2}\left(-\Omega_1, -\nu_1\right)$ denoting a complete symmetry with respect to both Ω_1 and ν_1.

Regarding the difference of differences $\Delta\left(\Delta\Omega\right) = \Delta\Omega_{\text{With SNR}} - \Delta\Omega_{\text{Without SNR}}$, the biggest variations appear to happen either for small values of the modulus of the angles of the right ascension of the ascending node $|\Omega_1| < 1°$ and for large ones $|\Omega_1| > 6°$. Differences appear to increase for small values of the true anomaly $|\nu_1| < 1°$ compared to big ones. However, the absolute variations are contained in 2°.

For the difference of differences $\Delta\left(\Delta\nu\right) = \Delta\nu_{\text{With SNR}} - \Delta\nu_{\text{Without SNR}}$ biggest variations appear to happen for high values of the modulus of the angle of the true anomaly, $|\Omega_1| > 6°$ regardless of the value of the right ascension of the ascending node Ω_1. Variations for the true anomaly appears to be very significative, up to 10° in absolute value.

The biggest variations of the difference in spacing angle $\Delta\gamma_{1,2} = \gamma_{1,2|\text{With SNR}} - \gamma_{1,2|\text{Without SNR}}$ are observed for small values of the modulus of the right ascension of the ascending node $|\Omega_1|$ and for high values of the modulus of the true anomaly $|\nu_1|$. Variations in the spacing angle $\gamma_{1,2}$ appear to be important in triangle geometry (i.e., the triangle $\triangle S_1 E S_2$) and differences can approximately be up to 65° in absolute value.

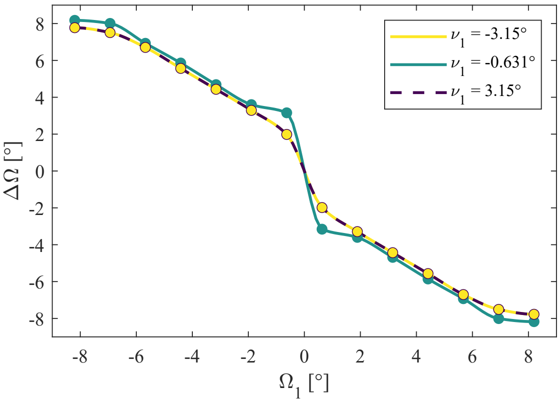

(a) Representation of the function $\Delta\Omega$ without the effect of SNR.

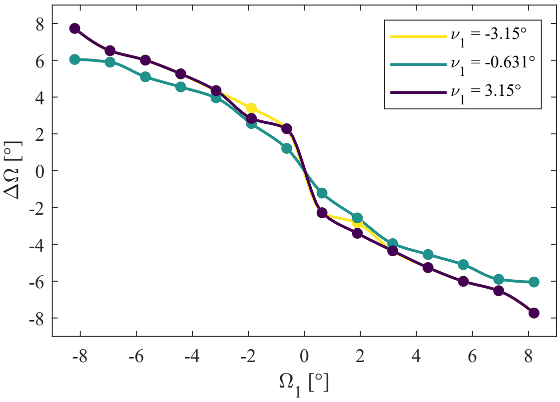

(b) Representation of the function $\Delta\Omega$ with the effect of SNR.

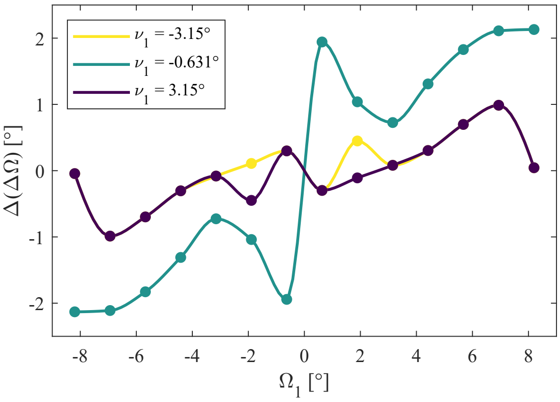

(c) Representation of the differences of differences $\Delta\left(\Delta\Omega\right)$.

Figure 4.13: Values of the difference of the right ascension of the ascending nodes $\Delta\Omega$ for the satellite S_2 with respect to the position of the satellite S_1 in terms of right ascension of the ascending node Ω_1 and the true anomaly ν_1. In (a) without the effect of SNR, in (b) with the effect of SNR, in (c) the difference between the two cases (with and without SNR).

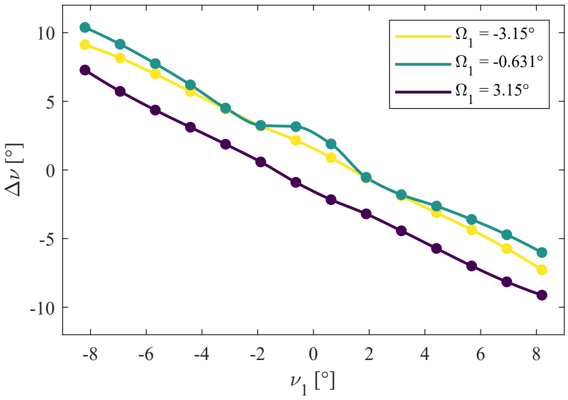

(a) Representation of the function $\Delta\nu$ without the effect of SNR.

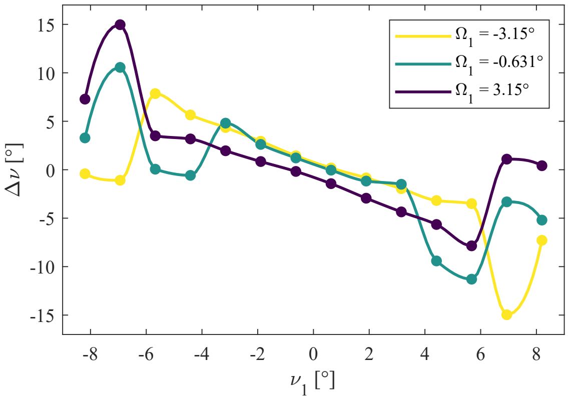

(b) Representation of the function $\Delta\nu$ with the effect of SNR.

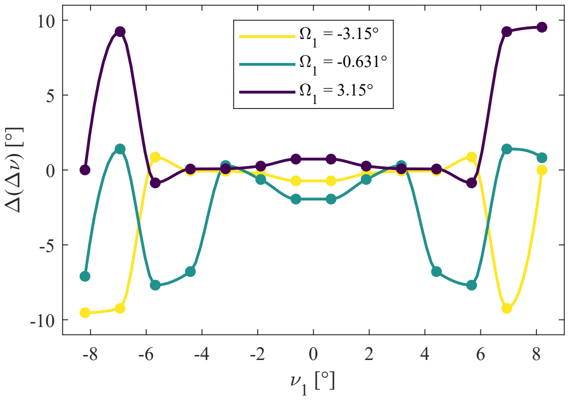

(c) Representation of the differences of differences $\Delta\left(\Delta\nu\right)$.

Figure 4.14: Values of the difference of the true anomalies $\Delta\nu$ for the satellite S_2 with respect to the position of the satellite S_1 in terms of right ascension of the ascending node Ω_1 and the true anomaly ν_1. In (a) without the effect of SNR, in (b) with the effect of SNR, in (c) the difference between the two cases (with and without SNR).

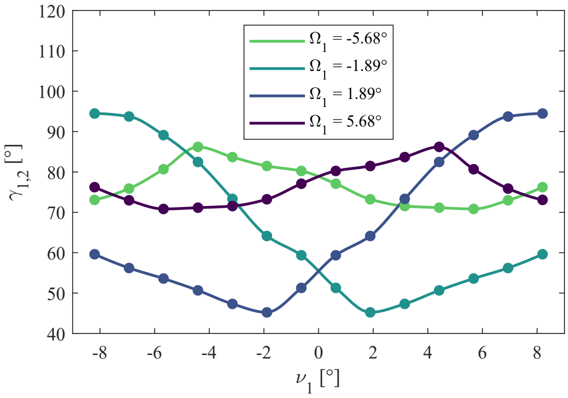

(a) Representation of the function $\gamma_{1,2}$ without the effect of SNR.

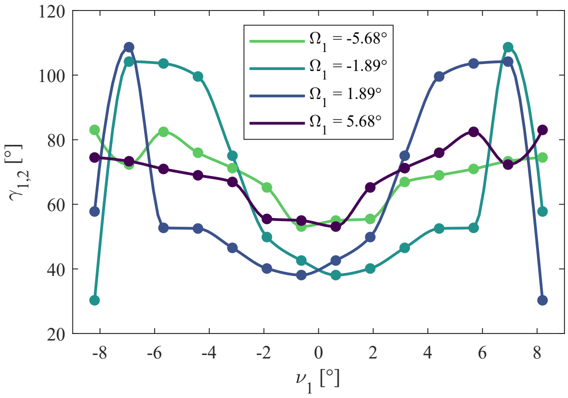

(b) Representation of the function $\gamma_{1,2}$ with the effect of SNR.

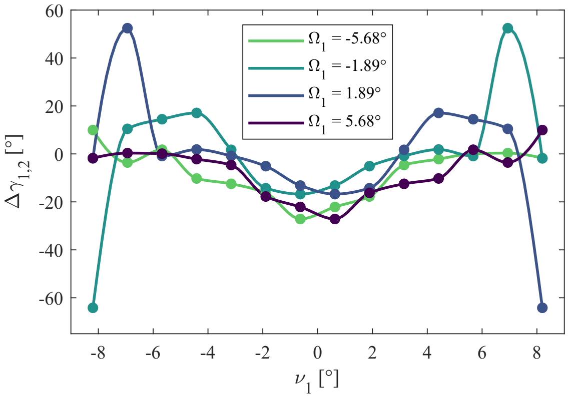

(c) Representation of the differences of the spacing angle $\Delta\gamma_{1,2}$.

Figure 4.15: Values of the spacing angle $\gamma_{1,2}$ for the satellite S_2 with respect to the position of the satellite S_1 in terms of right ascension of the ascending node Ω_1 and the true anomaly ν_1. In (a) without the effect of SNR, in (b) with the effect of SNR, in (c) the difference between the two cases (with and without SNR).

4.4.6 Different Receivers

The standard deviations, $\sigma_{\mathrm{l}|\hat{\zeta}_{\mathrm{Az}}}$ and $\sigma_{\mathrm{l}|\hat{\zeta}_{\mathrm{El}}}$, for a linear array can be obtained from the variance as shown in (1.50), where the subscript l denotes the linear array.

For planar arrays, the antenna elements are organized in a matrix, so the variance in every direction can be further reduced by exploiting the mean of rows and columns, as shown in (4.103), where the subscript p denotes the planar array.

$$\begin{aligned}\sigma_{\mathrm{p}|\hat{\zeta}_{\mathrm{Az,k}}} &= \frac{\sigma_{\mathrm{l}|\hat{\zeta}_{\mathrm{Az,k}}}}{M_{\mathrm{El,k}}}, \quad k = 1, 2\\ \sigma_{\mathrm{p}|\hat{\zeta}_{\mathrm{El,k}}} &= \frac{\sigma_{\mathrm{l}|\hat{\zeta}_{\mathrm{El,k}}}}{M_{\mathrm{Az,k}}}, \quad k = 1, 2\end{aligned} \tag{4.103}$$

In particular, since it is supposed that the payload is in target pointing, the (4.104) is also considered.

$$\begin{aligned}\sigma_{\mathrm{p}|\hat{\alpha}_{\mathrm{Az,k}}} &= \sigma_{\mathrm{p}|\hat{\zeta}_{\mathrm{Az,k}}}, \quad k = 1, 2\\ \sigma_{\mathrm{p}|\hat{\alpha}_{\mathrm{El,k}}} &= \sigma_{\mathrm{p}|\hat{\zeta}_{\mathrm{El,k}}}, \quad k = 1, 2\end{aligned} \tag{4.104}$$

For uniform antenna arrays, the number of elements along each direction is calculated considering (4.105): the elements of the antenna array are supposed to be evenly spaced with fixed distances, d_{Az} and d_{El}, equal to $1/4$ of the wavelength and it is considered as a first attempt to have an idea of the performance of the system.

$$\begin{aligned}M_{\mathrm{Az,k}} &= \left\lfloor \frac{L_{\mathrm{Az,k}}}{d_{\mathrm{Az,k}}} \right\rfloor = \left\lfloor \frac{4L_{\mathrm{Az,k}}f}{c} \right\rfloor, \quad k = 1, 2\\ M_{\mathrm{El,k}} &= \left\lfloor \frac{L_{\mathrm{El,k}}}{d_{\mathrm{El,k}}} \right\rfloor = \left\lfloor \frac{4L_{\mathrm{El,k}}f}{c} \right\rfloor, \quad k = 1, 2\end{aligned} \tag{4.105}$$

A convenient assumption of the study, used for evaluative purposes, considers squared AOA receivers for both of the satellites: $L_{\mathrm{Az,1}} = L_{\mathrm{El,1}} = L_1$ and $L_{\mathrm{Az,2}} = L_{\mathrm{El,2}} = L_2$.

Considering (4.105), the consequence of this assumption is $M_{\mathrm{Az,1}} = M_{\mathrm{El,1}} = M_1$ and $M_{\mathrm{Az,2}} = M_{\mathrm{El,2}} = M_2$.

The two cases of the study consider:

- Case 1 — Same receivers for the satellites S_1 and S_2, so $L_1 = L_2$ and $M_1 = M_2$;
- Case 2 — Different receivers for the satellites S_1 and S_2, so $L_1 \neq L_2$ and $M_1 \neq M_2$.

For evaluative purposes, the simulation of ‘case 2’ considered: $L_2 = 2L_1$.

The *PDOP* is based on the construction of the Fisher Information Matrix **F**, written in (4.106), the Geometric Design Matrix **H**, reported in (4.107), and the Covariance Matrix **C**, presented in (4.108).

$$\mathbf{F}_{3\times 3} = \mathbf{H}^{\mathrm{T}}_{4\times 3}\mathbf{C^{-1}}_{4\times 4}\mathbf{H}_{4\times 3} \tag{4.106}$$

$$\mathbf{H} = \begin{bmatrix} \frac{\partial \alpha_{\mathrm{Az},1}}{\partial x_{\mathrm{E}}} & \frac{\partial \alpha_{\mathrm{Az},1}}{\partial y_{\mathrm{E}}} & \frac{\partial \alpha_{\mathrm{Az},1}}{\partial z_{\mathrm{E}}} \\ \frac{\partial \alpha_{\mathrm{El},1}}{\partial x_{\mathrm{E}}} & \frac{\partial \alpha_{\mathrm{El},1}}{\partial y_{\mathrm{E}}} & \frac{\partial \alpha_{\mathrm{El},1}}{\partial z_{\mathrm{E}}} \\ \frac{\partial \alpha_{\mathrm{Az},2}}{\partial x_{\mathrm{E}}} & \frac{\partial \alpha_{\mathrm{Az},2}}{\partial y_{\mathrm{E}}} & \frac{\partial \alpha_{\mathrm{Az},2}}{\partial z_{\mathrm{E}}} \\ \frac{\partial \alpha_{\mathrm{El},2}}{\partial x_{\mathrm{E}}} & \frac{\partial \alpha_{\mathrm{El},2}}{\partial y_{\mathrm{E}}} & \frac{\partial \alpha_{\mathrm{El},2}}{\partial z_{\mathrm{E}}} \end{bmatrix} \tag{4.107}$$

$$\mathbf{C} = \mathrm{diag}\left(\sigma^2_{\hat{\alpha}_{\mathrm{p|Az},1}}, \sigma^2_{\hat{\alpha}_{\mathrm{p|El},1}}, \sigma^2_{\hat{\alpha}_{\mathrm{p|Az},2}}, \sigma^2_{\hat{\alpha}_{\mathrm{p|El},2}}\right) \tag{4.108}$$

The simulations of both the scenarios (with the same AOA receiver and with different AOA receivers) are performed in MATLAB environment.

In particular, Optimization Toolbox and Symbolic Math Toolbox have been employed to solve the optimization problem with the following settings: step tolerance of 10^{-15}, optimality tolerance of 10^{-12}, constraint tolerance of 10^{-12}, interior point algorithm, and scheme of central finite differences.

In the simulated scenarios, the ROC curve assumed for the detector has the following performances: probability of false alarm $p_{\mathrm{FA}} = 10^{-6}$, probability of detection $p_{\mathrm{D}} = 0.997$, and $SNR\left(p_{\mathrm{FA}}, p_{\mathrm{D}}\right) \approx 15$ dB. In order to guarantee the desired performances of detection in every instance of the problem, this value of SNR has been considered as the minimum value when the distance between the emitter and the satellite is maximum.

Furthermore, it has been considered $+3$ dB as a safety margin in order to account for other effects not considered in the study (e.g., the effects due to the atmosphere).

The simulation model is completed considering an example of emitter in the L1/E1 band with a central frequency of $f = 1575.42$ MHz, which is used for GNSS applications.

For ‘case 1’ scenario (i.e., satellites S_1 and S_1 have the same AOA receivers) it is assumed $L_1 = L_2 = 0.334$ m, resulting in $M_1 = M_2 = 7$.

For ‘case 2’ scenario (i.e., satellites S_1 and S_1 have different AOA receivers) it is assumed $L_1 = 0.334$ m and $L_2 = 0.62$ m, resulting in $M_1 = 7$ and $M_2 = 14$.

The height of the satellites are 400 km, resulting in $r = R_{\oplus} + h_{\mathrm{S}} = (6371 + 400)$ km.

The emitter position is placed on the surface of the Earth with $h_{\mathrm{E}} = 0$ m. Values of geodetic latitude and longitudes are $\Lambda = 0°$ and $\lambda = 0°$.

Results of the simulation are in Fig. 4.16 for the function $\Delta\Omega$, Fig. 4.17 for the function $\Delta\nu$, and Fig. 4.18 for the function $\gamma_{1,2}$.

Analyzing the results, it can be noticed that the function $\Delta\Omega$ has opposite general trends: in the first case (i.e., with same receiver) the function is decreasing with respect to the right ascension of the ascending node Ω_1, while in the second

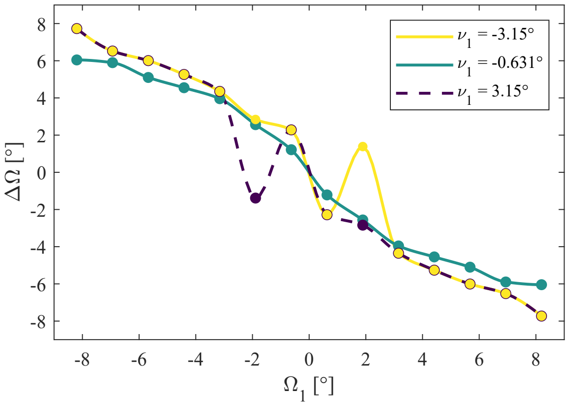

(a) Representation of the function $\Delta\Omega$ in scenario with same AOA receivers.

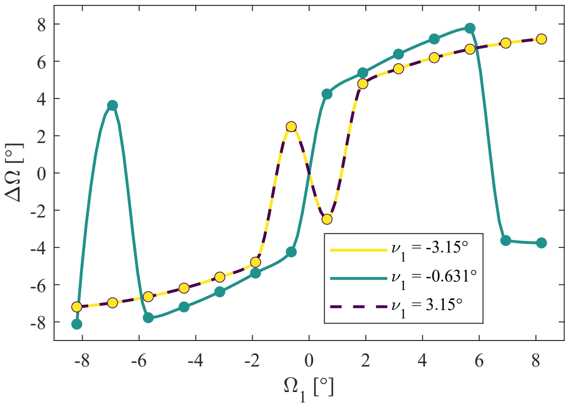

(b) Representation of the function $\Delta\Omega$ in scenario with different AOA receivers.

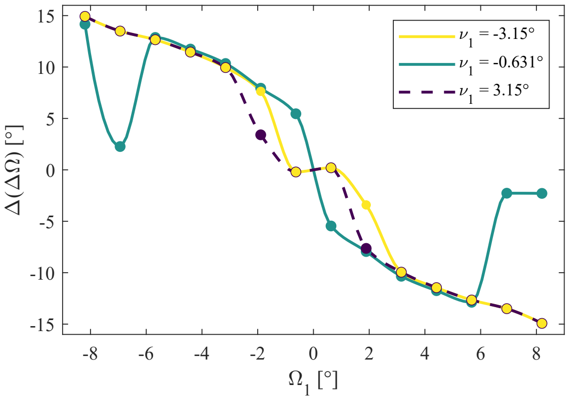

(c) Representation of the differences of differences $\Delta\left(\Delta\Omega\right)$.

Figure 4.16: Values of the difference of the right ascension of the ascending nodes $\Delta\Omega$ for the satellite S_2 with respect to the position of the satellite S_1 in terms of right ascension of the ascending node Ω_1 and the true anomaly ν_1. In (a) scenario with arrays of antennas of $L_1 = L_2 = 0.334$ m, in (b) scenario with arrays of antennas of $L_1 = 0.334$ m and $L_2 = 0.668$ m, in (c) the difference between the two cases.

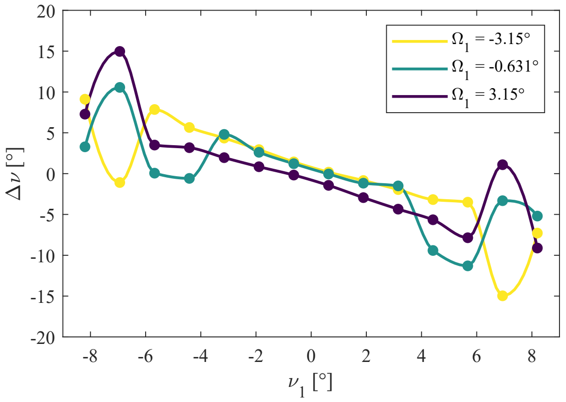

(a) Representation of the function $\Delta\nu$ in scenario with same AOA receivers.

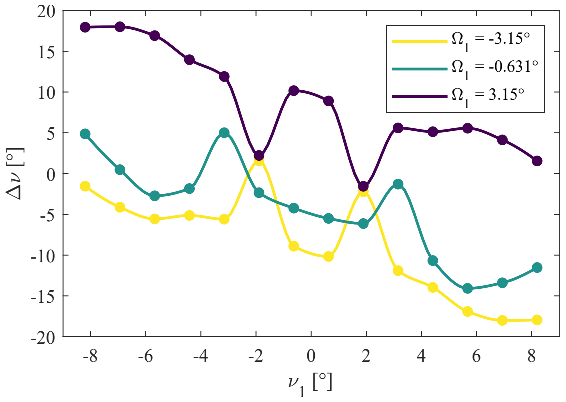

(b) Representation of the function $\Delta\nu$ in scenario with different AOA receivers.

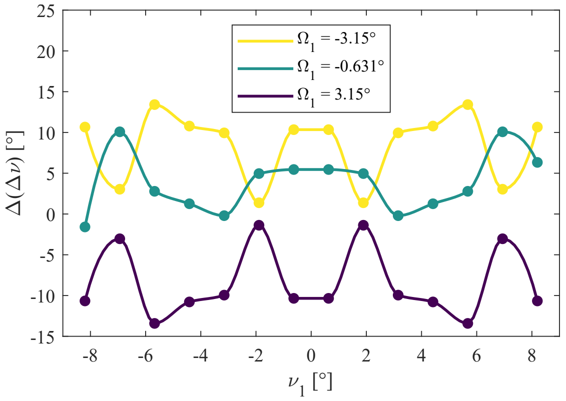

(c) Representation of the differences of differences $\Delta(\Delta\nu)$.

Figure 4.17: Values of the difference of the true anomalies $\Delta\nu$ for the satellite S_2 with respect to the position of the satellite S_1 in terms of right ascension of the ascending node Ω_1 and the true anomaly ν_1. In (a) scenario with arrays of antennas of $L_1 = L_2 = 0.334$ m, in (b) scenario with arrays of antennas of $L_1 = 0.334$ m and $L_2 = 0.668$ m, in (c) the difference between the two cases.

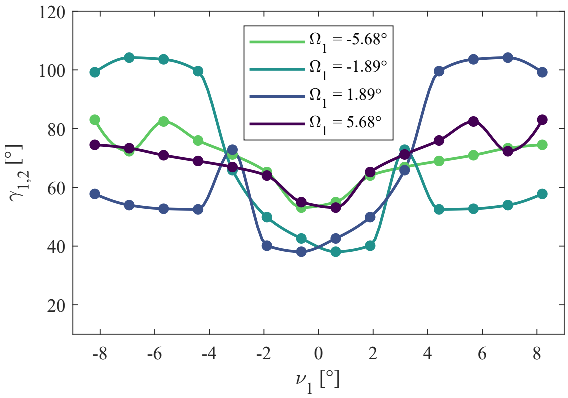

(a) Representation of the function $\gamma_{1,2}$ in scenario with same AOA receivers.

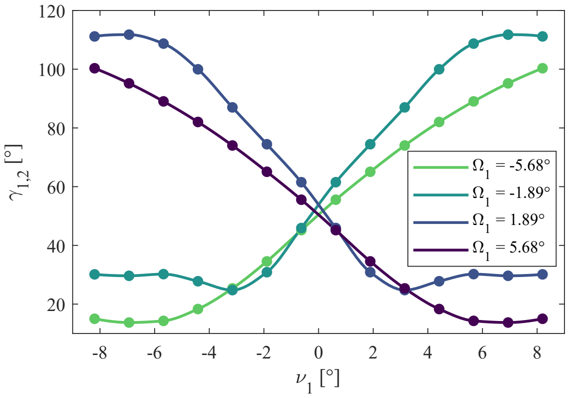

(b) Representation of the function $\gamma_{1,2}$ in scenario with different AOA receivers.

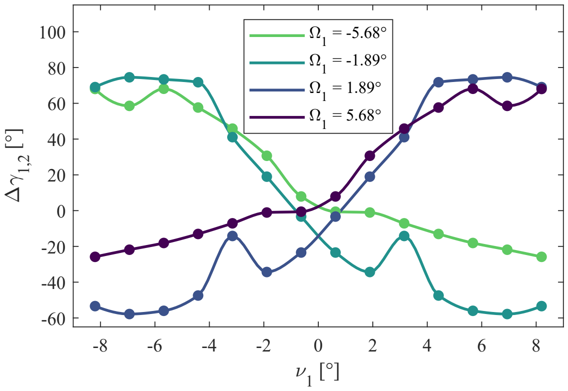

(c) Representation of the differences of the spacing angle $\Delta\gamma_{1,2}$.

Figure 4.18: Values of the spacing angle $\gamma_{1,2}$ for the satellite S_2 with respect to the position of the satellite S_1 in terms of right ascension of the ascending node Ω_1 and the true anomaly ν_1. In (a) scenario with arrays of antennas of $L_1 = L_2 = 0.334$ m, in (b) scenario with arrays of antennas of $L_1 = 0.334$ m and $L_2 = 0.668$ m, in (c) the difference between the two cases.

case (i.e., with different receivers) it appears globally increasing with some discontinuities.

In both cases some discontinuities appear for low values, i.e. $|\Omega_1| < 2°$, and for high values of the second case, i.e. $|\Omega_1| > 6°$: this behavior could reflect the role of the constraint $\delta_{1,2}$ or possibly the non-uniqueness of the solution; further investigation are needed to address this behavior.

The function $\Delta\nu$ has the same macroscopic decreasing trend in both the simulated cases.

Discontinuities appear for high values of the first case, i.e. $|\nu_1| > 6°$, while they are shifted in middle values for the second case, i.e. $-4° < \nu_1 < -2°$ and $2° < \nu_1 < 4°$.

The function $\Delta\nu$ is anti-symmetric with respect to both Ω_1 and ν_1 (with an additional shift depending on the value of the true anomaly ν_1), so $\Delta\nu\left(\Omega_1, \nu_1\right) = -\Delta\nu\left(-\Omega_1, -\nu_1\right) + f\left(\nu_1\right)$.

The function $\gamma_{1,2}$ has an almost monotonic behavior in the second case with $\partial\gamma_{1,2}/\partial\nu_1 > 0$ for $\Omega_1 < 0$ and $\partial\gamma_{1,2}/\partial\nu_1 < 0$ for $\Omega_1 > 0$. Instead, in the first case, $\gamma_{1,2}$ appears to be only locally monotonic and more unpredictable with respect to the variables Ω_1 and ν_1.

Furthermore, the function $\gamma_{1,2}$ results symmetric with respect to both the angles Ω_1 and ν_1, so $\gamma_{1,2}\left(\Omega_1, \nu_1\right) = \gamma_{1,2}\left(-\Omega_1, -\nu_1\right)$.

Difference of differences, i.e., $\Delta\left(\Delta\Omega\right)$, $\Delta\left(\Delta\nu\right)$, and $\Delta\gamma_{1,2}$, are non-negligible with an absolute value approximately up to 15° for the differences in the right ascension of the ascending node and true anomaly and with an absolute value approximately up to 80° for the spacing angle between the satellites.

Chapter 5

Hybrid Techniques and Multi Constellations

This chapter explores two main topics: in Sec. 5.1 the possibility to optimize clusters of satellites with hybrid payload composed of AOA and TDOA technologies is investigated; in Sec. 5.2 the evaluation of the set of conditions that can guarantee a combined measurement of different constellations of satellites is analyzed with the definition of a new metrics, named 'frequency of collisions', and a the development of an algorithm built for this purpose.

5.1 Optimization of Multi-Satellite Systems with Hybrid Payload AOA-TDOA

The approach, models and results of this section are extracted from the work of the author [23]. This activity has been commissioned on a *pro bono* basis without financial compensation by the European Commission, Joint Research Center, Space Sector (Italy).

5.1.1 Equations of Measurement for TDOA

TDOA considers the difference of the measured times of arrival (TOA) [89]. Denoting with $\tau_1, \tau_2, \ldots, \tau_\mathrm{k}, \ldots, \tau_\mathrm{n}$ the TOA measurements from the n satellites, the TDOAs are obtained considering the difference of two distinct TOA measurements.

In (5.1), the TOA measurement for a k-th satellite is reported, while in (5.2) a TDOA measurement for two distinct satellites k_1 and k_2 is reported.

$$\begin{aligned}\tau_{\mathrm{k}} = \frac{1}{c}\sqrt{\left(\mathbf{x}_{\mathrm{S_k}} - \mathbf{x}_{\mathrm{E}}\right)^{\mathrm{T}}\left(\mathbf{x}_{\mathrm{S_k}} - \mathbf{x}_{\mathrm{E}}\right)} &= \frac{1}{c}\sqrt{\begin{pmatrix} x_{\mathrm{S_k}} - x_{\mathrm{E}} \\ y_{\mathrm{S_k}} - y_{\mathrm{E}} \\ z_{\mathrm{S_k}} - z_{\mathrm{E}} \end{pmatrix}^{\mathrm{T}} \begin{pmatrix} x_{\mathrm{S_k}} - x_{\mathrm{E}} \\ y_{\mathrm{S_k}} - y_{\mathrm{E}} \\ z_{\mathrm{S_k}} - z_{\mathrm{E}} \end{pmatrix}} \\ &= \frac{1}{c}\sqrt{\left(x_{\mathrm{S_k}} - x_{\mathrm{E}}\right)^2 + \left(y_{\mathrm{S_k}} - y_{\mathrm{E}}\right)^2 + \left(z_{\mathrm{S_k}} - z_{\mathrm{E}}\right)^2}\end{aligned} \tag{5.1}$$

$$\Delta\tau_{\mathrm{k_1,k_2}} = \tau_{\mathrm{k_2}} - \tau_{\mathrm{k_1}}, \quad k_1 \neq k_2 \tag{5.2}$$

In general, for n satellites it is possible to write $N_{\mathrm{TDOA}} \leq n^2$ equations of (5.2). However, considering that by definition $\Delta\tau_{\mathrm{k_1,k_2=k_1}} = 0$, and that $\Delta\tau_{\mathrm{k_1,k_2}} = -\Delta\tau_{\mathrm{k_2,k_1}}$, for n receivers the number of equations is reduced to $N_{\mathrm{TDOA}} \leq \left(n^2 - n\right)/2 = n\left(n-1\right)/2$. This number is further reduced considering that some measurements can be obtained by linear combination of other measurements: e.g., $\Delta\tau_{\mathrm{k_2,k_3}} = \tau_{\mathrm{k_3}} - \tau_{\mathrm{k_2}} = \tau_{\mathrm{k_3}} - \tau_{\mathrm{k_2}} + \tau_{\mathrm{k_1}} - \tau_{\mathrm{k_1}} = \left(\tau_{\mathrm{k_3}} - \tau_{\mathrm{k_1}}\right) - \left(\tau_{\mathrm{k_2}} - \tau_{\mathrm{k_1}}\right) = \Delta\tau_{\mathrm{k_3,k_1}} - \Delta\tau_{\mathrm{k_2,k_1}}$. In the end, given n receivers, the number of possible TDOA independent equations is $N_{\mathrm{TDOA}} = n - 1$.

Assuming that the two platforms k_1 and k_2 have the same receivers for the TOA measurements, it is demonstrated [90] that the standard deviation $\sigma_{\mathrm{TDOA,k_1,k_2}}$ for the TDOA measurement is as reported in (5.3), where B is the noise bandwidth at receiver input, β is the root mean square (RMS) radian frequency in the received signal spectrum, T is the RMS of the integration time, and SNR_{k_1,k_2} is the effective input signal-to-noise ratio.

$$\sigma_{\mathrm{TDOA,k_1,k_2}} = \frac{1}{\beta}\frac{1}{\sqrt{SNR_{k_1,k_2}BT}} \tag{5.3}$$

The effective input signal noise ratio SNR_{k_1,k_2} is calculated as in (5.4), where SNR_{k_1} is the SNR of the k_1-th satellite platform and SNR_{k_2} is the SNR of the k_2-th satellite platform.

$$\frac{1}{SNR_{k_1,k_2}} = \frac{1}{2}\left(\frac{1}{SNR_{k_1}} + \frac{1}{SNR_{k_2}} + \frac{1}{SNR_{k_1}SNR_{k_2}}\right) \tag{5.4}$$

5.1.2 Derivatives for TDOA Measurement Equations

Here are reported the derivatives for TDOA equations (5.2).

In (5.5) there is the derivative of the equation of measurement for TDOA (5.2) with respect to the variable x_{E}.

$$\begin{aligned}
&\frac{\partial \Delta\tau_{\mathrm{k}_1,\mathrm{k}_2}}{\partial x_{\mathrm{E}}} = \frac{\partial \tau_{\mathrm{k}_2}}{\partial x_{\mathrm{E}}} - \frac{\partial \tau_{\mathrm{k}_1}}{\partial x_{\mathrm{E}}} \\
&= -\frac{1}{c}\frac{1}{2}\frac{2\left(x_{\mathrm{S}_{\mathrm{k}_2}} - x_{\mathrm{E}}\right)}{\sqrt{\left(x_{\mathrm{S}_{\mathrm{k}_2}} - x_{\mathrm{E}}\right)^2 + \left(y_{\mathrm{S}_{\mathrm{k}_2}} - y_{\mathrm{E}}\right)^2 + \left(z_{\mathrm{S}_{\mathrm{k}_2}} - z_{\mathrm{E}}\right)^2}} \\
&+\frac{1}{c}\frac{1}{2}\frac{2\left(x_{\mathrm{S}_{\mathrm{k}_1}} - x_{\mathrm{E}}\right)}{\sqrt{\left(x_{\mathrm{S}_{\mathrm{k}_1}} - x_{\mathrm{E}}\right)^2 + \left(y_{\mathrm{S}_{\mathrm{k}_1}} - y_{\mathrm{E}}\right)^2 + \left(z_{\mathrm{S}_{\mathrm{k}_1}} - z_{\mathrm{E}}\right)^2}}
\end{aligned} \tag{5.5}$$

In (5.6) there is the derivative of the equation of measurement for TDOA (5.2) with respect to the variable y_{E}.

$$\begin{aligned}
&\frac{\partial \Delta\tau_{\mathrm{k}_1,\mathrm{k}_2}}{\partial x_{\mathrm{E}}} = \frac{\partial \tau_{\mathrm{k}_2}}{\partial y_{\mathrm{E}}} - \frac{\partial \tau_{\mathrm{k}_1}}{\partial y_{\mathrm{E}}} \\
&= -\frac{1}{c}\frac{1}{2}\frac{2\left(y_{\mathrm{S}_{\mathrm{k}_2}} - y_{\mathrm{E}}\right)}{\sqrt{\left(x_{\mathrm{S}_{\mathrm{k}_2}} - x_{\mathrm{E}}\right)^2 + \left(y_{\mathrm{S}_{\mathrm{k}_2}} - y_{\mathrm{E}}\right)^2 + \left(z_{\mathrm{S}_{\mathrm{k}_2}} - z_{\mathrm{E}}\right)^2}} \\
&+\frac{1}{c}\frac{1}{2}\frac{2\left(y_{\mathrm{S}_{\mathrm{k}_1}} - y_{\mathrm{E}}\right)}{\sqrt{\left(x_{\mathrm{S}_{\mathrm{k}_1}} - x_{\mathrm{E}}\right)^2 + \left(y_{\mathrm{S}_{\mathrm{k}_1}} - y_{\mathrm{E}}\right)^2 + \left(z_{\mathrm{S}_{\mathrm{k}_1}} - z_{\mathrm{E}}\right)^2}}
\end{aligned} \tag{5.6}$$

In (5.7) there is the derivative of the equation of measurement for TDOA (5.2) with respect to the variable z_{E}.

$$\begin{aligned}
&\frac{\partial \Delta\tau_{\mathrm{k}_1,\mathrm{k}_2}}{\partial z_{\mathrm{E}}} = \frac{\partial \tau_{\mathrm{k}_2}}{\partial z_{\mathrm{E}}} - \frac{\partial \tau_{\mathrm{k}_1}}{\partial z_{\mathrm{E}}} \\
&= -\frac{1}{c}\frac{1}{2}\frac{2\left(z_{\mathrm{S}_{\mathrm{k}_2}} - z_{\mathrm{E}}\right)}{\sqrt{\left(x_{\mathrm{S}_{\mathrm{k}_2}} - x_{\mathrm{E}}\right)^2 + \left(y_{\mathrm{S}_{\mathrm{k}_2}} - y_{\mathrm{E}}\right)^2 + \left(z_{\mathrm{S}_{\mathrm{k}_2}} - z_{\mathrm{E}}\right)^2}} \\
&+\frac{1}{c}\frac{1}{2}\frac{2\left(z_{\mathrm{S}_{\mathrm{k}_1}} - z_{\mathrm{E}}\right)}{\sqrt{\left(x_{\mathrm{S}_{\mathrm{k}_1}} - x_{\mathrm{E}}\right)^2 + \left(y_{\mathrm{S}_{\mathrm{k}_1}} - y_{\mathrm{E}}\right)^2 + \left(z_{\mathrm{S}_{\mathrm{k}_1}} - z_{\mathrm{E}}\right)^2}}
\end{aligned} \tag{5.7}$$

5.1.3 Dilution of Precision for Hybrid Measurements

For this study, the geometric design matrix is composed by the set of derivatives of the equations of measurements (i.e., the derivatives of (4.41) for AOA derived in Sec. 4.3.2, and the derivatives of (5.2) for TDOA derived in Sec. 5.1.2) with respect to the position coordinates of the emitter $(x_\mathrm{E}, y_\mathrm{E}, z_\mathrm{E})$, as shown in (5.8). In particular, the matrix $\mathbf{H}$, has $N_\mathrm{AOA} + N_\mathrm{TDOA} = 2n + (n-1) = 3n-1$ rows (i.e., the number of AOA measurements plus the number of TDOA measurements), and the number of columns is 3 (i.e., the number of spatial variables for the partial derivatives). The matrix $\mathbf{H}$ is built stacking every set of partial derivatives for every measurement equation in every row. In particular, in the representation of $\mathbf{H}$ in (5.8), the first $2n$ rows include the partial derivatives of AOA measurements ordered in Azimuth-Elevation pairs, while the last $(n-1)$ rows include the partial derivatives of linearly independent TDOA equations. Note that in (5.8), without loss of generality, the first receiver has been chosen as reference for the $(n-1)$ independent TDOA measurements; i.e., considering $k_1 = 1$ and $k_2 = k'$, the derivatives are related to this set of measurement equations: $\Delta\tau_{1,2}, \Delta\tau_{1,3}, \ldots, \Delta\tau_{1,\mathrm{k'}}, \ldots, \Delta\tau_{1,\mathrm{n}}$.

$$\mathbf{H} = \left(\begin{array}{ccc}
\frac{\partial \alpha_{\mathrm{Az},1}}{\partial x_\mathrm{E}} & \frac{\partial \alpha_{\mathrm{Az},1}}{\partial y_\mathrm{E}} & \frac{\partial \alpha_{\mathrm{Az},1}}{\partial z_\mathrm{E}} \\
\frac{\partial \alpha_{\mathrm{El},1}}{\partial x_\mathrm{E}} & \frac{\partial \alpha_{\mathrm{El},1}}{\partial y_\mathrm{E}} & \frac{\partial \alpha_{\mathrm{El},1}}{\partial z_\mathrm{E}} \\
\frac{\partial \alpha_{\mathrm{Az},2}}{\partial x_\mathrm{E}} & \frac{\partial \alpha_{\mathrm{Az},2}}{\partial y_\mathrm{E}} & \frac{\partial \alpha_{\mathrm{Az},2}}{\partial z_\mathrm{E}} \\
\frac{\partial \alpha_{\mathrm{El},2}}{\partial x_\mathrm{E}} & \frac{\partial \alpha_{\mathrm{El},2}}{\partial y_\mathrm{E}} & \frac{\partial \alpha_{\mathrm{El},2}}{\partial z_\mathrm{E}} \\
\vdots & \vdots & \vdots \\
\frac{\partial \alpha_{\mathrm{Az},\mathrm{k}}}{\partial x_\mathrm{E}} & \frac{\partial \alpha_{\mathrm{Az},\mathrm{k}}}{\partial y_\mathrm{E}} & \frac{\partial \alpha_{\mathrm{Az},\mathrm{k}}}{\partial z_\mathrm{E}} \\
\frac{\partial \alpha_{\mathrm{El},\mathrm{k}}}{\partial x_\mathrm{E}} & \frac{\partial \alpha_{\mathrm{El},\mathrm{k}}}{\partial y_\mathrm{E}} & \frac{\partial \alpha_{\mathrm{El},\mathrm{k}}}{\partial z_\mathrm{E}} \\
\vdots & \vdots & \vdots \\
\frac{\partial \alpha_{\mathrm{Az},\mathrm{n}}}{\partial x_\mathrm{E}} & \frac{\partial \alpha_{\mathrm{Az},\mathrm{n}}}{\partial y_\mathrm{E}} & \frac{\partial \alpha_{\mathrm{Az},\mathrm{n}}}{\partial z_\mathrm{E}} \\
\frac{\partial \alpha_{\mathrm{El},\mathrm{n}}}{\partial x_\mathrm{E}} & \frac{\partial \alpha_{\mathrm{El},\mathrm{n}}}{\partial y_\mathrm{E}} & \frac{\partial \alpha_{\mathrm{El},\mathrm{n}}}{\partial z_\mathrm{E}} \\
\hdashline
\frac{\partial \Delta\tau_{1,2}}{\partial x_\mathrm{E}} & \frac{\partial \Delta\tau_{1,2}}{\partial y_\mathrm{E}} & \frac{\partial \Delta\tau_{1,2}}{\partial z_\mathrm{E}} \\
\frac{\partial \Delta\tau_{1,3}}{\partial x_\mathrm{E}} & \frac{\partial \Delta\tau_{1,3}}{\partial y_\mathrm{E}} & \frac{\partial \Delta\tau_{1,3}}{\partial z_\mathrm{E}} \\
\vdots & \vdots & \vdots \\
\frac{\partial \Delta\tau_{1,\mathrm{k'}}}{\partial x_\mathrm{E}} & \frac{\partial \Delta\tau_{1,\mathrm{k'}}}{\partial y_\mathrm{E}} & \frac{\partial \Delta\tau_{1,\mathrm{k'}}}{\partial z_\mathrm{E}} \\
\vdots & \vdots & \vdots \\
\frac{\partial \Delta\tau_{1,\mathrm{n}}}{\partial x_\mathrm{E}} & \frac{\partial \Delta\tau_{1,\mathrm{n}}}{\partial y_\mathrm{E}} & \frac{\partial \Delta\tau_{1,\mathrm{n}}}{\partial z_\mathrm{E}}
\end{array}\right) \tag{5.8}$$

The construction of the Covariance matrix $\mathbf{C}$ has to follow the same order of construction of the geometric design matrix $\mathbf{H}$, so considering the ordering of equations in (5.8), the first $2n$ elements on the main diagonal of the Covariance matrix are related to the pairs of AOA measurements, while the remaining $n-1$ elements are related to the linearly independent TDOA measurements chosen for $\mathbf{H}$, as shown in (5.9).

$$\begin{aligned}\mathbf{C} = \operatorname{diag}\Big(&\sigma^2_{\mathrm{AOA},\hat{\alpha}_{\mathrm{Az},1}}, \sigma^2_{\mathrm{AOA},\hat{\alpha}_{\mathrm{El},1}}, \sigma^2_{\mathrm{AOA},\hat{\alpha}_{\mathrm{Az},2}}, \sigma^2_{\mathrm{AOA},\hat{\alpha}_{\mathrm{El},2}}, \dots, \\ &\sigma^2_{\mathrm{AOA},\hat{\alpha}_{\mathrm{Az,k}}}, \sigma^2_{\mathrm{AOA},\hat{\alpha}_{\mathrm{El,k}}}, \dots, \sigma^2_{\mathrm{AOA},\hat{\alpha}_{\mathrm{Az,n}}}, \sigma^2_{\mathrm{AOA},\hat{\alpha}_{\mathrm{El,n}}}, \\ &\sigma^2_{\mathrm{TDOA},1,2}, \sigma^2_{\mathrm{TDOA},1,3}, \dots, \sigma^2_{\mathrm{TDOA},1,\mathrm{k}'}, \dots, \sigma^2_{\mathrm{TDOA},1,\mathrm{n}}\Big)\end{aligned} \tag{5.9}$$

Once the Geometric Design Matrix **H** and the Covariance Matrix **C** have been obtained, the $PDOP$ can be evaluated as in (5.10).

$$PDOP = \sqrt{Tr\left(\left(\mathbf{H}^{\mathrm{T}}\mathbf{C}^{-1}\mathbf{H}\right)^{-1}\right)} \tag{5.10}$$

Besides the set of hypotheses formulated in 4.3.3, an additional hypothesis can be reported[1].

In particular, it is supposed that every satellite has the same TOA receiver in terms of noise bandwidth at receiver input B, RMS of radian frequency in the received signal spectrum β, and RMS of the integration time T.

Hypothesis 8 — ($\mathbf{H}_8$): $B_1 = B_2 = \dots = B_{\mathrm{k}} = \dots = B_{\mathrm{n}} = B$, $\beta_1 = \beta_2 = \dots = \beta_{\mathrm{k}} = \dots = \beta_{\mathrm{n}} = \beta$, and $T_1 = T_2 = \dots = T_{\mathrm{k}} = \dots = T_{\mathrm{n}} = T$.

5.1.4 Simulations

The problem in (4.65) with conditions expressed in (4.66) and (4.69), and model for $PDOP$ defined in Sec.5.1.3 has been simulated with the Optimization Toolbox and Symbolic Math Toolbox of the MATLAB environment.

The following settings have been employed: step tolerance of 10^{-15}, optimality tolerance of 10^{-12}, constraint tolerance of 10^{-12}, interior point algorithm, scheme of central finite differences.

A couple of satellites in LEO has been considered with height of $h_{S_1} = h_{S_2} = 400$ km. For the examined study case, from Table 1.1 resulted a value of $\rho_{\mathrm{k}}^{-1} = 5.463$.

The value of the absolute condition for the LOS is $\delta = 19.7926°$, while the conservative relative condition is $\delta_{\mathrm{r}} = 8.1984°$.

A number of 14 evenly spaced values have been considered for Ω_1 and ν_1, resulting in a total of 196 simulations.

Assigning the probabilities of false alarm $p_{\mathrm{FA}} = 10^{-6}$ and of detection $p_{\mathrm{D}} = 0.997$, the ROC curve in Fig. 1.12 gives a minimum value of $SNR\left(p_{\mathrm{FA}}, p_{\mathrm{D}}\right) \approx 15$ dB, which has been used as worst case of maximum distance. Additionally, it has been assumed a value of 3 dB as a margin to take into account other non-modeled effects (e.g., atmospheric effects).

---

[1] It is remarked that ($\mathbf{H}_8$) has been reported, among other main hypothesis of the study, for a matter of completeness, since it has already been used in subsection 5.1.1 to derive the model (5.3)

The mission is supposed to monitor L1/E1 frequency bands with central value of $f = 1575.42$ MHz, which is one of the typical bands used by GPS (Global Position System) and Galileo systems for civil aviation.

Considering a set of CubeSat platforms as potential satellites, the AOA receiver is supposed to be a cross array of antennas with lengths equal to $L_{\mathrm{Az}} = L_{\mathrm{El}} = 0.334$ m. The number of antenna elements are supposed to be spaced by a 1/4 of the wavelength in each linear array, resulting in $M_{\mathrm{Az}} = M_{\mathrm{El}} = 7$ antenna elements per array.

Furthermore, since the detection is supposed to be already performed before the precise geolocation, a simplified scenario which considers an orientation of the satellite to align the broadside direction of the array with the direction towards the emitter has been considered for the deployment optimization.

For TDOA receivers, values of $B = 3$ MHz for the noise bandwidth at receiver input, $\beta = 100$ kHz for the root mean square (RMS) radian frequency in the received signal spectrum, and an integration time of $T = 100$ ms have been considered.

Results of the simulations are reported in Fig. 5.1, Fig. 5.2, and Fig. 5.3.

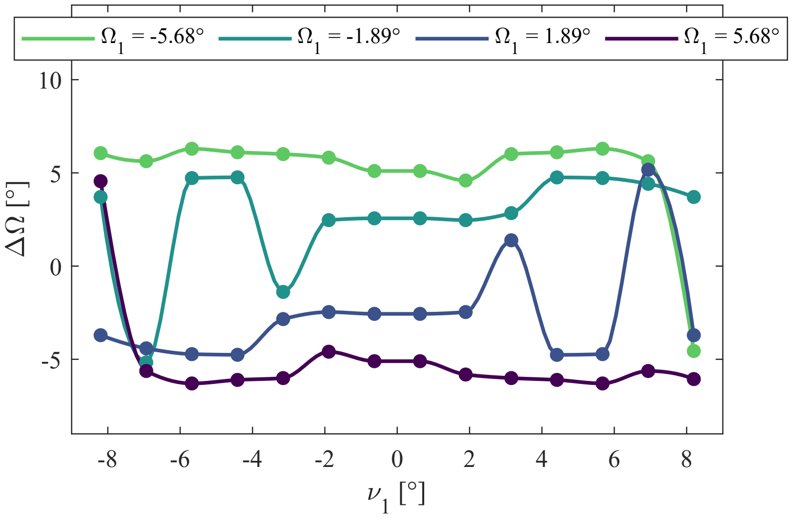

Figure 5.1: Values of the difference of the right ascension of the ascending nodes $\Delta\Omega$ for the satellite S_2 with respect to the position of the satellite S_1 in terms of right ascension of the ascending node Ω_1 and the true anomaly ν_1.

In the investigations on 2-satellites systems performing only AOA measurements the results on the $\Delta\Omega$ were symmetric with respect to Ω_1 and anti-symmetric with respect to ν_1, i.e., $\Delta\Omega_{\mathrm{AOA}}(\nu_1) = \Delta\Omega_{\mathrm{AOA}}(-\nu_1)$ and $\Delta\Omega_{\mathrm{AOA}}(\Omega_1) = -\Delta\Omega_{\mathrm{AOA}}(-\Omega_1)$.

For AOA+TDOA systems, the results in Fig. 5.1 show a complete anti-symmetry, resulting in $\Delta\Omega_{\mathrm{AOA+TDOA}}(\Omega_1, \nu_1) = -\Delta\Omega_{\mathrm{AOA+TDOA}}(-\Omega_1, -\nu_1)$ as a possible model of interpretation of data.

The values of $\Delta\nu$ in Fig. 5.2 show the same behavior of anti-symmetry with respect to Ω_1 and ν_1, and a shift on the value in the ordinates depending on the

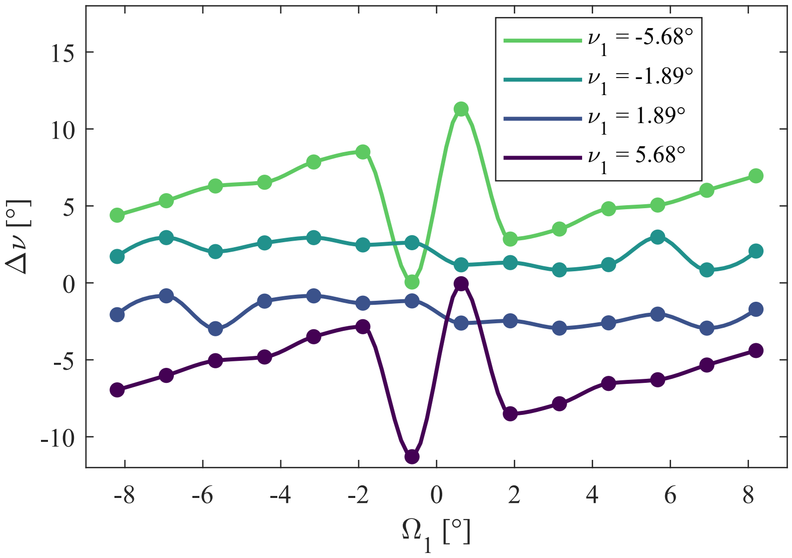

Figure 5.2: Values of the difference of the true anomalies $\Delta\nu$ for the satellite S_2 with respect to the position of the satellite S_1 in terms of right ascension of the ascending node Ω_1 and the true anomaly ν_1.

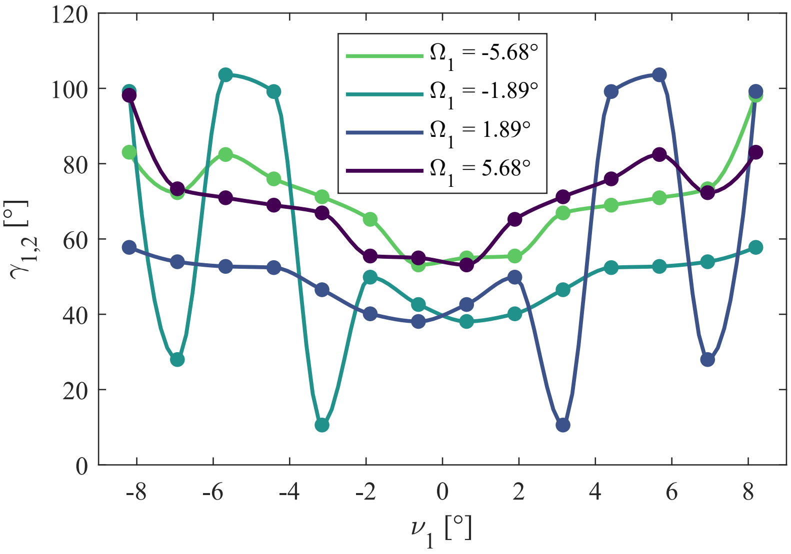

Figure 5.3: Values of the spacing angle $\gamma_{1,2}$ for the satellite S_2 with respect to the position of the satellite S_1 in terms of right ascension of the ascending node Ω_1 and the true anomaly ν_1.

value of ν_1. Therefore, $\Delta\nu_{\text{AOA+TDOA}}(\Omega_1, \nu_1) = -\Delta\nu_{\text{AOA+TDOA}}(-\Omega_1, -\nu_1) + f(\nu_1)$ is a possible model of interpretation of data.

For the spacing angle $\gamma_{1,2}$ the emerging property from Fig. 5.3 is of symmetry with respect to both the right ascension of the ascending node Ω_1 and the true anomaly ν_1. A possible model of interpretation of gathered data is then $\gamma_{1,2|\text{AOA+TDOA}}(\Omega_1, \nu_1) = \gamma_{1,2|\text{AOA+TDOA}}(-\Omega_1, -\nu_1)$.

5.2 Multi Constellations

The approach and models developed in this section are extracted from the work of the author [91]. This activity has been commissioned on a *pro bono* basis without financial compensation by the European Commission, Joint Research Center, Space Sector (Italy).

The context of the study is within the macroscopic area related to the evaluation of the set of conditions that can guarantee a combined measurement for a set of constellations of satellites. For simplicity, the study is confined to a simpler case of two constellations $\mathcal{C}_1$ and $\mathcal{C}_2$. Each constellation is also supposed to be, more specifically, a cluster of satellites that orbit very close to each other: given two satellites $\mathbf{x}_{\text{S}_1} \in \mathcal{C}_1$ and $\mathbf{x}_{\text{S}_2} \in \mathcal{C}_1$, their distance is small compared to the total lengths $\mathcal{L}_{\text{S}_1}$ and $\mathcal{L}_{\text{S}_2}$ of their orbits, so condition $\|\mathbf{x}_{\text{S}_1} - \mathbf{x}_{\text{S}_2}\| \ll \mathcal{L}_{\text{S}_1} \cup \|\mathbf{x}_{\text{S}_1} - \mathbf{x}_{\text{S}_2}\| \ll \mathcal{L}_{\text{S}_2}$ holds for each couple of satellites within the same cluster.

The objective of the problem is to evaluate when the two constellations $\mathcal{C}_1$ and $\mathcal{C}_2$ are close enough to perform a combined measurement.

Without loss of generality and to have a first simpler approach to the problem, it is supposed that each constellation is composed of one single satellite, which is a representative for the whole cluster. The actors of the problem are then satellites $\mathbf{x}_{\text{S}_1} \in \mathcal{C}_1$ and $\mathbf{x}_{\text{S}_2} \in \mathcal{C}_2$.

Each single satellite is supposed to have a generic payload composed of antenna array able to perform measurement with AOA technology and the combined presence of at least two satellites can perform a TDOA measurement [8].

These measurements are supposed to perform a possible geolocation of an emitter of electromagnetic waves placed in $\mathbf{x}_{\text{E}}$ on the surface of the Earth for search and rescue operations or spectrum monitoring of jamming signals.

For this study, circular orbits have been considered, then $\mathbf{x}_{\text{S}_1}(r_1, i_1, \Omega_1, \nu_1(t))$ and $\mathbf{x}_{\text{S}_2}(r_2, i_2, \Omega_2, \nu_2(t))$.

In order to predict the moments in which a combined measurement is possible, a higher level of abstraction is required. More generally, for a satellite S it is possible to say that a circular orbit, described by a closed curve γ_{S}, lies completely in an orbital plane π_{S}.

By definition, an orbital plane π_{S} contains both the orbit γ_{S} and the centre of mass of the planet, which for the Earth is denoted by $\mathbf{x}_{\oplus}$ in this study.

Then, the intersection of the planes $\pi_{\mathrm{S}_1} \cap \pi_{\mathrm{S}_2}$ gives the line $l_{\mathrm{S}_1,\mathrm{S}_2}$ in which the combined measurement of the two constellations $\mathcal{C}_1$ and $\mathcal{C}_2$ is supposed to be possible.

The set of points of the intersections I between this line and the orbits, formally

$$\begin{aligned} I &= \left\{\mathbf{x} \in \mathbb{R}^3 | \left(l_{\mathrm{S}_1,\mathrm{S}_2} \cap \gamma_{\mathrm{S}_1}\right) \vee \left(l_{\mathrm{S}_1,\mathrm{S}_2} \cap \gamma_{\mathrm{S}_2}\right)\right\} \\ &= \left\{\mathbf{x} \in \mathbb{R}^3 | \left(\left(\pi_{\mathrm{S}_1} \cap \pi_{\mathrm{S}_2}\right) \cap \gamma_{\mathrm{S}_1}\right) \vee \left(\left(\pi_{\mathrm{S}_1} \cap \pi_{\mathrm{S}_2}\right) \cap \gamma_{\mathrm{S}_2}\right)\right\}, \end{aligned} \tag{5.11}$$

are of interest, because they denote when the satellites of different constellations meet. It can be demonstrated that, if the orbital planes are not parallel $\pi_{\mathrm{S}_1} \nparallel \pi_{\mathrm{S}_2}$, this set of points I is finite and, in particular, it has two points for each orbit $I = \{\mathbf{x}_{1,\mathrm{A}}, \mathbf{x}_{1,\mathrm{B}}, \mathbf{x}_{2,\mathrm{A}}, \mathbf{x}_{1,\mathrm{B}}\}$.

Equivalently, this means that for each couple of orbital planes, two geometrical values of the true anomaly can be identified for each satellite; here, for two satellites S_1 and S_2 they are denoted with $\nu_{1,\mathrm{A}}$, $\nu_{1,\mathrm{B}}$, $\nu_{2,\mathrm{A}}$, and $\nu_{2,\mathrm{B}}$.

The position of each circular orbit is periodic with a period $T_{\mathrm{k}} = 2\pi\sqrt{\frac{r_{\mathrm{k}}^3}{\mu_\oplus}}$ with $k = 1{,}2$, where $\mu_\oplus$ is the standard gravitational parameter of the Earth. So also the passage of the satellites in the intersection is periodic with period T_{k}, so $\nu_{1,\mathrm{A}}(t) = \nu_{1,\mathrm{A}}(t + nT_1)$, $\nu_{1,\mathrm{B}}(t) = \nu_{1,\mathrm{B}}(t + nT_1)$, $\nu_{2,\mathrm{A}}(t) = \nu_{2,\mathrm{A}}(t + nT_2)$, $\nu_{2,\mathrm{B}}(t) = \nu_{2,\mathrm{B}}(t + nT_2)$ with $n \in \mathbb{N}$.

A true anomaly of intersection $\nu_{\mathrm{I}} = \{\nu \in \gamma_{\mathrm{S}} | \nu = \nu_{\mathrm{A}} \vee \nu = \nu_{\mathrm{B}}\}$ can be defined and considered to avoid the duplicated representation. In this representation, the periodicity is half of the orbital period: $\nu_{1,\mathrm{I}}(t) = \nu_{1,\mathrm{I}}(t + nT_1/2)$ and $\nu_{2,\mathrm{I}}(t) = \nu_{2,\mathrm{I}}(t + nT_2/2)$ with $n \in \mathbb{N}$.

A measurement exists when the emitter of signal is within the line of sight of the satellite. Considering the geometry reported in Fig. 5.4, the interval of true anomaly of visibility $\Delta\nu_{\mathrm{v}}$ can be calculated as in (5.12), where $R_\oplus$ is the radius of the Earth, assumed to be spherical for simplicity.

$$\Delta\nu_{\mathrm{v,k}} = 2 \arccos\left(\frac{R_\oplus}{r_{\mathrm{k}}}\right), \quad k = 1{,}2 \tag{5.12}$$

The interval of time visibility ΔT_{v} is then

$$\Delta T_{\mathrm{v,k}} = \frac{\Delta\nu_{\mathrm{v,k}} T_{\mathrm{k}}}{2\pi} = \frac{\arccos\left(\frac{R_\oplus}{r_{\mathrm{k}}}\right) T_{\mathrm{k}}}{\pi} = 2 \arccos\left(\frac{R_\oplus}{r_{\mathrm{k}}}\right)\sqrt{\frac{r_{\mathrm{k}}^3}{\mu_\oplus}}, \quad k = 1{,}2. \tag{5.13}$$

The passage of the satellites at the intersection points can be modeled with a train of rectangular pulses f_1 and f_2 with periodicities $T_1/2$ and $T_2/2$, and widths $\Delta T_{\mathrm{v},1}$ and $\Delta T_{\mathrm{v},2}$, as shown in (5.14); $t_{0,1}$ and $t_{0,2}$ represent the initial starting times.

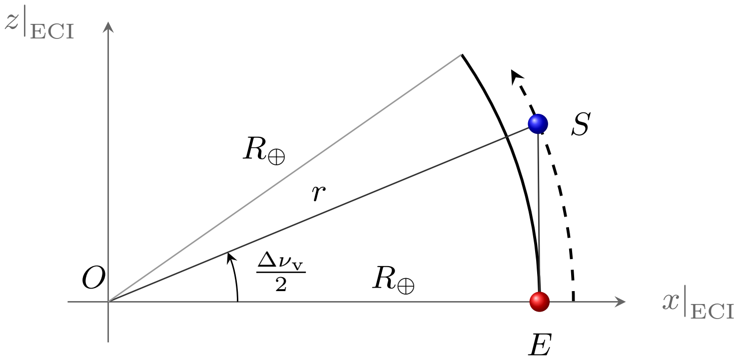

Figure 5.4: Reference geometry to calculate the true anomaly of visibility $\Delta\nu_{\mathrm{v}}$ from the Earth radius $R_\oplus$ and satellite orbit radius r.

$$f_{\mathrm{v,k}}\left(t\right)=\sum_{j=1}^{\infty}\Pi\left(\frac{\left(t-t_{0,\mathrm{k}}\right)-j\frac{T_{\mathrm{k}}}{2}}{\Delta T_{\mathrm{v,k}}}\right)=\sum_{j=1}^{\infty}\Pi\left(\frac{\left(t-t_{0,\mathrm{k}}\right)\sqrt{\frac{\mu_{\oplus}}{r_{\mathrm{k}}^{3}}}-j\pi}{2\arccos\left(\frac{R_{\oplus}}{r_{\mathrm{k}}}\right)}\right),\quad k=1{,}2. \tag{5.14}$$

Once the intersection intervals have been defined and modelled it is possible to check their superposition in a certain instant of time. Given starting instant of time $t_{\mathrm{Start}}=t_0+nT$ with $n\in\mathbb{N}$ and ending instant of time $t_{\mathrm{End}}=t_0+nT+\Delta T_{\mathrm{v}}$ with $n\in\mathbb{N}$, then the active interval for a satellite S can be defined as $I_{\mathrm{Act,S}}\left(n\right)=\left[t_{\mathrm{Start}}\left(n\right),t_{\mathrm{End}}\left(n\right)\right[$ with $n\in\mathbb{N}$; for satellites S_1 and S_2 they are as reported in (5.15).

$$\begin{aligned}I_{\mathrm{Act,S_1}}\left(n_1\right)&=\left[t_{0,1}+n_1T_1,t_{0,1}+n_1T_1+\Delta T_{\mathrm{v},1}\right[,\quad n_1\in\mathbb{N}\\I_{\mathrm{Act,S_2}}\left(n_2\right)&=\left[t_{0,2}+n_2T_2,t_{0,2}+n_2T_2+\Delta T_{\mathrm{v},2}\right[,\quad n_2\in\mathbb{N}\end{aligned} \tag{5.15}$$

Formally, the set $\mathcal{T}_{\mathrm{Sup}}$ of instants of time of superposition of the intervals can be written as $\mathcal{T}_{\mathrm{Sup}}=\left\{t\in\mathbb{R}_{>0}\middle|\left(t\in I_{\mathrm{Act,S_1}}\right)\wedge\left(t\in I_{\mathrm{Act,S_2}}\right)\right\}$. Because the train of pulses defined in (5.14) have values of 1 if the interval is active and 0 if the interval is not active, so formally $f_{\mathrm{v},1}\left(t\in I_{\mathrm{Act,S_1}}\right)=1$ and $f_{\mathrm{v},2}\left(t\in I_{\mathrm{Act,S_2}}\right)=1$, then from an intuitive point of view, the set $\mathcal{T}_{\mathrm{Sup}}$ can be obtained evaluating the domain of the product function $f_{\mathrm{v},1}f_{\mathrm{v},2}$. To check if a superposition between two active intervals exists, the following situation must happen: both of the starting instants of time $t_{\mathrm{Start},1}$ and $t_{\mathrm{Start},2}$ must happen before both the ending instants of time $t_{\mathrm{End},1}$ and $t_{\mathrm{End},2}$. This can be written formally as in (5.16).

$$\max\left(t_{\mathrm{Start},1}\left(n_1\right),t_{\mathrm{Start},2}\left(n_2\right)\right)<\min\left(t_{\mathrm{End},1}\left(n_1\right),t_{\mathrm{End},2}\left(n_2\right)\right),\quad n_1,n_2\in\mathbb{N} \tag{5.16}$$

Given the expected ending of the missions of a constellation in $T_{\mathrm{End},\mathcal{C}}$, then the scanning of the superposition of the intervals can happen within a maximum instant of time $T_{\mathrm{Max}}=\min\left(T_{\mathrm{End},\mathcal{C}_1},T_{\mathrm{End},\mathcal{C}_2}\right)$, because it is supposed that it is not possible to exploit a combined measurement. From the evaluation of T_{Max}, then it is possible to obtain the total number of intervals for the satellites with $N_1=2\left(T_{\mathrm{Max}}-t_{0,1}\right)/T_1$ and $N_2=2\left(T_{\mathrm{Max}}-t_{0,2}\right)/T_2$.

With the aid of the condition in (5.16), it is possible to build an algorithm to predict and count the number of events with the aid of a counter N_{Events}, here denoted as collisions between constellations. When the total number of events have been calculated, then the frequency of collisions $f_{\mathrm{c}}=N_{\mathrm{Events}}/T_{\mathrm{Max}}$. The metrics $f_{\mathrm{c}}\left(\mathcal{C}_1,\mathcal{C}_2\right)$ can be useful to evaluate if two constellations $\mathcal{C}_1$ and $\mathcal{C}_2$ can be operatively exploited to perform combined measurements.

It is possible to filter the total number of events evaluating the quality of the collision with respect to local metrics, such as the position dilution of precision $PDOP$, which depends on the distribution of the satellites $\mathbf{x}_{\mathrm{S_1}}$, $\mathbf{x}_{\mathrm{S_2}}$ with respect to a local emitter of signal $\mathbf{x}_{\mathrm{E}}$. Furthermore, models for the variances of the measurements are required, which commonly can be estimated through the CRLB; in particular, for two satellites, the variances of AOA $\sigma^2_{\mathrm{AOA},1}$, $\sigma^2_{\mathrm{AOA},2}$, and TDOA σ^2_{TDOA} can be employed. Possible models can be the ones reported in Ch. 4 and Sec. 5.1. Functional dependence is then in the form

$$PDOP = f\left(\mathbf{x}_{\mathrm{S}_1}, \mathbf{x}_{\mathrm{S}_2}, \mathbf{x}_{\mathrm{E}}, \sigma^2_{\mathrm{AOA},1}, \sigma^2_{\mathrm{AOA},2}, \sigma^2_{\mathrm{TDOA}}\right). \tag{5.17}$$

The algorithm is presented in Fig. 5.5.

```
load $\mathbf{x}_{S_1}, \mathbf{x}_{S_2}, \mathbf{x}_E, \sigma^2_{AOA,1}, \sigma^2_{AOA,2}, \sigma^2_{TDOA}$    ▷ Initial data
load $R_\oplus, \mu_\oplus$    ▷ Earth model
set $t_{0,1}, t_{0,2}$    ▷ Initial instants of time
set $T_{End,\mathcal{C}_1}, T_{End,\mathcal{C}_2}$    ▷ Mission ending
$T_1 \leftarrow f(\mu_\oplus, r_1)$, $T_2 \leftarrow f(\mu_\oplus, r_2)$    ▷ Evaluate periods
$\Delta\nu_{v,1} \leftarrow f(R_\oplus, r_1)$, $\Delta\nu_{v,2} \leftarrow f(R_\oplus, r_2)$    ▷ True anomaly of visibility, as in (5.12)
$\Delta T_{v,1} \leftarrow f(\Delta\nu_{v,1}, T_1)$, $\Delta T_{v,2} \leftarrow f(\Delta\nu_{v,2}, T_2)$    ▷ Interval of time of visibility, as in (5.13)
$T_{Max} = f(T_{End,\mathcal{C}_1}, T_{End,\mathcal{C}_2})$    ▷ Time interval of scanning
$N_1 = f(t_{0,1}, T_1, T_{Max})$, $N_2 = f(t_{0,2}, T_2, T_{Max})$    ▷ Number of time intervals
for $n_1 \leftarrow 1$ to $N_1$ do
    Evaluate $t_{Start,1}(n_1)$ and $t_{End,1}(n_1)$    ▷ Starting and ending instants of time for 1
end for
for $n_2 \leftarrow 1$ to $N_2$ do
    Evaluate $t_{Start,2}(n_2)$ and $t_{End,2}(n_2)$    ▷ Starting and ending instants of time for 2
end for
initialize $N_{Events} = 0.$
for $n_1 \leftarrow 1$ to $N_1$ do
    for $n_2 \leftarrow 1$ to $N_2$ do
        if Inequality (5.16) is true then    ▷ Check if superposition exists
            if Evaluate $PDOP$ as in (5.17) then    ▷ Filter result with local metrics
                $N_{Events} = N_{Events} + 1.$    ▷ Update counter
            end if
        end if
    end for
end for
$f_c = N_{Events}/T_{Max}$    ▷ Frequency of collisions
return $f_c$
```

Figure 5.5: Operative algorithm to calculate the frequency of collisions.

Bibliography

[1] The MathWorks, Inc. MATLAB and Simulink website. URL: https://www.mathworks.com/ [Last accessed 31 October 2025].

[2] Chobotov, Vladimir A. *Orbital Mechanics.* AIAA Education Series, Cambridge University Press, Reston, VA, USA, third edition, 2002. ISBN: 1-56347-537-5.

[3] Prussing, J. E., Conway, B. A. *Orbital mechanics.* Oxford University Press, Inc., 200 Madison Avenue, New York, New York 10016, 1993. ISBN: 0-19-507834-9.

[4] J. Zhu. Conversion of earth-centered earth-fixed coordinates to geodetic coordinates. *IEEE Transactions on Aerospace and Electronic Systems*, 30(3):957–961, 1994.

[5] International Civil Aviation Organization. *Doc 9674 AN/946 - World geodetic system - 1984 (WGS-84) Manual.* ICAO, 2nd edition, 2002.

[6] Marcello Asciolla and Francesco Dell'Olio. Modeling and estimation of relativistic and atmospheric effects on time delay for satellite applications. *CEAS Space Journal*, pages 15430–15436, 2025.

[7] De Martino, Andrea. *Introduction to Modern EW Systems.* Artech House, Norwood, MA, USA, second edition, 2018. ISBN: 9781630815134.

[8] Poisel, Richard A. *Antenna Systems and Electronic Warfare Applications.* Artech House, Norwood, MA, USA, first edition, 2012. ISBN: 9781608074853.

[9] Poisel, Richard A. *Target Acquisition in Communication Electronic Warfare Systems.* Artech House, Norwood, MA, USA, first edition, 2004. ISBN: 1580539130.

[10] Poisel, Richard A. *RF Electronics for Electronic Warfare.* Artech House, Norwood, MA, USA, first edition, 2019. ISBN: 9781630817053.

[11] Poisel, Richard A. *Introduction to Communication Electronic Warfare Systems.* Artech House, Norwood, MA, USA, second edition, 2008. ISBN: 9781596934528.

[12] Robert G. Stansfield. Statistical Theory of D.F. Fixing. *Journal of the Institution of Electrical Engineers - Part IIIA: Radiocommunication*, 94:762–770, 1947.

[13] Poisel, Richard A. *Electronic Warfare Target Location Methods.* Artech House,

Norwood, MA, USA, second edition, 2012. ISBN: 9781608075232.

[14] Wiley, Richard G. *ELINT: The Interception and Analysis of Radar Signals.* Artech House, Norwood, MA, USA, first edition, 2006. ISBN: 1580539254.

[15] J. Capon. High-resolution frequency-wavenumber spectrum analysis. *Proceedings of the IEEE*, 57(8):1408–1418, 1969.

[16] R. Schmidt. Multiple emitter location and signal parameter estimation. *IEEE Transactions on Antennas and Propagation*, 34(3):276–280, 1986.

[17] R. Roy and T. Kailath. Esprit-estimation of signal parameters via rotational invariance techniques. *IEEE Transactions on Acoustics, Speech, and Signal Processing*, 37(7):984–995, 1989.

[18] Griffiths, Hugh Duncan and Baker, Christopher John. *An Introduction to Passive Radar.* Artech House, Norwood, MA, USA, second edition, 2022. ISBN: 9781630818401.

[19] Mathworks. *MATLAB Phased Array Toolbox User's Guide.* Mathworks, USA, 2024a edition, 2024a.

[20] O'Donoughue, Nicholas. *Emitter Detection and Geolocation for Electronic Warfare.* Artech House, Norwood, MA, USA, first edition, 2019. ISBN: 9781630815646.

[21] ITU Recommendation ITU-R P.676-13. *Attenuation by Atmospheric Gases and Related Effects.* P Series Radiowave propagation, ITU, 2022.

[22] Kay, Steven M. *Fundamentals of Statistical Signal Processing - Estimation Theory.* Prentice Hall, Upper Saddle River, NJ, USA, first edition, 1993. ISBN: 9780133457117.

[23] Marcello Asciolla, Rodrigo Blázquez-García, Angela Cratere, Francesco Menzione, and Francesco Dell'Olio. Optimization of multi-satellite constellations for gnss spectrum monitoring applications via aoa-tdoa receivers in leo. *Progress in Engineering Science*, 2(3):100123, 2025.

[24] Mark A. Richards, James A. Scheer, and William A. Holm. *Principles of Modern Radar - Vol. I: Basic Principles.* SciTech Publishing, 379 Thornall Street Edison, NJ 08837, 1st edition, 2010. ISBN: 978-1-891121-52-4.

[25] Marcello Asciolla, Angela Cratere, and Francesco Dell'Olio. Doppler effect estimation and compensation for satellite systems in geolocation problems. *IEEE Access*, 13:15430–15436, 2025.

[26] Mazzoldi, Paolo, Nigro, Massimo, and Voci, Cesare. *Fisica Vol. II - Elettromagnetismo e Onde.* Edises, Napoli, Italia, second edition, 2002. ISBN: 8879590006.

[27] Marcello Asciolla, Witold Dyszynski, and Francesco Dell'Olio. Simulation of the longitude error due to signal propagation in a passive emitter tracking geolocation algorithm. In *2024 IEEE Radar Conference (RadarConf24)*, pages 1–6, 2024.

[28] Marcello Asciolla, Angela Cratere, and Francesco Dell'Olio. Emitter tracking

by passive sensors onboard satellites: Relativistic error estimation in geolocation algorithm. In *2024 IEEE Sensors Applications Symposium (SAS)*, pages 1–6, 2024.

[29] Marcello Asciolla, Angela Cratere, and Francesco Dell'Olio. Estimating relativistic errors in satellite-based geolocation algorithms with passive sensors. In *MDPI: Proceedings of the 5th International Electronic Conference on Applied Sciences*, 2024.

[30] Eddington, A. S. *The Mathematical Theory of Relativity.* Cambridge University Press, Cambridge University Press, second edition, 1923. ISBN: 9780521091657.

[31] L. R. Gibson. Ad-a154 a derivation of relativistic effects in satellite tracking. In *Final Report Naval Surface Weapons Center, Dahlgren, VA.*, 1983.

[32] J. J. Freeman. Range-Error Compensation for a Troposphere With Exponentially Varying Refractivity. In *Journal of Research of the National Bureau of Standards - D. Radio Propagation*, volume 66D,n6, 1962.

[33] J. H. Gladstone and Dale T. P. XIV Researches on the Refraction, Dispersion, and Sensitiveness of Liquids. In *Philosophcal Transactions The Royal Society*, volume 153, page 317–343, 1863.

[34] Wolfgang Merzkirch. *Flow VVisualization.* Academic Press Inc., Orlando, Florida, USA, second edition, 1987. ISBN: 0124913512.

[35] ITU. The Radio Refractive Index: Its Formula and Refractivity Data. In *P Series, Radiowave propagation, Recommendation ITU-R P.453-11*, 2015.

[36] ITU. Reference Standard Atmospheres. In *P Series, Radiowave propagation, Recommendation ITU-R P.835-6*, 2017.

[37] Jeffrey G. Mangum and Patrick Wallace. Atmospheric Refractive Electromagnetic Wave Bending and Propagation Delay. *Publications of the Astronomical Society of the Pacific*, 127(947):74–91, January 2015.

[38] Jeffrey G. Mangum. Atmospheric Refractive Signal Bending and Propagation Delay. *NRAO Public Wiki*, 2009.

[39] Marcello Asciolla, Marasco Ilaria, Angela Cratere, Rodrigo Blázquez-García, Francesco Dell'Olio, and Antonella D'Orazio. [Provisional title]: geodesic ray-tracing for cubesat aoa payloads: Estimation and correction of atmospheric refraction bias in rf geolocation. Paper in preparation for ScienceDirect Elsevier, Aerospace Science and Technology Journal, expected acceptance 2026.

[40] John W. Marini. Correction of satellite tracking data for an arbitrary tropospheric profile. *Radio Science*, 7(2):223–231, 1972.

[41] H. S. Hopfield. Tropospheric refraction effects on satellite range measurements, 1972. APL Technical Digest, Vol. 11.

[42] P.E. Schmidt. Atmospheric tracking errors at s- and c-band frequencies, 1972. NASA Technical Note.

[43] Harvey G. Safran. On the bending of a ray through a spherically symmetric atmosphere, 1969. NASA Technical Memorandum.

[44] ITU. Effects of Tropospheric Refraction on Radiowave Propagation. In *Recommendation ITU-R P.834-2*, 1997.

[45] Brown, Kevin. *Reflections on Relativity.* -, Norwood, MA, USA, second edition, 2024. ISBN: 979-8332284304.

[46] J. Saastamoinen. Contribution to the theory of atmospheric refraction - part ii. refraction corrections in satellite geodesy. *Bull. Geodesique*, 107:13–34, January 1973.

[47] Bass, Michael. *Handbook of Optics: Volume V - Atmospheric Optics, Modulators, Fiber Optics, X-Ray and Neutron Optics.* McGraw-Hill Professional, New York, third edition, 2010. ISBN: (online) 9780071633147, (print) 9780071633130.

[48] Mátè Galambos, Giulio Cossu, and Ernesto Ciaramella. Comparing models and approximations of beam wander. In *2024 14th International Symposium on Communication Systems, Networks and Digital Signal Processing (CSNDSP)*, pages 250–255, 2024.

[49] L. C. Andrews, R. L. Phillips, D. Wayne, T. Leclerc, P. Sauer, R. Crabbs, and J. Kiriazes. Near-ground vertical profile of refractive-index fluctuations. In Linda M. Wasiczko Thomas and G. Charmaine Gilbreath, editors, *Atmospheric Propagation VI*, volume 7324, page 732402. International Society for Optics and Photonics, SPIE, 2009.

[50] Vladimir A. Bushenkov, Michael Yu. Ovchinnikov, and Georgi V. Smirnov. Attitude stabilization of a satellite by magnetic coils. *Acta Astronautica*, 50(12):721–728, 2002.

[51] Mariana Londoño Orozco and Belarmino Segura Giraldo. Attitude determination and control in small satellites: A review. *IEEE Journal on Miniaturization for Air and Space Systems*, 5(3):182–186, 2024.

[52] Vincenzo Pesce, Pablo Hermosin, Aureliano Rivolta, Shyam Bhaskaran, Stefano Silvestrini, and Andrea Colagrossi. Chapter nine - navigation. In Vincenzo Pesce, Andrea Colagrossi, and Stefano Silvestrini, editors, *Modern Spacecraft Guidance, Navigation, and Control*, pages 441–542. Elsevier, 2023.

[53] M. N. "Armenise, C. Ciminelli, F. Dell'Olio, and V. M. N. Passaro. *MEMS Gyroscopes*, pages 83–102. Springer Berlin Heidelberg, Berlin, Heidelberg, 2011.

[54] Francesco Dell'Olio, Teresa Natale, Yen-Chieh Wang, and Yung-Jr Hung. Miniaturization of interferometric optical gyroscopes: A review. *IEEE Sensors Journal*, 23(24):29948–29968, 2023.

[55] Vittorio M. N. Passaro, Antonello Cuccovillo, Lorenzo Vaiani, Martino De Carlo, and Carlo Edoardo Campanella. Gyroscope technology and applications: A review in the industrial perspective. *Sensors*, 17(10), 2017.

[56] NASA. State-of-the-art of small spacecraft technology - report, 2024. Last accessed 07 July 2025.

[57] Marcello Asciolla, Rodrigo Blázquez-García, Angela Cratere, Bossi-Núñez Pedro, Teresa Natale, and Francesco Dell'Olio. [Provisional title]: influence of attitude errors on aoa receivers in satellite systems. Paper submmitted and under review, AIAA Journal of Spacecraft and Rockets, expected acceptance 2025-2026.

[58] Marcello Asciolla, Angela Cratere, and Francesco Dell'Olio. Determination of conditions of divergence for antenna array measurements due to changes in satellite attitude. In *MDPI: The 6th International Electronic Conference on Applied Sciences*, 2025.

[59] G. B. Arfken and H. J. Weber. *Mathematical Methods for Physicists.* Elsevier, Academic Press, 30 Corporate Drive, Suite 400, Burlington, MA 01803, USA, 6th edition, 2005. ISBN: 0-12-088584-0.

[60] R. W. Beard and T. W. McLain. *Small Unmanned Aircraft - Theory and Practice.* Princeton University Press, 6 Oxford Street, Woodstock, Oxfordshire OX20 1TW, 2nd edition, 2012. ISBN: 978-0-691-14921-9.

[61] J. Van Sickle. *Basic GIS Coordinates.* CRC Press, Taylor and Francis Group, 6000 Broken Sound Parkway NW, Suite 300 Boca Raton, FL 33487-2742, 3rd edition, 2017. ISBN: 978-1-4987-7462-8.

[62] Wakker, K. F. *Fundamentals of Astrodynamics.* Institutional Repository Library, Delft University of Technology, Delft, The Netherlands, 2015. ISBN: 978-94-6186-419-2.

[63] Marcello Asciolla, Angela Cratere, and Francesco Dell'Olio. [Provisional title]: predicting and clustering attitude-induced divergence in cross-array aoa measurements for leo satellites. Paper in preparation for IET Radar, Sonar and Navigation, expected acceptance 2025-2026.

[64] Marcello Asciolla, Angela Cratere, and Francesco Dell'Olio. A compensation strategy for cases of divergence in angle of arrival measurements due to satellite attitude. CEAS-AIDAA Conference, Dec. 2025, Turin, Italy.

[65] Marcello Asciolla, Rodrigo Blázquez-García, Angela Cratere, and Francesco Dell'Olio. [Provisional title]: a semi-analytical method for angle of sight and visibility window for satellite platforms in geolocation applications. Paper submmitted and under review for RadarConf26 Conference, expected presentation May 2026, Phoenix, USA.

[66] Atkinson, Kendall. *An Introduction to Numerical Analysis.* John Wiley and Sons, second edition, 1989. ISBN: 0-471-62489-6.

[67] Marcello Asciolla and Francesco Dell'Olio. Multi-satellite spatial optimization in geolocation algorithm via passive sensors onboard satellites. *75th International Astronautical Congress*, Session B4,7 Constellations and Distributed Systems, 2024.

[68] Marcello Asciolla, Rodrigo Blázquez-García, Angela Cratere, and Francesco Dell'Olio. On the optimum update of satellite constellations with aoa receivers: a comparative analysis. In *2025 IEEE 12th International Workshop*

on Metrology for AeroSpace (MetroAeroSpace), pages 424–429, 2025.

[69] Marcello Asciolla, Rodrigo Blázquez-García, Angela Cratere, and Francesco Dell'Olio. On the influence of the snr on the optimization of two-satellite systems with aoa receivers. In *2025 IEEE Sensors Applications Symposium (SAS)*, pages 1–6, 2025.

[70] Marcello Asciolla, Rodrigo Blázquez-García, Angela Cratere, Vittorio M. N. Passaro, and Francesco Dell'Olio. Satellite constellation optimization for emitter geolocalization missions based on angle of arrival techniques. *Sensors*, 25(11), 2025.

[71] James Bao-Yen Tsui. *Fundamentals of Global Positioning System Receivers: A Software Approach.* Wiley, 2004. ISBN: Print: 9780471706472, Online: 9780471712589.

[72] Spilker Jr., J. J. and Axelrad, P. and Parkinson, B. W. and Enge, P. *Global positioning system: theory and applications, volume I.* Aerospace Research Central, 1996. ISBN: 978-1-56347-106-3.

[73] Mark H. Bergen, Ahmed Arafa, Xian Jin, Richard Klukas, and Jonathan F. Holzman. Characteristics of angular precision and dilution of precision for optical wireless positioning. *Journal of Lightwave Technology*, 33(20):4253–4260, 2015.

[74] Bishop A. N., Fidan B., Anderson B. D. O., Dogancay K., and Pathirana P. N. Optimality analysis of sensor-target geometries in passive localization: part 1 - bearing-only localization. In *3rd International Conference on Intelligent Sensors, Sensor Networks and Information, Melbourne, VIC, Australia*, 2007.

[75] Pages-Zamora A., Vidal J., and Brooks D. H. Closed-form solution for positioning based on angle of arrival measurements. In *The 13th IEEE International Symposium on Personal, Indoor and Mobile Radio Communications, Lisbon, Portugal*, volume 4, pages 1522–1526, 2002.

[76] Do-Jin An and Joon-Ho Lee. Derivation of an approximate location estimate in angle-of-arrival based localization in the presence of angle-of-arrival estimate error and sensor location error. In *2018 IEEE World Symposium on Communication Engineering (WSCE)*, pages 1–5, 2018.

[77] Trung-Kien Le and K. C. Ho. Joint source and sensor localization by angles of arrival. *IEEE Transactions on Signal Processing*, 68:6521–6534, 2020.

[78] Shuqiang Xue and Yuanxi Yang. Understanding gdop minimization in gnss positioning: Infinite solutions, finite solutions and no solution. *Advances in Space Research*, 59(3):775–785, 2017. BDS/GNSS+: Recent Progress and New Applications - Part 1.

[79] Ao Yongcai, Zhang Bo, Zhou Baozhuo, and Wang Shili. Change of geometric dilution of precision (gdop) for integrated system. In *2016 IEEE Information Technology, Networking, Electronic and Automation Control Conference*, pages 660–662, 2016.

[80] Er-jie Zhong and Ting-zhu Huang. Geometric dilution of precision in navigation computation. In *2006 International Conference on Machine Learning and Cybernetics*, pages 4116–4119, 2006.

[81] Chien-Sheng Chen, Kai-Sheng Chen, Jen-Fa Huang, and Yi-Ruie Li. Using genetic algorithms to approximate weighted geometric dilution of precision. In *2016 International Symposium on Computer, Consumer and Control (IS3C)*, pages 895–898, 2016.

[82] R. B. Langley. Dilution of precision. *GPS World*, 10:52–59, 1999.

[83] A.G. Dempster. Dilution of precision in angle-of-arrival positioning systems. *Electronics Letters*, 42:291–292, 2006.

[84] R. Byrd, J. Gilbert, and J. Nocedal. A trust region method based on interior point techniques for nonlinear programming. *Math. Program.*, 89:149–185, 2000.

[85] Boyd, Stephen and Vandenberghe, Lieven. *Convex Optimization.* Cambridge University Press, The Edinburgh Building, Cambridge, CB2 8RU, United Kingdom, seventh edition, 2009. ISBN: 978-0-521-83378-3.

[86] Mathworks. Matlab optimization toolbox user guide r2024a, 2024. `https://www.mathworks.com/help/optim/index.html` [Accessed: (31 Mar. 2025)].

[87] F. N. Fritsch and R. E. Carlson. Monotone piecewise cubic interpolation. *SIAM Journal on Numerical Analysis*, 17(2):238–246, 1980.

[88] Zhang Jiao and Lu Jianfeng. Analytical evaluation of geometric dilution of precision for three-dimensional angle-of-arrival target localization in wireless sensor networks. *International Journal of Distributed Sensor Networks*, 16(5), 2020.

[89] Zachary Clements, Todd E. Humphreys, and Patrick Ellis. Dual-satellite geolocation of terrestrial gnss jammers from low earth orbit. In *2023 IEEE/ION Position, Location and Navigation Symposium (PLANS)*, pages 458–469, 2023.

[90] S. Stein. Algorithms for ambiguity function processing. *IEEE Transactions on Acoustics, Speech, and Signal Processing*, 29(3):588–599, 1981.

[91] Marcello Asciolla, Francesco Menzione, Angela Cratere, and Francesco Dell'Olio. A multi-constellation approach to space-based rf emissions monitoring through opportunistic satellite cluster collisions in leo. CEAS-AIDAA Conference, Dec. 2025, Turin, Italy.